

A System-Level Framework for Fatigue Life Prediction of a PWR Pressurizer-Surge-Line Nozzle under Design-basis Loading Cycles

*A Complete Tensile Test Based Material Properties Database and
Preliminary Results on Weld Process Modeling, Thermal-Mechanical
Stress Analysis and Environmental Fatigue Testing*

Nuclear Science and Engineering Division

About Argonne National Laboratory

Argonne is a U.S. Department of Energy laboratory managed by UChicago Argonne, LLC under contract DE-AC02-06CH11357. The Laboratory's main facility is outside Chicago, at 9700 South Cass Avenue, Argonne, Illinois 60439. For information about Argonne and its pioneering science and technology programs, see www.anl.gov.

DOCUMENT AVAILABILITY

Online Access: U.S. Department of Energy (DOE) reports produced after 1991 and a growing number of pre-1991 documents are available free via DOE's SciTech Connect (<http://www.osti.gov/scitech/>)

Reports not in digital format may be purchased by the public from the National Technical Information Service (NTIS):

U.S. Department of Commerce
National Technical Information Service
5301 Shawnee Rd
Alexandria, VA 22312
www.ntis.gov
Phone: (800) 553-NTIS (6847) or (703) 605-6000
Fax: (703) 605-6900
Email: orders@ntis.gov

Reports not in digital format are available to DOE and DOE contractors from the Office of Scientific and Technical Information (OSTI):

U.S. Department of Energy
Office of Scientific and Technical Information
P.O. Box 62
Oak Ridge, TN 37831-0062
www.osti.gov
Phone: (865) 576-8401
Fax: (865) 576-5728
Email: reports@osti.gov

Disclaimer

This report was prepared as an account of work sponsored by an agency of the United States Government. Neither the United States Government nor any agency thereof, nor UChicago Argonne, LLC, nor any of their employees or officers, makes any warranty, express or implied, or assumes any legal liability or responsibility for the accuracy, completeness, or usefulness of any information, apparatus, product, or process disclosed, or represents that its use would not infringe privately owned rights. Reference herein to any specific commercial product, process, or service by trade name, trademark, manufacturer, or otherwise, does not necessarily constitute or imply its endorsement, recommendation, or favoring by the United States Government or any agency thereof. The views and opinions of document authors expressed herein do not necessarily state or reflect those of the United States Government or any agency thereof,

A System-Level Framework for Fatigue Life Prediction of a PWR Pressurizer-Surge-Line Nozzle under Design-basis Loading Cycles

A Complete Tensile Test Based Material Properties Database and Preliminary Results on Weld Process Modeling, Thermal-Mechanical Stress Analysis and Environmental Fatigue Testing

Subhasish Mohanty, Joseph Listwan, and Jae Phil Park

**Nuclear Science and Engineering Division
Argonne National Laboratory**

September 2019

This page intentionally left blank

ABSTRACT

This report presents an update on the environmental fatigue research that is being conducted at Argonne National Laboratory in support of the US Department of Energy's Light Water Reactor Sustainability (LWRS) program. The report highlights some of the major work conducted during FY 2019.

In this report, we present a tensile-test-based material properties database, written in an industry-standard SQL format, that covers most of the important materials in a reactor coolant system. These include 316 stainless steel (SS), 508 low alloy steel (LAS), similar-metal welds (SMWs) between 316 SS and 316 SS, and dissimilar-metal welds (DMWs) between, e.g., 508LAS and 316SS. The DMWs include both In-82 filler welds and In-182 butter welds. The material properties were estimated from a total of 21 tensile tests conducted under the LWRS program. The tests were conducted either during FY 2019 or earlier. The database includes tensile properties, material-hardening properties, and thermal expansion coefficients. Information on most of these properties is hard to find in the public domain, especially for SMW and DMW materials. Hence, attempts will be made to place this database in the public domain (such as on the LWRS and/or USNRC website). We anticipate that the above-mentioned property database, along with this report, will be a vital resource for industry and regulatory agencies such as the USNRC. The property database can be used for firsthand thermal-mechanical stress analysis of a majority of the reactor pressure boundary components.

In addition to the above database, we also present an ABAQUS-MATLAB-PYTHON-based framework for complex 3D weld process modeling in a reactor nozzle. The approach developed here significantly reduces the complexity of weld process modeling. The presently available ABAQUS graphical user interface-based weld modeling approach is highly complex if many weld passes and chunks need to be modeled. The weld-modeling framework developed here is highly flexible and allows one to add any number of weld passes (with each pass comprising any number of weld chunks).

This report also presents some preliminary work on component-level fatigue estimation for reactor components such as a pressurizer-surge-line nozzle assembly. This method is based on the combined use of computational mechanics (such as through finite-element-analysis-based thermal-mechanical stress analysis of actual components under actual thermal-mechanical loading cycles) and uniaxial fatigue experiments (with loading inputs directly based on the finite element model-simulated strain histories). We demonstrated the approach with respect to the fatigue life estimation of a pressurizer-surge-line nozzle subjected to design-basis thermal-mechanical loading cycles. From the results, we found that environmental effects are sensitive to mean strain. We note that in the conventional $R=-1$ type strain-controlled tests (which are the basis for building the $S-N$ curves), the mean strain and strain amplitude are artificially forced to remain constant. However, under realistic loading cycles, the strain may ratchet, as demonstrated in this report. The evolution of the environmental effect can be tracked through the ratcheting strain and through the related strain amplitude and mean strain. On the basis of this observation, it is suggested that one should consider strain as the major damage affecting parameters, and hence its time evolution (with/without environment effect) should be tracked to achieve more mechanistically based low-cycle-fatigue evaluation of reactor components.

This page intentionally left blank

TABLE OF CONTENTS

<i>A System-Level Framework for Fatigue Life Prediction of a PWR Pressurizer-Surge-Line Nozzle under Design-basis Loading Cycles.....</i>	<i>iii</i>
ABSTRACT	1
Table of Contents	3
List of Figures.....	5
List of TABLES.....	10
Abbreviations	12
Acknowledgments.....	13
1 Introduction	15
1.1 Safe-life, Fail-safe, Damage-tolerance, and Online Structural Health Monitoring Approaches	15
1.1.1 Safe-life approach	15
1.1.2 Fail-safe approach:.....	15
1.1.3 Damage-tolerance approach:	16
1.1.4 Online structural health monitoring:	16
1.2 Physical-Digital-Twin Framework for Structural-integrity Prediction of Reactor Components.....	16
1.2.1 Computational mechanics-based structural-integrity prediction.....	18
1.2.2 Time-series data based online damage tolerance and probabilistic damage prediction:	18
1.2.3 Integrated physics/data-based online damage forecasting:.....	18
1.3 Organization of This Report	18
2 Tensile Tests and Properties of Base, Weld and Heat-affected-zone metals	20
2.1 Typical Materials Used in Reactor Pressure Boundary Components	20
2.2 Dissimilar Metal Weld Fabrication and Test Specimens.....	21
2.3 Summary of Results from Tensile Tests Conducted in FY 2019 and Earlier	24
3 Tensile Material-hardening Parameter Estimation and Finite-element Model Validation.....	32
3.1 Material Hardening Model.....	32
3.2 Estimated Material-hardening Parameters.....	34
3.3 Finite-element Validation of a Representative Test Cases	46
4 Estimation of Thermal Expansion Coefficients for Base and Welds.....	53
4.1 Expansion Coefficients for Argonne-Conducted Test Cases	53
4.2 Validity Check of Estimated Expansion Coefficients	61
5 Estimation of Cycle-Dependent Ramberg-Osgood Parameters for Similar Metal Welds.....	63
5.1 Ramberg-Osgood Model Theoretical Background	63
5.2 Input Data.....	64

5.3 Results of Cyclic Ramberg-Osgood Model.....	67
6 FE Modeling-based 3D Heat-Transfer Analysis of Nozzle Weld Processes	76
6.1 Thermal Properties for Weld Models	78
6.2 Weld Process Model Validation Based on Experimental Plate Weld Data	80
6.3 Preliminary Model Results of Surge Line Nozzle Weld.....	84
7 FE Modeling-based 3D Thermal-Mechanical Stress Analysis of Nozzle Assembly under Design-basis Loading Cycle	96
7.1 FE Model Thermal-Mechanical Boundary Conditions and Properties Used	96
7.1.1 Mechanical and Thermal Boundary Conditions	96
7.1.2 Material Properties	99
7.2 Heat Transfer Analysis Results	101
7.3 Thermal-Mechanical Stress Analysis Results.....	103
8 Fatigue Life Estimation of Pressurizer-Surge Line Nozzle under In-Air and PWR-Water Environment and under Design-Basis Loading Cycles	112
8.1 Various Methods for Component-level Fatigue Estimation	112
8.2 Uniaxial Fatigue Test Results of DMW-filler Weld Specimens	113
8.2.1 Fatigue test setup	113
8.2.2 Test inputs for fatigue tests	115
8.2.3 Study of the time-evolution of environmental effects	119
9 Summary and Future Studies	127
9.1 Summary	127
9.2 Future Studies	128
References	129

LIST OF FIGURES

Figure 1. 1 Schematic of the futuristic Physical-Digital-Twin framework (actual reactor image inset taken from [10]).	17
Figure 2 1 Schematic of typical PWR pressure boundary system and the materials used in a typical nozzle.	20
Figure 2 2 Weld plates before start of the DMW filler welding at Argonne machine shop.	22
Figure 2 3 Radiographic image of the welded DMW plate.	23
Figure 2 4 Cross-section of the weld plates (only near the weld region) and location of the along-the-length weld and HAZ specimens.	23
Figure 2 5 Geometry of hourglass-type specimens.	24
Figure 2 6 a) Test section with induction heating coil, b) LEPEL induction heating system, and c) close view of induction heating coil and specimen and extensometer location.	25
Figure 2 7 Schematic of MATLAB-PYTHON-SQL framework for automated material parameter estimation.	27
Figure 2 8 Screen shot of the SQL material database.	27
Figure 2 9 Full stress-strain curves of different metals at room temperature	28
Figure 2 10 Magnified stress-strain curves (below 2% strain) of different metals at room temperature	28
Figure 2 11 Full stress-strain curves of different metals at a temperature of 300°C	29
Figure 2 12 Magnified stress-strain curves (below 2% strain) of different metals at a temperature of 300°C	29
Figure 3. 1 Equivalent monotonic stress-strain curves over 50 cycles estimated from data obtained through a previously conducted environment fatigue test (316SS specimen).	34
Figure 3. 2 Nonlinear kinematic hardening constant $C1$ with respect to number of iterations during parameter estimation using a gradient-based optimization scheme and T14 stress-strain data (from 0.2% offset strain yield limit to 5% true total strain).	35
Figure 3. 3 Nonlinear kinematic hardening constant $\gamma1$ with respect to number of iterations during parameter estimation using a gradient-based optimization scheme and T14 stress-strain data (from 0.2% offset strain yield limit to 5% true total strain).	36
Figure 3. 4 L_2 norm (of incremental kinematic hardening constants $C1$ and $\gamma1$) with respect to number of iterations during parameter estimation using a gradient-based optimization scheme and T14 stress-strain data (from 0.2% offset strain yield limit to 5% true total strain).	36
Figure 3. 5 Comparison of regenerated true back stress (using nonlinear kinematic hardening parameters $C1$ and $\gamma1$ and considering 0.2% offset strain as yield limit strain) with experimental true back stress for T14 tensile test.	37
Figure 3. 6 Comparison of regenerated true total stress (using nonlinear kinematic hardening parameters $C1$ and $\gamma1$ and considering 0.2% offset strain as yield limit strain) with experimental true total stress for T14 tensile test.	37
Figure 3. 7 Screen shot of the ABAQUS property module showing the use of Chaboche nonlinear material-hardening parameters.	47
Figure 3. 8 Schematic of the equivalent FE model (of uniaxial tensile specimen).	48

Figure 3. 9 Experimental vs. FE model results for RT-T14 filler weld specimen with respect to different offset yield conditions.	48
Figure 3. 10 Magnified version of Figure 3.9.	49
Figure 3. 11 Experimental vs. FE model results for RT-T16 butter weld specimen with respect to different offset yield conditions.	49
Figure 3. 12 Magnified version of Figure 3.11.	50
Figure 3. 13 Experimental vs. FE model results for RT-T18 316SS HAZ specimen with respect to different offset yield conditions.	50
Figure 3. 14 Magnified version of Figure 3.13.	51
Figure 3. 15 Experimental vs. FE model results for RT-T20 508LAS HAZ specimen with respect to different offset yield conditions.	51
Figure 3. 16 Magnified version of Figure 3.15.	52
Figure 4. 1 Time vs. gauge area average temperature and strain measured during heating in T04 tensile test specimen: 316SS base metal.	55
Figure 4. 2 Temperature vs. estimated mean expansion coefficient from T04 tensile test data: 316SS base metal.	55
Figure 4. 3 Time vs. gauge area average temperature and strain measured during heating in T05 tensile test specimen: 316SS SMW filler weld.	56
Figure 4. 4 Temperature vs. estimated mean expansion coefficient from T05 tensile test data: 316SS SMW filler weld.	56
Figure 4. 5 Time vs. gauge area average temperature and strain measured during heating in T13 tensile test specimen: DMW In-82 filler weld.	57
Figure 4. 6 Temperature vs. estimated mean expansion coefficient from T13 tensile test data: DMW In-82 filler weld.	57
Figure 4. 7 Time vs. gauge area average temperature and strain measured during heating in T15 tensile test specimen: DMW In-82 butter weld.	58
Figure 4. 8 Temperature vs. estimated mean expansion coefficient from T15 tensile test data: DMW In-82 butter weld.	58
Figure 4. 9 Time vs. gauge area average temperature and strain measured during heating in T19 tensile test specimen: 508LAS DMW-HAZ.	59
Figure 4. 10 Temperature vs. estimated mean expansion coefficient from T19 tensile test data: 508LAS DMW-HAZ.	59
Figure 4. 11 Comparison of the Argonne-estimated expansion coefficients with ASME code (Section IID) expansion coefficients for similar-grade materials.	61
Figure 4. 12 FE-simulated nodal temperature (in °C) contour of PRZ-SL nozzle during the hot-standby to power-operation transition.	62
Figure 4. 13 FE-simulated thermal strain (in mm/mm) contour of PRZ-SL nozzle during the hot-standby to power-operation transition.	62
Figure 5. 1 Cyclic elastic modulus for fatigue testing cases from $N=1$ to $N=N_f$	65
Figure 5. 2 Cyclic elastic limit stress for fatigue testing cases from $N=1$ to $N=N_f$	66
Figure 5. 3 Cyclic Chaboche parameter $C1$ for fatigue testing cases from $N=1$ to $N=N_f$	66
Figure 5. 4 Cyclic Chaboche parameter $\gamma1$ for fatigue testing cases from $N=1$ to $N=N_f$	67
Figure 5. 5 Comparison of the reference tensile (RT-T05) stress-strain curve and reconstructed cyclic stress-strain curves for RT-F08 fatigue test case.	68

Figure 5. 6 Comparison of the reference tensile (ET-T05) stress-strain curve and reconstructed cyclic stress-strain curves for ET-F07 fatigue test case. 68

Figure 5. 7 Comparison of the reference tensile (ET-T05) stress-strain curve and reconstructed cyclic stress-strain curves for ET-F17 fatigue test case. 69

Figure 5. 8 Comparison of the reference tensile (ET-T05) stress-strain curve and reconstructed cyclic stress-strain curves for ET-F18 fatigue test case. 69

Figure 5. 9 Schematic illustration describing the definition of the elastic and plastic parts of the stress-strain curve..... 70

Figure 5. 10 Estimated Ramberg-Osgood parameters (hardening modulus K) for fatigue testing cases from $N=1$ to $N=N_f$ 71

Figure 5. 11 Estimated Ramberg-Osgood parameters (hardening exponent n) for fatigue testing cases from $N=1$ to $N=N_f$ 72

Figure 5. 12 Reconstructed R-O model-based cyclic stress-strain curves for RT-F08 fatigue test.72

Figure 5. 13 Reconstructed R-O model-based cyclic stress-strain curves for ET-F07 fatigue test.73

Figure 5. 14 Reconstructed R-O model-based cyclic stress-strain curves for ET-F17 fatigue test.73

Figure 5. 15 Reconstructed R-O model-based cyclic stress-strain curves for EN-F18 fatigue test.74

Figure 5. 16 Estimated stress amplitude-based R-O model..... 74

Figure 5. 17 Measured engineering maximum/minimum stress fatigue testing cases. 75

Figure 6. 1 Schematic of the ABAQUS-PYTHON-MATLAB weld model framework..... 77

Figure 6. 2 Screen shot of the ABAQUS/GUI-based weld interaction module. 77

Figure 6. 3 Temperature versus thermal conductivity. 78

Figure 6. 4 Temperature versus specific heat capacity. 79

Figure 6. 5 Temperature versus heat transfer or film coefficient 79

Figure 6. 6 Weld plate CAD model showing a) top view of the welded plate geometry and b) cross-section of weld plate. 81

Figure 6. 7 Section of the cross-section of weld plate showing the finite element mesh near the weld region. 82

Figure 6. 8 FE (nodal temperature) vs experiment (TC measurements) at three distances from the center of the weld..... 82

Figure 6. 9 FE (nodal temperature) along the length of the weld plate. 83

Figure 6. 10 FE simulated temperature contour at different times during the pass 1 welding. 83

Figure 6. 11 FE simulated temperature contour at different times during the pass 2 welding. 84

Figure 6. 12 Partial CAD model of PWR pressure control system showing the location of the surge line nozzle. 86

Figure 6. 13 CAD model of surge line nozzle and bottom head of pressurizer..... 86

Figure 6. 14 Cut section of the nozzle assembly showing different material systems. 87

Figure 6. 15 Finite element mesh of the whole nozzle assembly. 87

Figure 6. 16 Cut section of the nozzle assembly finite element mesh..... 88

Figure 6. 17 Weld pass sequence for the PWR surge line nozzle..... 88

Figure 6. 18 Weld circumferential chunks in a single pass of the nozzle weld (in SMW filler region). 89

Figure 6. 19 Nozzle weld simulation measurement nodes. 89

Figure 6. 20 Temperature histories at set 1 nodes of case 1 model (Only DMW butter weld modeled). 90

Figure 6. 21 Temperature histories at set 2 nodes of case 1 model (Only DMW butter weld modeled).	90
Figure 6. 22 Temperature histories at set 3 nodes of case 1 model (Only DMW butter weld modeled).	91
Figure 6. 23 Temperature contours at different times in the case 1 model (Only DMW butter weld modeled).	91
Figure 6. 24 Temperature histories at set 1 nodes of the case 2 model (both DMW butter and filler welds modeled).	92
Figure 6. 25 Temperature histories at set 2 nodes of the case 2 model (both DMW butter and filler welds modeled).	92
Figure 6. 26 Temperature histories at set 3 nodes of the case 2 model (both DMW butter and filler welds modeled).	93
Figure 6. 27 Temperature contours at different times in the case 2 model (both DMW butter and filler welds modeled).	93
Figure 6. 28 Temperature histories at set 1 nodes of the case 3 model (both DMW butter and filler welds and SMW filer weld modeled).	94
Figure 6. 29 Temperature histories at set 2 nodes of the case 3 model (both DMW butter and filler welds and SMW filer weld modeled).	94
Figure 6. 30 Temperature histories at set 3 nodes of the case 3 model (both DMW butter and filler welds and SMW filer weld modeled).	95
Figure 6. 31 Temperature contours at different times in the case 3 model (both DMW butter and filler welds and SMW filer weld modeled).	95
Figure 7. 1 Displacement boundary condition for nozzle FE model.	97
Figure 7. 2 Internal pressure boundary condition for nozzle FE model: (a) full cycle, (b) during heat-up, and (c) during cool-down.	98
Figure 7. 3 Temperature boundary condition for nozzle FE model: (a) full cycle, (b) during heat-up, and (c) during cool-down.	99
Figure 7. 4 Simulated OD surface temperature contour after 0.13212 days (3.1709 hours) from the start of the heat-up operation	101
Figure 7. 5 Simulated ID surface temperature contour after 0.13212 days (3.1709 hours) from the start of the heat-up operation.	101
Figure 7. 6 Simulated OD surface temperature contour after 1.3717 days (32.921 hours) from the start of the heat-up operation.	102
Figure 7. 7 Simulated ID surface temperature contour after 1.3717 days (32.921 hours) from the start of the heat-up operation.	102
Figure 7. 8 FE model (case-1) simulated total, thermal, and mechanical strain (along x-direction) at the maximum stress element of the DMW-filler weld: (a) full cycle, (b) during heat-up, and (c) during cool-down	104
Figure 7. 9 FE model (case-1) simulated total, thermal, and mechanical strain (along max. principal direction) at the maximum stress element of the DMW-filler: (a) full cycle, (b) during heat-up, and (c) during cool-down.	105
Figure 7. 10 Simulated (case-1) OD-side maximum principal thermal strain contour after 0.13212 days (3.1709 hours) from the start of the heat-up operation	106
Figure 7. 11 Simulated (case-1) ID-side maximum principal thermal strain contour after 0.13212 days (3.1709 hours) from the start of the heat-up operation	106

Figure 7. 12 Simulated (case-1) OD-side maximum principal thermal strain contour after 1.3717 days (32.921 hours) from the start of the heat-up operation 107

Figure 7. 13 Simulated (case-1) ID-side maximum principal thermal strain contour after 1.3717 days (32.921 hours) from the start of the heat-up operation 107

Figure 7. 14 FE model (case-1) simulated axial stress (along x-direction) and Von Mises stress at the maximum stress element of DMW filler weld: (a) full cycle, (b) during heat-up, and (c) during cool-down 108

Figure 7. 15 Experiment versus FE model (case-1) simulated stress-strain curve 108

Figure 7. 16 Simulated OD-side Von Mises stress contour after 0.13212 days (3.1709 hours) from the start of the heat-up operation 109

Figure 7. 17 Simulated ID-side Von Mises stress contour after 0.13212 days (3.1709 hours) from the start of the heat-up operation 109

Figure 7. 18 Simulated OD-side Von Mises stress contour after 1.3717 days (32.921 hours) from the start of the heat-up operation 110

Figure 7. 19 Simulated ID-side Von Mises stress contour after 1.3717 days (32.921 hours) from the start of the heat-up operation 110

Figure 8. 1 Chart showing different possible methods for fatigue life prediction of full-scale component/assembly 112

Figure 8. 2 Environmental test loop showing different subsystems. 113

Figure 8. 3 Thermocouple readings at different locations of the PWR-water test-loop during the heat-up and actual test..... 114

Figure 8. 4 Pressure histories at of the PWR-water test-loop during the heat-up and actual test 114

Figure 8. 5 Flow velocity of the PWR-water test-loop during the heat-up and actual test..... 115

Figure 8. 6 FE simulated and rescaled (in time-axis) mechanical strain history at the maximum stressed element of DMW-filler weld region (of PRZ-SL nozzle). 116

Figure 8. 7 Strain rates of the rescaled strain history shown in Figure 8.6..... 117

Figure 8. 8 Mapped stroke history applied to the test specimen. 117

Figure 8. 9 Stroke rates of the stroke profile shown in Figure 8.8 118

Figure 8. 10 Cycle versus applied stroke and observed frame actuator position for in-air (ET-F54) fatigue test..... 121

Figure 8. 11 Cycle versus observed gauge-area stress for in-air (ET-F54) fatigue test..... 121

Figure 8. 12 Cycle versus observed gauge-area strain for in-air (ET-F54) fatigue test..... 122

Figure 8. 13 Cycle versus applied stroke and observed frame actuator position for PWR-water (EN-F56) fatigue test. 122

Figure 8. 14 Cycle versus observed gauge-area stress for PWR-water (EN-F56) fatigue test... 123

Figure 8. 15 Comparison of cycle versus observed stress amplitude for in-air (ET-F54) and... 123

Figure 8. 16 Comparison of cycle versus observed mean stress for in-air (ET-F54) and 124

Figure 8. 17 Comparison of observed mean stress versus observed stress amplitude for in-air (ET-F54) and PWR-water (EN-F56) fatigue tests. 124

Figure 8. 18 Cycle versus observed gauge-area strain amplitude for in-air (ET-F54) test..... 125

Figure 8. 19 Cycle versus observed gauge-area mean strain for in-air (ET-F54) test. 125

Figure 8. 20 Comparison of cycle versus observed actuator-position amplitude for in-air (ET-F54) and PWR-water (EN-F56) fatigue tests. 126

Figure 8. 21 Comparison of cycle versus observed mean actuator-position for in-air (ET-F54) and PWR-water (EN-F56) fatigue tests. 126

LIST OF TABLES

Table 2. 1 Compositions of various base and welding materials.....	21
Table 2. 2 Test ID, environment, and material of different tensile specimens	26
Table 2. 3 Estimated tensile test material properties for different reactor pressure boundary metals at room temperature.	30
Table 2. 4 Estimated tensile test material properties for different reactor pressure boundary metals at a temperature of 300°C.....	31
Table 3. 1 Room-temperature tensile material-hardening parameters of different metals (in reactor pressure boundary components) assuming elastic limit as yield limit.....	38
Table 3. 2 Room-temperature tensile material-hardening parameters of different metals (in reactor pressure boundary components) assuming 0.05% offset strain as yield limit	39
Table 3. 3 Room-temperature tensile material-hardening parameters of different metals (in reactor pressure boundary components) assuming 0.1% offset strain as yield limit	40
Table 3. 4 Room-temperature tensile material-hardening parameters of different metals (in reactor pressure boundary components) assuming 0.2% offset strain as yield limit	41
Table 3. 5 Elevated-temperature (300°C) tensile material-hardening parameters of different metals (in reactor pressure boundary components) assuming elastic limit as yield limit.....	42
Table 3. 6 Elevated temperature (300°C) tensile material-hardening parameters of different metals (in reactor pressure boundary components) assuming 0.05% offset strain as yield limit	43
Table 3. 7 Elevated temperature (300°C) tensile material-hardening parameters of different metals (in reactor pressure boundary components) assuming 0.1% offset strain as yield limit	44
Table 3. 8 Elevated-temperature (300°C) tensile material-hardening parameters of different metals (in reactor pressure boundary components) assuming 0.2% offset strain as yield limit	45
Table 4. 1 Characteristics of tensile specimens whose heat-up data were used for estimating expansion coefficients.....	54
Table 4. 2 Argonne-estimated expansion coefficients for 316SS and 508LAS base, 316SS-SW filler, and 316SS-508LAS DW filler and butter welds	60
Table 5. 2 Experimental conditions for two tensile and four fatigue test cases.....	64
Table 5. 3 Estimated mechanical properties for tensile testing cases and fatigue testing cases at initial quarter cycle.....	65
Table 5. 4 Estimated R-O parameters for tensile testing cases and fatigue testing cases at first quarter-cycle.	71
Table 7. 1 Tensile elastic-plastic properties used for 316SS base metal	100
Table 7. 2 Tensile elastic-plastic properties used for 316SS SMW-Filler Weld and 316ss Cladding	100
Table 7. 3 Tensile elastic-plastic properties used for 508 LAS base metal	100
Table 7. 4 Tensile elastic-plastic properties used for DMW-Butter weld	100
Table 7. 5 Tensile elastic-plastic properties used for DMW-Filler weld.....	100
Table 7. 6 Summary of maximum stress and strain at the highest stressed element in the DMW-filler region of the nozzle assembly.....	111

Table 8. 1 Loading, environment and fatigue lives of DMW/filler weld specimens..... 118

ABBREVIATIONS

3D	Three Dimensional
ANL	Argonne National Laboratory
ASME	American Society of Mechanical Engineers
CL	Cold Leg
DMW	Dissimilar Metal Weld
ET	Elevated Temperature
FE	Finite Element
HAZ	Heat Affected Zone
HL	Hot Leg
HPC	High Performance Computing
HT	Heat Transfer
ID	Inner Diameter
LAS	Low Alloy Steel
LWR	Light Water Reactor
LWRS	Light Water Reactor Sustainability
OSHM	Online Structural Health Monitoring
PDT	Physical-Digital-Twin
PRZ	Pressurizer
PWR	Pressurized Water Reactor
RT	Room Temperature
RPB	Reactor Pressure Boundary
RPV	Reactor Pressure Vessel
RCS	Reactor Coolant System
SMW	Similar Metal Weld
SL	Surge Line
SS	Stainless Steel

ACKNOWLEDGMENTS

This research was supported through the U.S. Department of Energy's Light Water Reactor Sustainability program under the work package of environmental fatigue study, program manager Dr. Thomas. M. Rosseel. This report also includes some of the work conducted by PhD student Mr. Jae Phil Park (from Pusan National University, Busan, Republic of Korea) during his 2019 summer internship at Argonne National Laboratory. United States-Republic of Korea (ROK) International Nuclear Energy Research Initiative (INERI) funding supported Mr. Park's summer internship.

This page intentionally left blank

1 Introduction

Accurate structural integrity prediction of nuclear reactor components is important for safe and long-term economical operation of the US nuclear reactor fleet. Among different physics-based approaches to structural-integrity prediction, the safe-life and fail-safe approaches are common, particularly in the aerospace industry [1–3], whereas in the nuclear industry, the safe-life approach is more popular. In addition to the above physics- or mechanics-based methods, the non-destructive evaluation (NDE)-based damage-tolerance approach is also widely used for structural-integrity assessment of nuclear reactor and aerospace components. Inspection-based NDE techniques are primarily offline techniques; i.e., they are used when a component is not in operation. With recent advances in data analytics and internet-of-things (IOT) techniques, the online structural health monitoring (OSHM) technique [4–7] is increasingly becoming an option for real-time structural-integrity prediction of safety-critical structures. The OSHM technique is increasingly drawing the attention of the aerospace and energy industries for reducing high operation and maintenance (O&M) costs. In this section, we briefly discuss the four above-mentioned approaches and a futuristic physical-digital-twin (PDT) framework for more robust on-demand structural-integrity prediction of reactor components.

1.1 Safe-life, Fail-safe, Damage-tolerance, and Online Structural Health Monitoring Approaches

1.1.1 Safe-life approach

A component designed under the safe-life approach is assumed not to fail under the stated operating load and within a stated period called the design life. The benefits of safe-life designs include reducing the likelihood of unplanned maintenance and reducing the likelihood of any catastrophic failure. Under the safe-life approach, a design load is selected by considering a safety factor with respect to the ultimate load-carrying limit of a component. In general, most of the operating LWRs inside and outside the US are designed for a life of 40 years. Also, most of the pressure-boundary components of these reactors are originally designed with a safe-life assumption such that they are anticipated not to fail at all or to have a very low failure probability. However, owing to economical considerations, the LWR fleet needs to operate beyond its original design life of 40 years. With this need in mind, the basic requirement of safe-life design to restrict the operation of the reactor to its maximum design life is violated. When the safe-life criterion is violated, then the question arises whether those reactors are now safe to operate. That question leads to the discussion of fail-safe criteria.

1.1.2 Fail-safe approach:

A component designed under fail-safe conditions is designed to remain safe in the event of a failure. A fail-safe design does not prevent failure but withstand failure when it does occur. In the context of the aerospace industry, an example is the minimum requirement of two engines and multiple load paths for commercial aircraft. When the aircraft is airborne, if one engine fails, the aircraft can still fly and land using the second engine. Similarly, with multiple load paths, if a structural element of an aircraft fails, the airplane can still fly and land because the load can be transferred to other load-carrying members. In that context, a nuclear reactor component that has already exceeded the above mentioned safe-life limit of 40 years and is still operating can be considered as an example of a fail-safe component. This is true for a component without or with the presence of a detectable crack much smaller than the critical length (at which the component would completely or catastrophically fail). For a component with undetectable

cracks, the material of the component might have degraded (because it has already passed the initial safe-life limit of 40 years), but not enough to show any sign of failure, and the component can still survive many years of operation. Similarly, if detectable cracks are present but are much smaller than the critical length, the component can still survive many years of operation with/without minor repair (e.g., use of a weld overlay to prevent future growth of a crack in a reactor nozzle). The USNRC's approach to extend the license of some LWRs from 40 years to 60 years can be considered an example of rebranding a pressure-boundary component from safe-life to fail-safe. Under fail-safe conditions, the probability of detecting a crack during a routine inspection, before it could progress to catastrophic failure, is very high. A fail-safe regime allows the safe operation of a component up to a maximum detectable defect size (also known as the allowable damage limit).

1.1.3 Damage-tolerance approach:

A damage-tolerance approach assumes that flaws can be present in any structure and can propagate with usage or under operating loadings and environments, but the component can still be operated safely. However, the damage-tolerance approach emphasizes rigorous inspections to detect flaws before they can progress to critical limits. Damage tolerance requires an inspection regime (e.g., through NDE) tailored to the flaw progression characteristics of a particular component under the expected loading spectrum and environment. Damage tolerance places a much higher emphasis on a frequent inspection regime to detect flaws before they progress to critical or unsafe limits, whereas a fail-safe approach allows cracks to grow to obvious and easily detected dimensions.

1.1.4 Online structural health monitoring:

OSHM techniques are becoming increasingly popular because of the advancement of IOT, advanced sensor, data analytics, and artificial intelligence techniques. The research on OSHM substantially increased in the US and elsewhere after the start of NASA's integrated vehicle health management (IVHM) program [8]. Within the last 10–15 years, substantial research has been conducted on OSHM techniques, including the first author's work in both the aerospace and nuclear energy domains [4-7]. Recently, the nuclear reactor industry has also tried to adapt OSHM for more frequent or on-demand structural integrity prediction of safety-critical reactor pressure boundary components [9]. OSHM techniques are primarily based on deciphering damage information on structural components in real time and based on real-time sensor measurements. The damage information is inferred from sensor measurements by using advanced data analytics and sensor fusion techniques. The OSHM technique has high potential for reducing O&M costs, since it is autonomous.

1.2 Physical-Digital-Twin Framework for Structural-integrity Prediction of Reactor Components

Although the data-based OSHM technique has high potential for autonomous structural-integrity assessment, it has limitations in its prediction horizon. For example, the use of data analytics techniques, which is one of the backbones of OSHM, has its own limitations; in particular, it works badly when not enough data are available. Usually, artificial intelligence and data analytics techniques work well only if substantial data are available. But this is not the case for nuclear reactors, where the availability of historical data is limited in terms of numbers and time-lengths of data sets. For example, not much information is available on how a reactor component would behave if it operated for, say, 80–100 years. In this context, physics-based modeling can be used along with OSHM techniques to predict the

structural integrity of a reactor component more reliably and, at the same time, in real time and autonomously. This result can be achieved through a PDT framework, which depends not only on real-time sensor measurements from an actual/physical component (physical twin) but also on data or modeling from a computational mechanics-based virtual component (digital twin).

Though the major focus of this report is computational mechanics-based prediction (which is part of the overall PDT framework), below we present a broad overview of the PDT system to show the links between the individual building blocks. The proposed PDT system will eventually be developed and demonstrated for real-time structural-integrity prediction of reactor components. The futuristic PDT framework is schematically shown in Figure 1.1. The PDT framework will have three major sub-technology areas, i.e., 1) computational mechanics- or physics-based safe-life and fail-safe damage prediction, 2) data-based online damage tolerance monitoring and damage forecasting, and 3) integrated physics/data-based online damage forecasting. The proposed framework will initially be demonstrated in real time using existing Argonne test loops. These demonstrations will use both historical thermal-mechanical loading cycles and future anticipated loading cycles, which consider the likelihood that US utilities would increasingly adapt the grid-load-following (or flexible operation) power operation cycles to deal with the increased penetration of intermittent power sources such as renewable energy. The three sub-technology areas of the overall PDT framework are briefly discussed below.

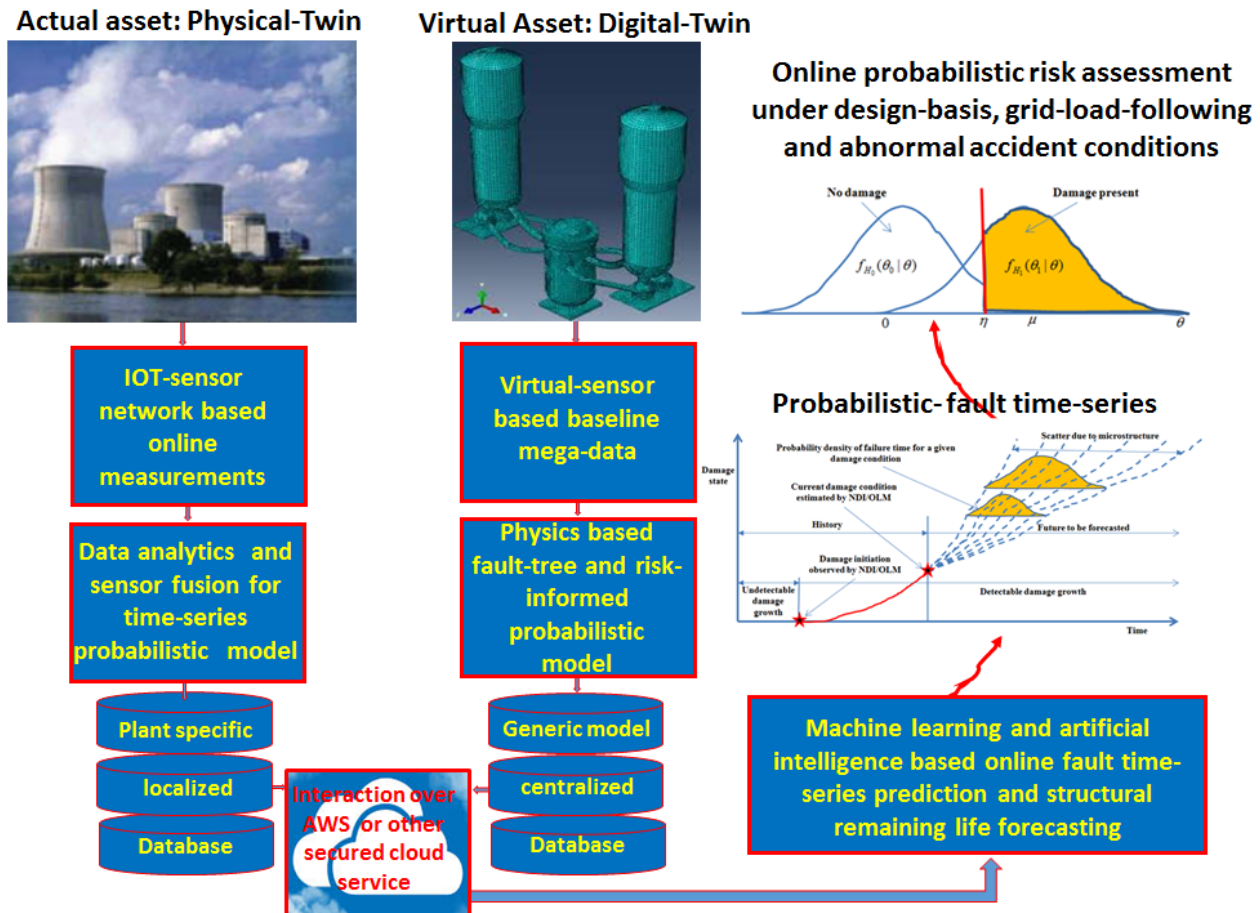


Figure 1. 1 Schematic of the futuristic Physical-Digital-Twin framework (actual reactor image inset taken from [10]).

1.2.1 Computational mechanics-based structural-integrity prediction

Under this approach, a robust physics-based modeling framework needs to be developed to predict the safe-life and fail-safe life of reactor pressure boundary components subjected to design-basis and grid-load-following flexible-operation loading cycles [11]. This is done by incorporating both cycle-independent material models (e.g., material models to capture tensile behavior of base and weld metals) and cycle-dependent material models (e.g., material models to capture the cyclic hardening/softening behavior of base and weld metals) [12], multi-physics computational modeling (e.g. to capture the boundary-condition effect associated with thermal-fluid-structure interaction) [13], original manufacturing and repair process modeling (e.g., simulating the original welding sequence and weld overlay for weld repair), and a high-performance-computing-based computational modeling [14] framework.

1.2.2 Time-series data based online damage tolerance and probabilistic damage prediction:

Under this approach, a data-analytics-based approach needs to be developed to estimate the state of the structure at a given time and to forecast the projected state of the structure at a future time [4–7]. Online sensor measurements from heterogeneous sensor nodes (e.g., thermocouples, pressure gauges, strain gauges, accelerometers, flow meters, water chemistry sensors, and infrared and regular optical camera feeds) need to be processed in real time to decipher the hidden damage-state information. Advanced machine learning, sensor fusion, and system identification techniques need to be used to decipher the incipient damage; on the basis of that state of the structure, the future state and remaining life of the structure can be forecast long before the actual final failure of the component [4]. This approach also requires time-series probabilistic damage-state modeling and risk assessment [15].

1.2.3 Integrated physics/data-based online damage forecasting:

Through our earlier work [4–7, 11–15], we have developed some of the techniques required for both physics- and data-based prediction techniques. However, under the integrated approach, the physics-based and sensor data-based approaches need to be integrated to increase the prediction horizon and prediction accuracy, and at the same time to predict the structural integrity in real time. The physics-based models will be used as virtual sensors along with the actual sensor measurements from the reactor. While real sensor measurements would help in modeling the un-modeled/not-yet-understood physics, the physics-based virtual sensor measurements would help provide the information where actual sensor data are not available (owing to unavailability of the sensor or failure of the sensor during operation).

1.3 Organization of This Report

A broad overview of the proposed PDT framework for reactor component structural-integrity prediction is presented above. The individual components of the PDT framework are being developed under the LWRS program. The present report discusses some of the work specifically intended to improve the physics-based prediction capability. This capability is directed towards tensile and fatigue testing of reactor pressure boundary component materials, material model development, component manufacturing

process modeling (e.g., weld process modeling), and thermal-mechanical stress analysis. These topics are discussed in detail in the following sections:

Section 2: Tensile Tests and Properties of Base, Weld and Heat-affected-zone metals

Section 3: Tensile Material-hardening Parameter Estimation and Finite-element Model
Validation

Section 4: Estimation of Thermal Expansion Coefficients for Base and Welds

Section 5: Estimation of Cycle-Dependent Ramberg-Osgood Parameters for Similar Metal Welds

Section 6: FE Modeling-based 3D Heat-Transfer Analysis of Nozzle Weld Processes

Section 7: FE Modeling-based 3D Thermal-Mechanical Stress Analysis of Nozzle Assembly
under Design-basis Loading Cycle

Section 8: Fatigue Life Estimation of Pressurizer-Surge Line Nozzle under In-Air and PWR-
Water Environment and under Design-Basis Loading Cycles

Section 9: Summary and Future Studies

2 Tensile Tests and Properties of Base, Weld and Heat-affected-zone metals

In this section, we summarize the results of tensile tests and tensile property determinations of base, weld and heat-affected zone (HAZ) metals. Some of the tests were conducted earlier [12, 16], and some were conducted in FY 2019.

2.1 Typical Materials Used in Reactor Pressure Boundary Components

Reactor pressure boundary (RPB) components, for example, PWRs are made from different base materials and weldments. The RPB components comprise various nozzles and instrument penetrations consisting of both similar-metal weld (SMW) and dissimilar-metal weld (DMW) joints. The SMW and DMW joints are some of the most vulnerable locations in the primary-loop components of operating light water reactor (LWR) fleets. This vulnerability is due to the residual-stress buildup during the welding process and its complex, multi-dimensional interaction with the reactor coolant environment and thermal-mechanical loading cycles. The resulting interaction could lead to stress-corrosion cracking and accelerated corrosion fatigue damage. Figure 2.1 shows a schematic of a typical PWR pressure boundary system and the materials used in typical nozzles (comprising different base metals, SMWs, and DMWs). For example, as shown in Figure 2.1, the reactor pressure vessel (RPV) to hot-leg (HL) nozzle can be composed of different base metals such as 316 stainless steel (316SS) and 508 low alloy steel (508LAS), DMWs (e.g., comprising both In-182 butter weld and In-82 filler weld) and SMWs (e.g., comprising SS weld material such as E316-16 alloy). Similar nozzles are also present in other RPB locations, such as between pressurizer (PRZ)-to-surge-line (SL) joints. In this section we provide tensile test results for the above-mentioned materials. Some of these tensile test results are also used in the finite-element (FE) modeling of the PRZ-SL nozzle, which is discussed in a later section of this report. The chemical compositions of the relevant materials are summarized in Table 2.1.

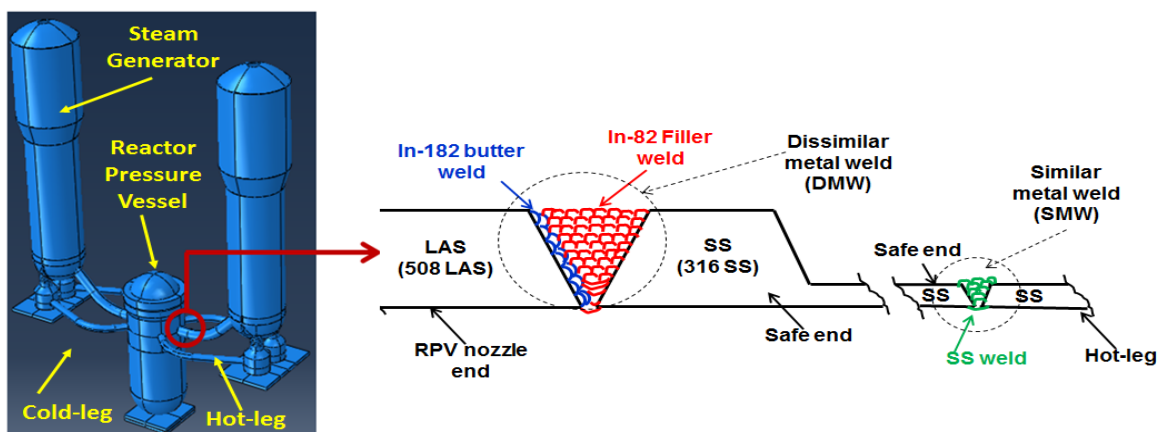


Figure 2.1 Schematic of typical PWR pressure boundary system and the materials used in a typical nozzle.

Table 2. 1 Compositions of various base and welding materials

Composition (%)	316 SS	E316-16	508/533 LAS (Both forged and rolled)	In82 or ERNiCr-3 (UNS NO6082)	In182 or ENiCrFe-3 (UNS W86182)	Alloy 600
Nickel	10.0-14.0	11.0-14.0	0.620	67.0000	59.0000	72.0000
Chromium	16.0-18.0	17.0-20.0	0.180	18.0-22.0	13.0-17.0	14.0-17.0
Iron	Balance	Balance	Balance	3.0000	10.0000	6.0-10.0
Molybdenum	2.0-3.0	2.0-3.0	0.510	NA	NA	NA
Niobium & Tantalum	NA	NA	0.001	2.0-3.0	1.0-2.5	NA
Carbon	0.080	0.040	0.180	0.1000	0.1000	0.1500
Manganese	2.000	0.5-2.5	1.430	2.5-3.5	5.0-9.5	1.0000
Silicon	0.750	1.000	0.220	0.5000	1.0000	0.5000
Phosphorus	0.045	0.040	0.006	0.0300	0.0300	NA
Sulfur	0.030	0.030	0.001	0.0150	0.0150	0.0150
Aluminum	NA	NA	0.025	NA	NA	NA
Titanium	NA	NA	0.002	0.7500	1.0000	NA
Cobalt	NA	NA	NA	NA	NA	NA
Calcium	NA	NA	0.00010	NA	NA	NA
Copper	NA	0.750	0.110	0.5000	0.5000	0.5000
Nitrogen	0.100	NA	NA	NA	NA	NA
Boron	NA	NA	0.002	NA	NA	NA
Vanadium	NA	NA	0.002	NA	NA	NA
Others	NA	NA	NA	0.5000	0.5000	NA
Comments	Related Argonne test properties are used for base metal in PRZ-SL Nozzle FE model	Related Argonne test properties are used for SMW-Filler weld and cladding in PRZ-SL nozzle FE model	Related Argonne test properties are used for base metal in PRZ-SL nozzle FE model	Related Argonne test properties are used for DMW-Filler weld and cladding in PRZ-SL nozzle FE model	Related Argonne test properties are used for DMW-butter weld and cladding in PRZ-SL nozzle FE model	Used in different nozzles of instrument and other penetrations (not used in the discussed PRZ-SL nozzle FE model)
Source of information	[17]	[18]	[19]	[20]	[21]	[22]

2.2 Dissimilar Metal Weld Fabrication and Test Specimens

In this report, mostly results from tensile and fatigue tests of DMW specimens are presented. The DMW specimens were fabricated from a weld plate fabricated at Argonne. At first, 68 butter weld passes were laid on to a 508LAS plate. The butter weld passes were made by using a shielded metal arc welding

(SMAW) process and In-182 or ENiCrFe-3 weld rods. While laying down the butter passes, the maximum interpass temperature was maintained at 390°F (199°C). After completion of the butter welding, post-weld heat treatment (PWHT) of the LAS-butter plate was conducted at an approximate temperature of 1150°F (621°C). Then the excess butter weld was machined and cleaned. After that, the filler weld passes were laid using In-82 or ERNiCr-3 weld rods. A total of 88 filler weld passes were made to join the butter section (1 inch thick) of the weld to the 1-inch-thick 316SS plate. For the filler weld, the gas tungsten arc welding (GTAW) process was used. As with the butter weld, an interpass temperature of 390°F (199°C) was maintained. Figure 2.2 shows the weld setup before the start of filler welding but after the excess butter weld was machined. Once the overall DMW weld plate was fabricated, it was qualified through radiographic inspection. Figure 2.3 shows a radiographic image of the welded DMW plate, showing no visible voids. After that, along-the-length weld specimens were fabricated to conduct the tensile and fatigue tests discussed in this report. Figure 2.4 shows the cross-section of the weld plates and location of the along-the-length specimen. Specimens from both welds and HAZs (see Figure 2.4) were tensile tested. Figure 2.5 shows the geometry of the hourglass-type specimens used for the tensile and fatigue testing.

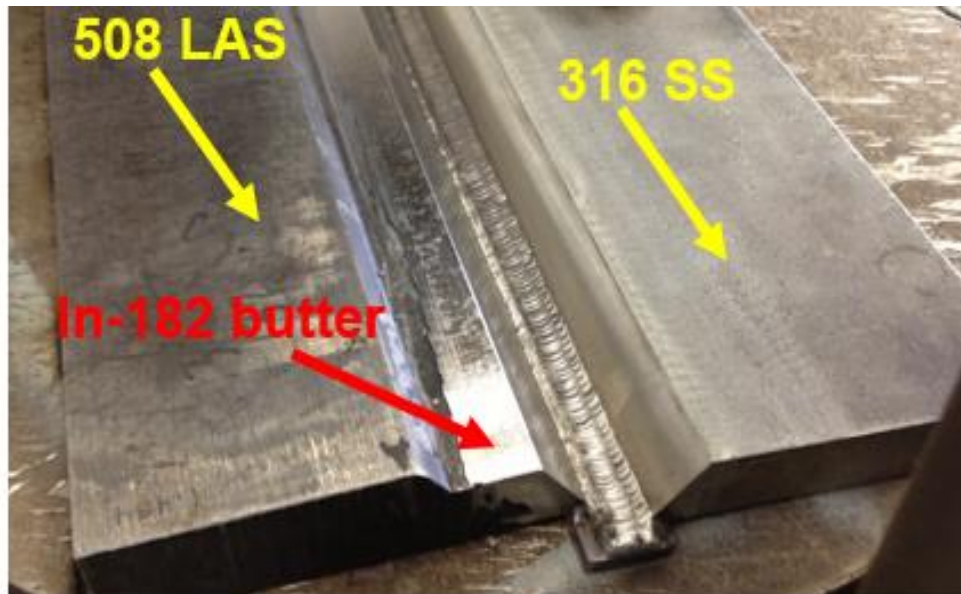


Figure 2.2 Weld plates before start of the DMW filler welding at Argonne machine shop.



Figure 2 3 Radiographic image of the welded DMW plate.

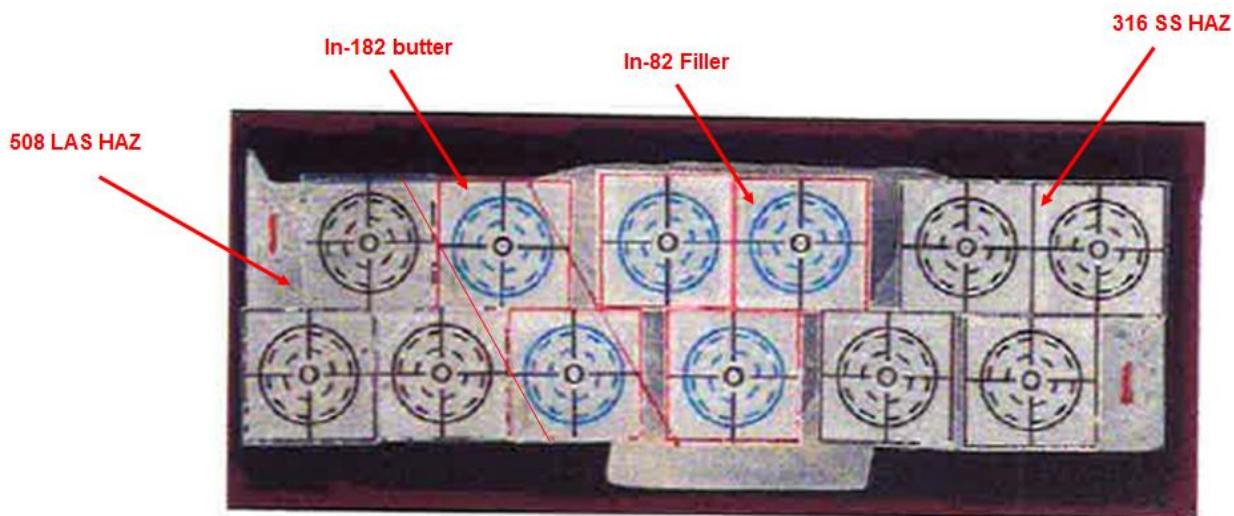


Figure 2 4 Cross-section of the weld plates (only near the weld region) and location of the along-the-length weld and HAZ specimens.

similar stress-strain curves, as do the 508LAS HAZ and pristine base metal. However, from these figures, it can be seen that the 316SS HAZ and pristine base metal have significantly different stress-strain curves. This difference could be due to welding-process-related material hardening of the surrounding base metal; which is more severe in the case of the 316SS HAZ compared to the 508LAS HAZ. Results of a repeat room-temperature tensile test on 316SS HAZ show similar abnormal behavior with respect to the corresponding base metal results (see T18, T21 and T02 stress-strain curves in Figure 2.9). From Figure 2.11, it can be seen that as was the case at room temperature, at 300°C, the 508LAS base metal and HAZ show very similar tensile behavior (see T08 and T09 curves). However, as at room temperature, at 30°C, the stress-strain curves for 316SS base metal and HAZ (see T04 and T17 curves) differ significantly. Also note that the 300°C curve for the In-182 butter weld (T15 curve) shows no necking, but rather shows instantaneous rupture. Additionally, the 300°C tensile curve of In-82 filler (see T13 curve) shows less smooth necking. This unusual necking behavior could be due to a larger heterogeneity in weld microstructure compared to the corresponding base metal. This heterogeneity is associated with welding-process-related irregular material microstructure. Tensile properties were also estimated using the above-mentioned tensile curves. These are given in Tables 2.3 and 2.4 for room temperature and 300°C, respectively. From Table 2.3, it can be seen that the 316SS HAZ has significantly higher 0.2% offset yield stress compared to the 316SS pristine base metal at room temperature. This finding is consistent with the difference in stress-strain curves shown in Figure 2.9. Similarly to room temperature, at 300°C the 316SS HAZ has significantly higher 0.2% offset yield stress compared to the 316SS pristine base metal. These types of findings may necessitate studying the tensile and fatigue behavior of HAZ metals independently of their corresponding pristine base metals, rather than considering their tensile and fatigue properties to be similar.

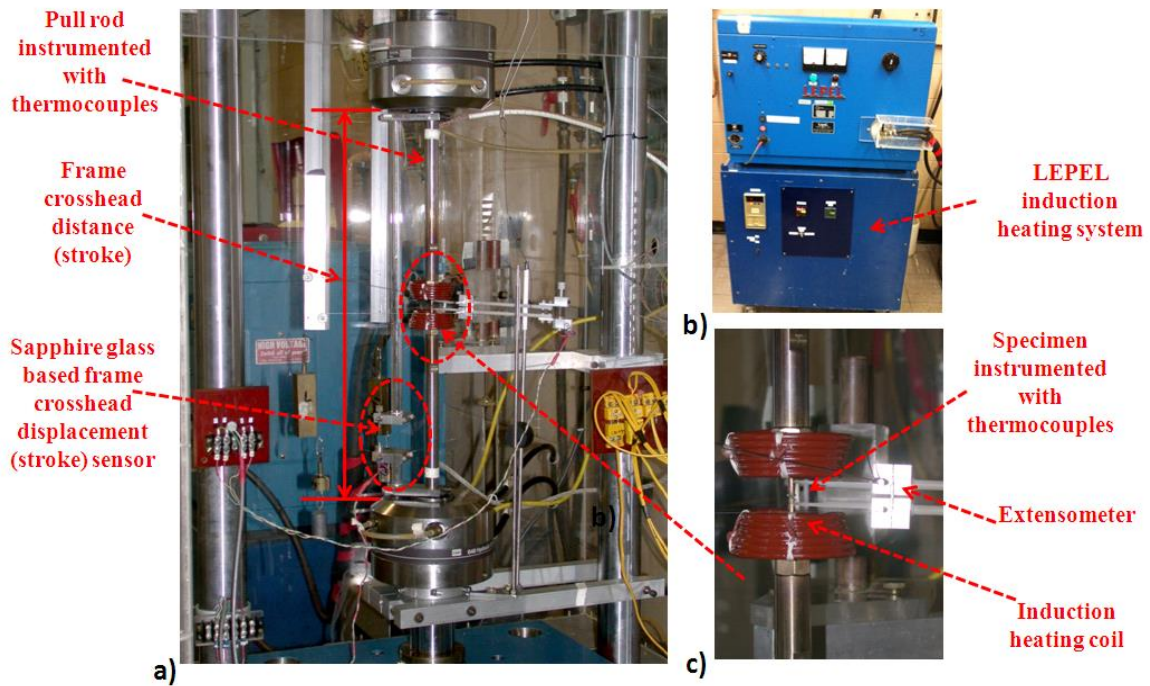


Figure 2.6 a) Test section with induction heating coil, b) LEPEL induction heating system, and c) close view of induction heating coil and specimen and extensometer location.

Table 2. 2 Test ID, environment, and material of different tensile specimens

Test ID	Environment	Temperature (°C)	Material type
T01	air	22	316SS Base
T02	air	22	316SS Base
T03	air	22	316SS SMW
T04	air	300	316SS Base
T05	air	300	316SS SMW
T06	air	22	508LAS Base
T07	air	22	508LAS DMW HAZ
T08	air	300	508LAS Base
T09	air	300	508LAS DMW HAZ
T10	air	300	508LAS Base
T11	air	300	316SS Base
T12	air	300	316SS Base
T13	air	300	DMW-In 82 Filler
T14	air	22	DMW-In 82 Filler
T15	air	300	DMW-In 182 Butter
T16	air	22	DMW-In 182 Butter
T17	air	300	316SS DMW HAZ
T18	air	22	316SS DMW HAZ
T19	air	300	508LAS DMW HAZ
T20	air	22	508LAS DMW HAZ
T21	air	22	316SS DMW HAZ

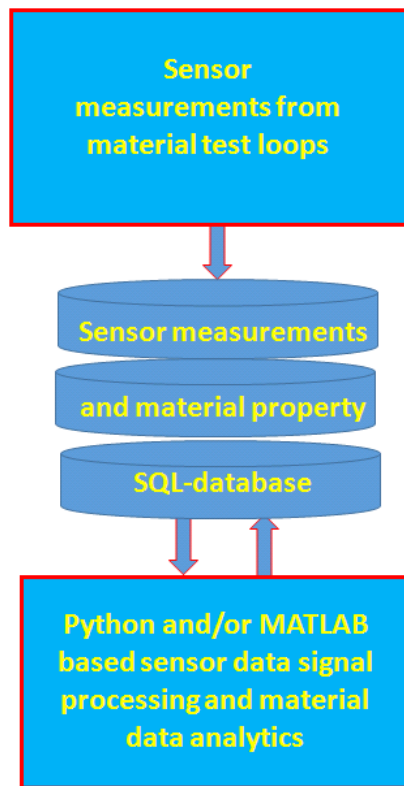


Figure 2 7 Schematic of MATLAB-PYTHON-SQL framework for automated material parameter estimation

	Test_id	Env	Temp_oC	Material	Edot_perPs	Emod_GPa	
	Filter	Filter	Filter	Filter	Filter	Filter	Filter
1	T01	air	22	316SS Base	0.01	172.5	84.4
2	T02	air	22	316SS Base	0.1	175.1	83.1
3	T03	air	22	316SS SW	0.1	131.98	62.2
4	T04	air	300	316SS Base	0.1	157.92	69.4
5	T05	air	300	316SS SW	0.1	129.11	44.6
6	T06	air	22	508LAS Base	0.1	209.72	73.9
7	T07	air	22	508LAS DW H...	0.1	208.4	76.2
8	T08	air	300	508LAS Base	0.1	197.65	69.7
9	T09	air	300	508LAS DW H...	0.1	195.04	73.2
10	T10	air	300	508LAS Base	0.01	194.01	74.3

Figure 2 8 Screen shot of the SQL material database

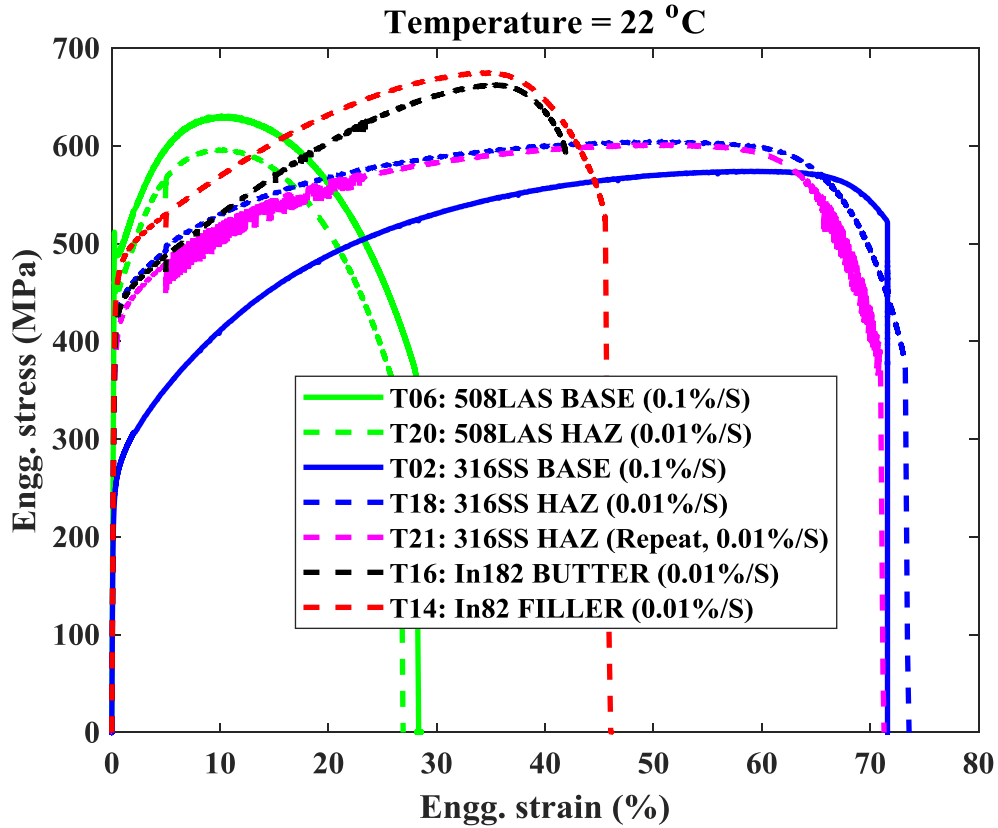


Figure 2 9 Full stress-strain curves of different metals at room temperature

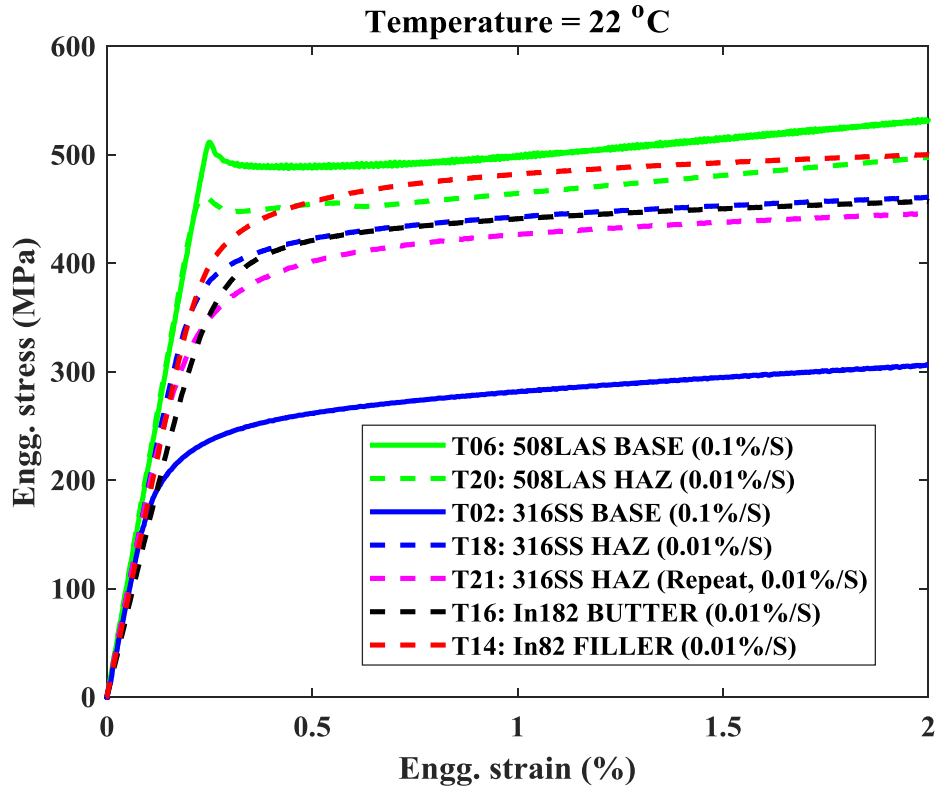


Figure 2 10 Magnified stress-strain curves (below 2% strain) of different metals at room temperature

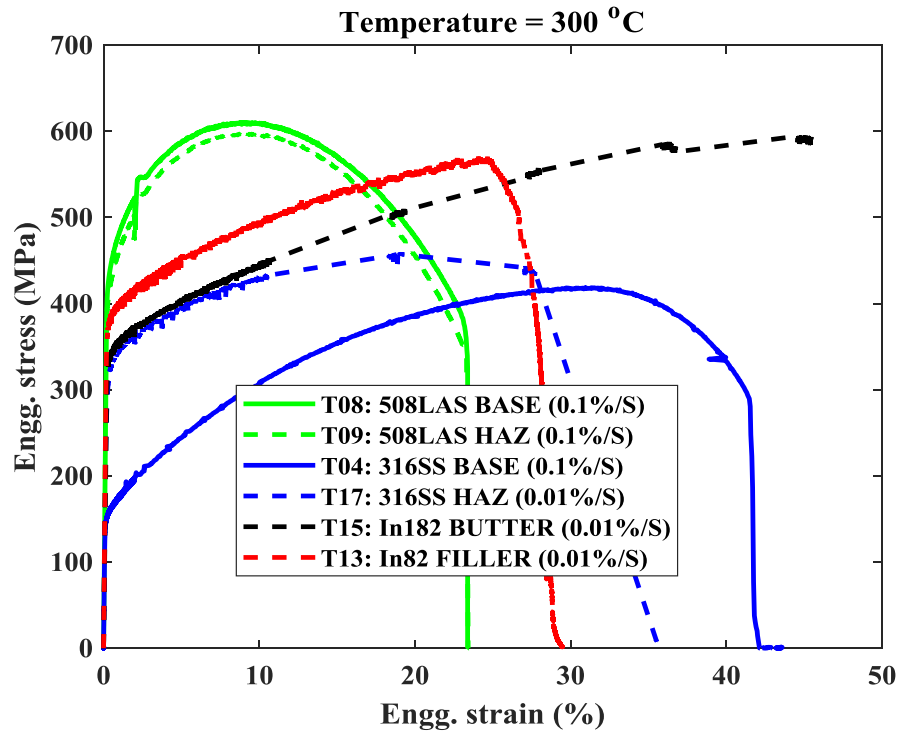


Figure 2 11 Full stress-strain curves of different metals at a temperature of 300°C

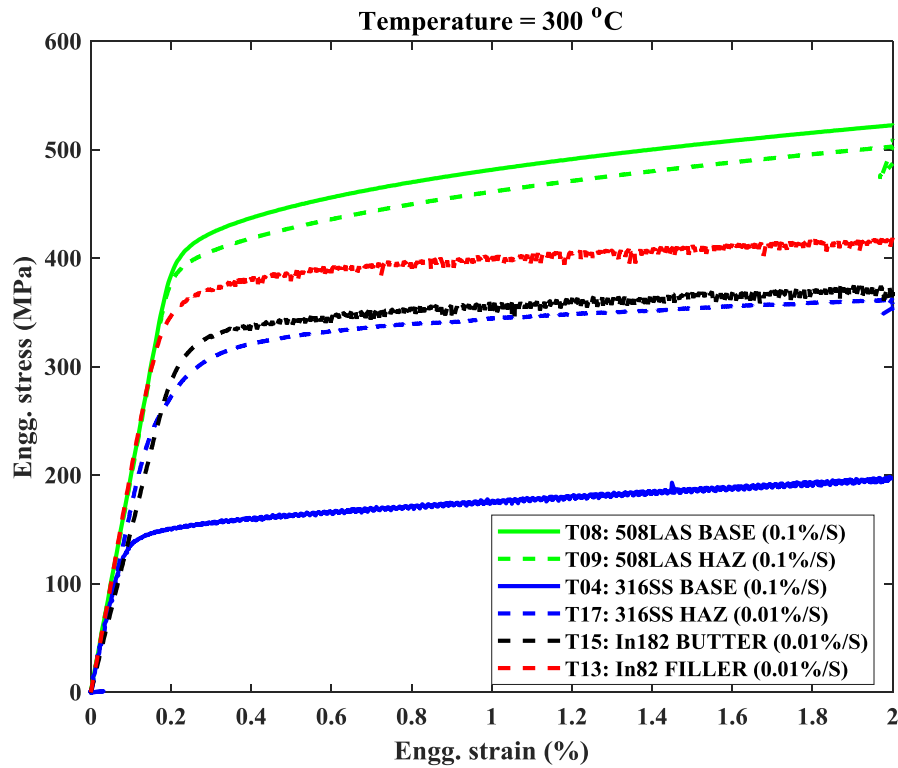


Figure 2 12 Magnified stress-strain curves (below 2% strain) of different metals at a temperature of 300°C

Table 2. 3 Estimated tensile test material properties for different reactor pressure boundary metals at room temperature.

Tensile test properties		T06 (508 LAS BASE, 22 °C, strain: 0.1%/s)	T20 (508 LAS HAZ, 22 °C, strain: 0.01%/s) (T07 Repeat test , 22 °C, strain: 0.1%/s)	T02 (316 SS BASE, 22 °C, strain: 0.1%/s) (T01 Repeat test , 22 °C, strain: 0.01%/s)	T18 (316 SS HAZ, 22 °C, strain: 0.01%/s) (T21 Repeat test , 22 °C, strain: 0.01%/s)	T16 (In 182 butter weld, 22 °C, strain: 0.01%/s)	T14 (In 82 filler weld, 22 °C, strain: 0.01%/s)	T03 (SMW-E316-16 filler weld, 22 °C, strain: 0.1%/s)
Elastic modulus (GPa)		209.72	212.64 (208.4)	175.10 (172.5)	183.34 (177.01)	149.7	172.64	131.98
Reduction in gauge area (%)		73.997	74.893 (76.217)	83.149 (84.424)	80.515 (76.574)	39.249	39.811	62.207
0.2% offset yield	Stress (MPa)	488.2	451.02 (462.24)	249.58 (245.09)	416.89 (392.81)	419.71	453.41	431.32
	Strain (%)	0.433	0.41463 (0.42214)	0.343 (0.34394)	0.429 (0.42265)	0.4828	0.4649	0.5279
Ultimate	Stress (MPa)	630.53	595.91 (610.01)	574.04 (568.42)	605.34 (601.32)	662.57	675.29	596.28
	Strain (%)	10.836	10.125 (10.481)	59.46 (57.204)	51.422 (50.519)	35.166	34.337	34.58
Fracture	Stress (MPa)	362.12	329.6 (337)	521.3 (369.9)	368.9 (364.0)	592.9	513.9	476.2
	Strain (%)	28.231	26.65 (28.08)	71.6 (72.01)	73.25 (70.96)	41.89	45.57	55.53

Table 2. 4 Estimated tensile test material properties for different reactor pressure boundary metals at a temperature of 300°C.

Tensile test properties		T08 (508 LAS BASE, 300 °C, strain: 0.1%/s) (T10 repeat test , 300 °C, strain: 0.01%/s)	T09 (508 LAS HAZ, 300 °C, strain: 0.1%/s) (T19 repeat test , 300 °C, strain: 0.01%/s)	T04 (316 SS BASE, 300 °C, strain: 0.1%/s) (T11 repeat test, 300 °C, stress: 2.5253 MPa/s) [T12 repeat test, 300 °C, stroke: 2.1116 mil/s]	T17 (316 SS HAZ, 300 °C, strain: 0.01%/s)	T15 (DMW-In 182 butter weld, 300 °C, strain: 0.01%/s)	T13 (DMW-In 82 filler weld, 300 °C, strain: 0.01%/s)	T05 (SMW-E316-16 filler weld, 300 °C, strain: 0.1%/s)
Elastic modulus (GPa)		197.65 (194.01)	195.04 (196.79)	157.92 (155.74) [156.75]	164.0	146.28	196.57	129.11
Reduction in gauge area (%)		69.729 (74.329)	73.246 (56.958)	69.474 (69.482) [66.716]	52.914	46.799	25.564	44.693
0.2% offset yield	Stress (MPa)	439.96 (434.93)	420.21 (414.69)	155.77 (150.77) [136.6]	321.06	338.41	377.81	356.05
	Strain (%)	0.42485 (0.42525)	0.41654 (0.41085)	0.29988 (0.29705) [0.28758]	0.397	0.4334	0.394	0.47578
Ultimate	Stress (MPa)	610.75 (618.29)	597.93 (591.33)	418.66 (419.92) [417.47]	461.2	595.38	570.53	476.97
	Strain (%)	9.5018 (10.077)	9.371 (9.2333)	30.958 (29.823) [29.731]	18.912	44.782	24.077	19.125
Fracture	Stress (MPa)	263.5 (260.9)	294 (356.649)	280.7 (239) [287.8]	433.4	591.6	433.5	409
	Strain (%)	23.41 (23.39)	23.33 (24.895)	41.53 (41.17) [38.55]	27.75	45.45	27.5	27.26

3 Tensile Material-hardening Parameter Estimation and Finite-element Model Validation

In this section, we present the material-hardening parameters, which were estimated on the basis of the tensile test results discussed in the previous section. Note that out of the total 21 tensile test cases (see Table 2.2), material hardening parameters were already estimated for some of the test cases and reported in our earlier work [12]. In the present report, we present the material-hardening parameters for the rest of the cases along with the earlier data sets. This approach is taken for easier comparison and for single-source accessibility. Also note that an improved version of the material modeler code was used to estimate the parameters; hence, all the previously estimated parameters are re-estimated for consistency. These hardening parameters, along with the tensile properties discussed in the previous section, can be used for component-level stress analysis codes. In addition, we present the FE model validation of some of the estimated parameters. This validation is performed by FE modeling of the DMW tensile-test specimens (filler-weld, butter-weld and HAZ specimens). Through the FE model results, we also explain the importance of various offset strain yield stresses in capturing the material behavior in a mechanistic (FE) modeling approach, particularly while modeling the plasticity-driven low-cycle-fatigue damage of a structural component.

3.1 Material Hardening Model

The FE modeling of reactor components such as welded nozzles requires a knowledge of material-hardening parameters. In our earlier work [12], we developed a detailed methodology for estimating the tensile-test-based cycle-independent and fatigue-test-based cycle-dependent material models. This approach is based on a Chaboche [23]-type material-hardening model to model the stress-strain behavior beyond yield stress. The details of the approach are discussed in our earlier work [12]. However, in this subsection we briefly discuss the basic background behind the model to familiarize readers with the terminology of different parameters.

The stress state of a component can be expressed through the yield function, which is given as

$$f(\boldsymbol{\sigma}^j - \boldsymbol{\alpha}^j) = \sigma^y \quad (3.1)$$

In Eq. 3.1, $\boldsymbol{\sigma}^j$ and $\boldsymbol{\alpha}^j$ are, respectively, the total stress and back stress tensor at the j^{th} instance, whereas σ^y is the yield stress. In Eq. 3.1, the back stress $\boldsymbol{\alpha}^j$ can be estimated using the following linear or nonlinear mapping function of hardening stress (i.e., $\sigma^j - \sigma^y$), with respect to the accumulated plastic strain ($\bar{p} = \int_0^{\varepsilon^{pl}} d\varepsilon^{pl}$). The expressions for the linear and nonlinear hardening models are given in Eqs. 3.2 and 3.3, respectively.

$$d\boldsymbol{\alpha}^j = \frac{2}{3} C_1 d\varepsilon^{pl} \quad (3.2)$$

$$d\boldsymbol{\alpha}^j = \frac{2}{3} C_1 d\varepsilon^{pl} - \gamma_1 \boldsymbol{\alpha}^j \bar{p} \quad (3.3)$$

In Eqs. 3.2 and 3.3, C_1 and γ_1 are the two material-hardening parameters. These parameters are estimated using numerical optimization such that the L_2 norm of the incremental parameters (i.e., $\|\Delta C_1 \ \Delta \gamma_1\|$) is less than a chosen tolerance value. These parameters were estimated using an Argonne-developed MATLAB-PYTHON-SQL-based material-modeling code (see Figure 2.7). For more details of the material model theoretical background, refer to our earlier work [12]. While estimating the hardening parameters, we assumed different yield limits such as using the elastic limit (assumed end of elastic portion of stress-strain curve) and various offset strains such as 0.05%, 0.1% and 0.2% offset strain yield limits. The reason for selecting different yield limits than for the conventional 0.2% offset yield strain is to check at what offset yield limit the material model and the corresponding FE model better capture the plasticity portion of the stress-strain curves. It is well known that the conventional 0.2% offset strain-based hardening model can satisfactorily capture the elastic-plastic region of the tensile stress-strain curves. However, for low-cycle fatigue loading, for which the maximum strain amplitude rarely exceeds 0.5–0.6%, the 0.2% offset strain-based hardening model may not be sensitive enough to accurately capture the lower portion (below 0.2% offset strain) of the stress-strain curve. Below 0.2% offset strain, there could be a substantial plastic regime driving the accumulative fatigue failure. For example, for the T16 butter weld case (see Table 2.3), the 0.2% offset strain is estimated to be 0.4828%, which is too high to be considered the boundary of the elastic regime. For fatigue-loading cases, say, with a strain amplitude of 0.5%, the model may not accurately capture the plasticity-driven fatigue failure when a 0.2% offset strain yield limit is used.

For these reasons, the assumption of a 0.2% offset strain yield limit for mechanistic modeling of low cycle fatigue may not be a good idea for accurate modeling of fatigue failure, although it is conventionally being used for stress-analysis approaches. To justify this claim further, we show in Figure 3.1 the equivalent monotonic stress-strain curves over 50 cycles estimated from the data obtained through a previously conducted environment fatigue test (316SS specimen with test conducted at 300°C and PWR primary-water conditions [24]). Figure 3.1 clearly shows that the plastic regime starts well before the 0.2% offset yield limit. For the above-mentioned reasons, we estimated the material-hardening parameters of the tensile test cases for different yield limits. These are estimated using 0.0% (the elastic limit or the assumed end of the elastic portion of the stress-strain curve) and other offset strain limits, such as 0.05%, 0.1% and 0.2%. Users can choose the appropriate set of parameters according to their need.

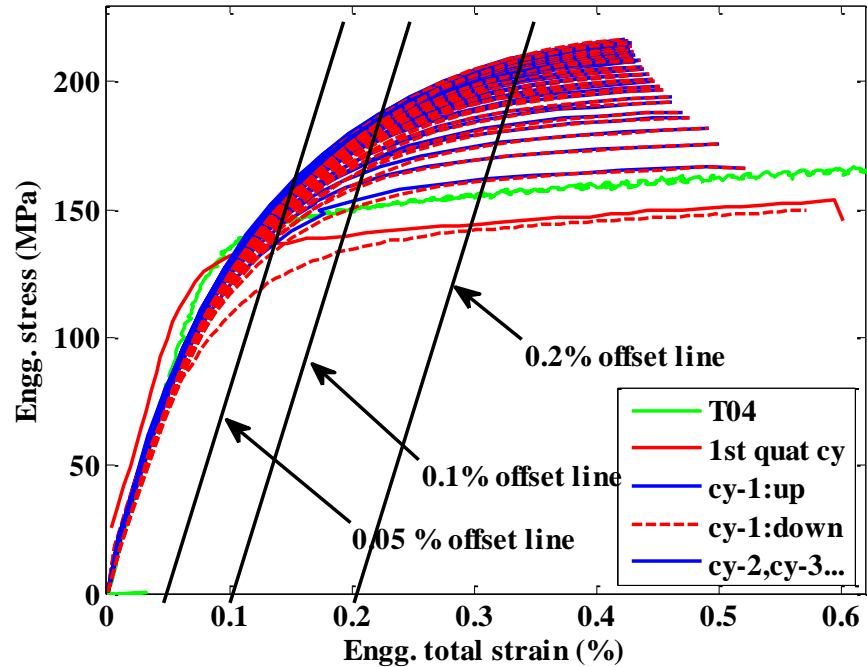


Figure 3. 1 Equivalent monotonic stress-strain curves over 50 cycles estimated from data obtained through a previously conducted environment fatigue test (316SS specimen).

3.2 Estimated Material-hardening Parameters

The material-hardening parameters were estimated for the tensile test cases in Table 2.2. Note that the hardening parameters were already presented for some of the test cases in our earlier work [12]. In FY 2019, we estimated the parameters for new test cases (for both new tests conducted in FY 2019 and old tests for which parameters were not previously reported). The overall results are presented in this section as a complete database for easier access and comparison (with respect to different materials, e.g., pristine base material versus corresponding HAZ metal). An improved version of the material modeler code was used to estimate the parameters; hence, all the previously estimated parameters were re-estimated for consistency. The parameters were estimated for 0% (the elastic limit, or the assumed end of the elastic portion of the stress-strain curve) and other offset strain limit cases, such as 0.05%, 0.1% and 0.2%. Users can choose the appropriate properties for their requirements.

Unless specified otherwise, while estimating hardening parameters we considered total true strain up to 2% for the 0.0% offset strain limit (or elastic limit) case and true strain up to 5% for other offset strain yield limit cases. True total strain of 2% was selected because beyond 2% the current two-parameter Chaboche model could not accurately capture the stress-strain curve. Similarly, a 5% total strain limit was used for the 0.05%, 0.1% and 0.2% offset strain yield limit cases. Hence, while using these material model parameters for constructing FE models, the user should be mindful of the accuracy regime of the material-hardening parameters. Also note that a multi-parameter (with more than 2 parameters) Chaboche model with more than 2 parameters may capture the plastic regime beyond 5% strain, but is not relevant/required for fatigue-modeling cases, where strain amplitude rarely exceeds 0.5–0.6%. Also use of the multi-parameter Chaboche model may increase the computational time of FE models.

In this section, we present some example results to demonstrate the iterative procedure used while estimating the above-discussed hardening parameters. For example, Figures 3.2 and 3.3 show the variation of C_1 and γ_1 with different iteration numbers, while Figure 3.4 shows the convergence of the corresponding L_2 norm of the incremental parameters (i.e., $\|\Delta C_1 \Delta \gamma_1\|$), and Figures 3.5 and 3.6 show the accuracy of the regenerated true back stress and true total strain for the corresponding experimental values. Figures 3.2 through 3.6 show the example material model results associated with the T14 filler weld test case with 0.2% offset strain yield limits. The estimated material parameters at room temperature are given in Tables 3.1 through 3.4 for the 0.0%, 0.05%, 0.1% and 0.2% offset strain yield limit cases, respectively. The estimated material parameters at 300°C are given in Tables 3.5 through 3.8 for 0.0%, 0.05%, 0.1% and 0.2% offset strain yield limit cases, respectively. The detailed validity of the parameters can be judged from the results/figures presented in the appendix sections of our earlier published report [12] and from those presented in the appendix sections of this report. Some of the results summarized in Tables 3.1 through 3.8 may vary slightly from the results given in our earlier published report [12]. This is because a newer version of the material modeler code was used. Chaboche parameters C_1 and γ_1 for one test case (or from an earlier version of the same test case) cannot be compared individually with the parameters of other test cases. Being fitting parameters, the Chaboche parameters C_1 and γ_1 in combination capture the stress-strain curve. To note that, the earlier version of the results for a particular test case (published in [12]) can vary significantly compared with the version of the results presented in this report if the parameters are compared individually. However, when the resulting stress-strain curve, which can only be constructed using the full set of parameters (elastic modulus, yield stress and Chaboche hardening parameters C_1 and γ_1), is compared, any discrepancy is minimal.

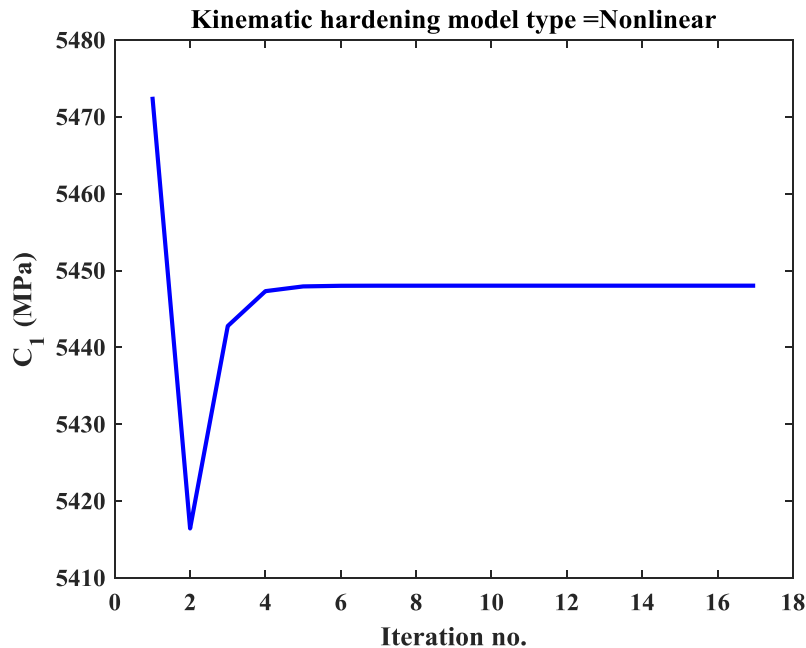


Figure 3. 2 Nonlinear kinematic hardening constant C1 with respect to number of iterations during parameter estimation using a gradient-based optimization scheme and T14 stress-strain data (from 0.2% offset strain yield limit to 5% true total strain).

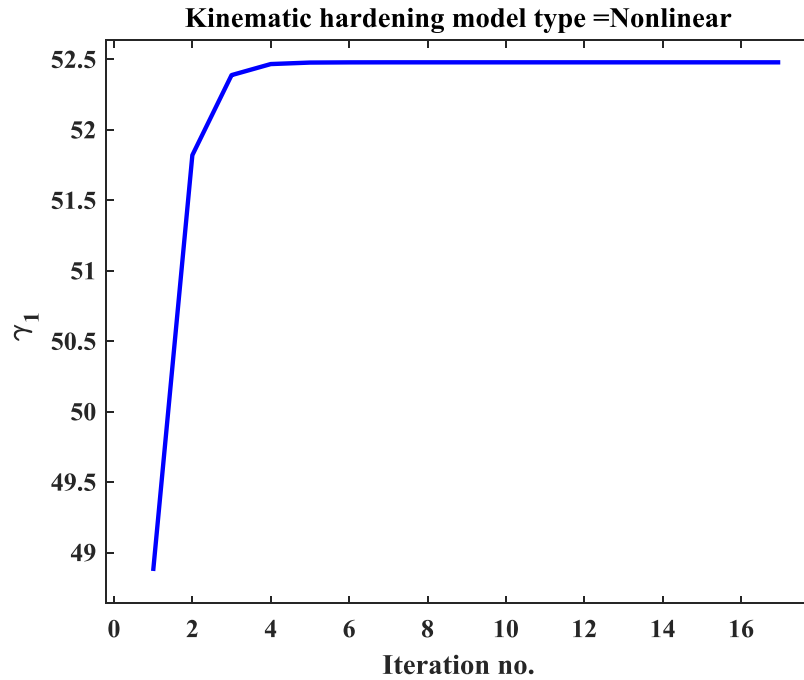


Figure 3. 3 Nonlinear kinematic hardening constant γ_1 with respect to number of iterations during parameter estimation using a gradient-based optimization scheme and T14 stress-strain data (from 0.2% offset strain yield limit to 5% true total strain).

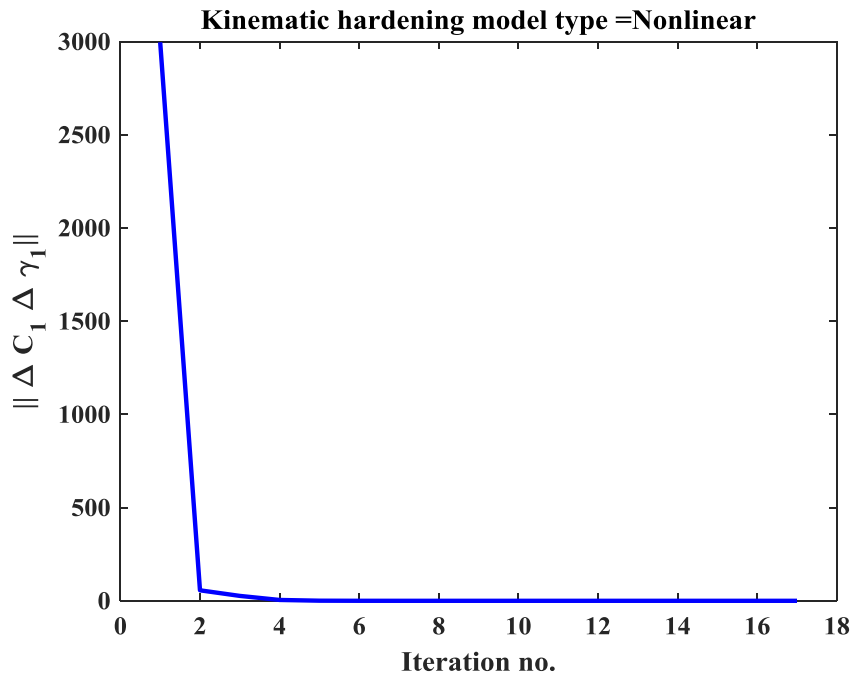


Figure 3. 4 L_2 norm (of incremental kinematic hardening constants C_1 and γ_1) with respect to number of iterations during parameter estimation using a gradient-based optimization scheme and T14 stress-strain data (from 0.2% offset strain yield limit to 5% true total strain).

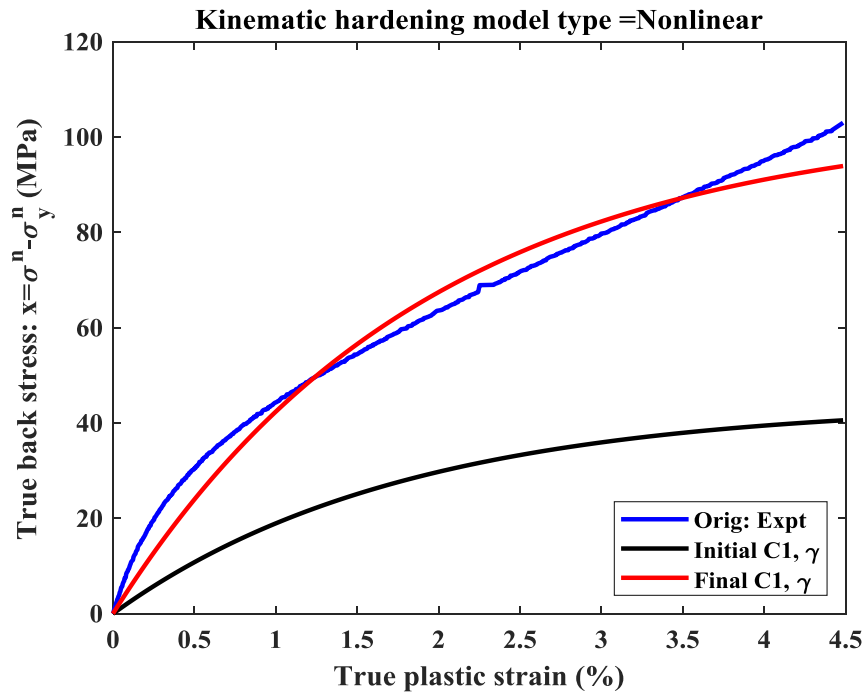


Figure 3. 5 Comparison of regenerated true back stress (using nonlinear kinematic hardening parameters C1 and γ_1 and considering 0.2% offset strain as yield limit strain) with experimental true back stress for T14 tensile test.

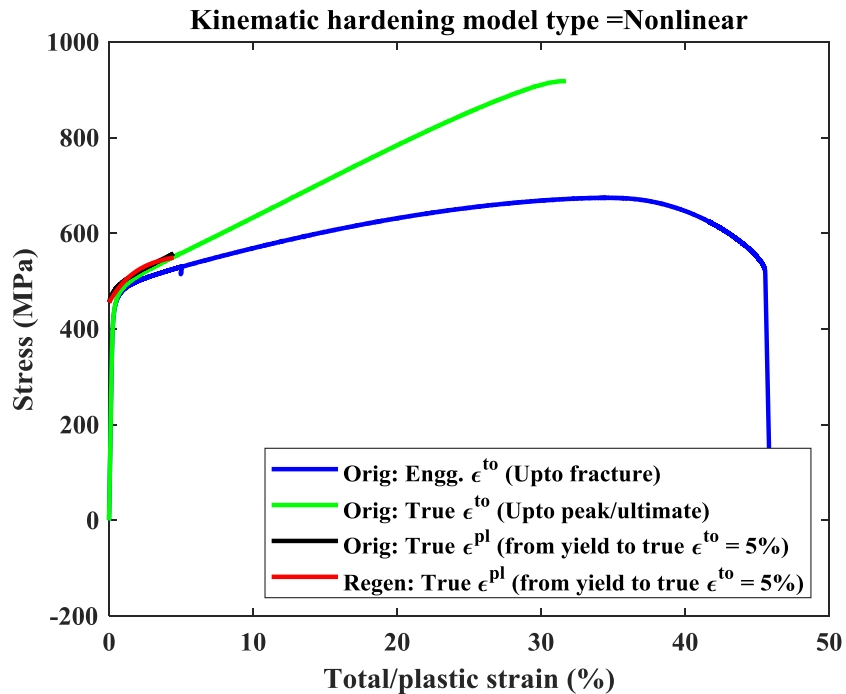


Figure 3. 6 Comparison of regenerated true total stress (using nonlinear kinematic hardening parameters C1 and γ_1 and considering 0.2% offset strain as yield limit strain) with experimental true total stress for T14 tensile test.

Table 3. 1 Room-temperature tensile material-hardening parameters of different metals (in reactor pressure boundary components) assuming elastic limit as yield limit

Material-Hardening properties (valid up to 2% true total strain)		T06 (508 LAS BASE, 22 °C, strain: 0.1%/s)	T20 (508 LAS HAZ, 22 °C, strain: 0.01%/s)	T02 (316 SS BASE, 22 oC, strain: 0.1%/s) (T01 Repeat test , 22 oC, strain: 0.01%/s)	T18 (316 SS HAZ, 22 °C, strain: 0.01%/s) (T21 Repeat test , 22 °C, strain: 0.01%/s)	T16 (In 182 butter weld, 22 °C, strain: 0.01%/s)	T14 (In 82 filler weld, 22 °C, strain: 0.01%/s)	T03 (SW-E316-16 filler weld, 22 °C, strain: 0.1%/s)
Assumed elastic limit as yield limit	Yield stress (MPa)	493.03	452.65 (460.46)	183.61 (195.27)	363.5 (311.76)	354.9	398.2	371.08
	Yield strain (%)	0.2359	0.219 (0.2218)	0.112 (0.1226)	0.215 (0.1916)	0.253	0.250	0.2918
Linear. kinematic hardening parameter	C1 (MPa)	2560.9	2766.5 (2953.4)	9448.1 (7665.2)	8045 (11334)	8806.9	8655.4	8115.4
	$\gamma 1$	NA	NA	NA	NA	NA	NA	NA
Nonlinear. kinematic hardening parameter	C1 (MPa)	1471	1691.4 (2059.5)	38021 (29459)	32089 (52003)	43313	33232	52678
	$\gamma 1$	-69.801	-65.312 (-45.983)	334.85 (329.24)	334.11 (399.97)	433.5	323.38	635.74

Table 3. 2 Room-temperature tensile material-hardening parameters of different metals (in reactor pressure boundary components) assuming 0.05% offset strain as yield limit

Material-Hardening properties (valid up to 5% true total strain except the T02 case which is valid up to 3%)		T06 (508 LAS BASE, 22 °C, strain: 0.1%/s)	T20 (508 LAS HAZ, 22 °C, strain: 0.01%/s) (T07 Repeat test , 22 °C, strain: 0.1%/s)	T02 (316 SS BASE, 22 oC, strain: 0.1%/s) (T01 Repeat test , 22 oC, strain: 0.01%/s)	T18 (316 SS HAZ, 22 °C, strain: 0.01%/s) (T21 Repeat test , 22 °C, strain: 0.01%/s)	T16 (In 182 butter weld, 22 °C, strain: 0.01%/s)	T14 (In 82 filler weld, 22 °C, strain: 0.01%/s)	T03 (SW-E316-16 filler weld, 22 °C, strain: 0.1%/s)
0.05% offset strain as yield limit	Yield stress (MPa)	494.36	454.17 (465.44)	217.41 (224.97)	388.76 (348.12)	387.64	420.14	414.56
	Yield strain (%)	0.286	0.2645 (0.27423)	0.17548 (0.18115)	0.264 (0.24687)	0.311	0.295	0.3649
Linear. kinematic hardening parameter	C1 (MPa)	2861.4	3137.6 (2949.3)	5334 (3805.5)	3388.8 (4362.6)	3330.8	3694.2	2926.3
	γ 1	NA	NA	NA	NA	NA	NA	NA
Nonlinear . kinematic hardening parameter	C1 (MPa)	2466.4	3042.5 (2713.8)	13942 (7457.4)	9298 (16568)	9964.5	12023	5901.8
	γ 1	-7.8188	-1.8025 (-4.5795)	128.24 (60.445)	78.937 (123.7)	90.498	99.532	65.922

Table 3. 3 Room-temperature tensile material-hardening parameters of different metals (in reactor pressure boundary components) assuming 0.1% offset strain as yield limit

Material-Hardening properties (valid up to 5% true total strain except the T02 case which is valid up to 3%)		T06 (508 LAS BASE, 22 °C, strain: 0.1%/s)	T20 (508 LAS HAZ, 22 °C, strain: 0.01%/s) (T07 Repeat test , 22 °C, strain: 0.1%/s)	T02 (316 SS BASE, 22 °C, strain: 0.1%/s) (T01 Repeat test , 22 °C, strain: 0.01%/s)	T18 (316 SS HAZ, 22 °C, strain: 0.01%/s) (T21 Repeat test , 22 °C, strain: 0.01%/s)	T16 (In 182 butter weld, 22 °C, strain: 0.01%/s)	T14 (In 82 filler weld, 22 °C, strain: 0.01%/s)	T03 (SW-E316-16 filler weld, 22 °C, strain: 0.1%/s)
0.1% offset strain as yield limit	Yield stress (MPa)	489.31	447.84 (463.04)	233.63 (234.86)	402.55 (370.51)	405.13	436.37	424.37
	Yield strain (%)	0.334	0.312 (0.3225)	0.23432 (0.23657)	0.321 (0.3103)	0.371	0.353	0.4236
Linear. kinematic hardening parameter	C1 (MPa)	3062.9	3394.9 (3066.3)	4424 (3367.5)	2964.3 (3631.6)	2768.7	3185.6	2455.1
	γ_1	NA	NA	NA	NA	NA	NA	NA
Nonlinear. kinematic hardening parameter	C1 (MPa)	3018.9	3691.9 (3015.2)	8723.7 (5734.7)	6688.4 (10474)	6187.5	8308.9	4024.9
	γ_1	-0.78979	5.0854 (-0.94661)	77.411 (44.737)	59.962 (88.349)	60.343	75.05	42.136

Table 3. 4 Room-temperature tensile material-hardening parameters of different metals (in reactor pressure boundary components) assuming 0.2% offset strain as yield limit

Material-Hardening properties (valid up to 5% true total strain except the T02 case which is valid up to 3%		T06 (508 LAS BASE, 22 °C, strain: 0.1%/s)	T20 (508 LAS HAZ, 22 °C, strain: 0.01%/s)	T02 (316 SS BASE, 22 oC, strain: 0.1%/s) (T01 Repeat test , 22 oC, strain: 0.01%/s)	T18 (316 SS HAZ, 22 °C, strain: 0.01%/s) (T21 Repeat test , 22 °C, strain: 0.01%/s)	T16 (In 182 butter weld, 22 °C, strain: 0.01%/s)	T14 (In 82 filler weld, 22 °C, strain: 0.01%/s)	T03 (SW-E316-16 filler weld, 22 °C, strain: 0.1%/s)
0.2% offset strain as yield limit	Yield stress (MPa)	488.2	451.02 (462.24)	249.58 (245.09)	416.89 (392.81)	419.71	453.41	431.32
	Yield strain (%)	0.433	0.415 (0.42214)	0.3432 (0.34394)	0.429 (0.42265)	0.483	0.465	0.5279
Linear. kinematic hardening parameter	C1 (MPa)	3184.1	3388.4 (3179)	3598.7 (2970.7)	2543.6 (2923.3)	2325.4	2672.2	2166.8
	γ 1	NA	NA	NA	NA	NA	NA	NA
Nonlinear. kinematic hardening parameter	C1 (MPa)	3391.6	3696.9 (3331.5)	5777.4 (4466.7)	4644 (6195.8)	4021.1	5448	3126.6
	γ 1	3.5661	5.4086 (2.7302)	48.232 (32.484)	42.362 (57.223)	38.78	52.48	29.626

Table 3. 5 Elevated-temperature (300°C) tensile material-hardening parameters of different metals (in reactor pressure boundary components) assuming elastic limit as yield limit

Material-Hardening properties (valid up to 2% true total strain)		T08 (508 LAS BASE, 300 °C, strain: 0.1%/s) (T10 Repeat test, 300 °C, strain: 0.01%/s)	T09 (508 LAS HAZ, 300 oC, strain: 0.1%/s) (T19 Repeat test, 300 °C, strain: 0.01%/s)	T04 (316 SS BASE, 300 °C, strain: 0.1%/s) (T11 repeat test, 300 °C, stress: 2.5253 MPa/s) [T12 repeat test, 300 °C, stroke : 2.1116 mil/s]	T17 (316 SS HAZ, 300 °C, strain: 0.01%/s)	T15 (In 182 butter weld, 300 °C, strain: 0.01%/s)	T13 (In 82 filler weld, 300 °C, strain: 0.01%/s)	T05 (SW-E316-16 filler weld, 300 °C, strain: 0.1%/s)
Assumed elastic limit as yield limit	Yield stress (MPa)	391.01 (379.83)	382.19 (378.76)	130.73 (120.81) [113.99]	247.81	298.41	335.48	333.43
	Yield strain (%)	0.2072 (0.2072)	0.2072 (0.2072)	0.09077 (0.09077) [0.08528]	0.1617	0.215	0.183	0.2755 8
Linear. kinematic hardening parameter	C1 (MPa)	9630.2 (10543)	8920.1 (8486.8)	4751.9 (5197.9) [4211.4]	9127.1	6475.2	6763.2	4738
	γ 1	NA	NA	NA	NA	NA	NA	NA
Nonlinear . kinematic hardening parameter	C1 (MPa)	22011 (25869)	17567 (15849)	13339 (15205) [8900.1]	55079	37654	33182	11955
	γ 1	155.94 (174.25)	129.59 (111.49)	218.45 (214.94) [126.98]	511.16	541.69	417.25	230.94

Table 3. 6 Elevated temperature (300°C) tensile material-hardening parameters of different metals (in reactor pressure boundary components) assuming 0.05% offset strain as yield limit

Material-Hardening properties (valid up to 5% true total strain)		T08 (508 LAS BASE, 300 °C, strain: 0.1%/s) (T10 Repeat test, 300 °C, strain: 0.01%/s)	T09 (508 LAS HAZ, 300 oC, strain: 0.1%/s) (T19 Repeat test, 300 °C, strain: 0.01%/s)	T04 (316 SS BASE, 300 °C, strain: 0.1%/s) (T11 repeat test, 300 °C, stress: 2.5253 MPa/s) [T12 repeat test, 300 °C, stroke : 2.1116 mil/s]	T17 (316 SS HAZ, 300 °C, strain: 0.01%/s)	T15 (In 182 butter weld, 300 °C, strain: 0.01%/s)	T13 (In 82 filler weld, 300 °C, strain: 0.01%/s)	T05 (SW-E316-16 filler weld, 300 °C, strain: 0.1%/s)
0.05% offset strain as yield limit	Yield stress (MPa)	414.71 (406.63)	399.03 (391.9)	145.03 (135.77) [126.09]	284.86	322	359.72	345.8
	Yield strain (%)	0.2603 2 (0.26052)	0.25532 (0.2494)	0.14197 (0.13776) [0.13046]	0.2240 8	0.271	0.234	0.3183 6
Linear kinematic hardening parameter	C1 (MPa)	5933.3 (6597.5)	5890.6 (5950.3)	2701.5 (3020.9) [2867.9]	4025.7	2686.9	2950.4	2301.3
	γ 1	NA	NA	NA	NA	NA	NA	
Nonlinear kinematic hardening parameter	C1 (MPa)	11017 (12240)	10133 (10146)	4373.5 (4941) [4028]	13820	6307	6556.5	4285.5
	γ 1	52.906 (57.768)	46.36 (46.715)	33.25 (32.963) [27.578]	134.67	64.861	56.92	41.449

Table 3. 7 Elevated temperature (300°C) tensile material-hardening parameters of different metals (in reactor pressure boundary components) assuming 0.1% offset strain as yield limit

Material-Hardening properties (valid up to 5% true total strain)		T08 (508 LAS BASE, 300 °C, strain: 0.1%/s) (T10 Repeat test , 300 °C, strain: 0.01%/s)	T09 (508 LAS HAZ, 300 °C, strain: 0.1%/s) (T19 Repeat test , 300 °C, strain: 0.01%/s)	T04 (316 SS BASE, 300 °C, strain: 0.1%/s) (T11 repeat test, 300 °C, stress: 2.5253 MPa/s) [T12 repeat test, 300 °C, stroke : 2.1116 mil/s]	T17 (316 SS HAZ, 300 °C, strain: 0.01%/s)	T15 (In 182 butter weld, 300 °C, strain: 0.01%/s)	T13 (In 82 filler weld, 300 °C, strain: 0.01%/s)	T05 (SW-E316-16 filler weld, 300 °C, strain: 0.1%/s)
0.1% offset strain as yield limit	Yield stress (MPa)	425.8 (419.31)	407.71 (401.55)	150.72 (143.24) [131.13]	305.47	331.98	371.09	350.56
	Yield strain (%)	0.31549 (0.3163)	0.30912 (0.30439)	0.19642 (0.19289) [0.18371]	0.2869	0.3272	0.289	0.37153
Linear. kinematic hardening parameter	C1 (MPa)	5512.4 (6060.3)	5564.2 (5573.8)	2517.2 (2798.8) [2687.6]	3150.5	2356	2609.7	2155
	γ 1	NA	NA	NA	NA	NA	NA	NA
Nonlinear. kinematic hardening parameter	C1 (MPa)	9602.7 (10398)	9144 (9016.5)	3668.5 (4072.9) [3535]	6954.7	4454.7	4753.6	3603.4
	γ 1	46.367 (48.829)	41.677 (41.238)	25.19 (24.459) [21.898]	68.949	45.065	40.562	33.243

Table 3. 8 Elevated-temperature (300°C) tensile material-hardening parameters of different metals (in reactor pressure boundary components) assuming 0.2% offset strain as yield limit

Material-Hardening properties (valid up to 5% true total strain)		T08 (508 LAS BASE, 300 °C, strain: 0.1%/s) (T10 Repeat test , 300 °C, strain: 0.01%/s)	T09 (508 LAS HAZ, 300 °C, strain: 0.1%/s) (T19 Repeat test , 300 °C, strain: 0.01%/s)	T04 (316 SS BASE, 300 °C, strain: 0.1%/s) (T11 repeat test, 300 °C, stress: 2.5253 MPa/s) [T12 repeat test, 300 °C, stroke : 2.1116 mil/s]	T17 (316 SS HAZ, 300 °C, strain: 0.01%/s)	T15 (In 182 butter weld, 300 °C, strain: 0.01%/s)	T13 (In 82 filler weld, 300 °C, strain: 0.01%/s)	T05 (SW-E316-16 filler weld, 300 °C, strain: 0.1%/s)
0.2% offset strain as yield limit	Yield stress (MPa)	439.96 (434.93)	420.21 (414.69)	155.77 (150.77) [136.6]	321.06	338.41	377.81	356.05
	Yield strain (%)	0.42485 (0.42525)	0.41654 (0.41085)	0.29988 (0.29705) [0.28758]	0.39689	0.4334	0.394	0.47578
Linear. kinematic hardening parameter	C1 (MPa)	5034 (5474.9)	5144.6 (5114.4)	2397.2 (2612.2) [2536.4]	2537.2	2181.5	2449.8	2009
	γ 1	NA	NA	NA	NA	NA	NA	NA
Nonlinear. kinematic hardening parameter	C1 (MPa)	8212.7 (8705.4)	8022.8 (7802)	3288.7 (3443.9) [3167.3]	4291.8	3728.3	4079.3	3005.6
	γ 1	40.092 (40.764)	36.546 (35.441)	20.934 (17.818) [17.675]	41.227	37.268	34.333	25.474

3.3 Finite-element Validation of a Representative Test Cases

To check the validity of the estimated parameters in the context of 3D FE modeling, we used the material model parameters and tensile properties presented in Section 3.2 to develop elastic-plastic 3D FE models for four DMW tensile test cases (T14, T16, T18 and T20). The estimated material parameters can be used directly in commercially available FE codes such as ABAQUS. Figure 3.7 is a screen shot of the ABAQUS property module showing the use of Chaboche nonlinear material-hardening parameters. All of the FE models were constructed using a single 3D brick element to model only the cylindrical gage section of the specimens with a length of 0.5 in. Figure 3.8 shows the schematic of the equivalent FE model for a uniaxial tensile specimen. The selected length of gage section was equal to the initial distance between the two legs of the extensometer that was used for measuring the gage area displacement and the corresponding strain. The cylindrical cross-section of the specimen was converted to an equivalent square cross-section so that the FE models could be constructed using only a single 3D brick element.

The FE models were developed to check how accurately the material model captures the stress-strain behavior of the test specimens under different assumptions of yield stress and yield limits. We also conducted an elastic analysis to compare the corresponding elastic-plastic results. The FE models were developed using the ABAQUS CAE, which allows direct use of the Chaboche material models (both linear and nonlinear hardening models). While optimizing the material model parameters, the material model sometimes estimates a negative value for Chaboche parameter γ_1 , particularly when the true total strain versus the true total stress curve is linear and when the elastic limit is used as the yield limit (see Figure 3.15 for RT-T20 test case). However, the ABAQUS CAE doesn't allow a negative value of γ_1 . In that case, the ABAQUS user material (UMAT) option can be used, which doesn't have any restriction on the sign of material parameters. Note that both C_1 and γ_1 in the nonlinear Chaboche model are fitting parameters and will produce accurate FE results when only values of these parameters used in combination and with appropriate sign.

In most of the cases, the nonlinear model better captures the stress-strain behavior than the linear model does. In all cases except two, we used nonlinear hardening models (with C_1 and γ_1). The two exceptions used 0.0% and 0.05% offset strain yield limits for the RT-T20 FE model, for which we used the linear hardening model (with only C_1). In these two cases, since the true total strain versus true total stress curve is mostly linear, the linear hardening model was sufficient. This allowed us to use a negative value for γ_1 (for the nonlinear hardening model) in ABAQUS CAE-based FE models.

The nonlinear hardening model can easily be used with the ABAQUS UMAT option for any sign of these parameters. Figure 3.9 shows the experimental versus elastic-plastic FE model results for the RT-T14 filler weld specimen for different offset yield conditions. It can be seen that elastic analysis produces inaccurate results compared with the corresponding elastic-plastic FE results. It can also be seen that the elastic-limit case (i.e., with 0% offset strain) well captures the stress-strain behavior up to 2% of true total strain, whereas the other offset strain cases well capture the stress-strain curve up to 5% total true strain. This is as expected, since while developing the material models a total true strain of 2% was considered for estimating the material models using elastic limit as yield limit. The same is the case for other offset strain limits, for which a total true strain of 5% was used while estimating the corresponding Chaboche parameters. A magnified section of Figure 3.9 is shown in Figure 3.10. It can be seen that the elastic limit (i.e., with 0% offset strain)-based material model better captures the low-strain-amplitude plastic regime (of the stress-strain curve) than do the higher offset strain-based material

models. The higher the offset strain, the higher is the inaccuracy in capturing the low-strain-amplitude plastic regions of stress-strain curves.

As discussed in Section 3.2, although the 0.2% offset strain-based model is satisfactory to use for most of the FE modeling cases, for better accuracy it is advisable to use lower offset strain-based hardening parameters, particularly for mechanistic-based FE modeling of plasticity-driven low-cycle fatigue cases. The above-discussed observations can also be made from the FE model results of T16, butter weld specimen (Figures 3.11 and 3.12); T18, 316SS HAZ specimen (Figures 3.13 and 3.14); and T20, 508LAS HAZ specimen (Figures 3.15 and 3.16).

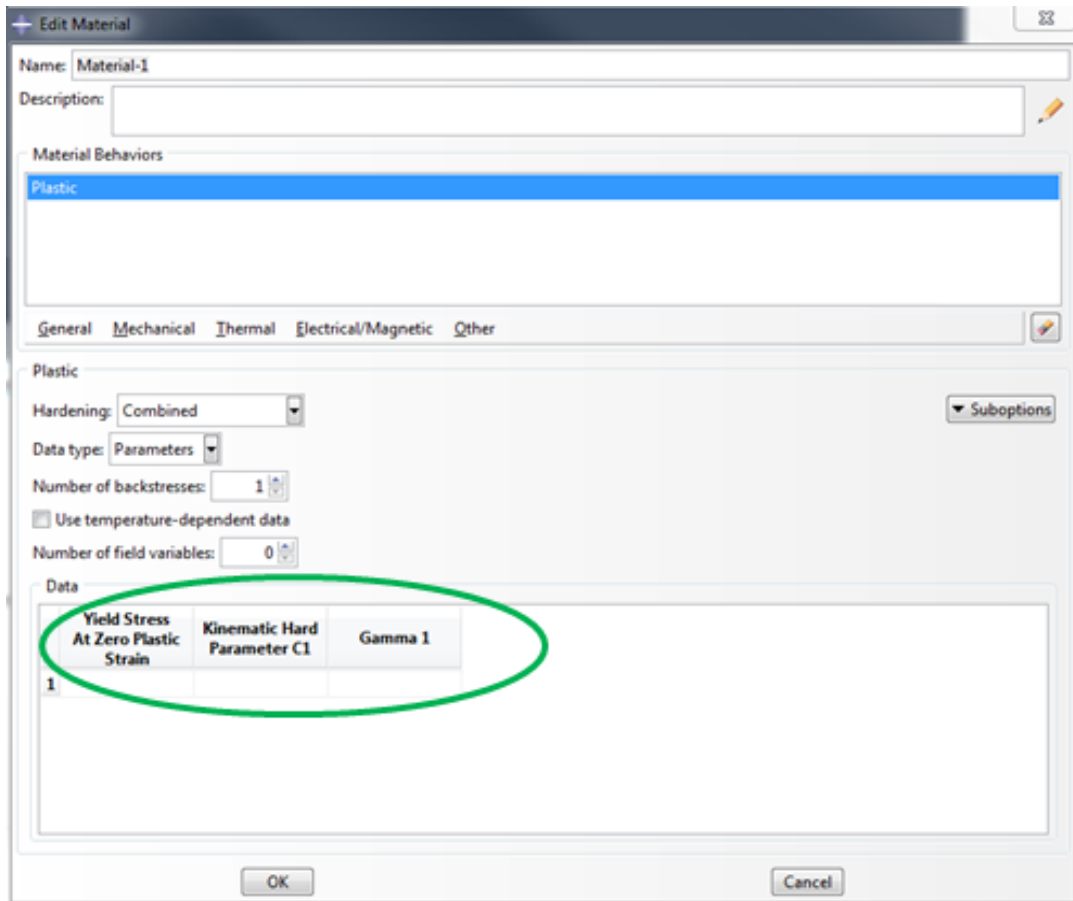


Figure 3. 7 Screen shot of the ABAQUS property module showing the use of Chaboche nonlinear material-hardening parameters.

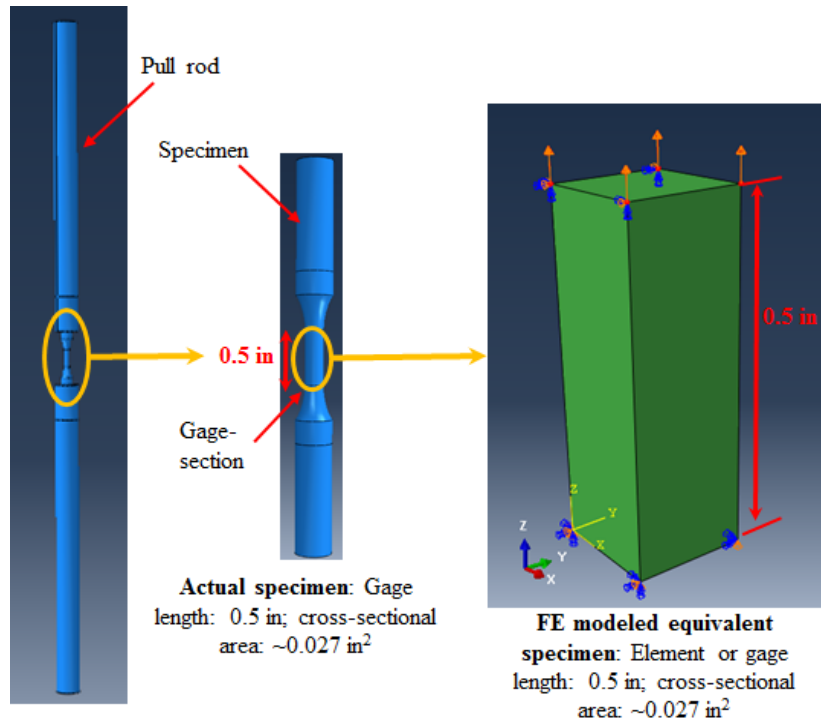


Figure 3. 8 Schematic of the equivalent FE model (of uniaxial tensile specimen).
RT-T14 Filler weld

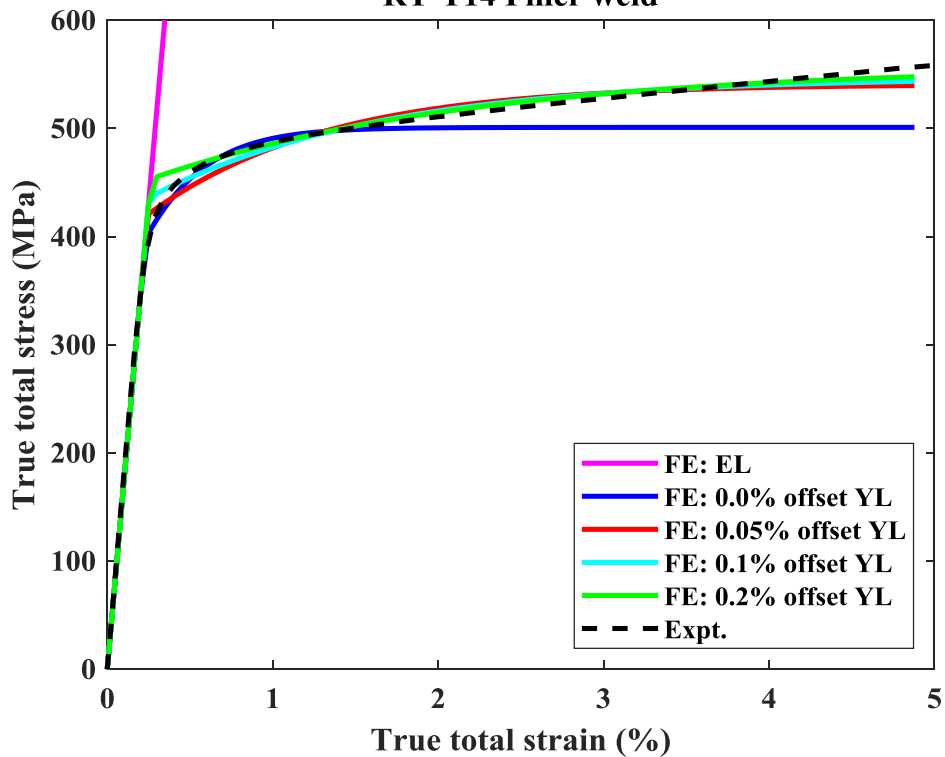


Figure 3. 9 Experimental vs. FE model results for RT-T14 filler weld specimen with respect to different offset yield conditions.

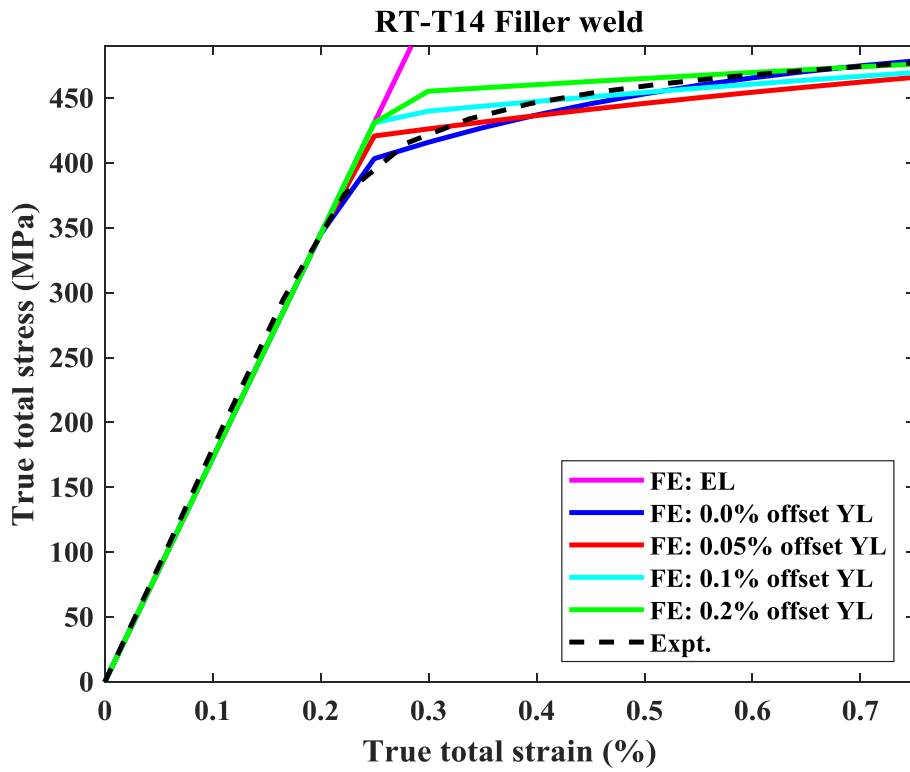


Figure 3. 10 Magnified version of Figure 3.9.

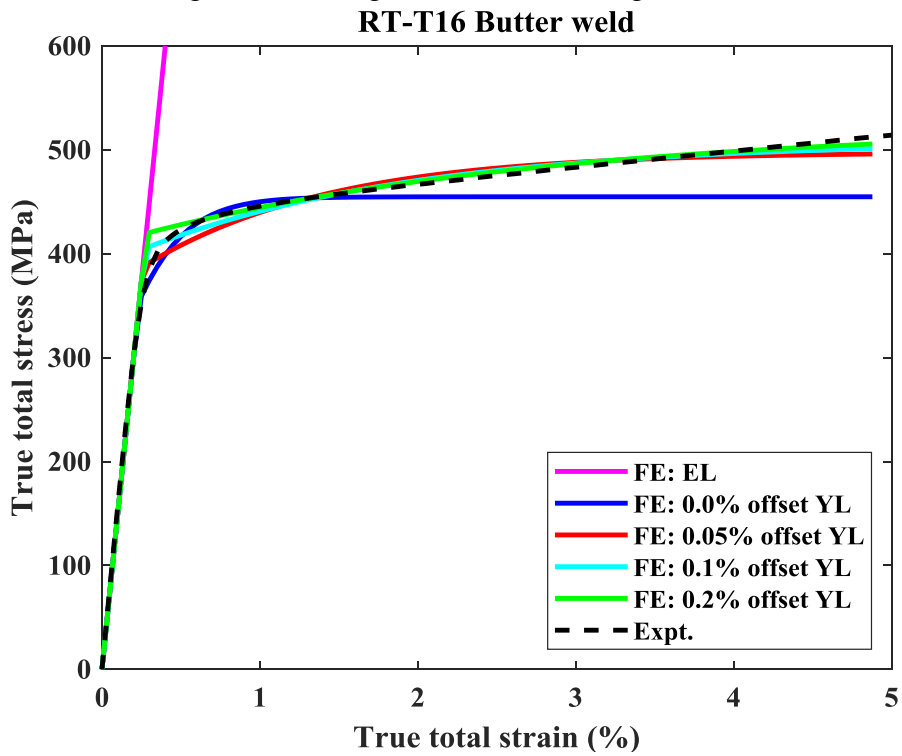


Figure 3. 11 Experimental vs. FE model results for RT-T16 butter weld specimen with respect to different offset yield conditions.

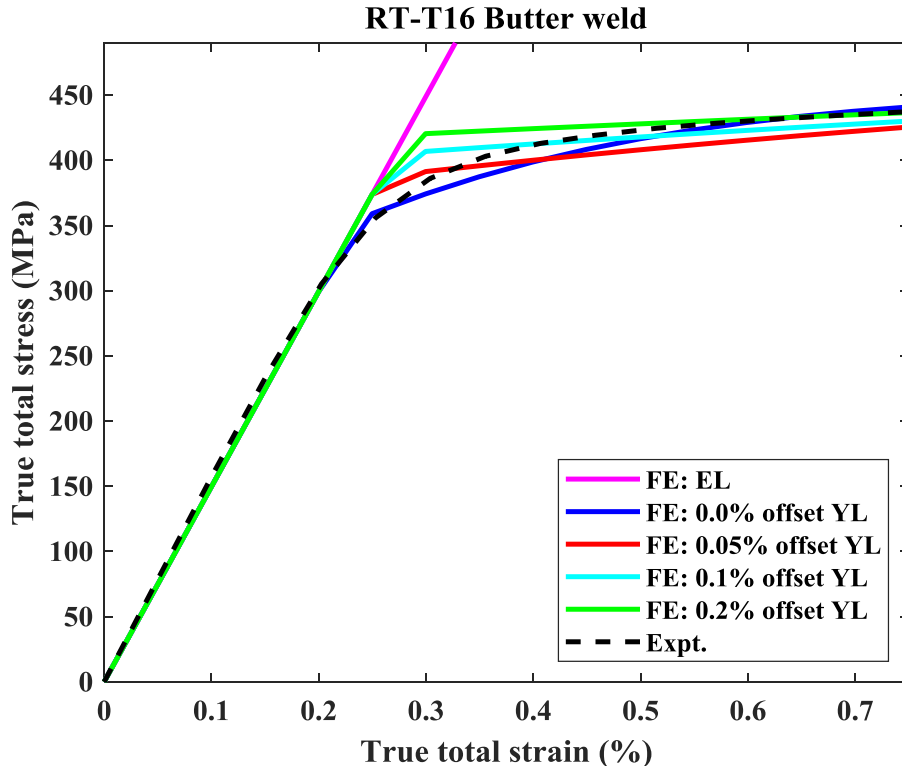


Figure 3. 12 Magnified version of Figure 3.11.

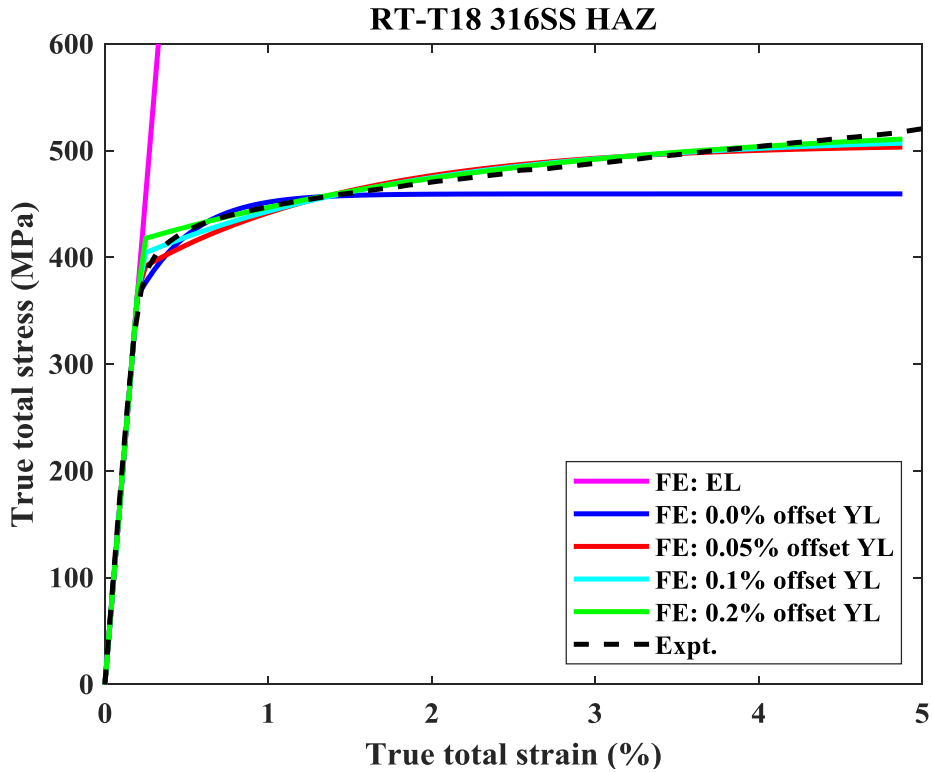


Figure 3. 13 Experimental vs. FE model results for RT-T18 316SS HAZ specimen with respect to different offset yield conditions.

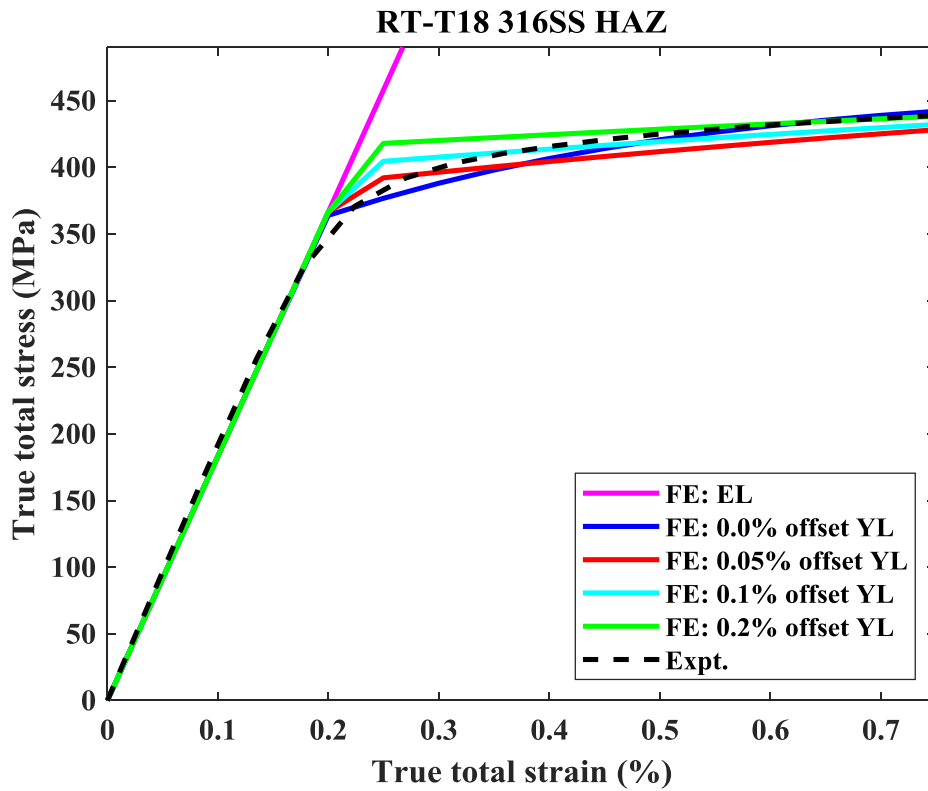


Figure 3. 14 Magnified version of Figure 3.13.

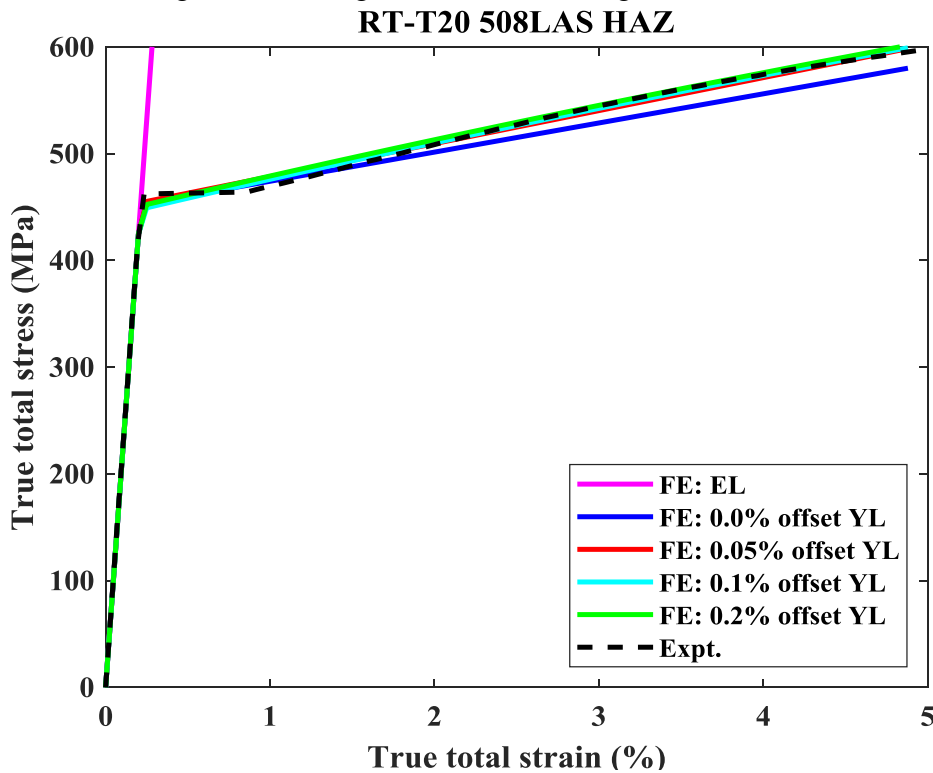


Figure 3. 15 Experimental vs. FE model results for RT-T20 508LAS HAZ specimen with respect to different offset yield conditions.

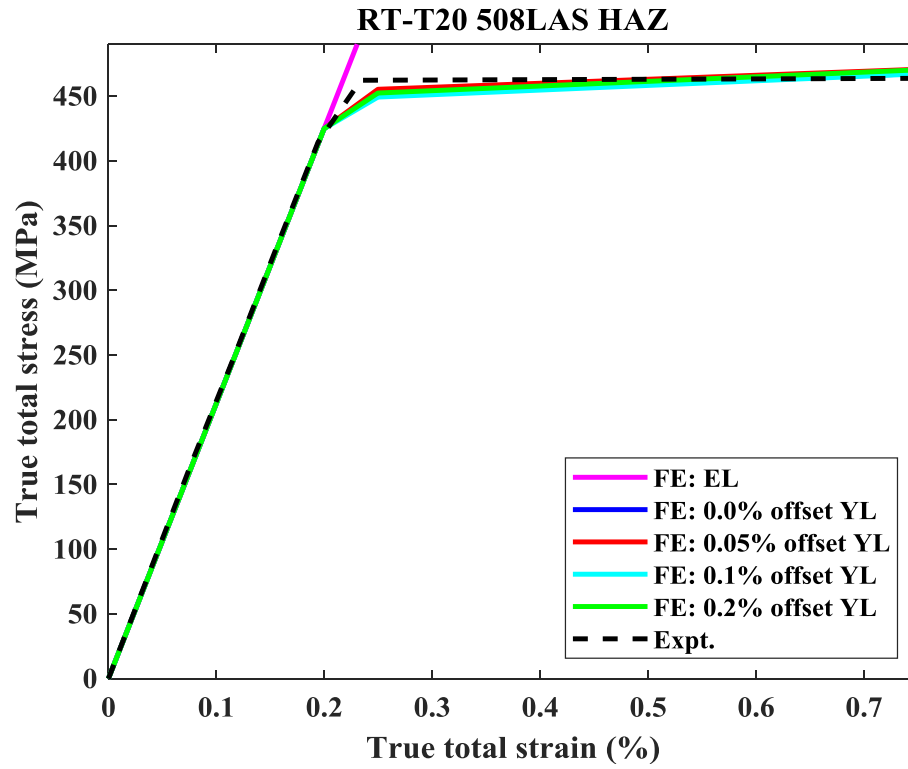


Figure 3. 16 Magnified version of Figure 3.15.

4 Estimation of Thermal Expansion Coefficients for Base and Welds

The thermal expansion coefficient is an important component in thermal-mechanical stress analysis of reactor components. For our thermal-mechanical stress analysis models (discussed in Section 7), we initially used the expansion coefficients given in Section IID of the 2017 version of the ASME code [25]. However, while performing the heat transfer and subsequent structural analysis of the PRZ-SL nozzle, we found a discrepancy of 0.2–0.3% between the FE-estimated thermal strain and the corresponding experimental data (obtained during the heat-up phase of Argonne-conducted uniaxial tensile tests).

Thermal strain is the free expansion strain and depends solely on the temperature boundary conditions and not the displacement boundary conditions of a material. A discrepancy of 0.2–0.3% can lead to substantial over/underestimation of component stress (at a given location) and can lead to erroneous calculation of fatigue life. A reactor component would normally experience a maximum thermal strain of 0.4–0.5%. A discrepancy of 0.2–0.3% thermal strain is substantial, considering that thermal strain (or associated temperature rise/fall) is the major cause of stress.

In our earlier work [26], we performed a detailed system-level study of a two-loop PWR to compare the contribution of thermal load with the contribution of reactor internal pressure. We showed that thermal strain due to temperature increase/decrease was the major cause of high stress in reactor components. Nevertheless, in the nozzle stress analysis model (discussed in Section 7), we found that the discrepancy in thermal strain calculation occurred because the expansion coefficients were taken from Section IID of the ASME 2017 code. We adopted the expansion coefficients from the ASME code for materials with compositions most comparable to the base and weld metals used in our stress analysis models (316SS and 508LAS base, 316SS-SW filler, and 316SS-508LAS DW filler and butter weld).

The discrepancy between our model results and experimental results could be due to the fact that the ASME code properties are average properties obtained from different sources (with tests conducted using various temperatures and grades of materials). To address this issue, we estimated the expansion coefficients from our own test data and used them in the FE model. The corresponding expansion coefficient results and the FE validation results are given below. We anticipate that these types of results may help industry as a guideline for choosing appropriate expansion coefficients for reactor component thermal-mechanical stress analysis.

4.1 Expansion Coefficients for Argonne-Conducted Test Cases

Thermal expansion coefficients were estimated from various tensile test cases given in Table 4.1. We estimated the expansion coefficient of 316SS and 508LAS base, 316SS-SMW filler, and 316SS-508LAS DMW filler and butter welds. We used temperature versus thermal-strain data obtained during the heat-up operation of Argonne-conducted corresponding tensile tests. In each tensile test (see Section 2), the gauge area of a tensile specimen was monitored using three thermocouples. The specimens were initially heated up (from room temperature to a targeted temperature of 300°C) before conducting the isothermal main tensile tests.

During the heat-up, in addition to the temperature, the gauge area strain was measured using an extensometer. We used the average gauge area temperature measurements (from three thermocouples) and the thermal strain measurements (from the extensometer) to estimate the expansion coefficients of 316SS and 508LAS base, 316SS-SW filler, and 316SS-508LAS DW filler and butter welds. The expansion coefficients were estimated from the actual data up to 300°C and, after that, linearly extrapolated up to 350°C. Extrapolation is required to perform the stress analysis of the PRZ-SL nozzle, which experiences a maximum temperature of 350°C. The related results are given in Figures 4.1 through 4-10.

The 508LAS-HAZ and pure base metal have similar tensile behaviors, so we assumed they would have very similar expansion coefficients. All expansion coefficients were estimated with a reference temperature of 21.11°C to be consistent with the ASME code data. The expansion coefficients for the test cases are given in Table 4.2 We also present the overall comparison of the Argonne-estimated expansion coefficients with respect to the ASME code expansion coefficients for similar-grade materials. This comparison is shown in Figure 4.11, which indicates a wide variation of expansion coefficients between Argonne’s data and the ASME code data. An attempt will be made to include the reported expansion coefficient data in the ASME code as a code case.

Table 4. 1 Characteristics of tensile specimens whose heat-up data were used for estimating expansion coefficients

Test ID	Environment	Main test isothermal temperature (°C)	Material type
T04	air	300	316SS base
T05	air	300	316SS SMW filler weld
T13	air	300	DMW-In 82 filler weld
T15	air	300	DMW-In 182 butter weld
T19	air	300	508LAS DMW HAZ

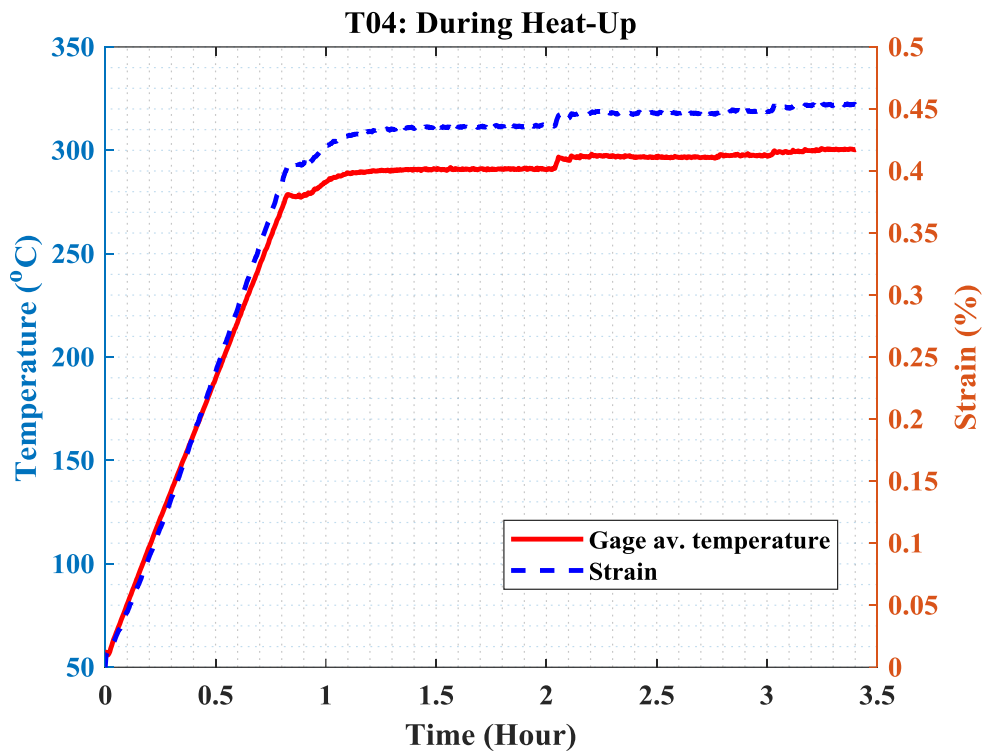


Figure 4. 1 Time vs. gauge area average temperature and strain measured during heating in T04 tensile test specimen: 316SS base metal.

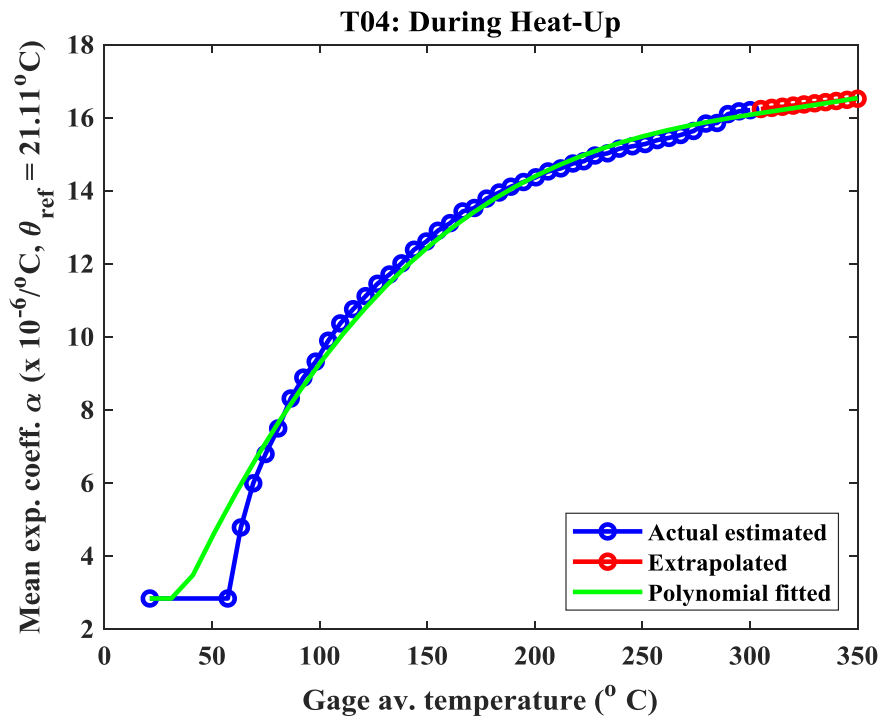


Figure 4. 2 Temperature vs. estimated mean expansion coefficient from T04 tensile test data: 316SS base metal.

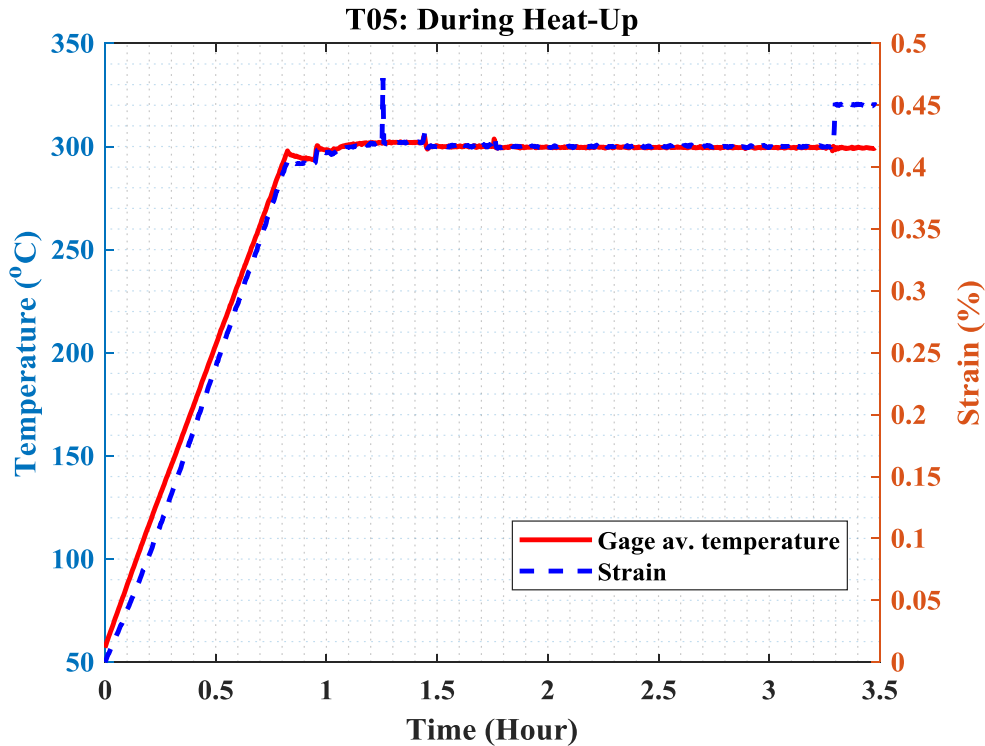


Figure 4. 3 Time vs. gauge area average temperature and strain measured during heating in T05 tensile test specimen: 316SS SMW filler weld.

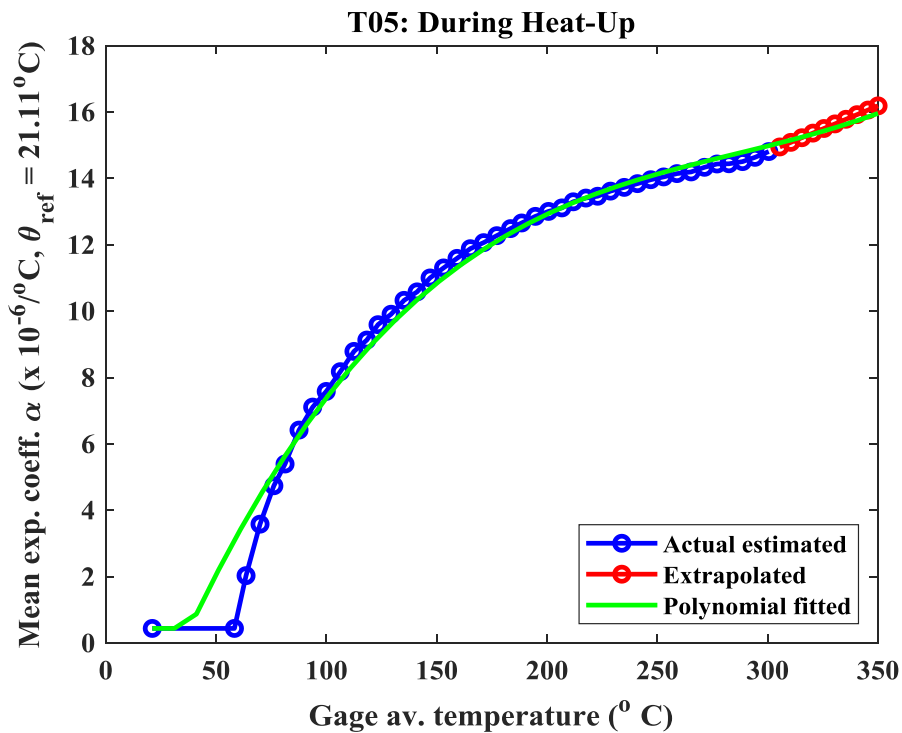


Figure 4. 4 Temperature vs. estimated mean expansion coefficient from T05 tensile test data: 316SS SMW filler weld.

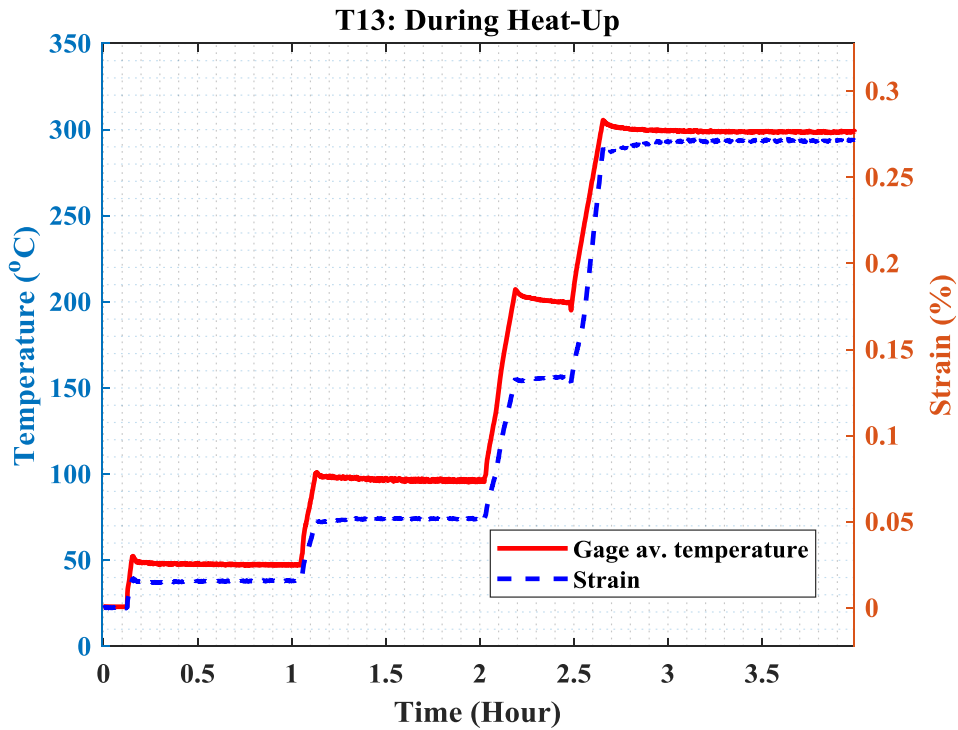


Figure 4. 5 Time vs. gauge area average temperature and strain measured during heating in T13 tensile test specimen: DMW In-82 filler weld.

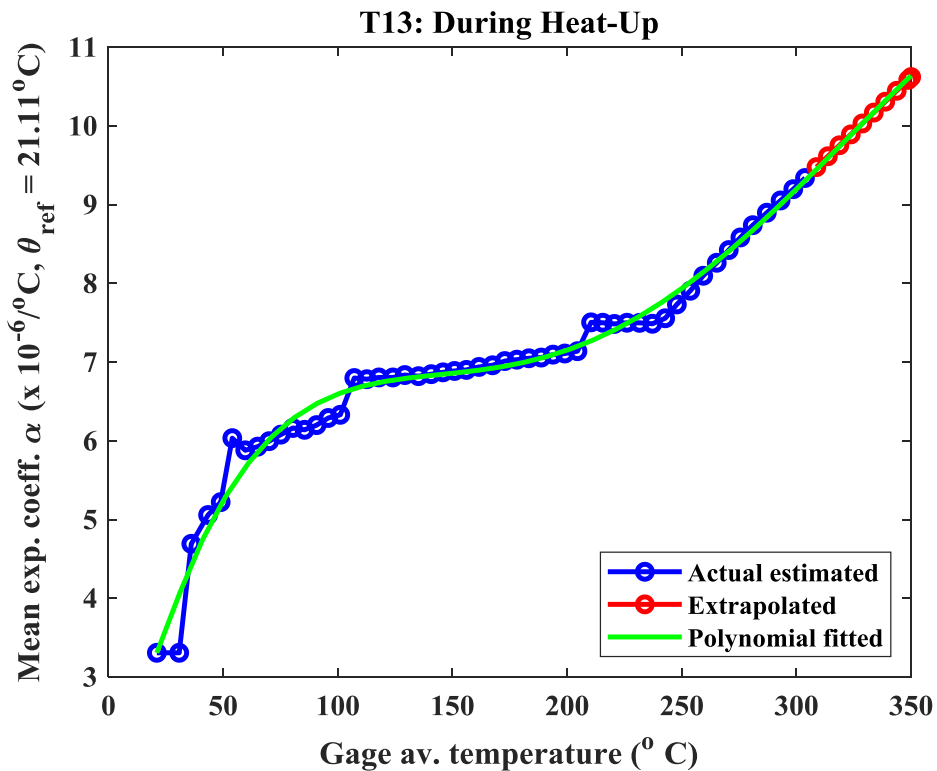


Figure 4. 6 Temperature vs. estimated mean expansion coefficient from T13 tensile test data: DMW In-82 filler weld.

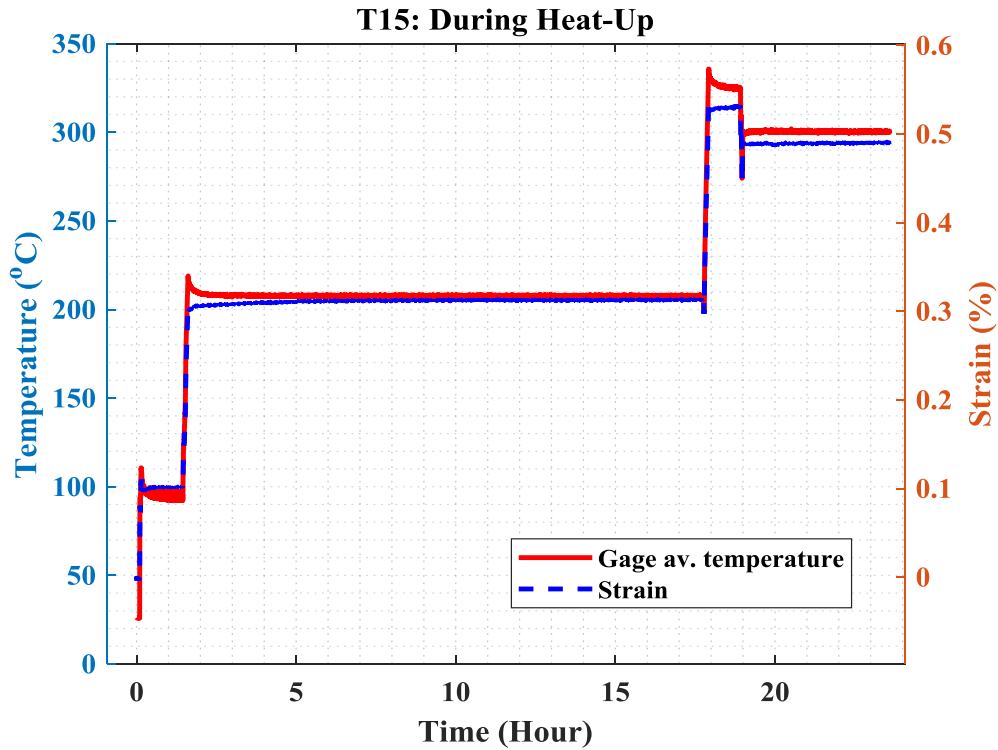


Figure 4. 7 Time vs. gauge area average temperature and strain measured during heating in T15 tensile test specimen: DMW In-82 butter weld.

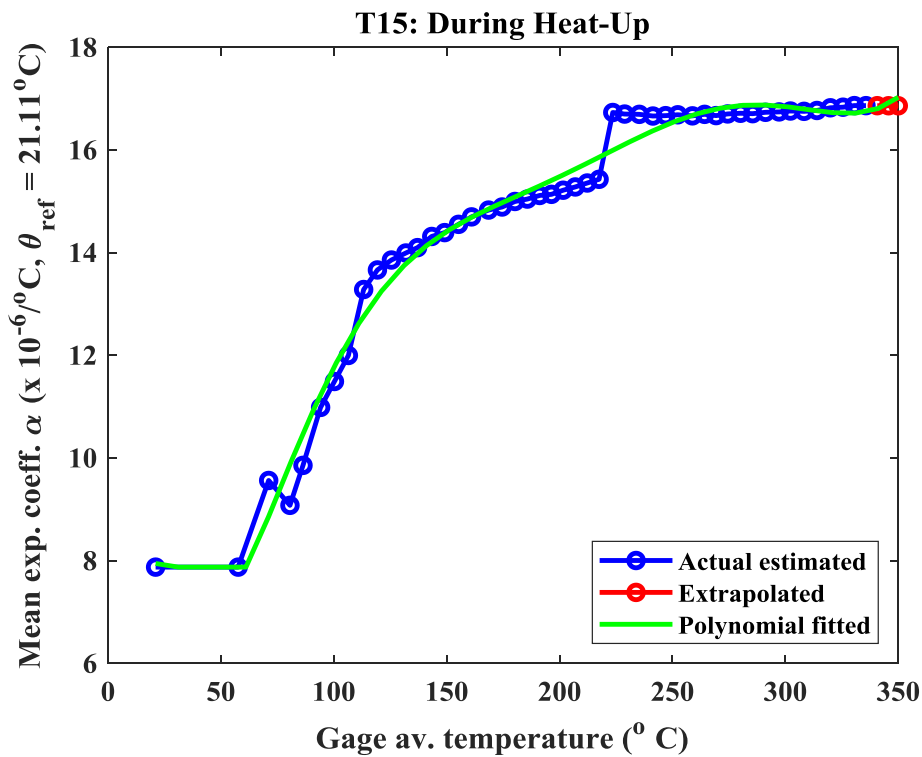


Figure 4. 8 Temperature vs. estimated mean expansion coefficient from T15 tensile test data: DMW In-82 butter weld.

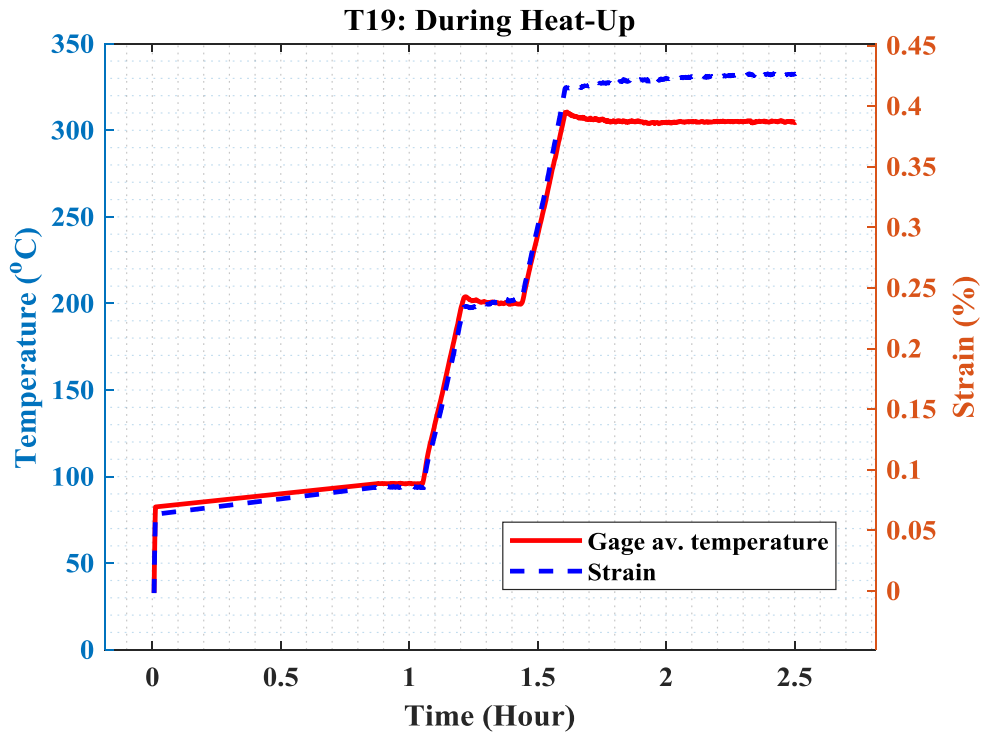


Figure 4. 9 Time vs. gauge area average temperature and strain measured during heating in T19 tensile test specimen: 508LAS DMW-HAZ.

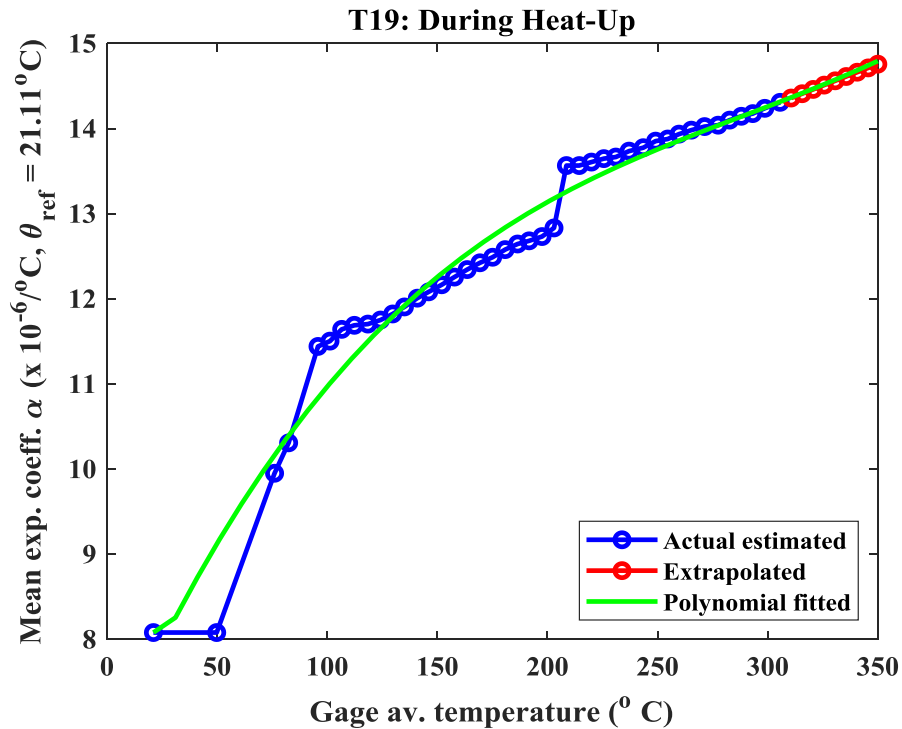


Figure 4. 10 Temperature vs. estimated mean expansion coefficient from T19 tensile test data: 508LAS DMW-HAZ.

Table 4. 2 Argonne-estimated expansion coefficients for 316SS and 508LAS base, 316SS-SW filler, and 316SS-508LAS DW filler and butter welds

Temp (°C)	T04 (300 °C Air, 316 SS Base)	T19 (300 °C Air, 508LAS HAZ)	T05 (300 °C Air, SW- E316-16 Filler weld)	T13 (300 °C Air, DW-In 82 Filler weld)	T15 (300 °C Air, DW-In 182 Butter weld)
	Expansion coeff (1 / °C)	Expansion coeff (1 / °C)	Expansion coeff (1 / °C)	Expansion coeff (1 / °C)	Expansion coeff (1 / °C)
21.11	2.84E-06	8.0805e-06	4.4273e-07	3.3078e-06	7.9477e-06
31.11	2.84E-06	8.2561e-06	4.4273e-07	4.067e-06	7.8772e-06
41.11	3.47E-06	8.7299e-06	8.7463e-07	4.7487e-06	7.8772e-06
51.11	4.64E-06	9.1746e-06	2.2e-06	5.2931e-06	7.8772e-06
61.11	5.72E-06	9.5914e-06	3.4306e-06	5.7206e-06	7.8772e-06
71.11	6.74E-06	9.9815e-06	4.5703e-06	6.0495e-06	8.8574e-06
81.11	7.68E-06	1.0346e-05	5.6232e-06	6.2969e-06	9.9318e-06
91.11	8.55E-06	1.0686e-05	6.5934e-06	6.4781e-06	1.0949e-05
101.11	9.35E-06	1.1003e-05	7.4849e-06	6.6072e-06	1.1855e-05
111.11	1.01E-05	1.1298e-05	8.3017e-06	6.6965e-06	1.2624e-05
121.11	1.08E-05	1.1572e-05	9.0479e-06	6.7574e-06	1.3251e-05
131.11	1.14E-05	1.1826e-05	9.7275e-06	6.7998e-06	1.375e-05
141.11	1.20E-05	1.2062e-05	1.0344e-05	6.8322e-06	1.414e-05
151.11	1.25E-05	1.2281e-05	1.0903e-05	6.8621e-06	1.4445e-05
161.11	1.30E-05	1.2483e-05	1.1407e-05	6.896e-06	1.4693e-05
171.11	1.34E-05	1.267e-05	1.186e-05	6.9392e-06	1.4906e-05
181.11	1.38E-05	1.2843e-05	1.2267e-05	6.9961e-06	1.5104e-05
191.11	1.41E-05	1.3004e-05	1.2632e-05	7.0699e-06	1.5301e-05
201.11	1.44E-05	1.3153e-05	1.2958e-05	7.1633e-06	1.5506e-05
211.11	1.47E-05	1.3292e-05	1.325e-05	7.278e-06	1.572e-05
221.11	1.49E-05	1.3422e-05	1.3512e-05	7.415e-06	1.5941e-05
231.11	1.52E-05	1.3544e-05	1.3747e-05	7.5745e-06	1.6162e-05
241.11	1.53E-05	1.3659e-05	1.396e-05	7.7563e-06	1.6372e-05
251.11	1.55E-05	1.3768e-05	1.4155e-05	7.9594e-06	1.6558e-05
261.11	1.56E-05	1.3873e-05	1.4336e-05	8.1823e-06	1.6709e-05
271.11	1.58E-05	1.3974e-05	1.4506e-05	8.4232e-06	1.6816e-05
281.11	1.59E-05	1.4073e-05	1.4671e-05	8.6799e-06	1.6872e-05
291.11	1.60E-05	1.4172e-05	1.4833e-05	8.9497e-06	1.6878e-05
301.11	1.61E-05	1.427e-05	1.4998e-05	9.2298e-06	1.6842e-05
311.11	1.62E-05	1.437e-05	1.5168e-05	9.5171e-06	1.6783e-05
321.11	1.63E-05	1.4473e-05	1.5348e-05	9.8083e-06	1.6728e-05
331.11	1.64E-05	1.4579e-05	1.5543e-05	1.01e-05	1.672e-05
341.11	1.65E-05	1.469e-05	1.5755e-05	1.0389e-05	1.6811e-05
350	1.65E-05	1.4794e-05	1.5963e-05	1.0642e-05	1.7028e-05

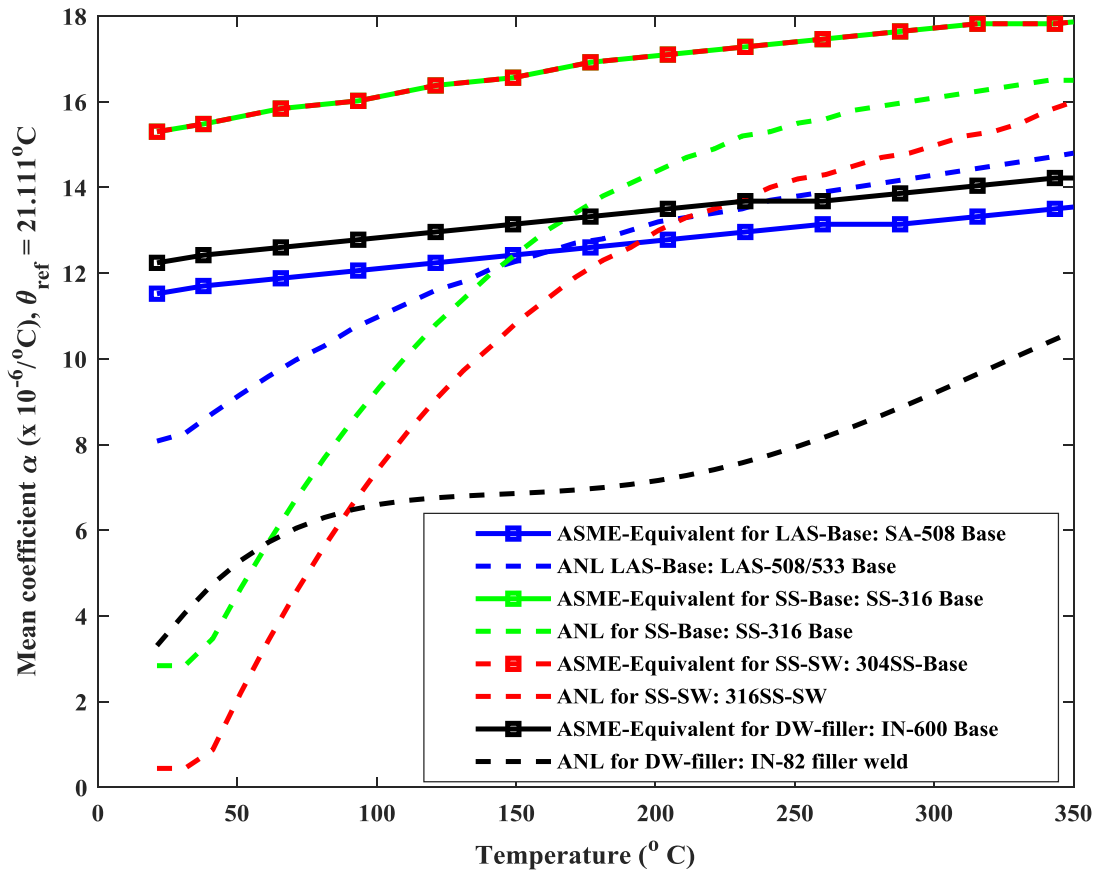


Figure 4. 11 Comparison of the Argonne-estimated expansion coefficients with ASME code (Section IID) expansion coefficients for similar-grade materials.

4.2 Validity Check of Estimated Expansion Coefficients

Although the detailed thermal-mechanical stress analysis results will be discussed later in this report (Section 7), we present here some validation results to show that the Argonne-estimated expansion coefficients capture the actual/experimental thermal expansion behavior when they are used in the FE model. Figure 4.12 shows the FE-simulated nodal temperature distribution of the PRZ-SL nozzle during the hot-standby to power-operation transition, with a temperature of approximately 295.5°C at the DMW filler weld location (highlighted). Figure 4.13 shows the FE- simulated thermal strain of 0.26% at the corresponding location and time. Comparing these results with the Argonne-conducted experimental results, we see a good-correlation between experimental and FE-simulated results (see Figure 4.5, which shows the experimentally observed thermal strain in T13, DMW In-82 filler weld, at different temperatures). These results give us confidence that the Argonne-estimated expansion coefficients can be used for stress analysis of reactor pressure boundary components, such as the PRZ-SL nozzle (discussed in detail in Section 7 of this report).

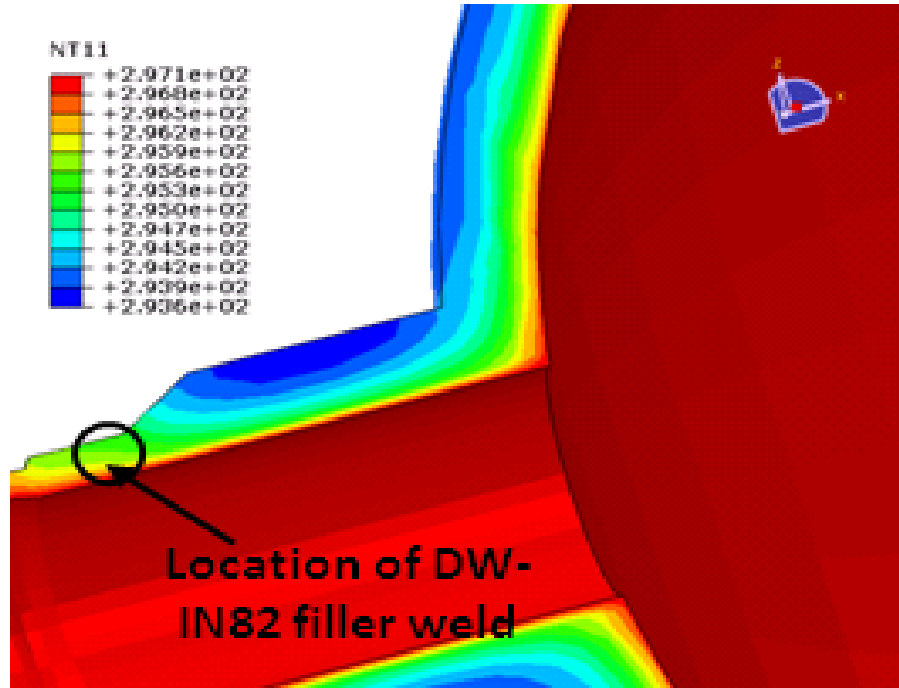


Figure 4. 12 FE-simulated nodal temperature (in °C) contour of PRZ-SL nozzle during the hot-standby to power-operation transition.

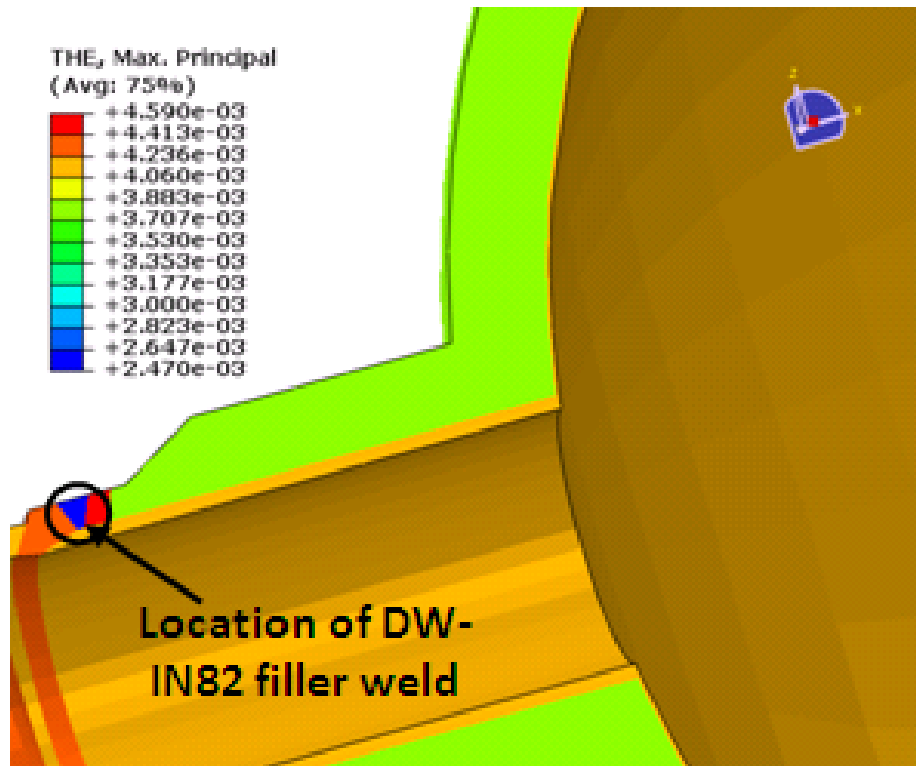


Figure 4. 13 FE-simulated thermal strain (in mm/mm) contour of PRZ-SL nozzle during the hot-standby to power-operation transition.

5 Estimation of Cycle-Dependent Ramberg-Osgood Parameters for Similar Metal Welds

Available Ramberg-Osgood (R-O) parameters are static and generally based on the tensile curve [27, 28]. These static R-O parameters cannot necessarily be used for accurately modeling the cyclic plasticity behavior of reactor components. However, R-O parameters are required to develop continuum damage mechanics-based damage models [29], which are part of our future work. Following continuum damage mechanics type model our aim is to estimate some type of cycle versus accumulative damage states (e.g. equivalent of a monotonic tensile curve encompassing the entire fatigue life). This section discusses the estimation of cyclic R-O parameters for 316SS SMWs. The parameters were estimated under various conditions: in-air at room temperature, in-air at 300°C, and in-air under primary-loop water conditions for a PWR. The details of the R-O model’s theoretical background and the associated results are presented below.

5.1 Ramberg-Osgood Model Theoretical Background

The R-O equation is widely used to formulate the stress-strain curve of the material, which is expressed as follows [27-29]:

$$\varepsilon_t = \varepsilon_e + \varepsilon_p = \frac{\sigma}{E} + \left(\frac{\sigma}{K}\right)^{\frac{1}{n}} \quad (5.1)$$

where

$$\begin{aligned} \varepsilon_e &= \frac{\sigma}{E} \\ \varepsilon_p &= \left(\frac{\sigma}{K}\right)^{\frac{1}{n}} \end{aligned}$$

In Eq. 5.1, $K = K(N)$ is the hardening modulus, and $n = n(N)$ is the hardening exponent. The functional form of $K = K(N)$ and $n = n(N)$ with respect to cycle N shows that these two parameters are cycle-dependent. These parameters can be estimated from the cyclic stress-strain data. To estimate the parameters of the R-O model, we can linearize the plastic strain component (ε_p) of Eq. 5.1 as follows:

$$(\ln \sigma) = n(\ln \varepsilon_p) + \ln K \quad (5.2)$$

Equation 5.2 implies that when we take \log for both stress and plastic strain, the relationship between the two terms will be linear, having the slope of n and intercept of $(\ln K)$. With the given stress and strain data, the hardening modulus K and hardening coefficient n can be estimated by numerically solving Eq. 5.2. The cycle-dependent parameters need to be estimated on the basis of the cycle-dependent equivalent monotonic stress-strain curves.

5.2 Input Data

The R-O parameters were estimated for the fatigue test cases given in Table 5.1. This table also gives the details about two tensile test cases, the results of which were also compared with the corresponding temperature fatigue test-based results. To estimate the cyclic R-O parameters, we need the input cyclic stress-strain curves. The cyclic stress-strain curves for 316SS SMW were estimated using the cyclic elastic modulus, yield stress, and cyclic Chaboche hardening parameters ($C1$ and $\gamma1$). These parameters are taken from our earlier work [12]. For convenience, these input data are presented below. For example Figures 5.1, 5.2, 5.3, and 5.4 show the cyclic elastic modulus, yield stress, and Chaboche parameters $C1$ and $\gamma1$, respectively. Table 5.2 gives the corresponding first quarter of cyclic test case parameters, which are required to construct the first quarter stress-strain curves. Table 5.2 also gives the parameters required to construct the tensile strain curves of the SMW.

Table 5. 1 Experimental conditions for two tensile and four fatigue test cases.

Test Case	Loading	Environment
RT-T03	Strain controlled tensile test, strain rate = 0.1%/s	In-air, 22 °C
ET-T05	Strain controlled tensile test, strain rate = 0.1%/s	In-air, 300 °C
RT-F08	Cyclic loading (fatigue test), Strain controlled, Strain amplitude = 0.5%, Strain rate = 0.1%/s	In-air, 22 °C
ET-F07	Cyclic loading (fatigue test), Strain controlled, Strain amplitude = 0.5%, Strain rate = 0.1%/s	In-air, 300 °C
ET-F17	Cyclic loading (fatigue test), Stroke controlled, Stroke amplitude = 0.1944 mm, Stroke rate = 0.003888 mm/s	In-air, 300 °C
EN-F18	Cyclic loading (fatigue test), Stroke controlled, Stroke amplitude = 0.1944 mm, Stroke rate = 0.003888 mm/s	PWR water, 300°C, Water chemistry: 1000 ppm B as H3BO3, 2 ppm Li ⁺ as LiOH, 20% H ₂ /bal. N ₂ cover gas, and DO < 5 ppb

* RT, ET, and EN refer to room temperature, elevated temperature, and PWR environment, respectively.

Table 5. 2 Estimated mechanical properties for tensile testing cases and fatigue testing cases at initial quarter cycle.

Test Case	Elastic Modulus [GPa]	Stress at Elastic Limit [MPa]	Nonlinear Chaboche Parameter, $C1$ [MPa]	Nonlinear Chaboche Parameter, $\gamma1$
T03	131.93	371.08	43190	501.26
T05	130.66	320.85	21913	369.61
F08	149.288	296.1296	209697.5	1283.876
F07	138.157	253.4464	148832.1	1597.759
F17	131.278	225.6982	134843.7	1180.948
F18	161.538	253.2277	106633.8	1162.601

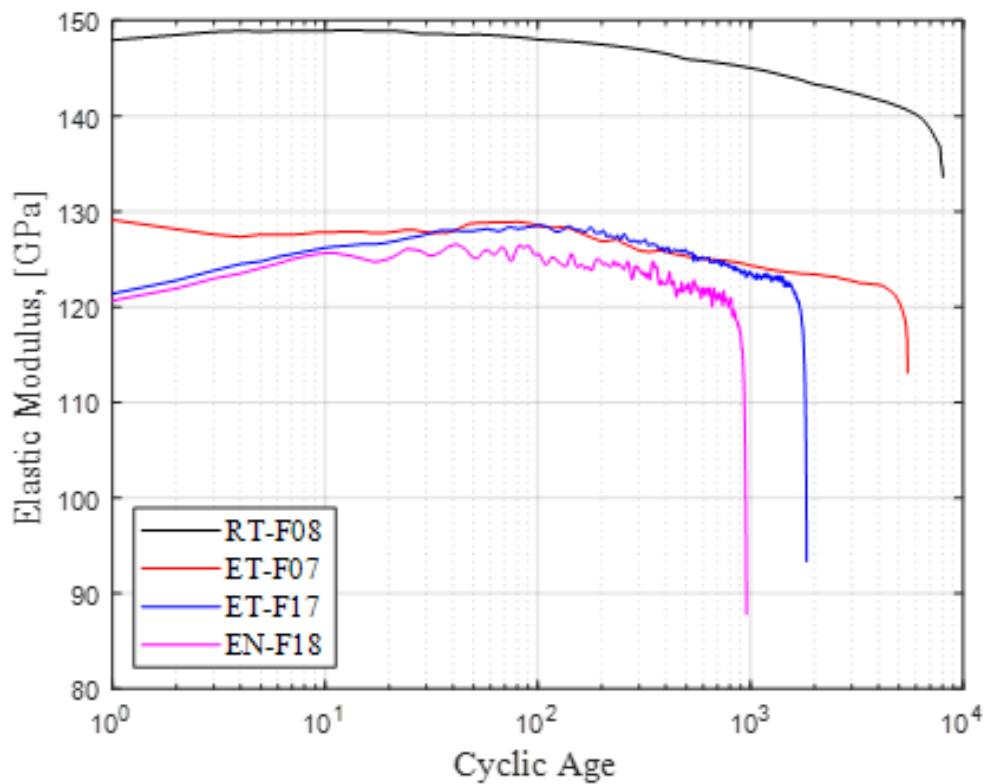


Figure 5. 1 Cyclic elastic modulus for fatigue testing cases from $N=1$ to $N=N_f$.

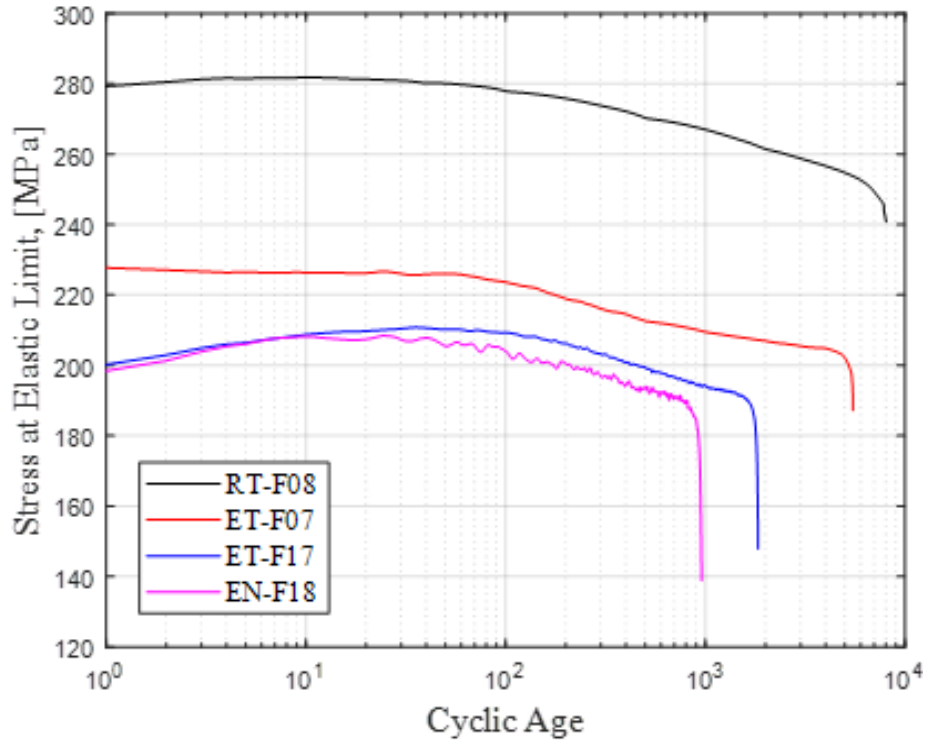


Figure 5. 2 Cyclic elastic limit stress for fatigue testing cases from N=1 to N=N_f.

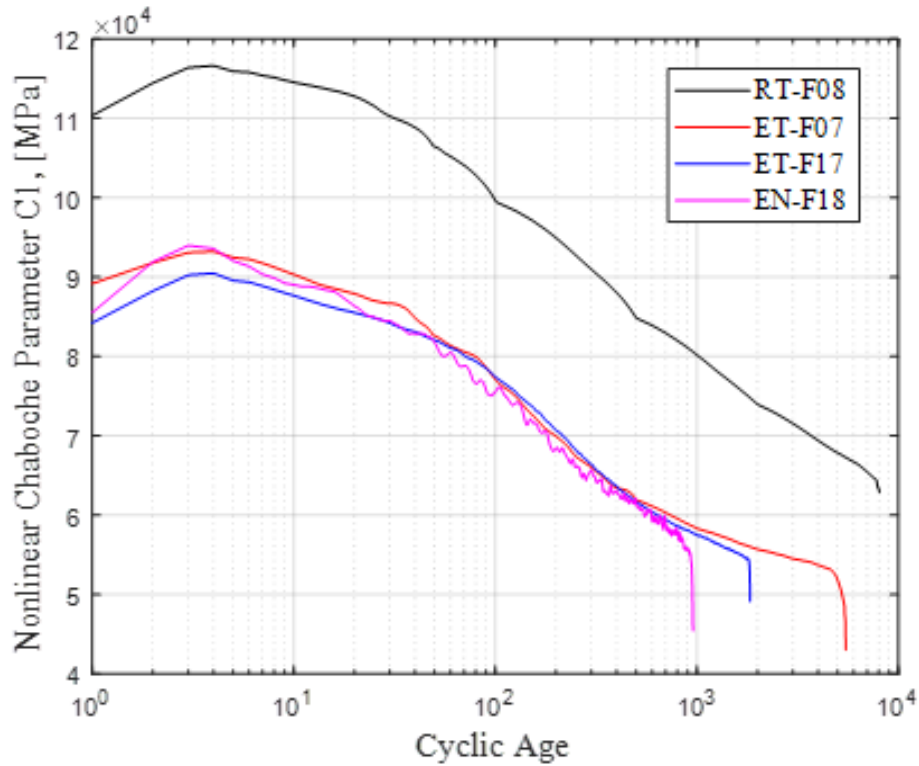


Figure 5. 3 Cyclic Chaboche parameter $C1$ for fatigue testing cases from N=1 to N=N_f.

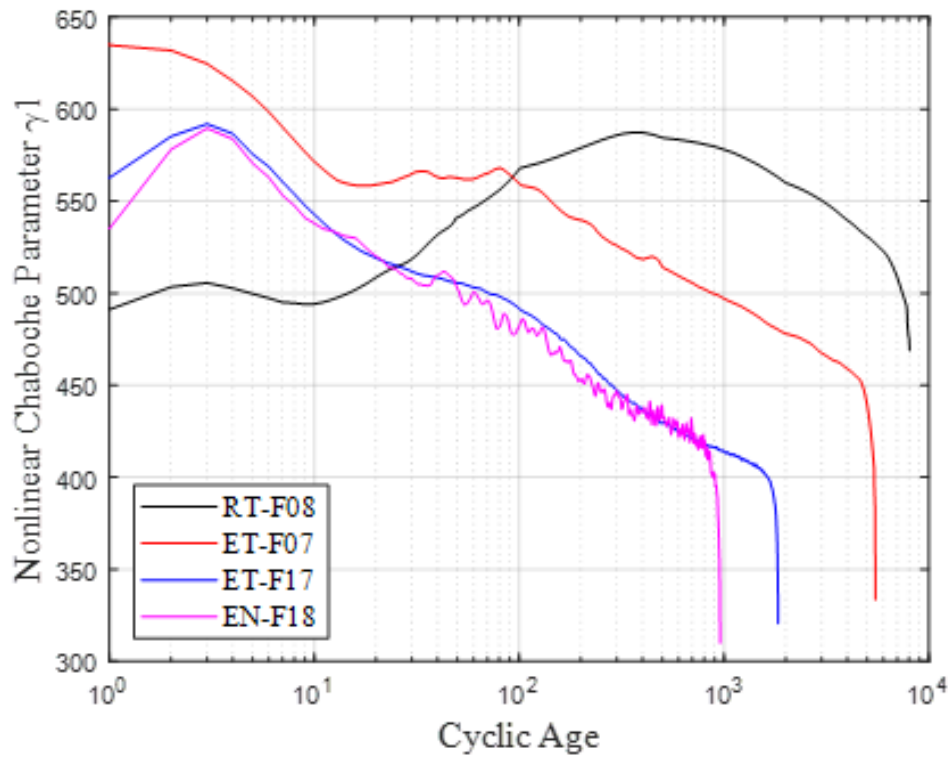


Figure 5. 4 Cyclic Chaboche parameter γ_1 for fatigue testing cases from $N=1$ to $N=N_f$.

5.3 Results of Cyclic Ramberg-Osgood Model

Using the above-mentioned cyclic parameters, we first estimated the cyclic stress-strain curves (equivalent monotonic stress-strain curves) using the Chaboche model. Then, using these cyclic stress-strain curves, we estimated the corresponding cyclic R-O parameters. The reconstructed Chaboche model-based cyclic stress-strain curves are shown in Figures 5.5 to 5.8. These figures show that the cyclic stress-strain curves are initially similar to the reference tensile test stress-strain curve (i.e., when $N = 0.25$), but then significantly vary. These results show that estimating a single set of R-O parameters on the basis of tensile test-based stress-strain curves cannot capture the cyclic hardening and softening in a reactor metal. We used the linear regression of the reconstructed stress-strain curve data (see Figures 5.5 to 5.8) to estimate the cyclic R-O parameters. In this work, we considered only the plastic stress-strain curve data ranging from the 0.1% offset point to strain amplitude ϵ_a (see Figure 5.9). The offset value of 0.1% was chosen instead of the usual 0.2% offset strain to capture more of the plastic regime in the equivalent monotonic SS curves. Note that unlike the tensile stress-strain curves, the maximum strain amplitude of the equivalent monotonic stress-strain curve (for fatigue loading) hardly exceeds 0.5%, so considering a higher offset strain can lead to significant exclusion of the plastic regime of the equivalent-monotonic stress-strain curves. A detailed explanation can be found in Argonne report [12].

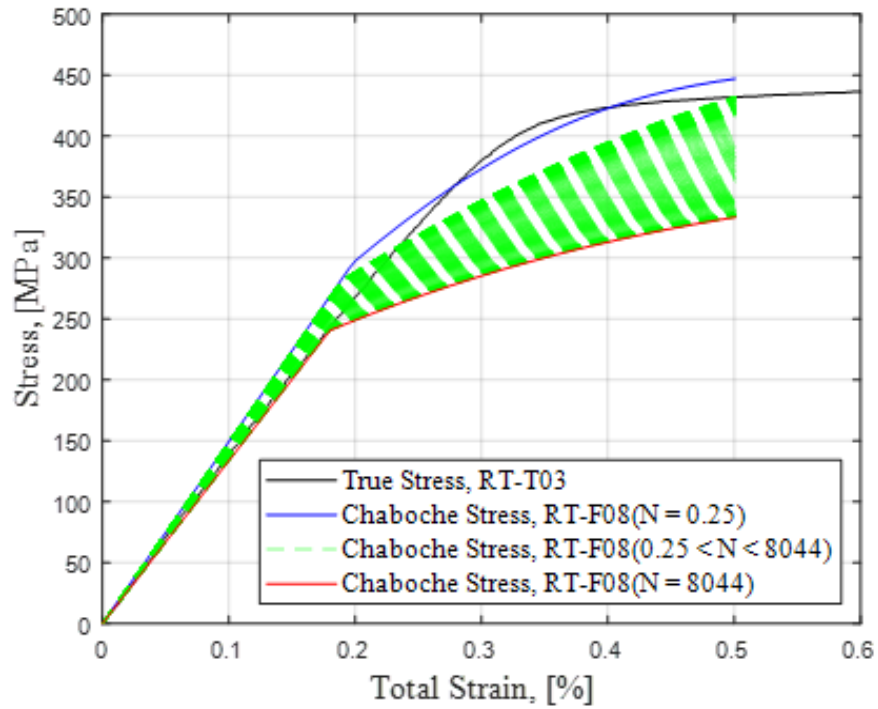


Figure 5. 5 Comparison of the reference tensile (RT-T05) stress-strain curve and reconstructed cyclic stress-strain curves for RT-F08 fatigue test case.

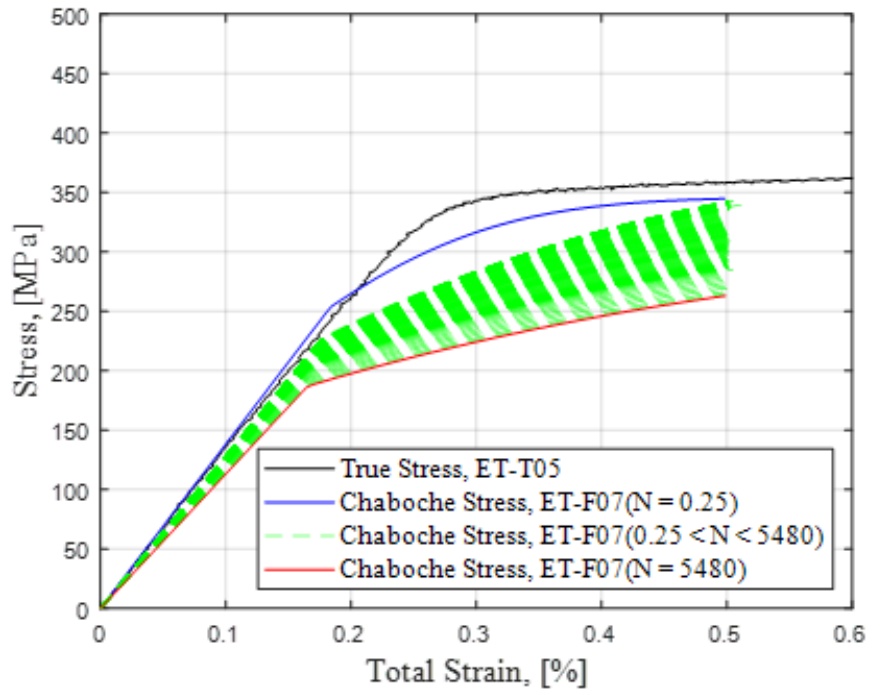


Figure 5. 6 Comparison of the reference tensile (ET-T05) stress-strain curve and reconstructed cyclic stress-strain curves for ET-F07 fatigue test case.

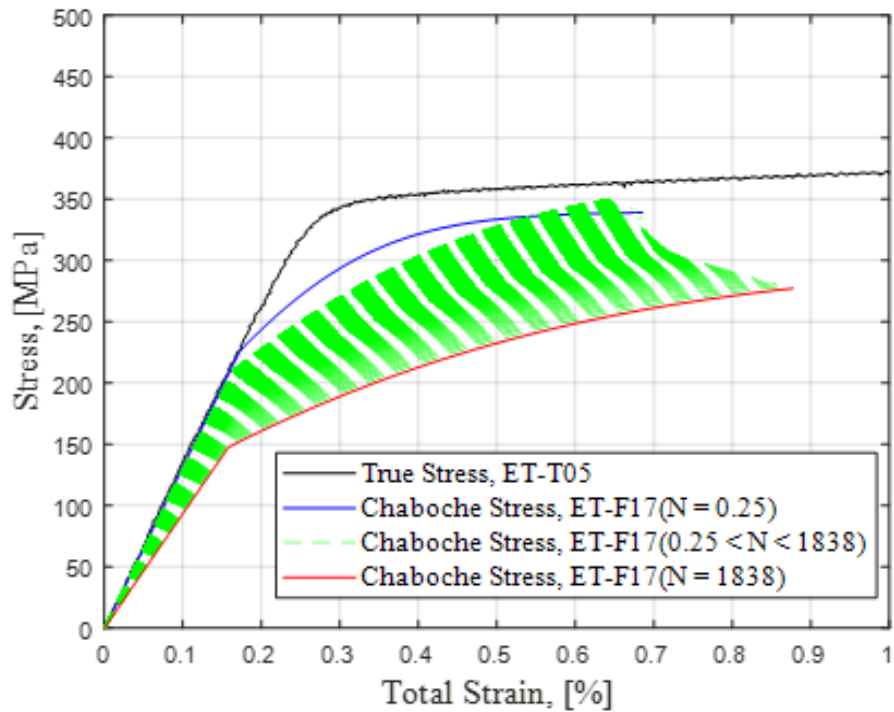


Figure 5. 7 Comparison of the reference tensile (ET-T05) stress-strain curve and reconstructed cyclic stress-strain curves for ET-F17 fatigue test case.

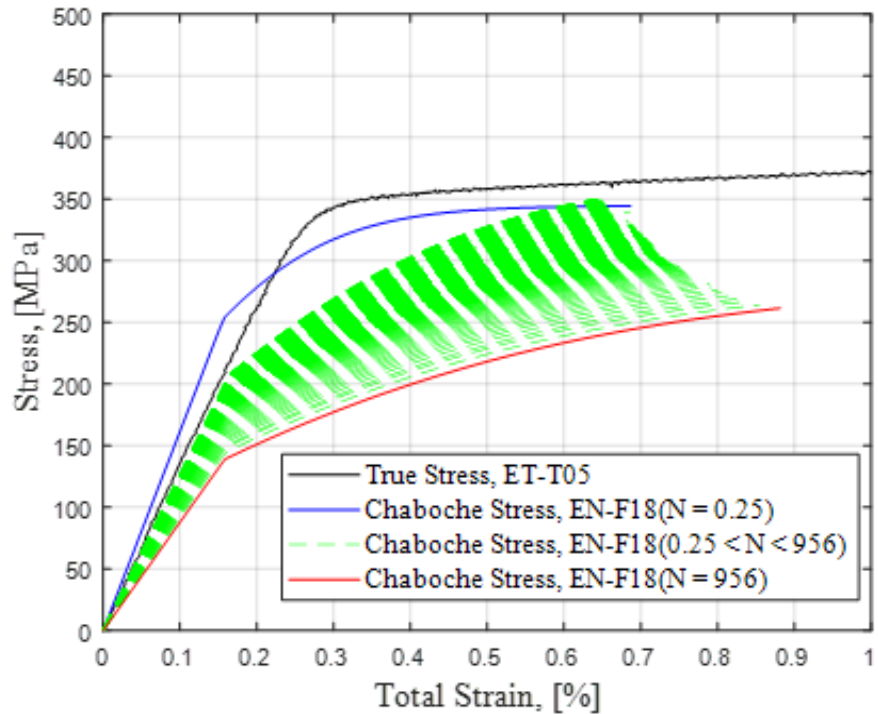


Figure 5. 8 Comparison of the reference tensile (ET-T05) stress-strain curve and reconstructed cyclic stress-strain curves for ET-F18 fatigue test case.

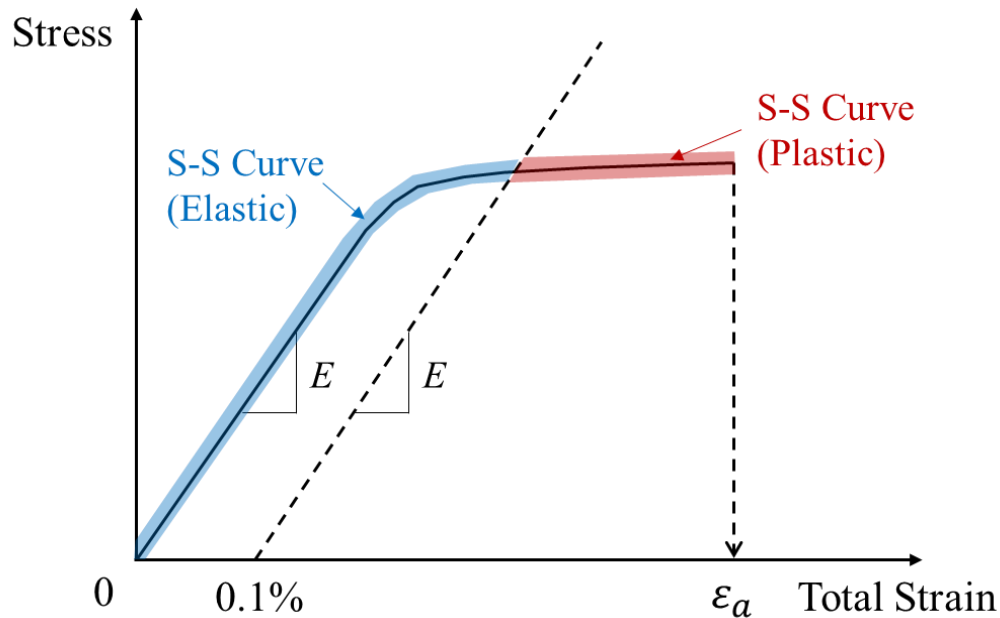


Figure 5. 9 Schematic illustration describing the definition of the elastic and plastic parts of the stress-strain curve.

Table 5.3 shows the resulting estimated Ramberg-Osgood parameters for two tensile testing cases and four fatigue testing cases at first quarter ($N=0.25$) cycle. The applicable strain range is determined by the associated strain amplitude for each case. Figures, 5.10 and 5.11 show the estimated R-O parameters for fatigue testing cases from $N = 1$ to $N = N_f$. From the results above, it can be seen that both the hardening modulus K and exponent n initially increase (i.e., cyclic hardening) and then decrease (i.e., cyclic softening) until just before the final failure. When the cyclic age reaches the end of its fatigue life, the values of the R-O parameters jump dramatically.

The overall results show that there is a significant cyclic dependency of the R-O parameters. That means that the conventional static or fixed R-O parameter set (hardening modulus K and exponent n) alone cannot be used to accurately model the cyclic stress-strain behavior associated with reactor pressure boundary components. Figures 5.12 to 5.15 show the reconstructed stress-strain curves using the estimated R-O parameters and Eq. 5.1. It can be shown that the behaviors of the cyclic stress-strain curve estimated by both the Chaboche model and the Ramberg-Osgood model are very similar (comparing Figures 5.4–5.8 with Figures 5.12–5.15). Figure 5.16 shows the stress amplitudes σ_a of the estimated R-O models with respect to the cyclic age, while Figure 5.17 shows the maximum and minimum values of the experimentally observed stress amplitudes for different fatigue test cases. From Figures 5.16 and 5.17, it can be seen that the measured stress amplitude (maximum stress) and the estimated R-O stress amplitude are well correlated. Therefore, we conclude that the estimated R-O cyclic parameters may be used to model the stress-strain curve of the material for component-level dynamic aging modeling of reactor components, which is one of our future tasks.

Table 5. 3 Estimated R-O parameters for tensile testing cases and fatigue testing cases at first quarter-cycle.

Test Case	Hardening Modulus, K [MPa]	Hardening Exponent, n	Applicable Strain Range
RT-T03	541.6	0.03488	[0, 0.5%]
ET-T05	413.9	0.02350	[0, 0.5%]
RT-F08	1,017	0.13072	[0, 0.5%]
ET-F07	562.3	0.07925	[0, 0.5%]
ET-F17	557.0	0.08706	[0, 0.69%]
EN-F18	490.6	0.06295	[0, 0.69%]

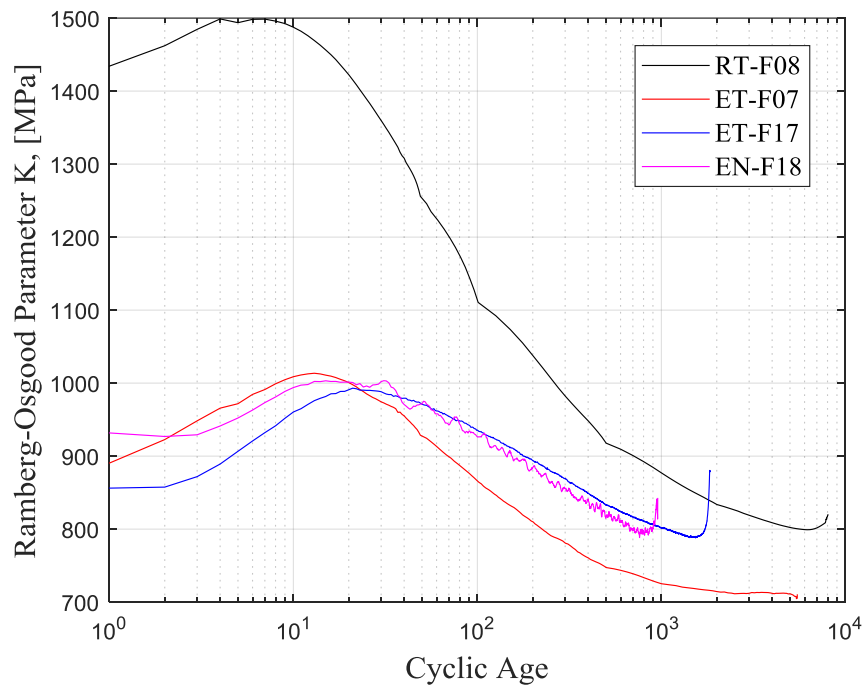


Figure 5. 10 Estimated Ramberg-Osgood parameters (hardening modulus K) for fatigue testing cases from $N=1$ to $N=N_f$.

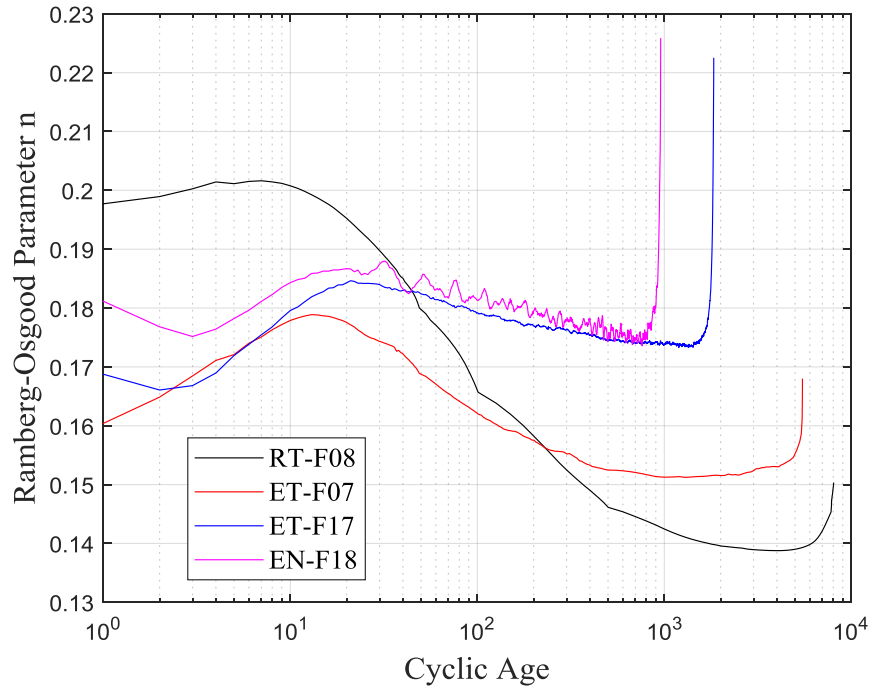


Figure 5. 11 Estimated Ramberg-Osgood parameters (hardening exponent n) for fatigue testing cases from $N=1$ to $N=N_f$.

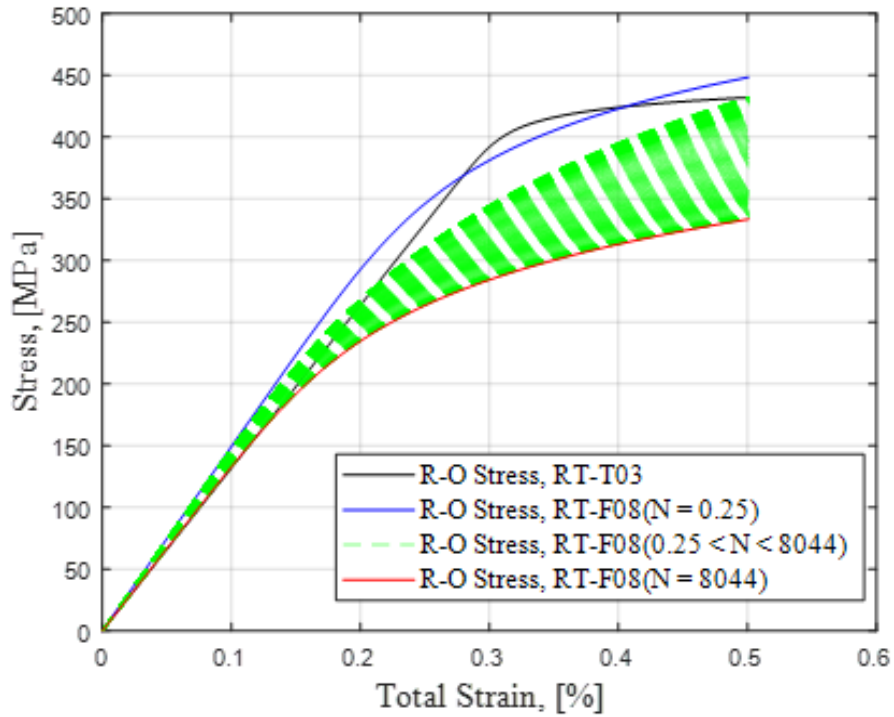


Figure 5. 12 Reconstructed R-O model-based cyclic stress-strain curves for RT-F08 fatigue test.

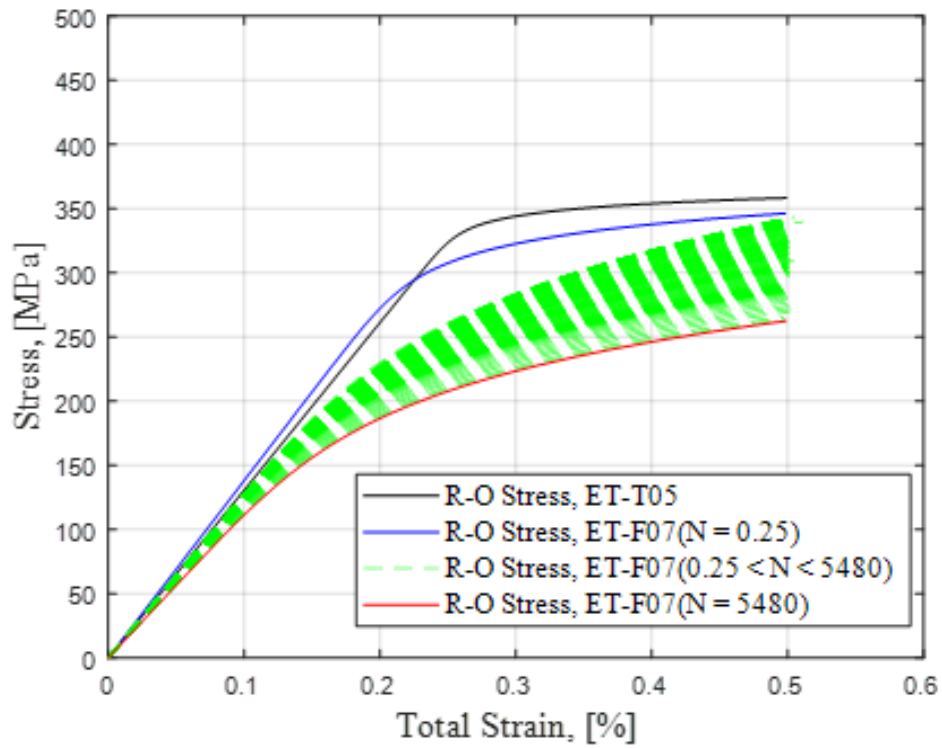


Figure 5. 13 Reconstructed R-O model-based cyclic stress-strain curves for ET-F07 fatigue test.

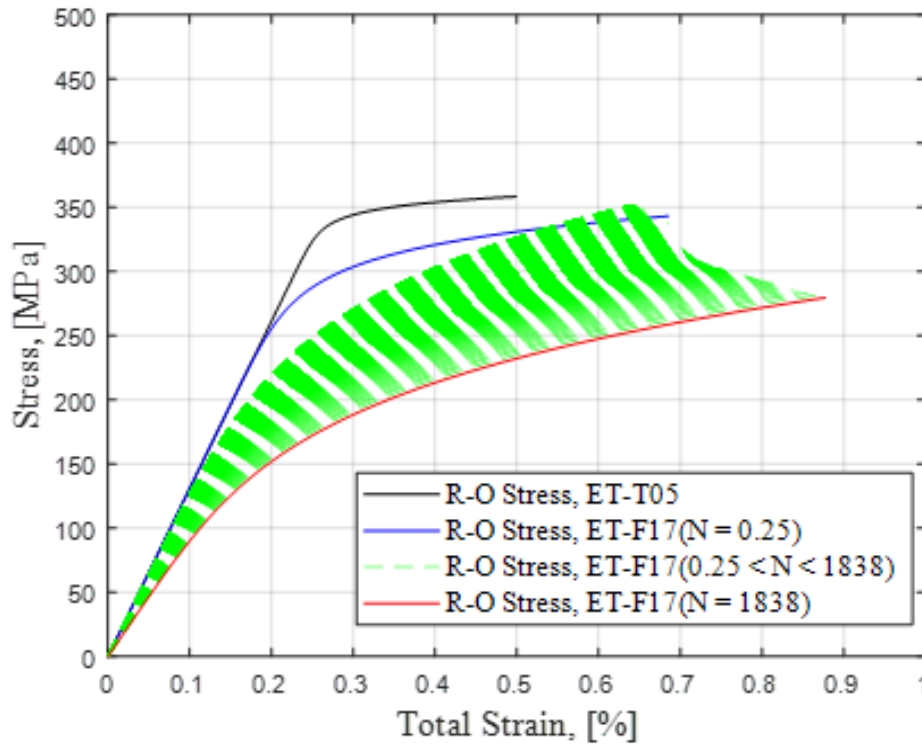


Figure 5. 14 Reconstructed R-O model-based cyclic stress-strain curves for ET-F17 fatigue test.

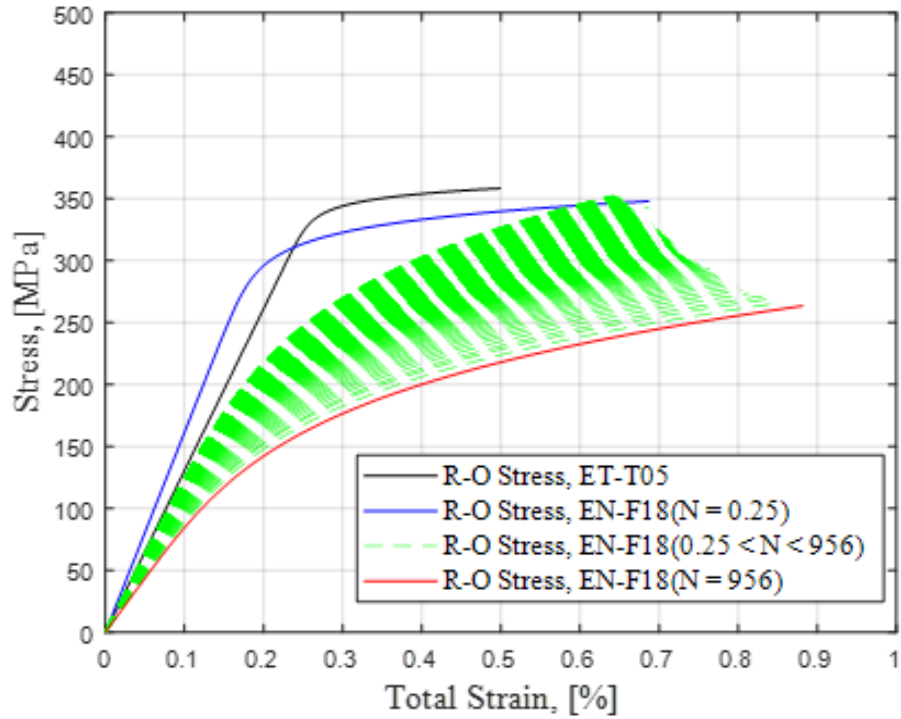


Figure 5. 15 Reconstructed R-O model-based cyclic stress-strain curves for EN-F18 fatigue test.

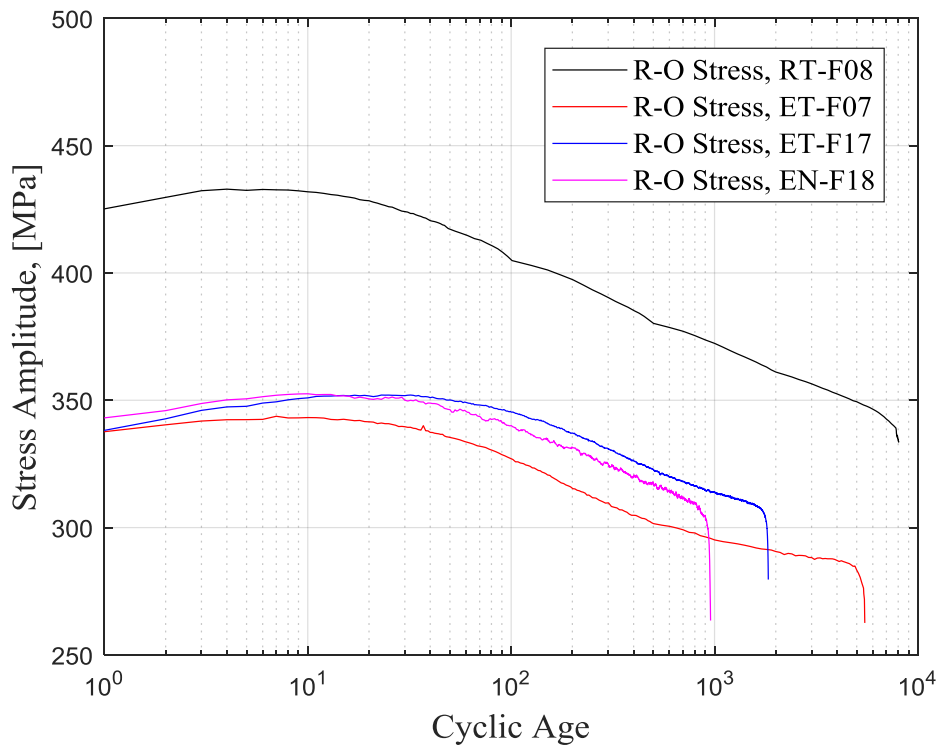


Figure 5. 16 Estimated stress amplitude-based R-O model.

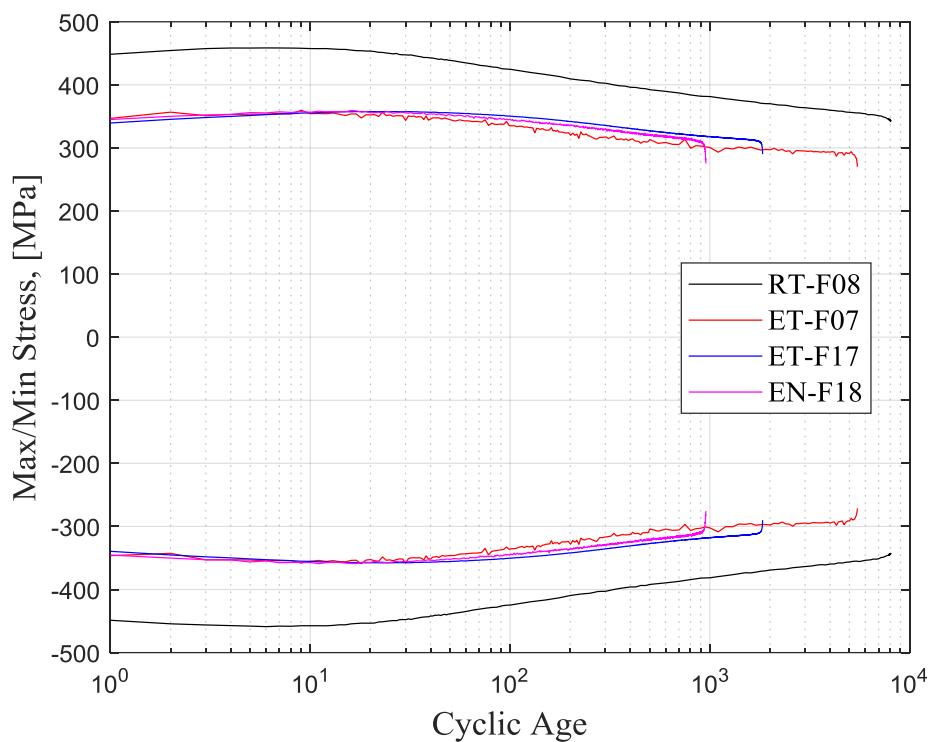


Figure 5. 17 Measured engineering maximum/minimum stress fatigue testing cases.

6 FE Modeling-based 3D Heat-Transfer Analysis of Nozzle Weld Processes

The pressurizer of a PWR is connected to a surge line through a nozzle that has both DMWs and SMWs. This welded nozzle might be subjected to a stressed state even before it is subjected to a reactor loading cycle because of the buildup (tensile and/or compressive) of residual stress during the manufacturing of the welded joints. Welding-related stress, also known as weld residual stress, can have a significant adverse effect on overall fatigue life, owing not only to the initial stress/strain itself but also to its interaction with the reactor loading cycle and environment. These residual stresses in a safety-critical reactor pressure boundary component need to be properly accounted for, particularly when a reactor is required to operate beyond its 40-year safe life or design life. In this section, we present some of the preliminary work related to weld process modeling of a PWR surge line nozzle. We present only a modeling procedure to simulate the heat transfer during the weld layup; subsequent thermal-mechanical stress analysis to estimate the residual stress is future work.

The heat transfer analysis process is based on the combined use of the ABAQUS finite element code and a MATLAB-PYTHON-based heat-transfer analysis step and interaction modeler. This hybrid approach helps avoid the use of a complex graphical user interface (GUI)-based approach. Figure 6.1 shows a schematic of the overall welding model procedure. The GUI-based approach is easy to use when there are only a limited number of weld passes and weld chunks to model. However, when the number of weld passes increases (each with multiple weld chunks), using a GUI-based approach becomes extremely complex in terms of the time required to develop the model. In addition, manually defining a large number of weld heat transfer steps and interactions might become error-prone. To show the complexity involved in weld process modeling, Figure 6.2 shows a screen shot of the interaction module of a GUI-based model with only two weld passes (each with eight weld chunks).

As shown in Figure 6.1, we developed an ABAQUS-MATLAB-PYTHON based hybrid framework to automate welding process steps and interaction generation. This automated framework swiftly creates the steps and interaction for any number of weld passes and weld chunks. Below we present the related results. Note that in this report we present preliminary model results related to heat transfer analysis only. Further work and validation are required to conduct the subsequent thermal-mechanical stress analysis to estimate the weld process-related residual stress in a nozzle.

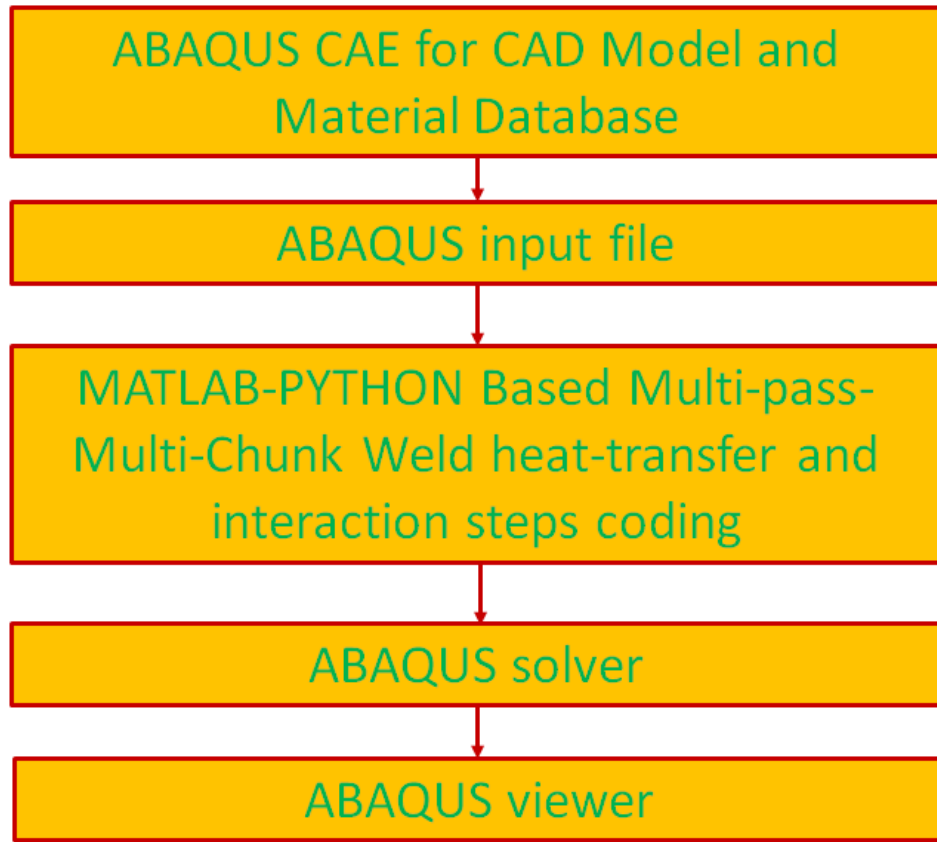


Figure 6. 1 Schematic of the ABAQUS-PYTHON-MATLAB weld model framework.

Interaction Manager																			
Name	Initial	S1_Rem all Be	S2_B1C1_J	(B S3_B1C1_HT	(S4_B1C2_J	S5_B1C2_HT	S6_B1C3_J	S7_B1C3_HT	S8_B1C4_J	S9_B1C4_HT	S10_B1C5_J	S11_B1C5_HT	S12_B1C6_J	S13_B1C6_HT	S14_B1C7_J	S15_B1C7_HT	S16_B1C8_J	S17_B1C8_HT	Bead-1 (B11 C
✓ II-Base INI ev	Created	Propagated	Propagated	Propagated	Propagated	Propagated	Propagated	Propagated	Propagated	Propagated	Propagated	Propagated	Propagated	Propagated	Propagated	Propagated	Propagated	Propagated	Propagated
✓ I2-Rem all bea	Created	Propagated	Propagated	Propagated	Propagated	Propagated	Propagated	Propagated	Propagated	Propagated	Propagated	Propagated	Propagated	Propagated	Propagated	Propagated	Propagated	Propagated	Propagated
✓ I3-B1C1-1 (Bea		Created	Propagated	Propagated	Propagated	Propagated	Propagated	Propagated	Propagated	Propagated	Propagated	Propagated	Propagated	Propagated	Propagated	Propagated	Propagated	Propagated	Propagated
✓ I4-B1C1-SF (Bx			Created	Inactive	Inactive	Inactive	Inactive	Inactive	Inactive	Inactive	Inactive	Inactive	Inactive	Inactive	Inactive	Inactive	Inactive	Inactive	Inactive
✓ I5-B1C2-1				Created	Propagated	Propagated	Propagated	Propagated	Propagated	Propagated	Propagated	Propagated							
✓ I6-B1C2-SF					Created	Inactive	Inactive	Inactive	Inactive	Inactive	Inactive	Inactive	Inactive						
✓ I7-B1C3-1						Created	Propagated	Propagated	Propagated	Propagated	Propagated	Propagated	Propagated	Propagated	Propagated	Propagated	Propagated	Propagated	Propagated
✓ I8-B1C3-SF							Created	Inactive	Inactive	Inactive	Inactive	Inactive	Inactive	Inactive	Inactive	Inactive	Inactive	Inactive	Inactive
✓ I9-B1C4-1								Created	Propagated	Propagated	Propagated	Propagated	Propagated	Propagated	Propagated	Propagated	Propagated	Propagated	Propagated
✓ I10-B1C4-SF									Created	Inactive	Inactive	Inactive	Inactive	Inactive	Inactive	Inactive	Inactive	Inactive	Inactive
✓ I11-B1C5-1										Created	Propagated	Propagated	Propagated	Propagated	Propagated	Propagated	Propagated	Propagated	Propagated
✓ I12-B1C5-SF											Created	Inactive	Inactive	Inactive	Inactive	Inactive	Inactive	Inactive	Inactive
✓ I13-B1C6-1												Created	Propagated	Propagated	Propagated	Propagated	Propagated	Propagated	Propagated
✓ I14-B1C6-SF													Created	Inactive	Inactive	Inactive	Inactive	Inactive	Inactive
✓ I15-B1C7-1														Created	Propagated	Propagated	Propagated	Propagated	Propagated
✓ I16-B1C7-SF															Created	Inactive	Inactive	Inactive	Inactive
✓ I17-B1C8-1																Created	Propagated	Propagated	Propagated
✓ I18-B1C8-SF																	Created	Inactive	Inactive

Figure 6. 2 Screen shot of the ABAQUS/GUI-based weld interaction module.

6.1 Thermal Properties for Weld Models

Thermal properties, such as thermal conductivity and specific heat, are required for weld heat transfer analysis. For our model, these properties were taken from section IID of the 2017 version of the American Society of Mechanical Engineers' (ASME's) pressure vessel and piping code [25]. The thermal properties considered were for material types that are the same as or very similar to those used in the nozzle FE model. For example, the properties of SA-508 were used for modeling the 50LAS, while the properties of 304SS were used for modeling the nozzle SMW and SS cladding. The thermal properties of Inconel® alloy In-600 were used for modeling the DMW filler and butter welds in the nozzle model. The thermal properties of 316SS are available in the ASME code and were used for modeling the 316SS base metal of the nozzle assembly. Figures 6.3 and 6.4 show temperature versus thermal conductivity and temperature versus specific heat capacity, respectively. The heat transfer model also requires the film coefficients, which were taken from the literature [30]. The film coefficient data are shown in Figure 6.5.

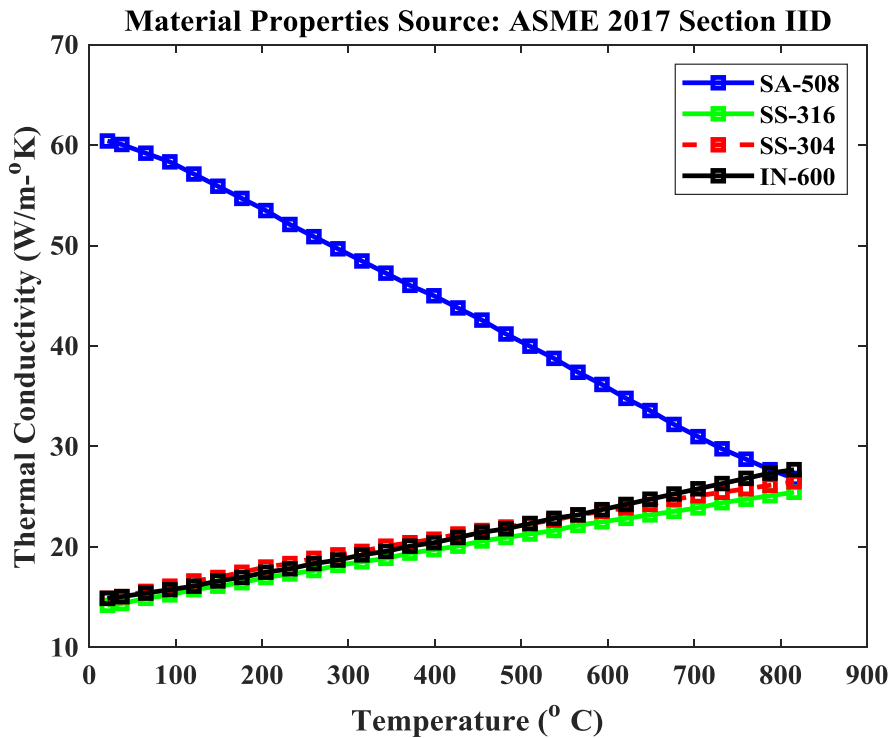


Figure 6. 3 Temperature versus thermal conductivity.

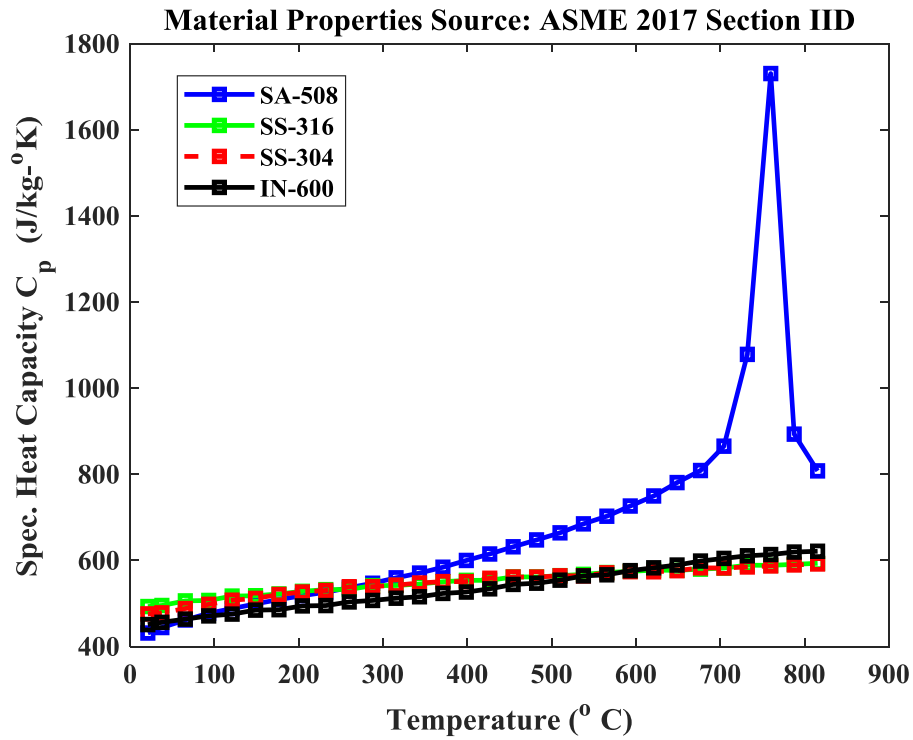


Figure 6. 4 Temperature versus specific heat capacity.

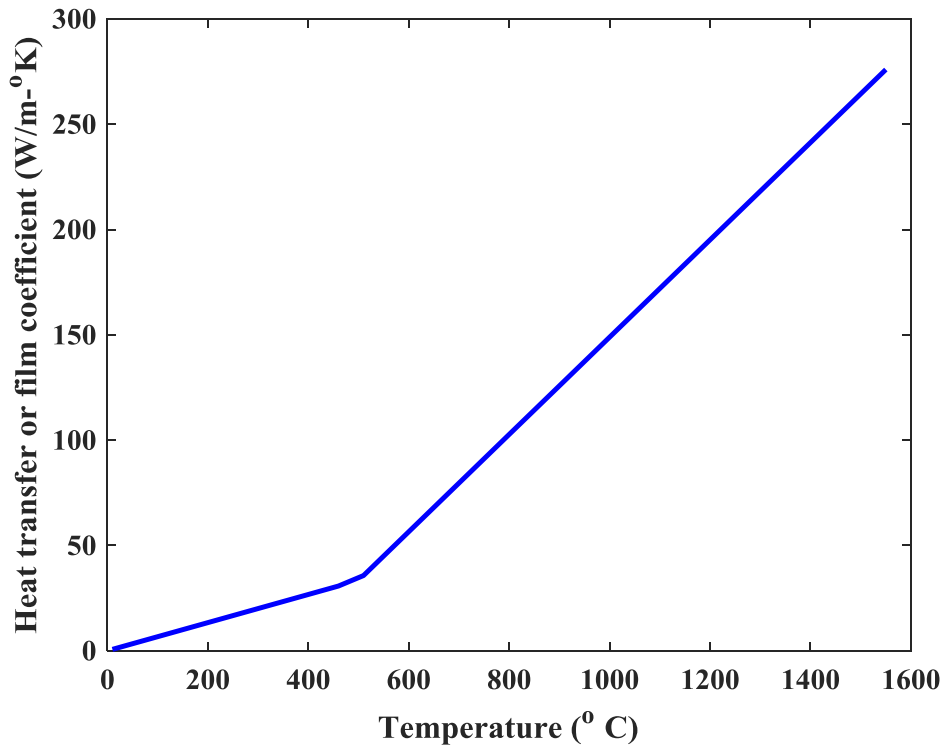


Figure 6. 5 Temperature versus heat transfer or film coefficient

6.2 Weld Process Model Validation Based on Experimental Plate Weld Data

First, to validate the welding model procedure, a weld case for which the experimental data (thermocouple measurements) were available was modeled. The experimental data were taken from the literature [31]. Thermocouple measurements were taken while an SMW between two stainless steel (304SS) plates was manufactured. There were two weld passes in the experimental SMW plate. These two weld passes were modeled in the Argonne-developed FE model. Each weld pass was divided into eight equal-length weld chunks to distribute the weld heat transfer over a period of time. A weld pull temperature of 1510°C was selected. Individual weld chunks were laid using the ABAQUS weld birth and death techniques and also overlaid on a time step based on the weld speed. Weld chunk melting temperature was applied following a trapezoidal time step.

Figure 6.6 shows the weld plate CAD model, showing the location of pass 1 and pass 2 and different chunks within a weld pass. Figure 6.7 shows a cross-section of the weld plate showing the FE mesh near the weld region. A heat transfer analysis was performed using the Argonne FE model. Figure 6.8 shows the FE simulated nodal temperature versus experimentally observed (from thermocouple measurements) temperature at three distances from the center of the weld. This figure shows that there is a good correlation between FE simulated temperature and experimentally observed temperature. Figure 6.9 shows the FE simulated nodal temperature along the length of the weld plate. Figure 6.10 and 6.11 show the FE simulated temperature contour at different times during the pass 1 and pass 2 welding, respectively.

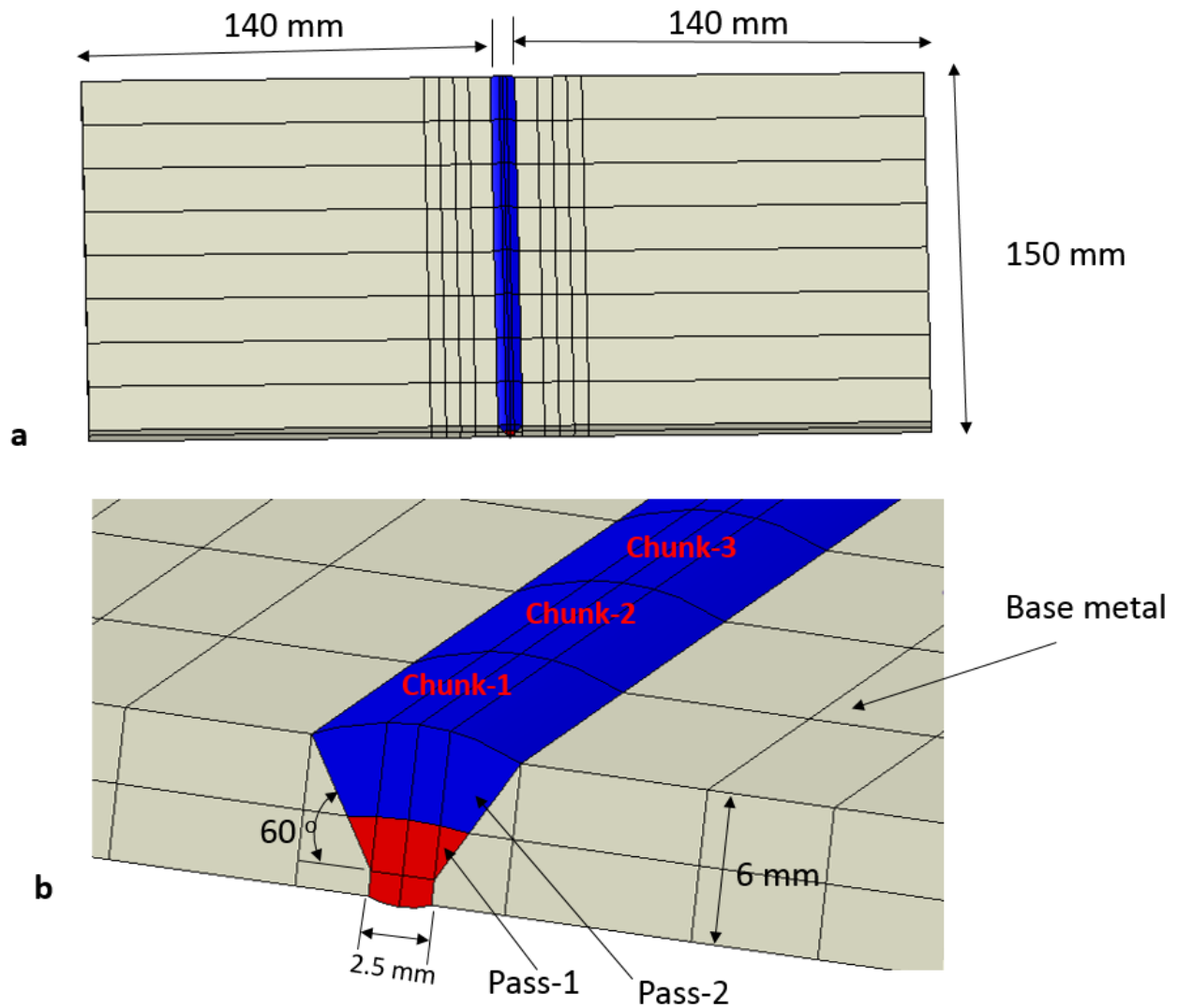


Figure 6.6 Weld plate CAD model showing a) top view of the welded plate geometry and b) cross-section of weld plate.

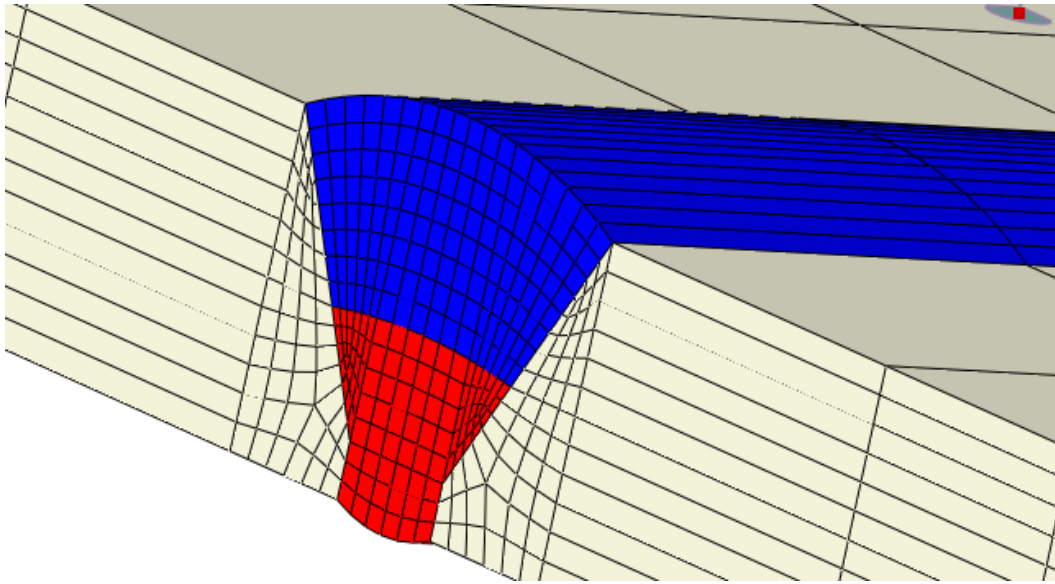


Figure 6. 7 Section of the cross-section of weld plate showing the finite element mesh near the weld region.

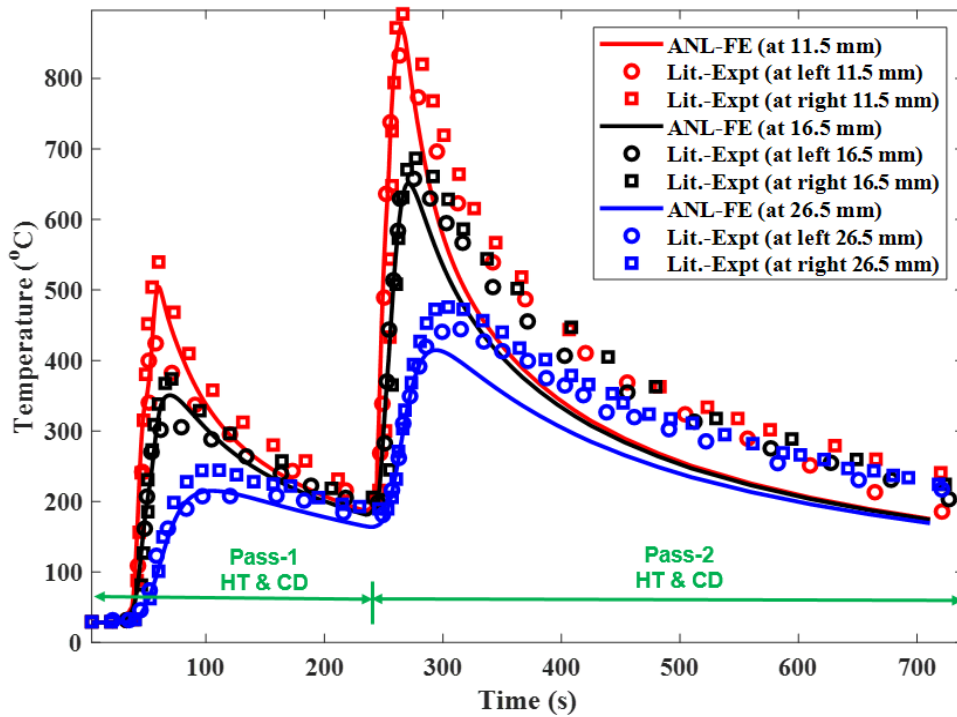


Figure 6. 8 FE (nodal temperature) vs experiment (TC measurements) at three distances from the center of the weld.

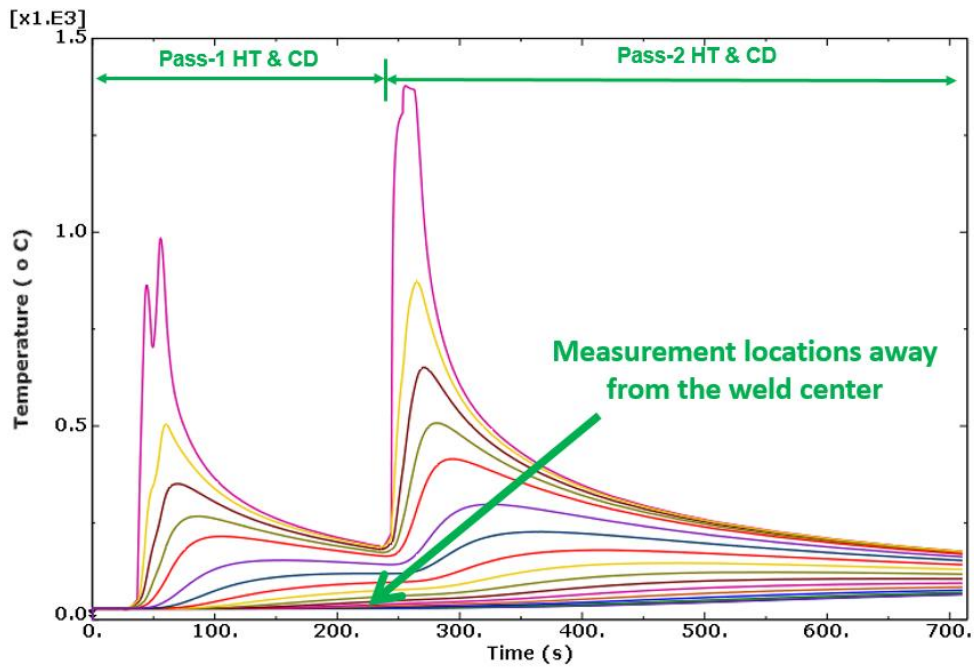


Figure 6. 9 FE (nodal temperature) along the length of the weld plate.

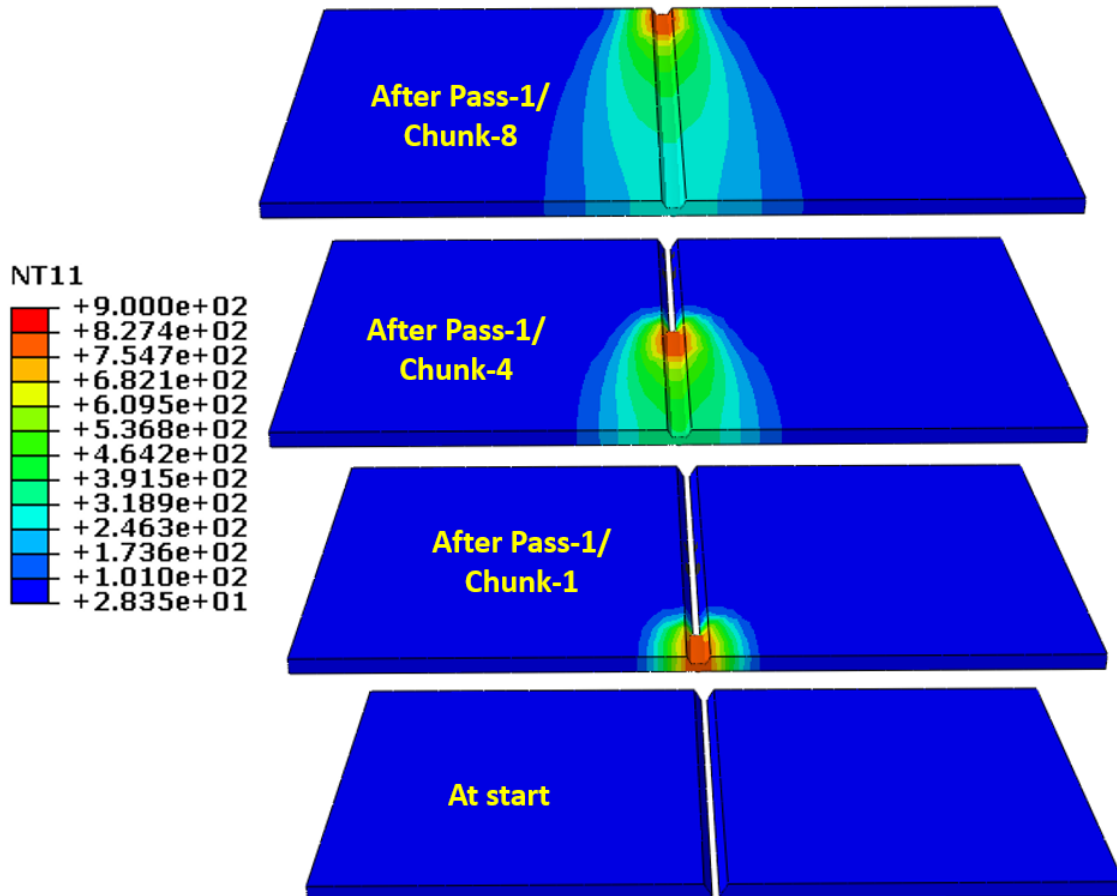


Figure 6. 10 FE simulated temperature contour at different times during the pass 1 welding.

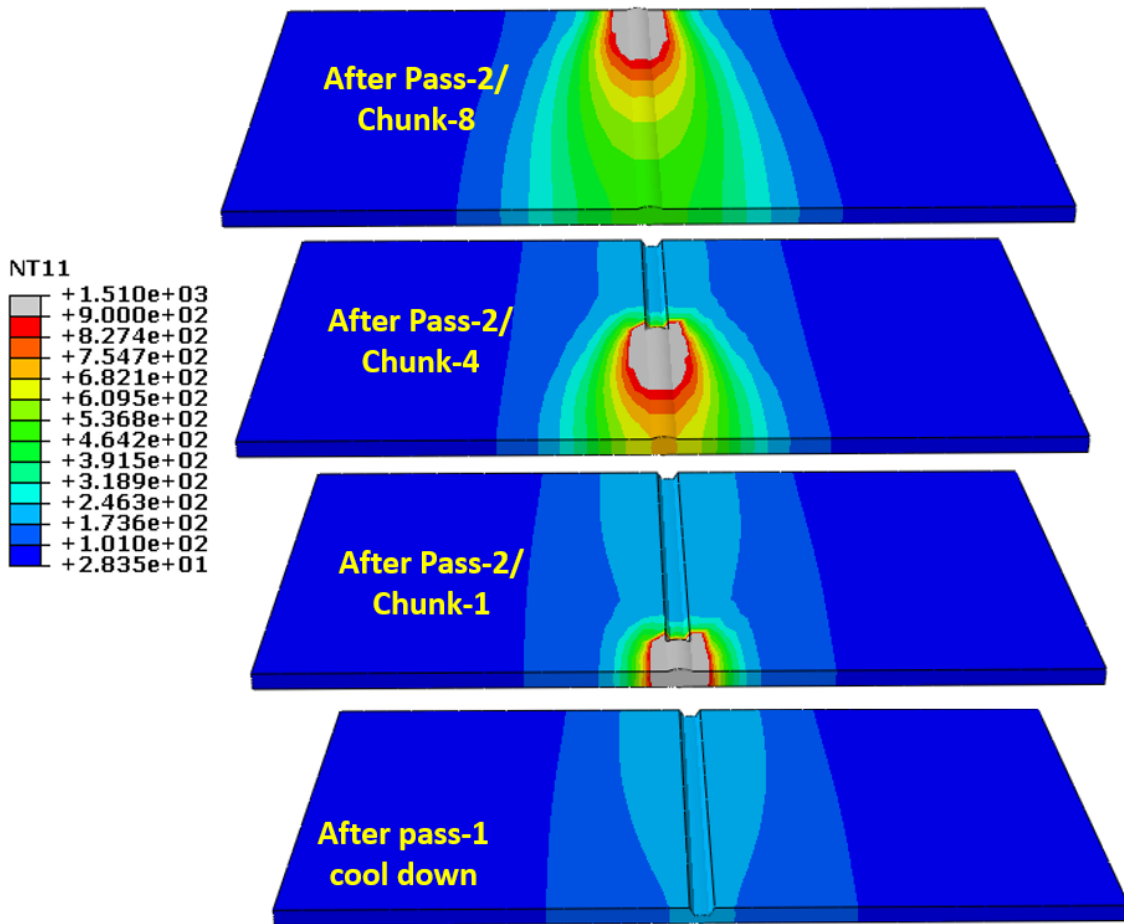


Figure 6. 11 FE simulated temperature contour at different times during the pass 2 welding.

6.3 Preliminary Model Results of Surge Line Nozzle Weld

The results from the above plate weld model gave us the confidence to extend the modeling procedure to the weld processes of the PRZ-SL nozzle. This model and its results are discussed in this subsection. The PRZ-SL nozzle is a part of the PWR pressure control system. Figure 6.12 shows the partial CAD model of a PWR pressure control system and the location of the surge line nozzle. In addition to the nozzle region, we added the bottom head of the pressurizer to the model to simulate a more realistic displacement boundary condition of the PRZ-SL assembly. The thermal-mechanical stress analysis results for the nozzle assembly are presented in section 7. However, note that our stress analysis model does not include weld process-related residual stress. Modeling the weld process residual stress is one of our future projects. Below, we only present the heat transfer analysis results of the nozzle weld process. The full and cut sections of the nozzle assembly CAD model are shown in Figures 6.13 and 6.14, respectively. Figure 6.14 shows the different materials used for modeling the weld process (discussed in this section) and the thermal-mechanical stress analysis (discussed in Section 7).

Figures 6.15 and 6.16 show the FE meshes of the full and cut sections of the nozzle assembly, respectively. Using the Argonne FE model, the welding processes were modeled to estimate the nodal temperature at a given time and location on the nozzle assembly. This nodal temperature information is required for assessing the residual stress in the nozzle assembly. Figure 6.17 shows the weld pass sequence of the model with both DMW and SMW. Each weld pass is over the entire circumference of the nozzle and was divided into four chunks, each a 90° section of the circumference. Figure 6.18 shows the 90° sectional chunks in a single pass. This figure also shows the direction of the weld within one pass.

Three different FE models were simulated in order to better understand the weld process-related temperature history with the addition of increasing complexity (through adding more welds). Following are the three models or cases, the results of which are presented below.

- a) Case 1: Only DMW butter weld modeled
- b) Case 2: Both DMW butter and filler welds modeled
- c) Case 3: Both DMW butter and filler welds and SMW filler weld modeled

Figure 6.19 shows the locations of the three sets of measurement nodes at which the simulated temperature histories are presented in the following figures. Note that values of the FE simulated nodal temperature depend on the locations of the nodes with respect to the welding location and the time duration of the welding (from its start). Differential thermal expansion (due to the presence of different materials at different locations) in addition to the differential temperature can lead to significant differential residual stress, leading to increased fatigue damage in nozzle areas. This will be studied in detail in our future work.

Figure 6.20 shows the temperature histories at the set 1 nodes of the case 1 DMW butter weld model. Figure 6.21 and 6.22 show the corresponding temperature histories at the set 2 and set 3 nodes, respectively. Figure 6.23 shows the temperature contours at different times in the case 1 DMW butter weld simulation. The case 2 model was constructed to simulate the effects of both DMW butter and filler welds. Figures 6.24, 6.25, and 6.26 show the temperature histories at the set 1, set 2, and set 3 nodes, respectively. Figure 6.27 shows the temperature contours at different times in the case 2 model. The case 3 model was constructed to include both the DMW and SMW of the PRZ-SL nozzle assembly. Figures 6.28, 6.29, and 6.30 show the corresponding temperature histories at the set 1, set 2 and set 3 nodes, respectively, and Figure 6.31 shows the example temperature contours at different times in the case 3 weld simulation. From these results, it can be seen that the temperature history depends entirely on the location of the nodes with respect to welding location and the time in the welding process. The temperature at a given location and time also depends on the sequence in which the weld passes were laid and on the interpass cooldown time. The results presented are only representative and intended to demonstrate the overall weld modeling framework and its capability.

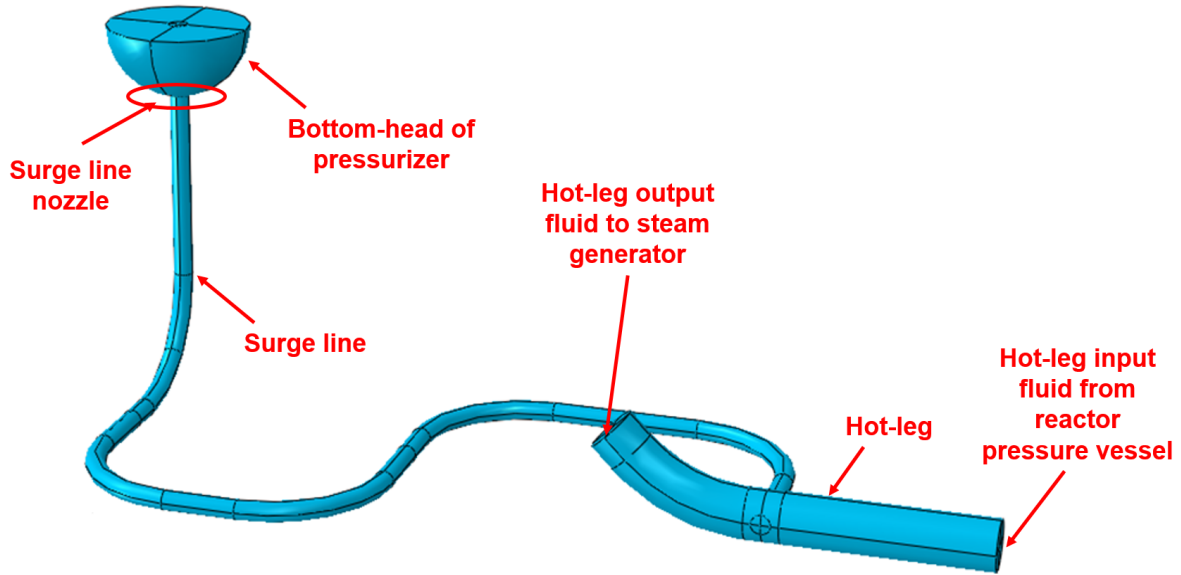


Figure 6. 12 Partial CAD model of PWR pressure control system showing the location of the surge line nozzle.

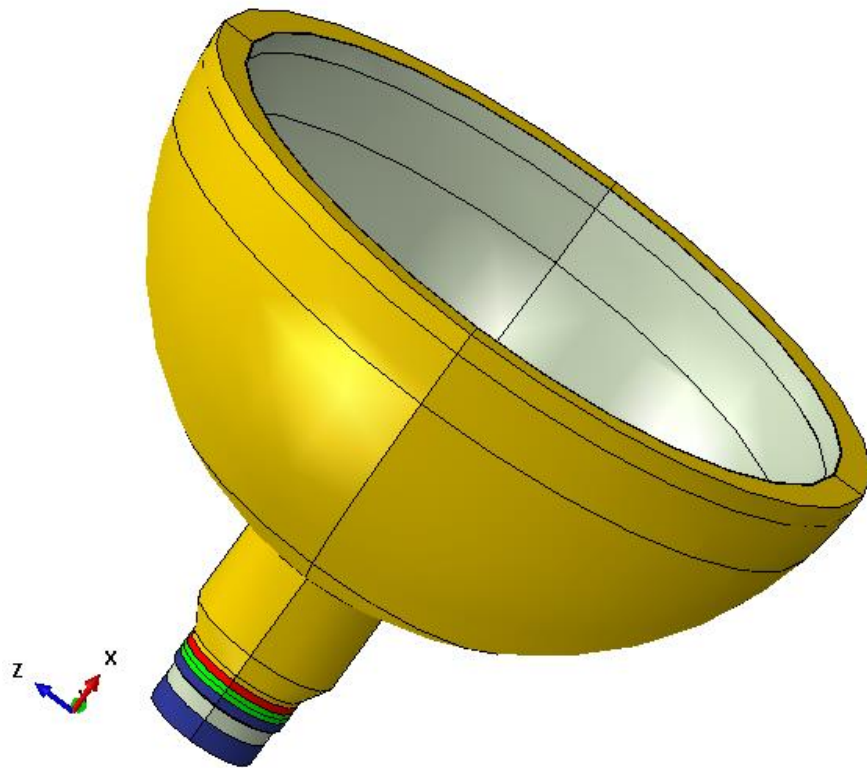


Figure 6. 13 CAD model of surge line nozzle and bottom head of pressurizer.

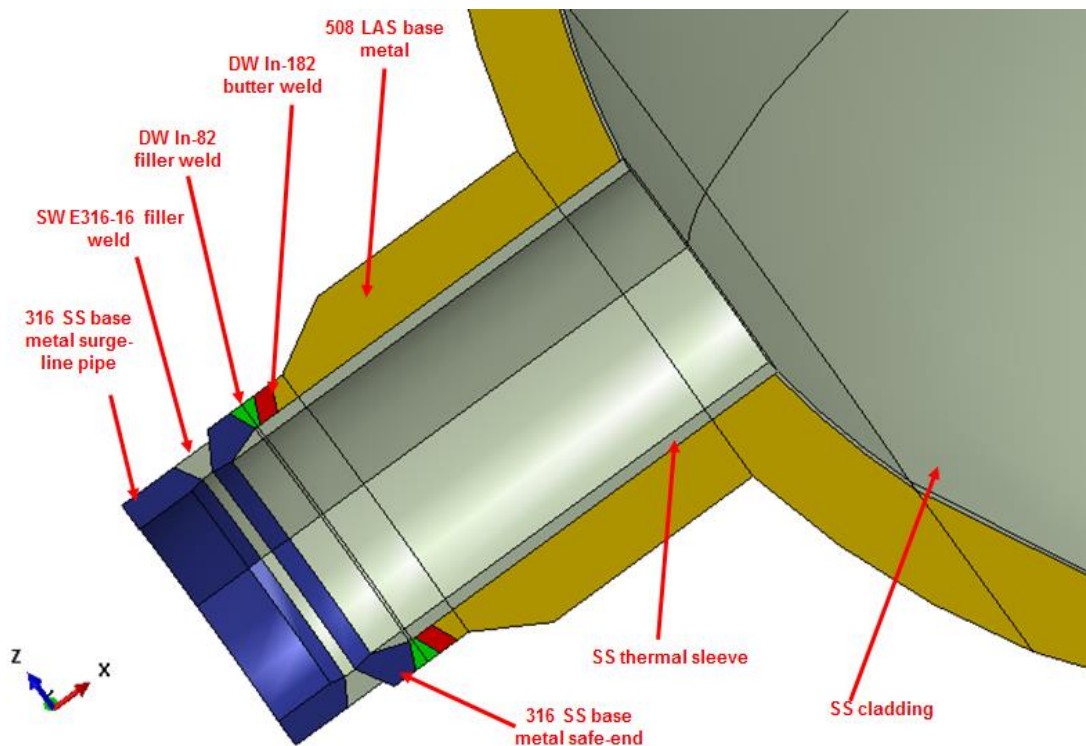


Figure 6. 14 Cut section of the nozzle assembly showing different material systems.

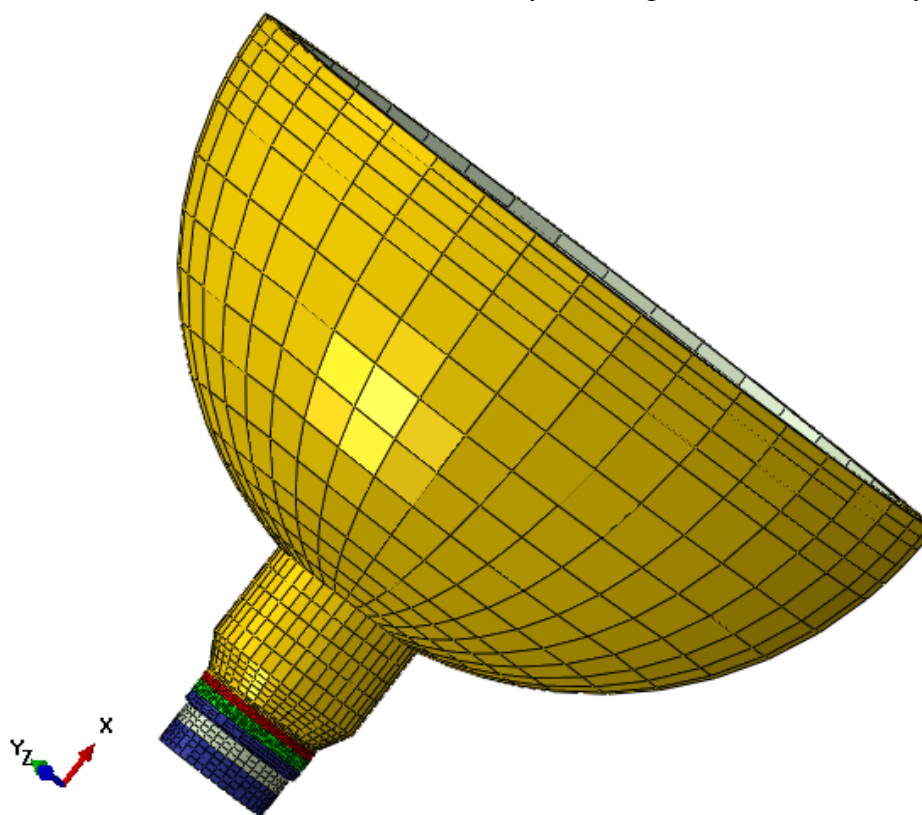


Figure 6. 15 Finite element mesh of the whole nozzle assembly.

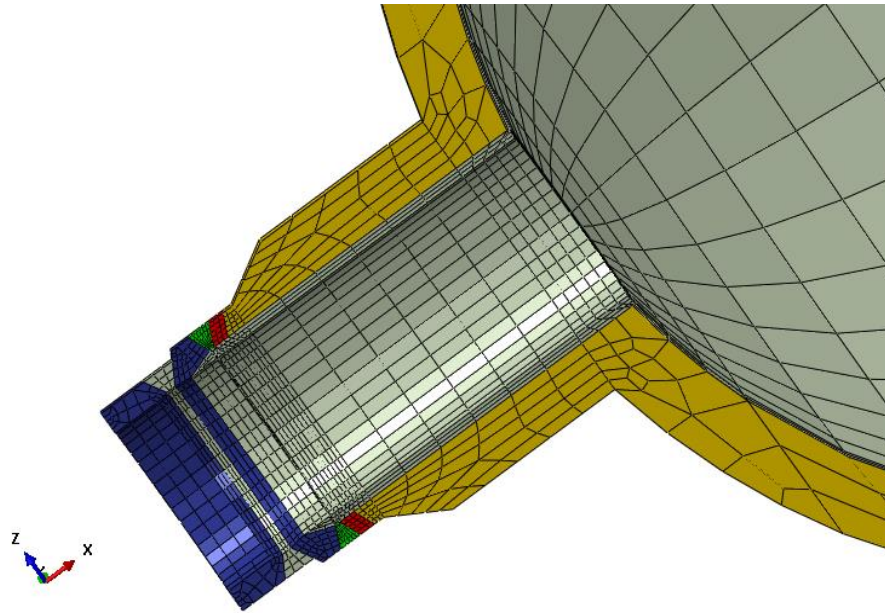


Figure 6. 16 Cut section of the nozzle assembly finite element mesh.

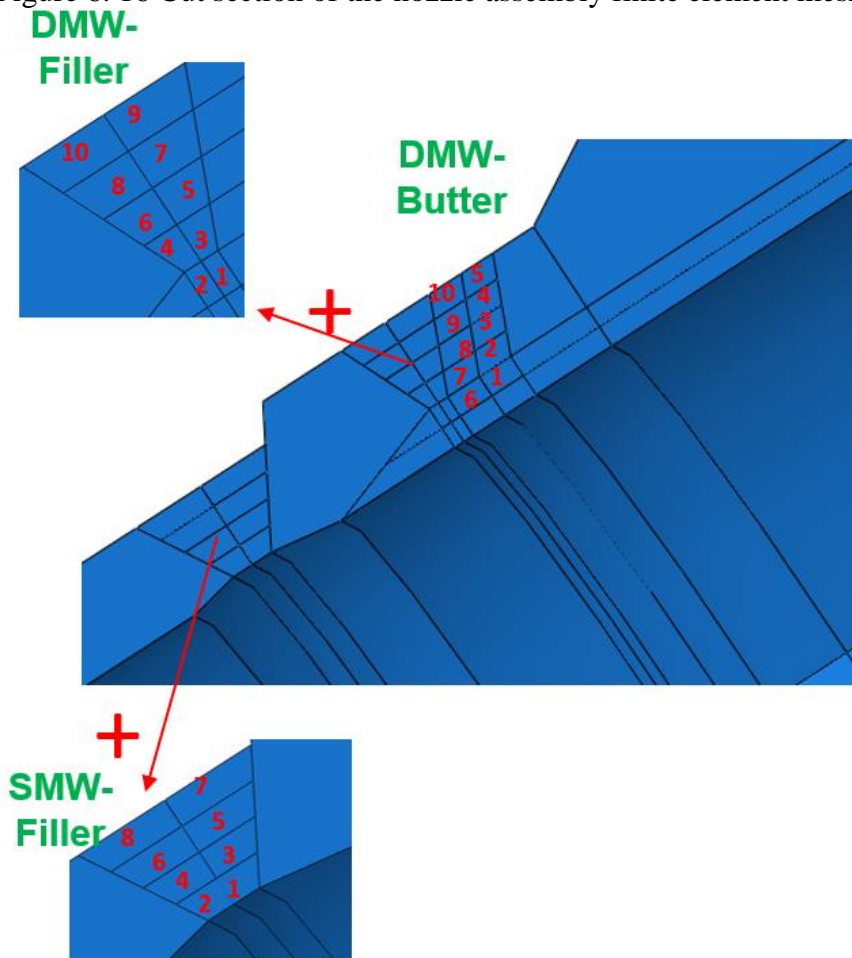


Figure 6. 17 Weld pass sequence for the PWR surge line nozzle.

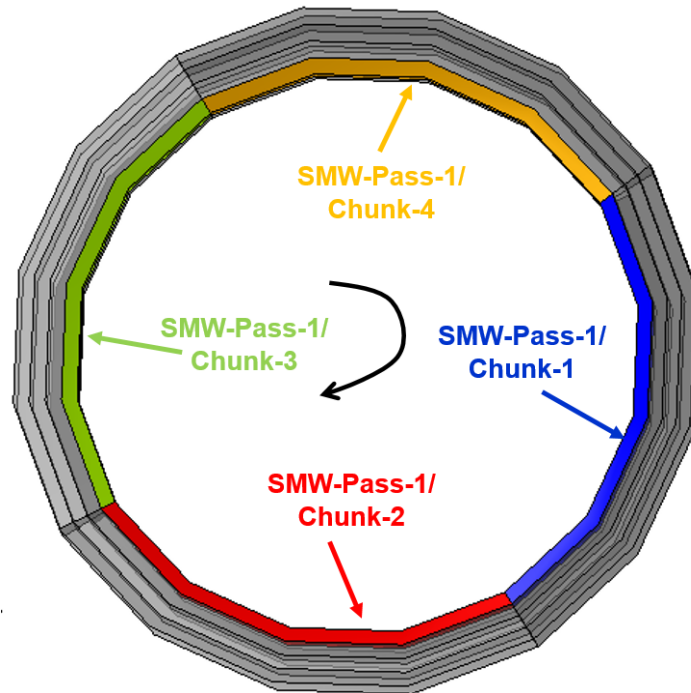


Figure 6. 18 Weld circumferential chunks in a single pass of the nozzle weld (in SMW filler region).

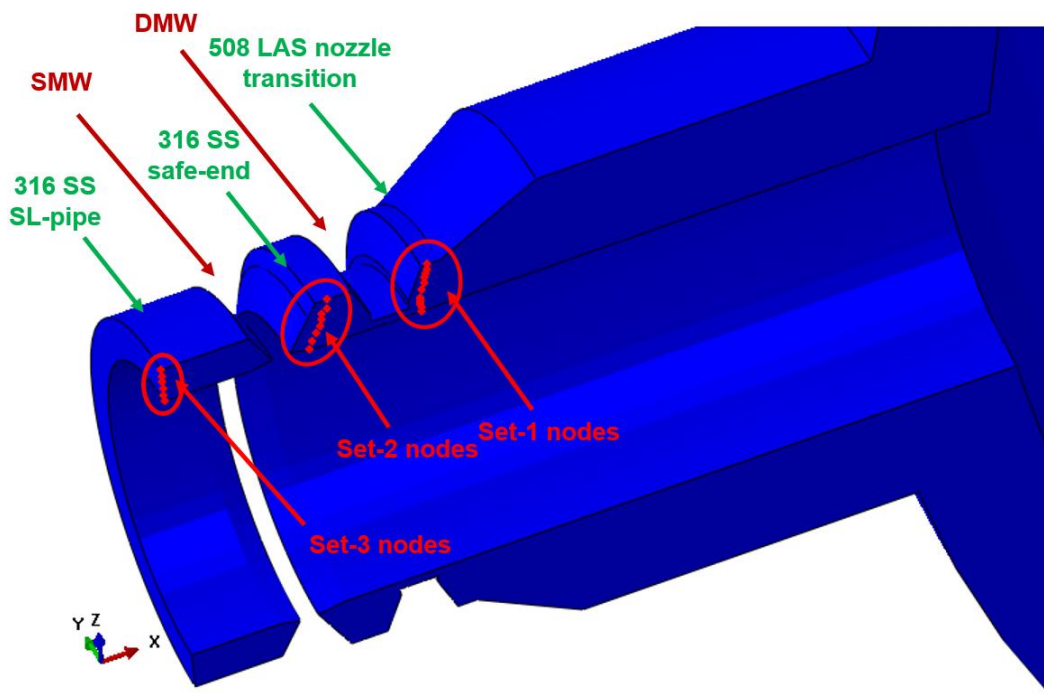


Figure 6. 19 Nozzle weld simulation measurement nodes.

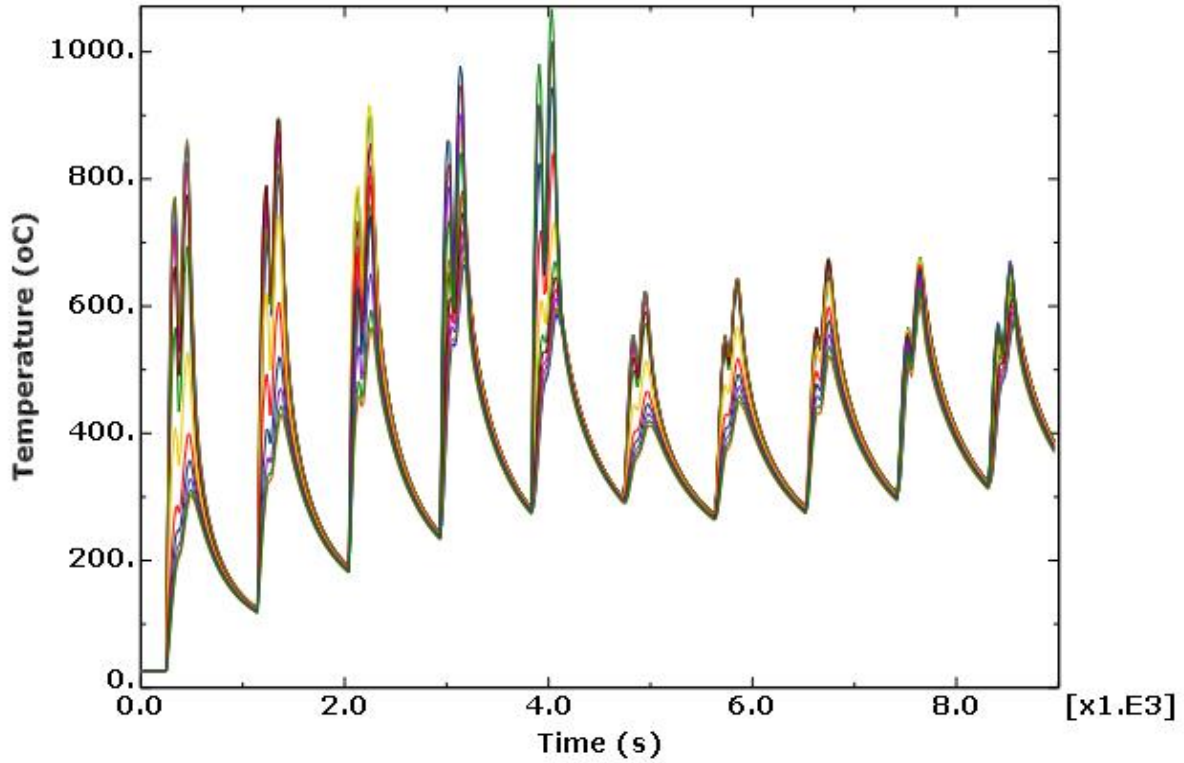


Figure 6. 20 Temperature histories at set 1 nodes of case 1 model (Only DMW butter weld modeled).

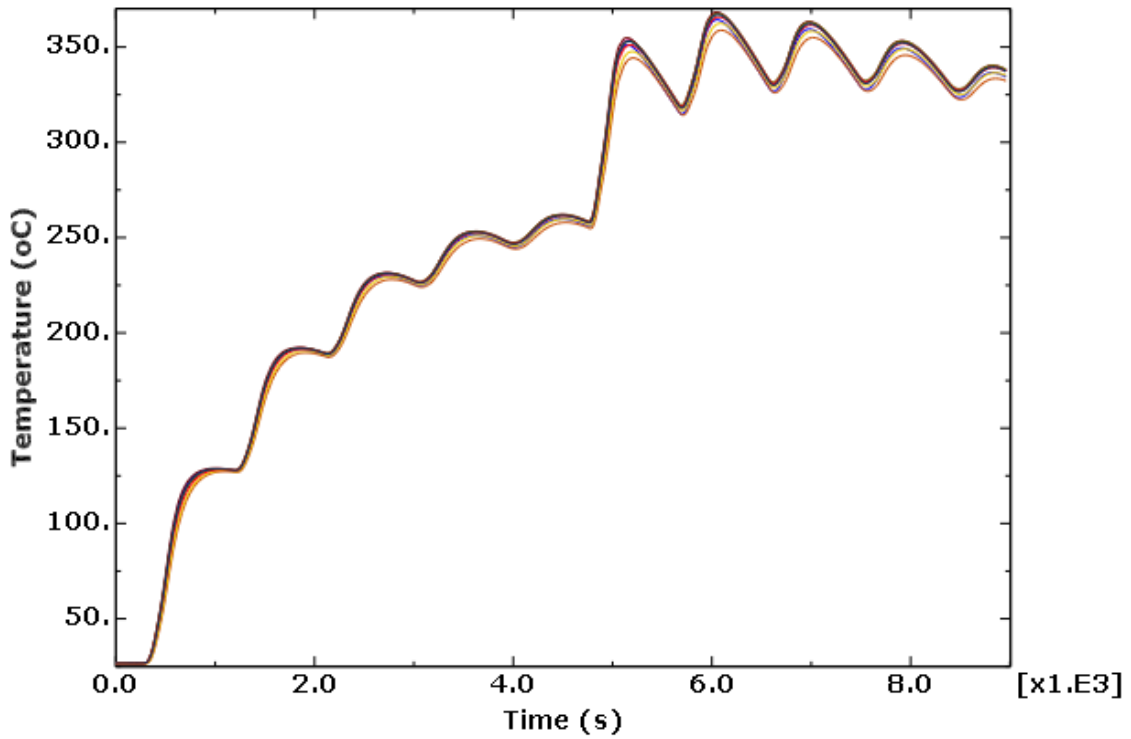


Figure 6. 21 Temperature histories at set 2 nodes of case 1 model (Only DMW butter weld modeled).

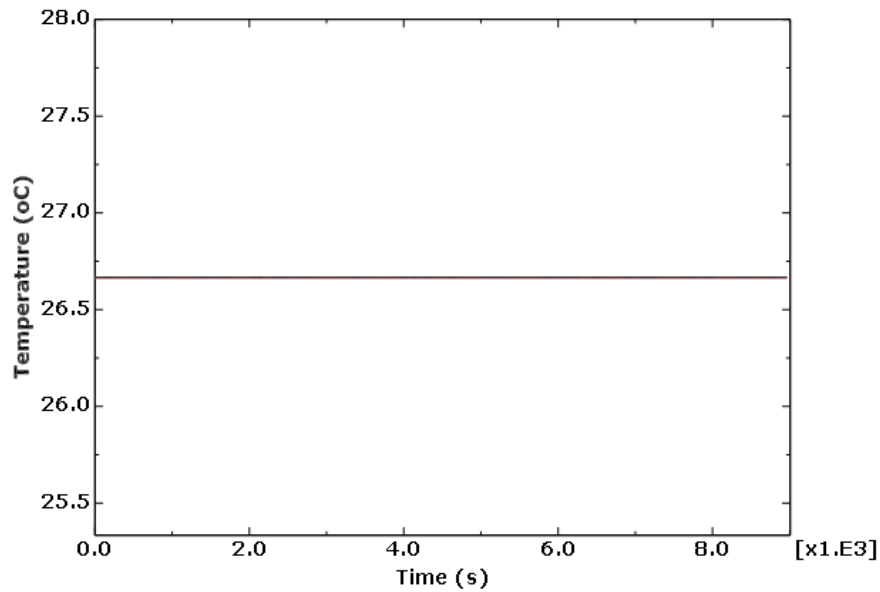


Figure 6. 22 Temperature histories at set 3 nodes of case 1 model (Only DMW butter weld modeled).

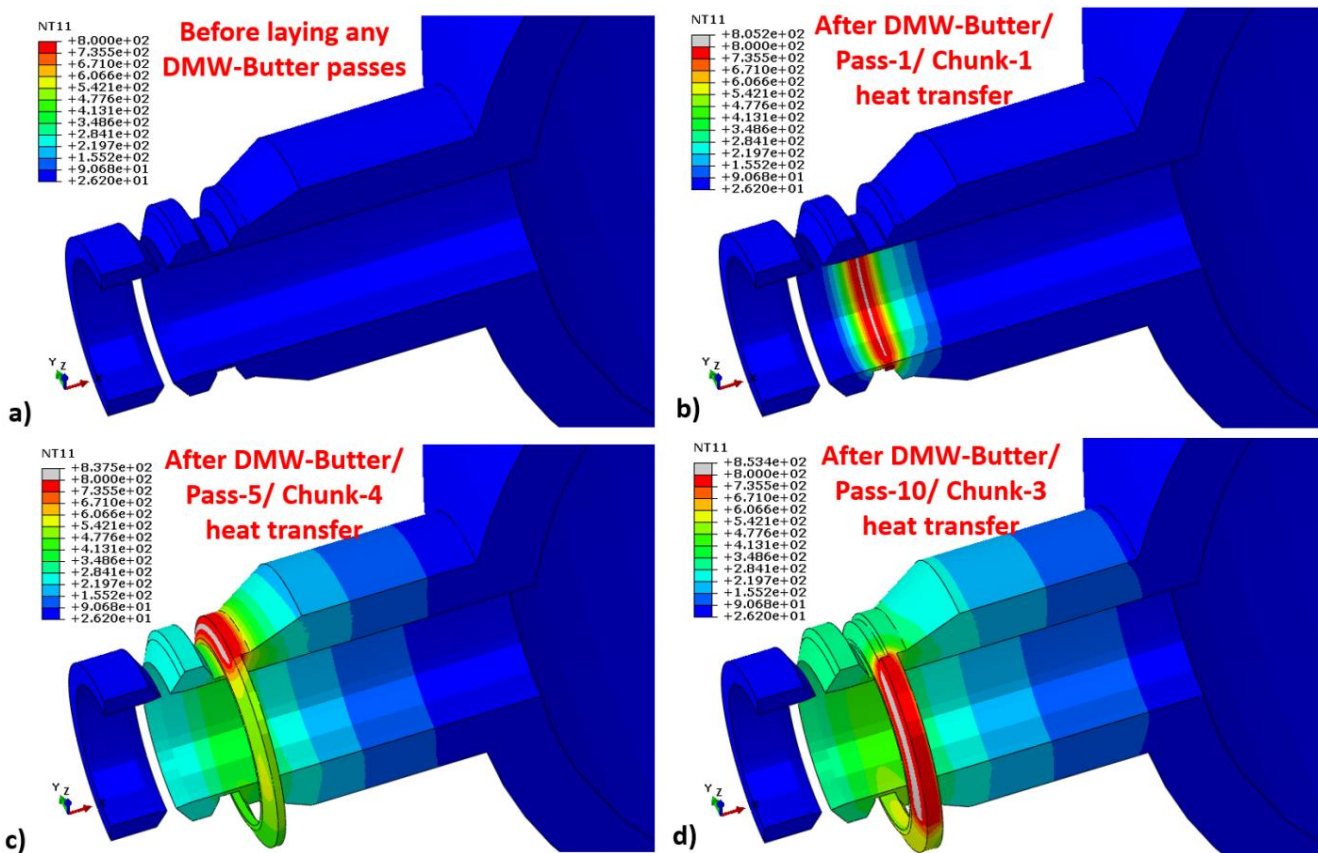


Figure 6. 23 Temperature contours at different times in the case 1 model (Only DMW butter weld modeled).

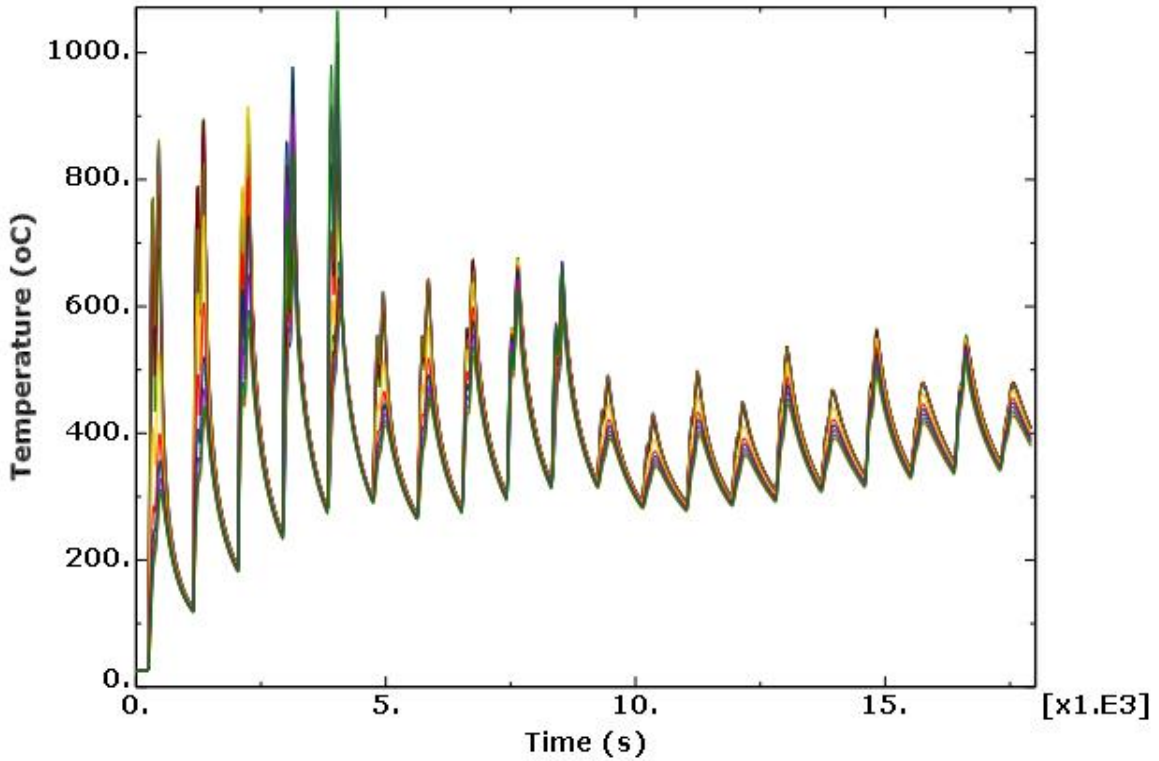


Figure 6.24 Temperature histories at set 1 nodes of the case 2 model (both DMW butter and filler welds modeled).

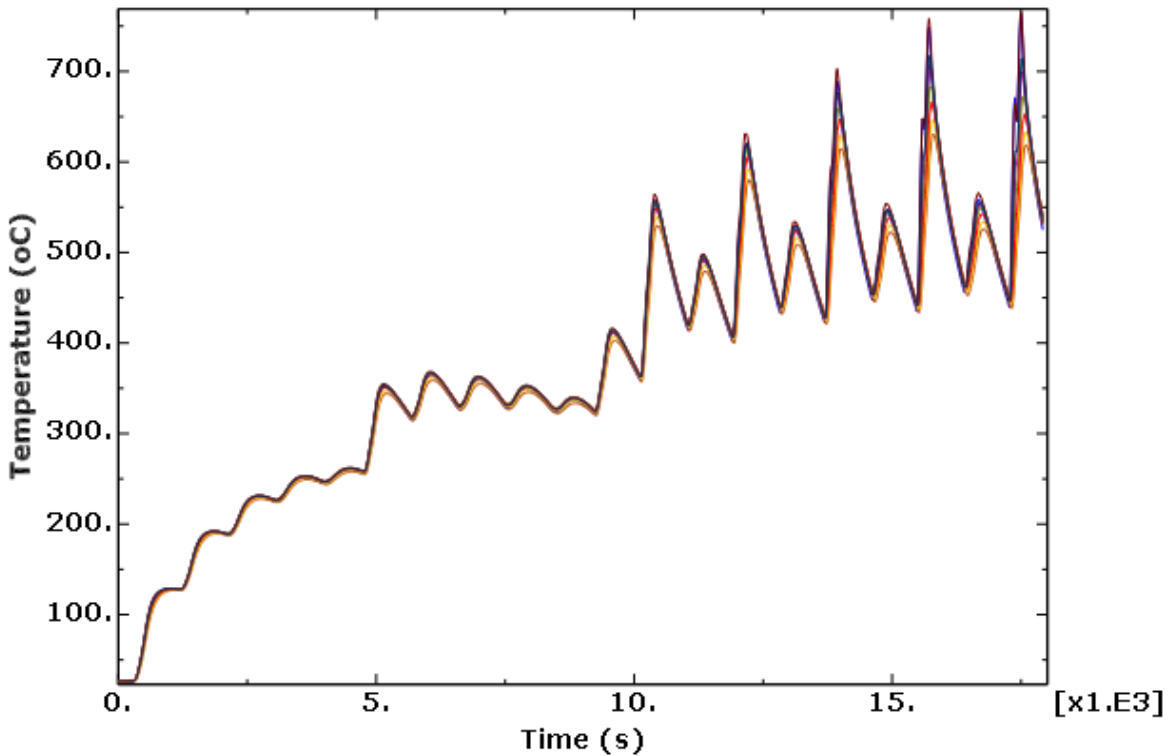


Figure 6.25 Temperature histories at set 2 nodes of the case 2 model (both DMW butter and filler welds modeled).

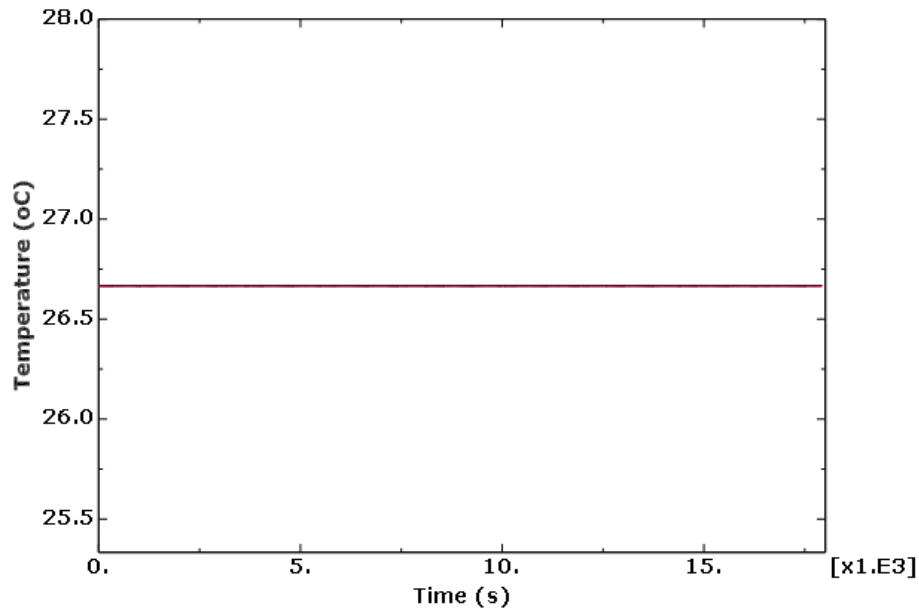


Figure 6. 26 Temperature histories at set 3 nodes of the case 2 model (both DMW butter and filler welds modeled).

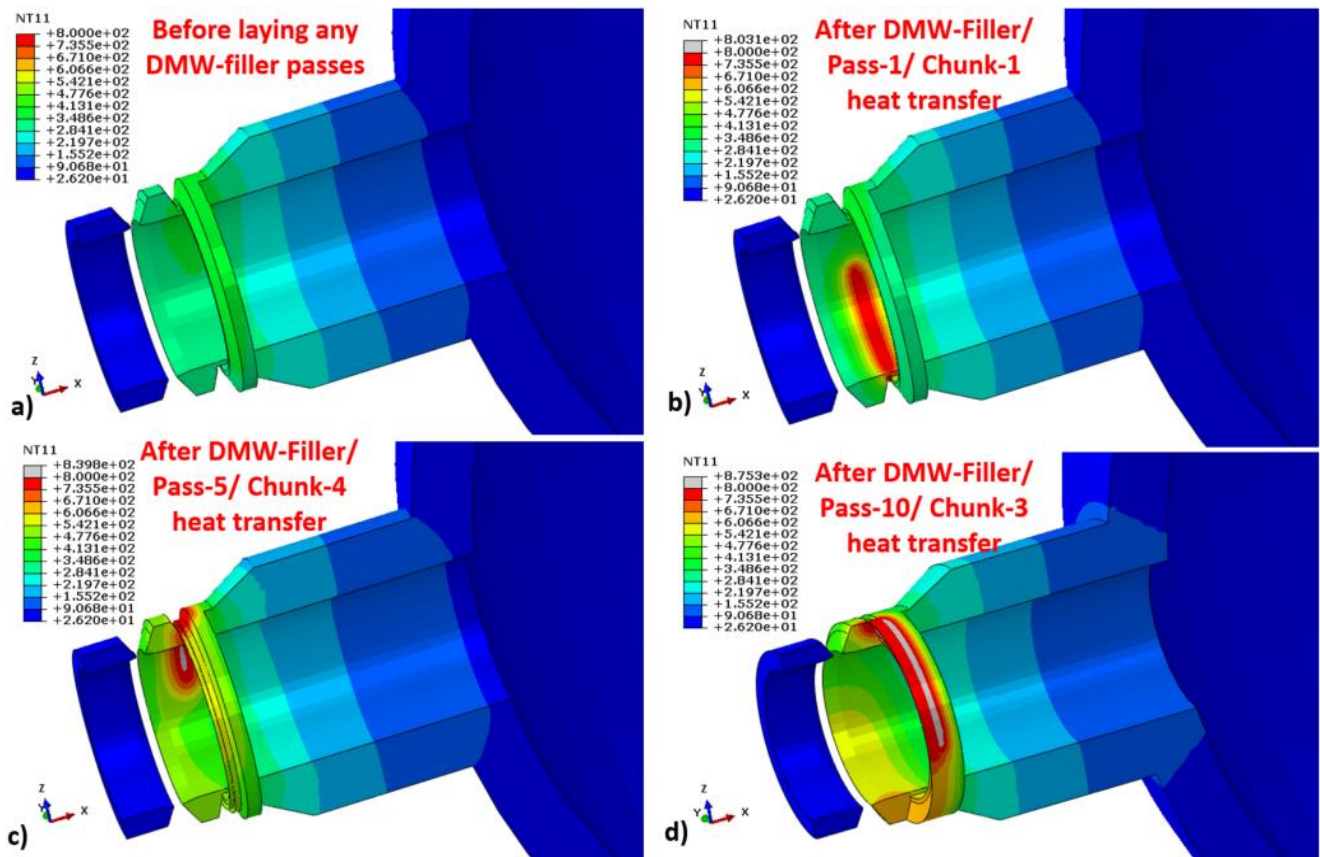


Figure 6. 27 Temperature contours at different times in the case 2 model (both DMW butter and filler welds modeled).

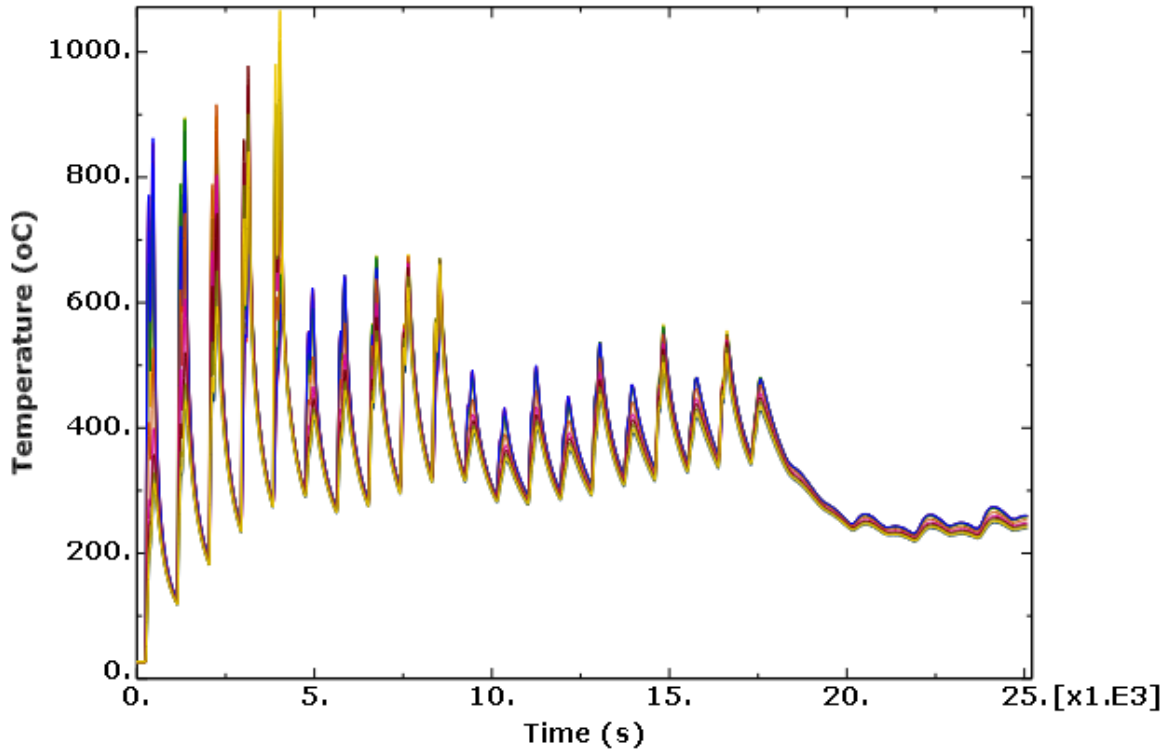


Figure 6. 28 Temperature histories at set 1 nodes of the case 3 model (both DMW butter and filler welds and SMW filer weld modeled).

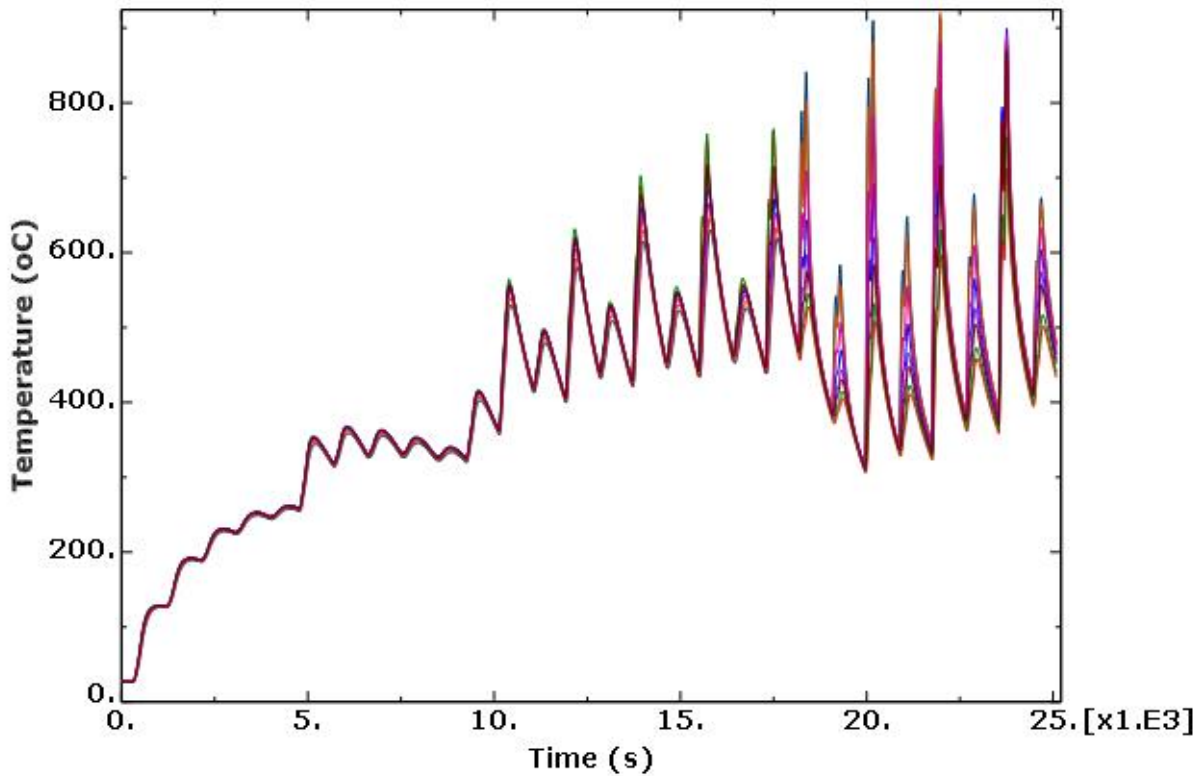


Figure 6. 29 Temperature histories at set 2 nodes of the case 3 model (both DMW butter and filler welds and SMW filer weld modeled).

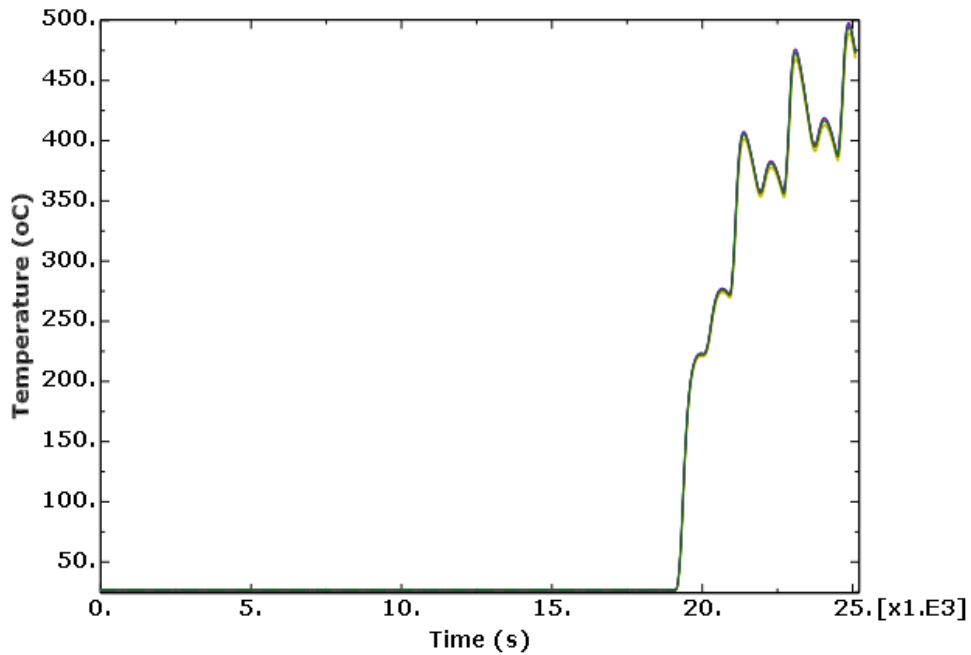


Figure 6. 30 Temperature histories at set 3 nodes of the case 3 model (both DMW butter and filler welds and SMW filer weld modeled).

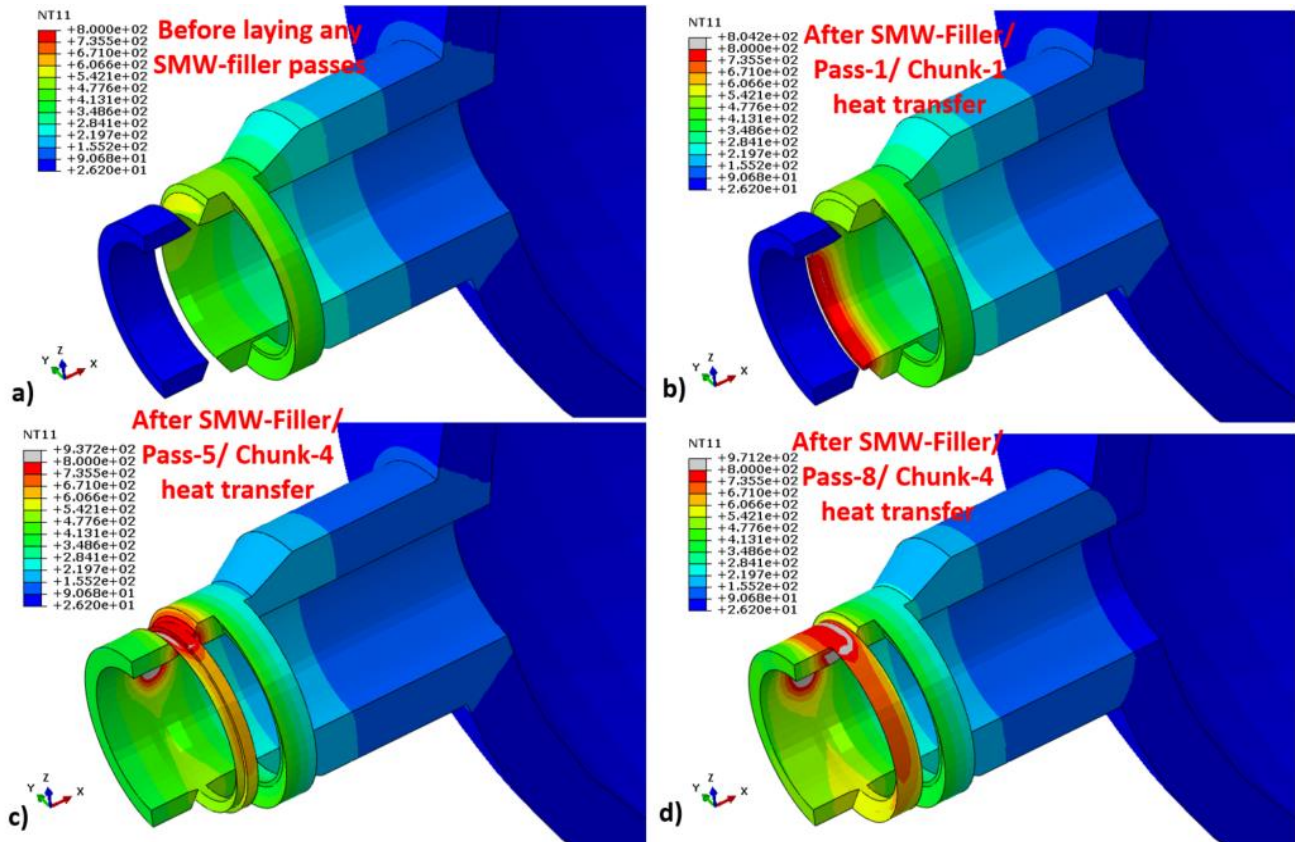


Figure 6. 31 Temperature contours at different times in the case 3 model (both DMW butter and filler welds and SMW filer weld modeled).

7 FE Modeling-based 3D Thermal-Mechanical Stress Analysis of Nozzle Assembly under Design-basis Loading Cycle

This section presents the results from the thermal-mechanical stress analysis of the PRZ-SL nozzle. The analysis was performed using the ABAQUS code, and the details of the CAD model and FE mesh of the nozzle were presented in Section 6.

Note that the stress analysis did not model the residual stresses due to SMW and DMW (see Figure 6.14). Although our future work could include the residual stress (to explicitly predict the effect of weld manufacturing process), the present model assumes that the residual stress is indirectly included in the model through the material properties. For example, we used tensile test-based material properties to conduct the stress analysis. In the tensile weld specimen, we assumed that the effects of weld residual stress (due to the welding of the plates from which the specimens were fabricated) are already ingrained.

The stress analysis models were simulated under a design-basis thermal-mechanical loading cycle. Based on the discussed FE model results, we designed fatigue tests (discussed in Section 8) to evaluate the effect of PWR-water environment on the fatigue life of overall nozzle assembly. First the heat transfer analysis was performed, and then we used the resulting nodal temperature and displacement boundary conditions to perform a thermal-mechanical stress analysis. Section 7.1 presents the details of boundary conditions and material properties. Whereas, sections 7.2 and 7.3 presents the detail heat transfer and thermal-mechanical stress analysis results, respectively.

7.1 FE Model Thermal-Mechanical Boundary Conditions and Properties Used

7.1.1 Mechanical and Thermal Boundary Conditions

The SL pipe end of the nozzle was constrained (or fixed) in all directions. This fixed constraint was chosen to simulate the most severe stress condition. However, actual displacement boundary conditions might vary significantly, depending on the overall load path of the PRZ-SL-HL assembly. In addition to the SL pipe-end constraint, a circumferential strip at the outer diameter of the pressurizer bottom-head was also constrained in all directions to simulate the welded skirt joint of an actual nuclear plant (refer to IAEA report [32]). Note that the pressurizer bottom-head skirt is usually restrained (in all directions) through the pressurizer support flange. In addition to these two constraints, a CAP pressure was applied to the top section of the pressurizer bottom-head (refer Figure 7.1). The applied time-dependent CAP pressure $P_{CAP}(t)$ can be expressed as:

$$P_{CAP}(t) = \frac{R_i^2}{(R_o^2 - R_i^2)} P_{int}(t) \quad (7.1)$$

where R_i and R_o are, respectively, the inner and outer radius of the pressurizer bottom-head. $P_{int}(t)$ is the time-dependent internal pressure applied to the internal diameter surface of the nozzle and pressurizer bottom-head. Figure 7.2 shows the applied internal pressure (both full-cycle and during heat-up and cool-down; for more detail, refer to [11, 13]). In addition to the internal pressure, a time-dependent temperature $\theta_{int}(t)$ was applied to the internal diameter surface of the nozzle and pressurizer

bottom-head. Figure 7.3 shows the applied internal temperature (both full-cycle and during heat-up and cool-down; for more detail, refer to [11, 13]).

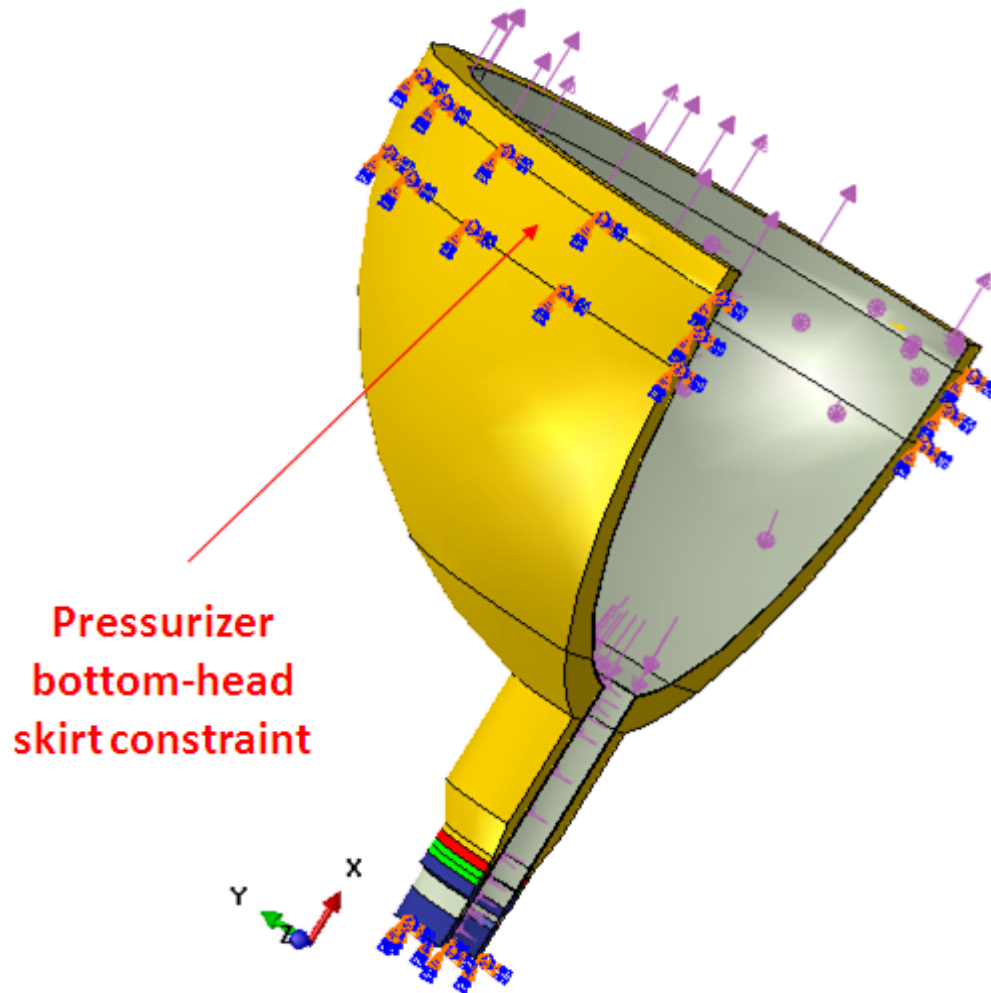


Figure 7. 1 Displacement boundary condition for nozzle FE model.

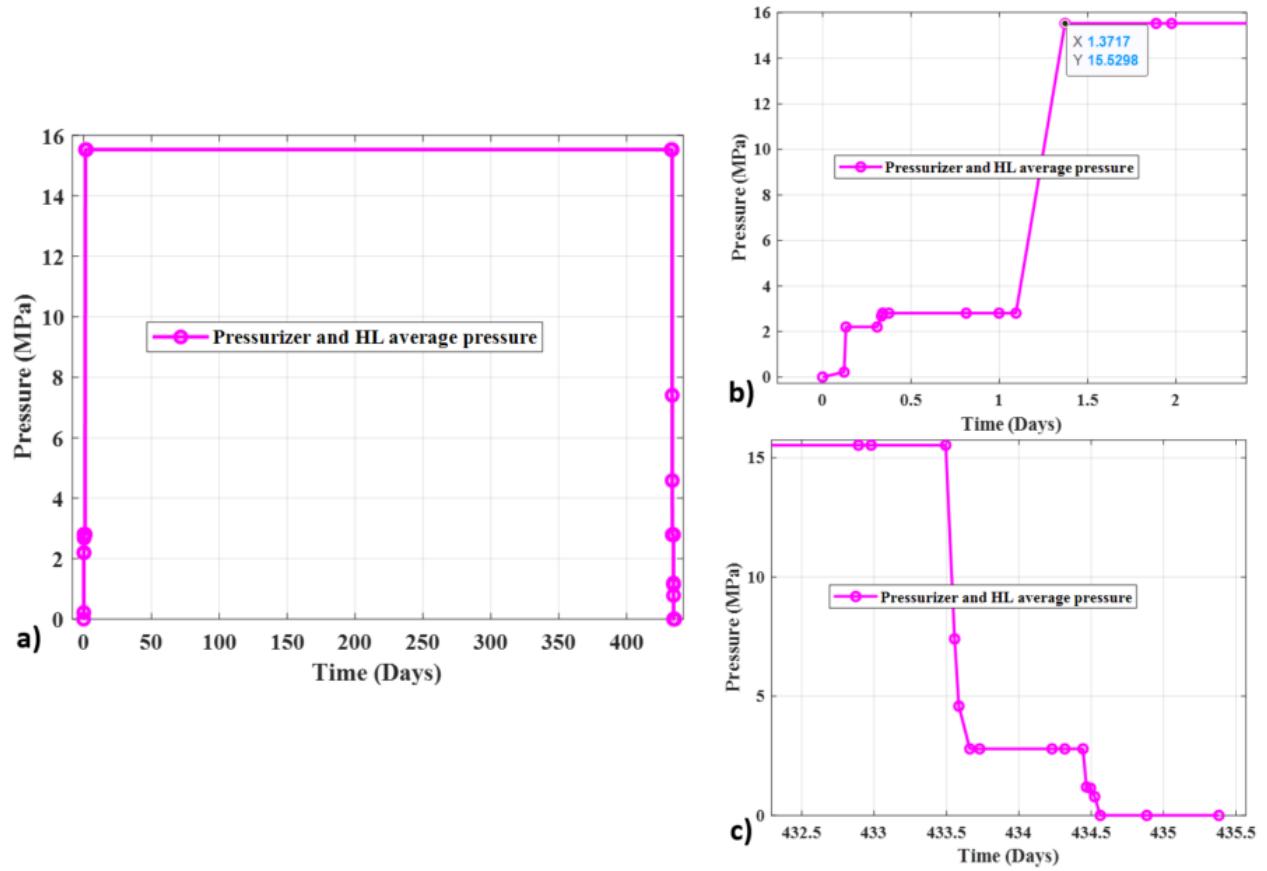


Figure 7. 2 Internal pressure boundary condition for nozzle FE model: (a) full cycle, (b) during heat-up, and (c) during cool-down

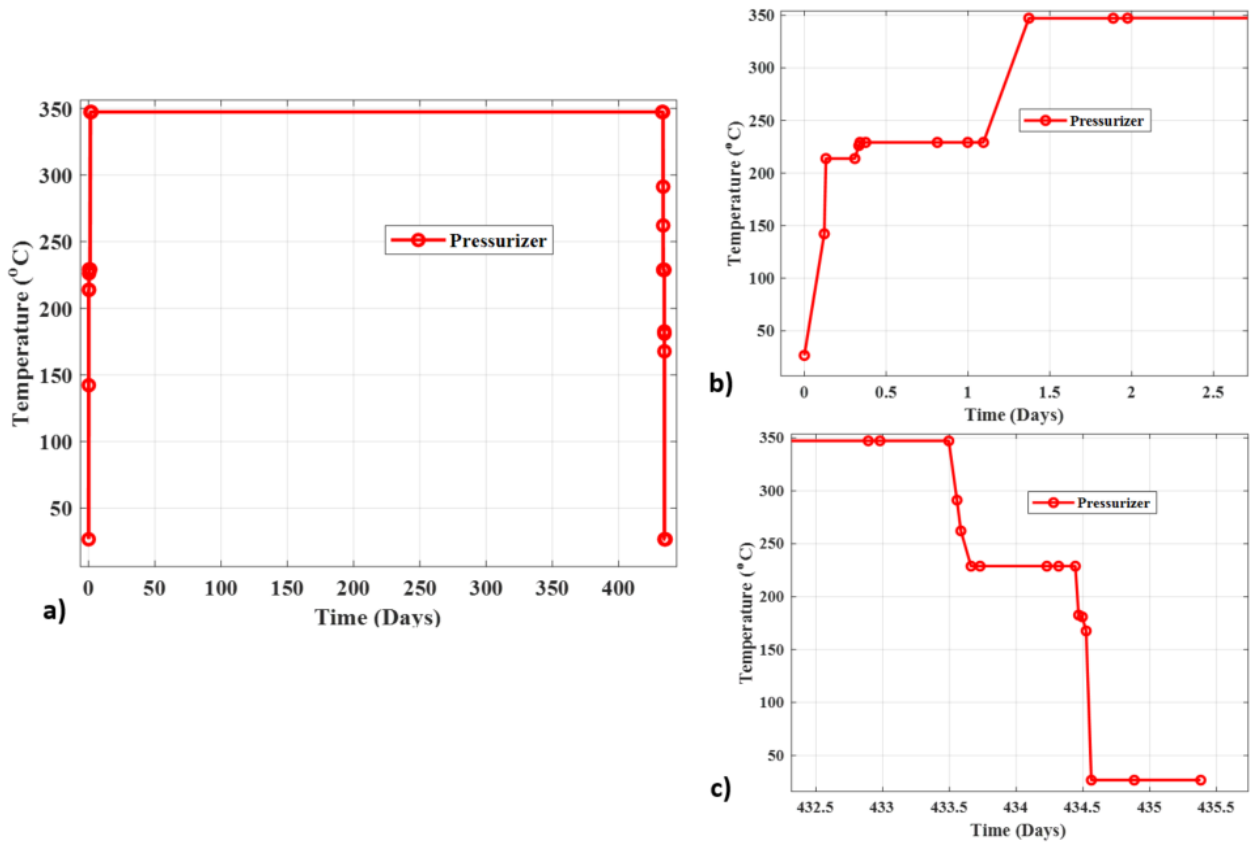


Figure 7. 3 Temperature boundary condition for nozzle FE model: (a) full cycle, (b) during heat-up, and (c) during cool-down

7.1.2 Material Properties

The heat transfer analysis requires thermal properties such as temperature-dependent thermal conductivity, specific heat capacity and film coefficients. The thermal properties which were earlier considered for weld process models (section 7) were also considered for the discussed heat transfer model. We considered elastic-plastic material properties when conducting the subsequent thermal-mechanical stress analysis. For the stress analysis model, we need temperature-dependent thermal expansion coefficients, elastic modulus, yield stress, and hardening parameters. We used the expansion coefficients given in Table 4.2 in Section 4. For hardening and yield conditions, we selected a 0.05% offset yield condition. The related tensile and hardening properties are presented in Sections 2 and 3. However, for convenience, the exact mechanical properties used in the FE model are also summarized in Tables 7.1 through 7.5.

Table 7. 1 Tensile elastic-plastic properties used for 316SS base metal

Tensile test no.	Temperature (°C)	Elastic modulus (GPa)	Poisson ratio	Yield stress at zero plastic strain (MPa)	Kinematic hardening parameter C1 (MPa)	Kinematic hardening parameter γ
T02	22	175.1	0.27	217.41	13942	128.24
T04	300	157.92	0.27	145.03	4373.5	33.25

Table 7. 2 Tensile elastic-plastic properties used for 316SS SMW-Filler Weld and 316ss Cladding

Tensile test no.	Temperature (°C)	Elastic modulus (GPa)	Poisson ratio	Yield stress at zero plastic strain (MPa)	Kinematic hardening parameter C1 (MPa)	Kinematic hardening parameter γ
T03	22	131.98	0.27	414.56	5901.8	65.922
T05	300	129.11	0.27	345.8	4285.5	41.449

Table 7. 3 Tensile elastic-plastic properties used for 508 LAS base metal

Tensile test no.	Temperature (°C)	Elastic modulus (GPa)	Poisson ratio	Yield stress at zero plastic strain (MPa)	Kinematic hardening parameter C1 (MPa)	Kinematic hardening parameter γ
T06	22	209.72	0.27	494.36	2861.4	0
T10	300	194.01	0.27	406.63	12240	57.768

Table 7. 4 Tensile elastic-plastic properties used for DMW-Butter weld

Tensile test no.	Temperature (°C)	Elastic modulus (GPa)	Poisson ratio	Yield stress at zero plastic strain (MPa)	Kinematic hardening parameter C1 (MPa)	Kinematic hardening parameter γ
T16	22	149.7	0.27	387.64	9964.5	90.498
T15	300	146.28	0.27	322	6307	64.861

Table 7. 5 Tensile elastic-plastic properties used for DMW-Filler weld

Tensile test no.	Temperature (°C)	Elastic modulus (GPa)	Poisson ratio	Yield stress at zero plastic strain (MPa)	Kinematic hardening parameter C1 (MPa)	Kinematic hardening parameter γ
T14	22	172.64	0.27	420.14	12023	99.532
T13	300	196.57	0.27	359.72	6556.5	56.92

7.2 Heat Transfer Analysis Results

The heat transfer analysis was performed to estimate the nodal temperature for the subsequent thermal-mechanical stress analyses. Figures 7.4 through 7.7 show several examples of the heat transfer analysis. For example, Figures 7.4 and 7.5, respectively, show the simulated outer diameter (OD) and inner diameter (ID) surface temperature contour, after 0.13212 days (3.1709 hours) from the start of the heat-up operation. Figures 7.6 and 7.7, respectively, show the simulated OD and ID surface temperature contour after 1.3717 days (32.921 hours) from the start of the heat-up operation.

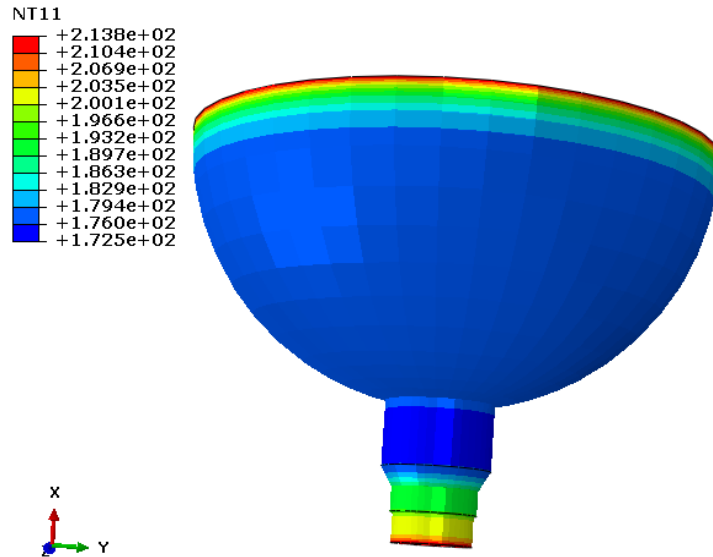


Figure 7. 4 Simulated OD surface temperature contour after 0.13212 days (3.1709 hours) from the start of the heat-up operation

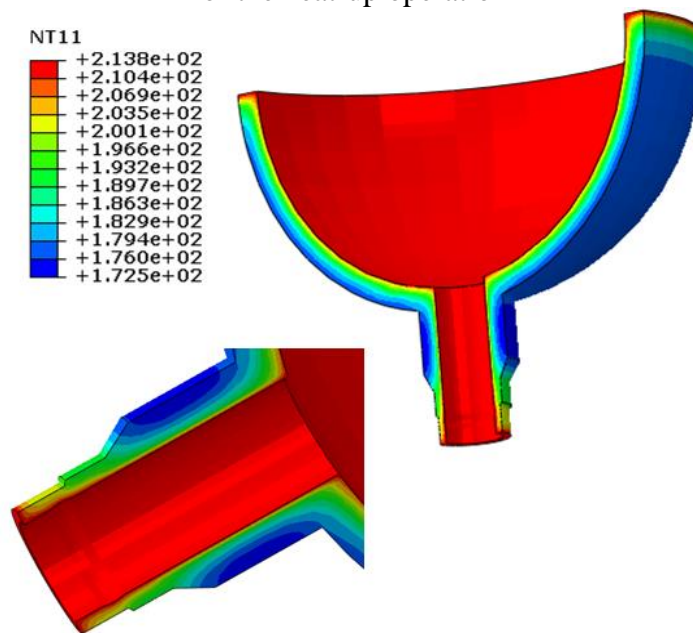


Figure 7. 5 Simulated ID surface temperature contour after 0.13212 days (3.1709 hours) from the start of the heat-up operation

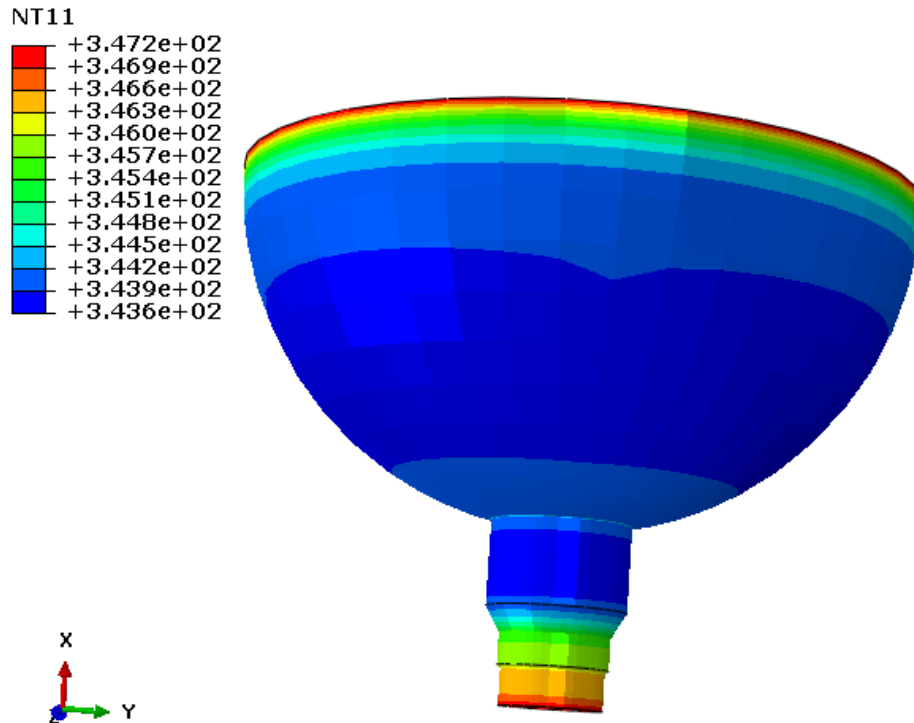


Figure 7. 6 Simulated OD surface temperature contour after 1.3717 days (32.921 hours) from the start of the heat-up operation

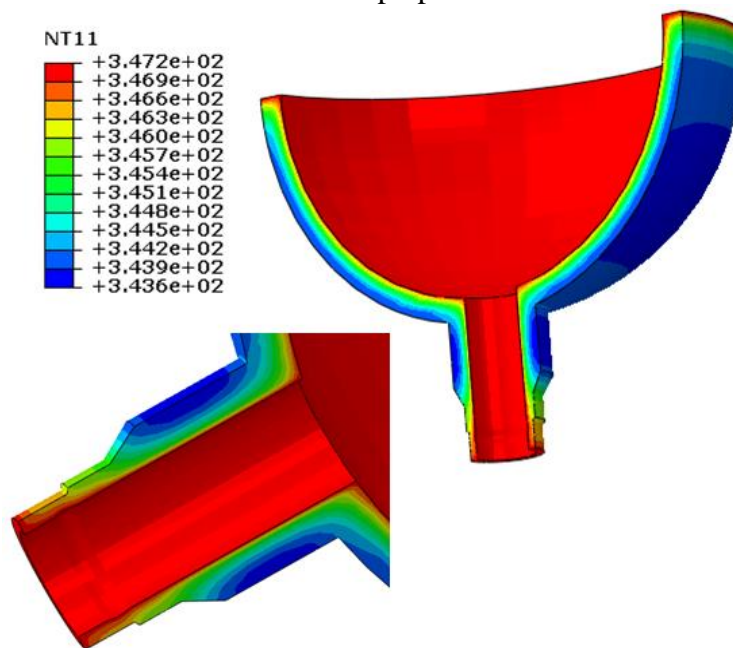


Figure 7. 7 Simulated ID surface temperature contour after 1.3717 days (32.921 hours) from the start of the heat-up operation

7.3 Thermal-Mechanical Stress Analysis Results

The subsequent thermal-mechanical stress analysis was performed considering the nodal temperature estimated in the above-mentioned heat transfer analysis. Figures 7.8 through 7.19 show some representative stress analysis results. For example, Figures 7.8 and 7.9 show the total, thermal, and mechanical strain along the 'x' (along the axial direction of the SL pipe) and the maximum principal direction, respectively. These results were taken at the maximum stress element of the DMW-filler weld region of the nozzle assembly.

Figures 7.10 and 7.11, respectively, show the OD- and ID- side maximum principal thermal strain contour after 0.13212 days (3.1709 hours) from the start of the heat-up operation. Similarly Figures 7.12 and 7.13, respectively, show the OD and ID side maximum principal thermal strain contour after 1.3717 days (32.921 hours) from the start of the heat-up operation.

Figures 7.10 through 7.13 show that different regions of nozzle assembly experience different levels of thermal strain. Thermal strain depends on underlying expansion coefficients and the temperature at a given time. For example, Figure 7.13 shows that the DMW filler weld regions experience the lowest thermal strain, whereas the DMW butter weld regions experience the highest thermal strain. These results are obvious if we check the experimental results presented in Section 4. For example, Figure 4.5 shows that the T13 DMW In-82 filler-weld specimen experiences an approximate thermal strain of 0.26% at 300°C. However, Figure 4.7 shows that the T15 DMW In-182 butter-weld specimen experiences an approximate thermal strain of 0.5% at 300°C.

Figures 7.10 to 7.13 follow a similar trend in the experimental results. Note that in homogeneous media, thermal strain in all three (x, y, and z) directions increases and decreases at the same rate. Hence, the thermal strain progression in a multi-axial domain such as a 3D nozzle assembly would be similar to the thermal strain progression in a uni-axial specimen made of the same material. However, differential material properties (e.g., expansion coefficients) lead to differential thermal strain rates in a heterogeneous material region such as the subject nozzle assembly. These types of differential strains can lead to crack initiation across the material boundaries.

In addition to the above strain results, several more stress results are presented below. For example, Figure 7.14 compares axial stress (along the x-direction) and Von Mises stress at the maximum stress element of the DMW filler weld. Figure 7.15 compares the experiment to FE model simulated stress-strain curves. Figure 7.15 shows that the FE simulated stress-strain curves for the filler weld (axial strain versus Von Mises stress and axial strain versus axial stress) are very comparable to the corresponding 300°C tensile curve (T13 DMW In-82 filler-weld). The FE curves are comparable to the tensile curve up to the first quarter cycle; after that, they should not be compared because the sign of the stress changes. Furthermore, we present some contour plots below to show the distribution of stress at a given time. For example, Figures 7.16 and 7.17, respectively, show the OD- and ID-side Von Mises stress contour after 0.13212 days (3.1709 hours) from the start of the heat-up operation. Similarly, Figures 7.18 and 7.19, respectively, show the OD- and ID-side Von Mises stress contour after 1.3717 days (32.921 hours) from the start of the heat-up operation. Figure 7.19 shows that different regions experience different stresses. The stress depends on the location of the displacement boundary conditions, in addition to the effects of material properties and temperature distributions.

Figure 7.19 shows that the maximum stress is at the skirt region of the pressurizer bottom-head. This is due to the fixed constraints in the skirt region. As shown in Figure 7.19, the maximum stress in the skirt region is approximately 550 MPa.

Table 7.3 reveals that the yield stress of 508 LAS (chosen as the pressurizer material in the above-discussed FE model) is 406.63 MPa (at 300°C). That means the skirt region of the pressurizer might experience plastic yielding due to repetitive thermal-mechanical loading cycles (associated with the power cycles). Nevertheless, our primary goal in this FE modeling and the subsequent experimental study was to access the fatigue performance of DMW filler welds. Hence, only the FE simulated stress and strain histories at the highest stress element of the DMW filler-weld region (highlighted in Figure 19) are presented in this report.

Overall stress in different regions strongly depends on the displacement and thermal boundary conditions in addition to the differential material properties. Table 7.7 summarizes the maximum stress and strain at the highest stressed element in the DMW filler region of the above-discussed nozzle assembly. The simulated strain history at this highest element was used to conduct the in-air and PWR-water fatigue tests; these results are discussed in Section 8.

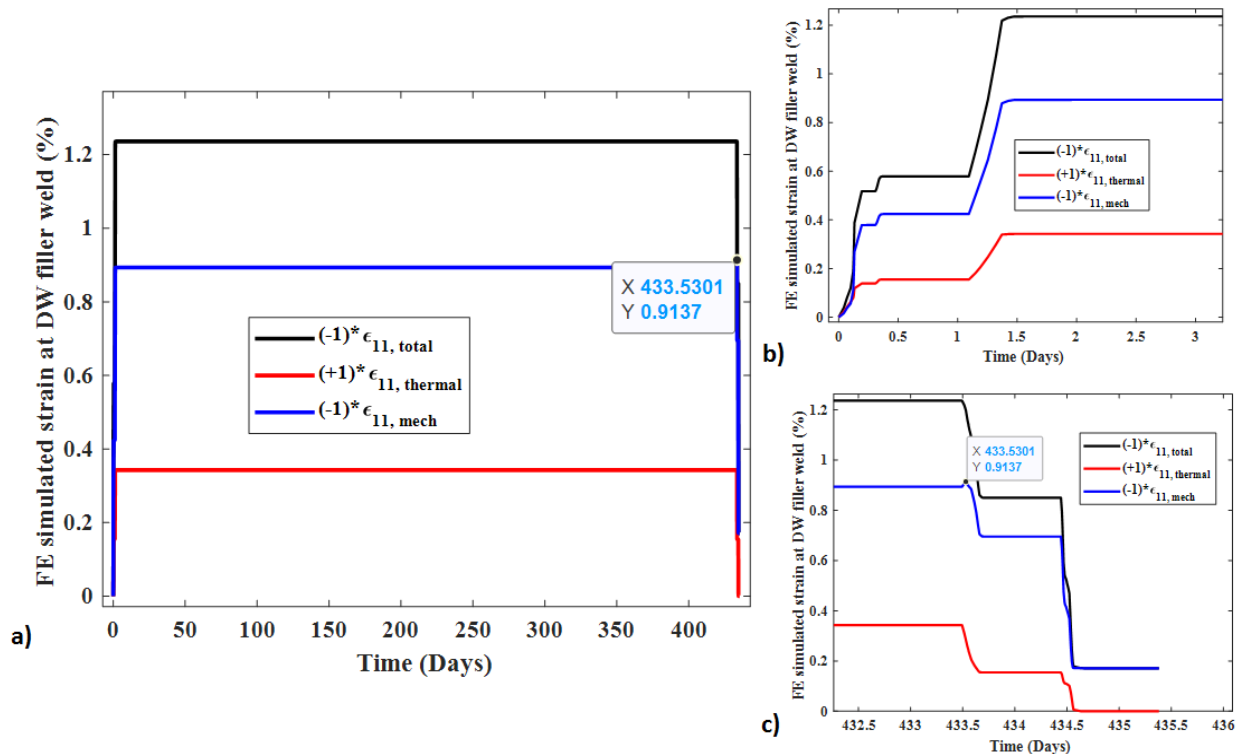


Figure 7. 8 FE model (case-1) simulated total, thermal, and mechanical strain (along x-direction) at the maximum stress element of the DMW-filler weld: (a) full cycle, (b) during heat-up, and (c) during cool-down

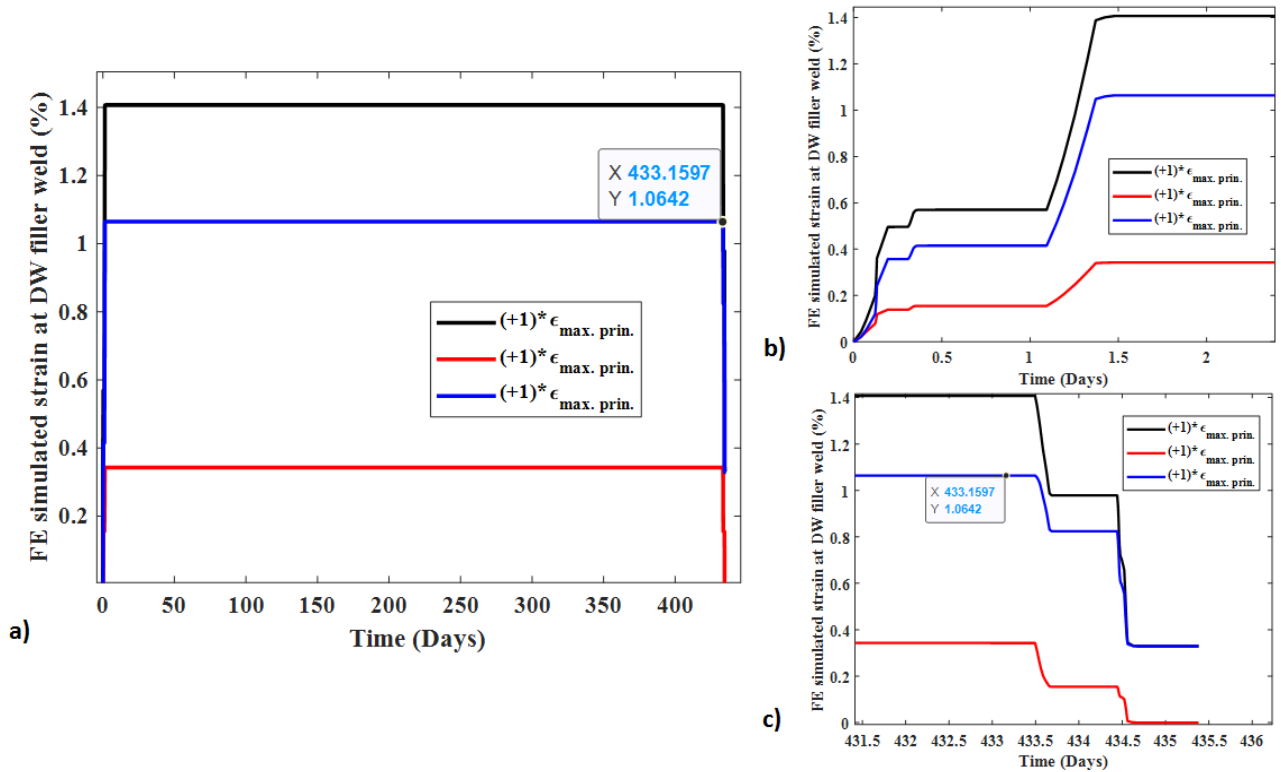


Figure 7. 9 FE model (case-1) simulated total, thermal, and mechanical strain (along max. principal direction) at the maximum stress element of the DMW-filler: (a) full cycle, (b) during heat-up, and (c) during cool-down

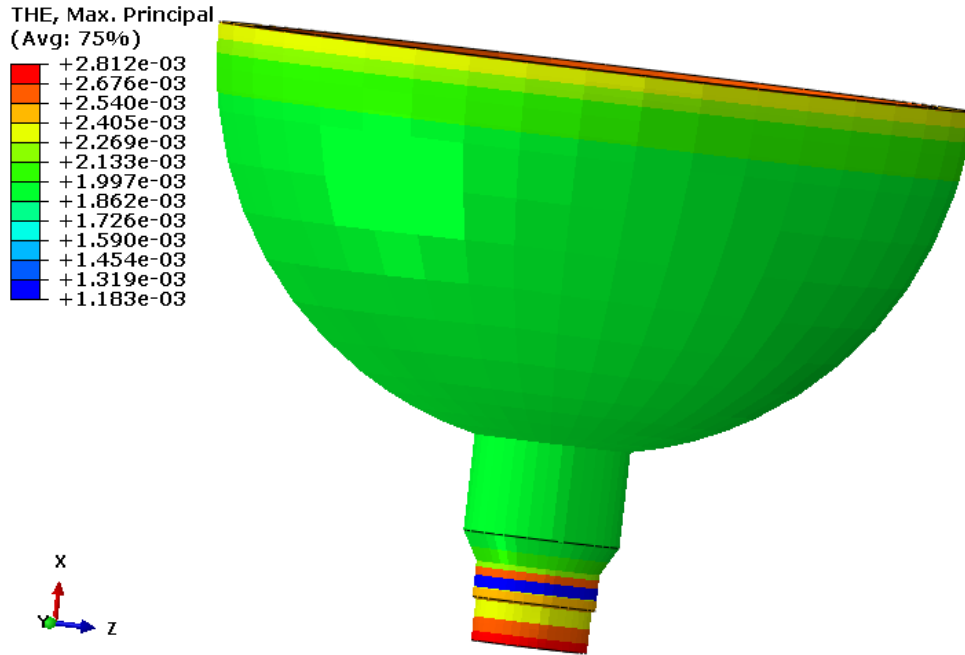


Figure 7. 10 Simulated (case-1) OD-side maximum principal thermal strain contour after 0.13212 days (3.1709 hours) from the start of the heat-up operation

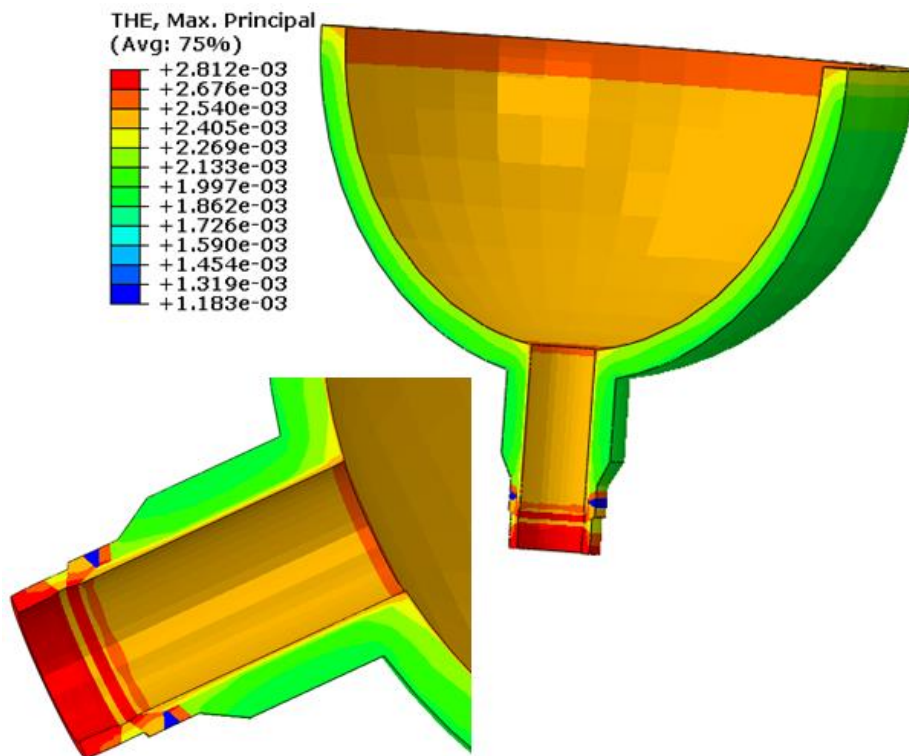


Figure 7. 11 Simulated (case-1) ID-side maximum principal thermal strain contour after 0.13212 days (3.1709 hours) from the start of the heat-up operation

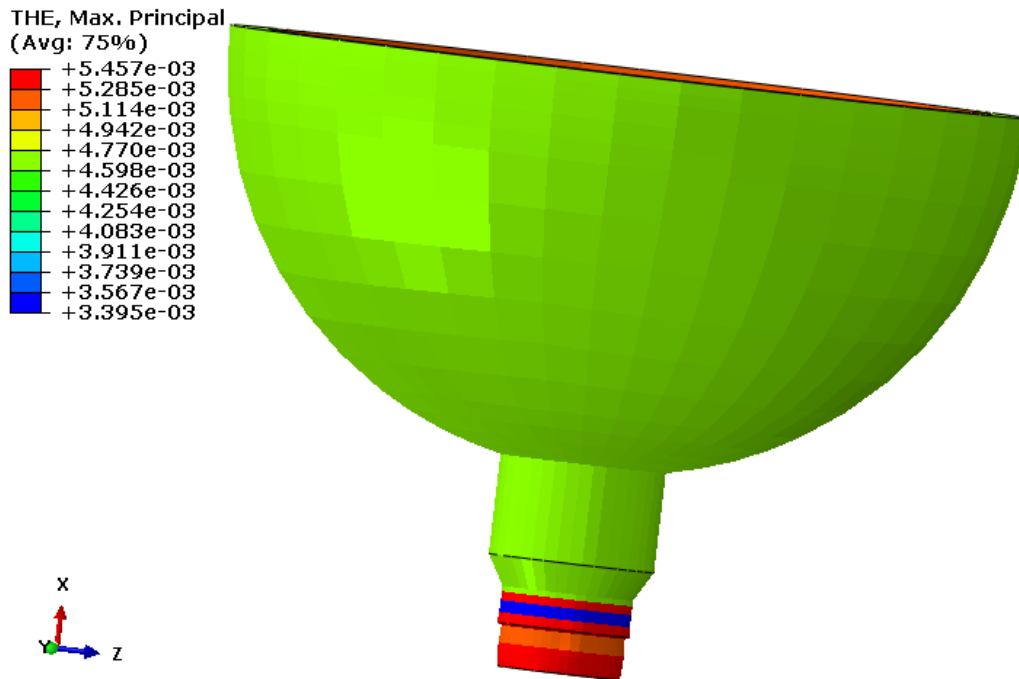


Figure 7. 12 Simulated (case-1) OD-side maximum principal thermal strain contour after 1.3717 days (32.921 hours) from the start of the heat-up operation

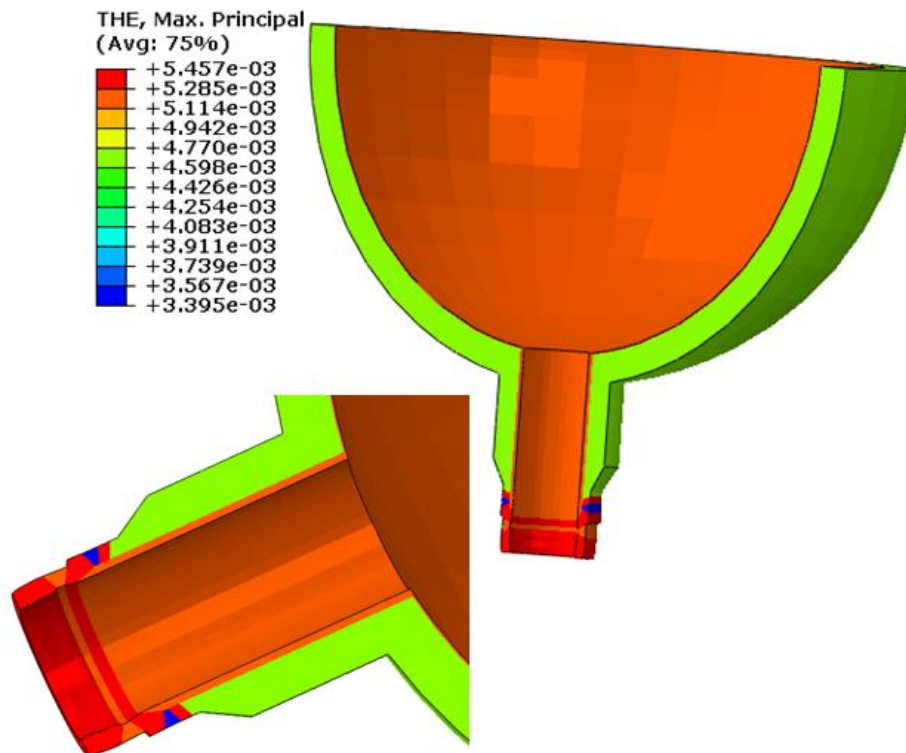


Figure 7. 13 Simulated (case-1) ID-side maximum principal thermal strain contour after 1.3717 days (32.921 hours) from the start of the heat-up operation

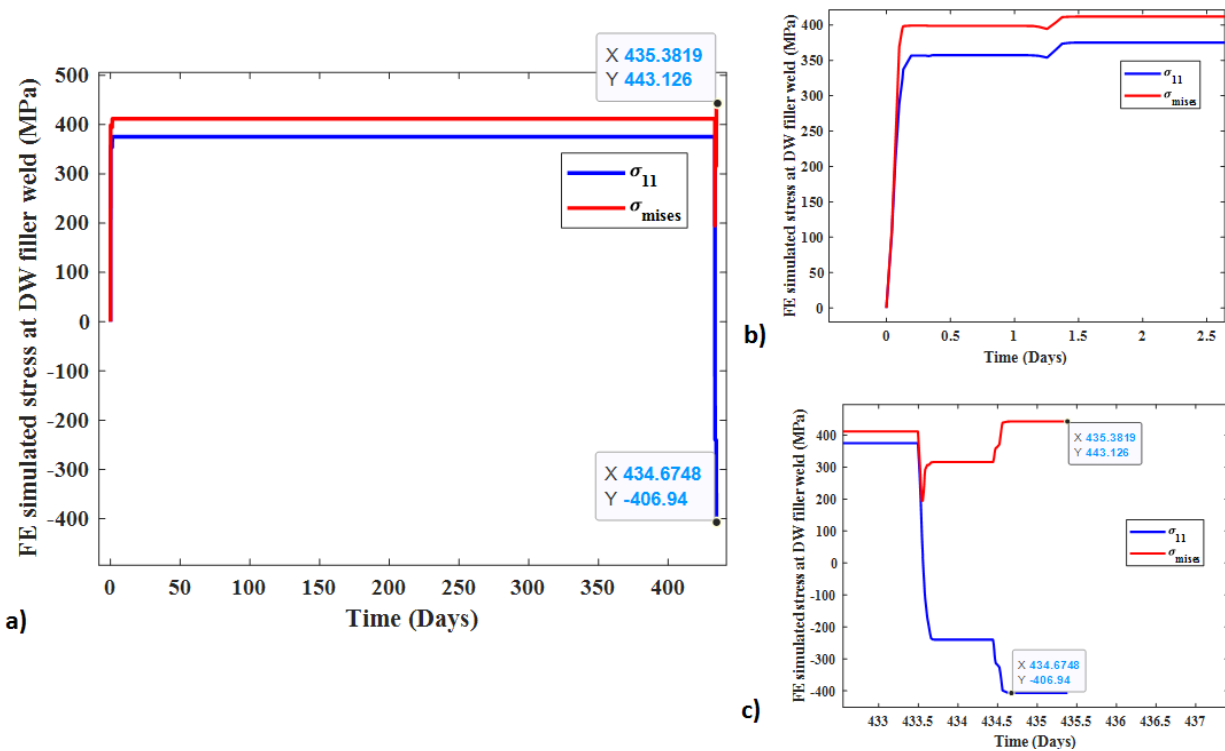


Figure 7. 14 FE model (case-1) simulated axial stress (along x-direction) and Von Mises stress at the maximum stress element of DMW filler weld: (a) full cycle, (b) during heat-up, and (c) during cool-down

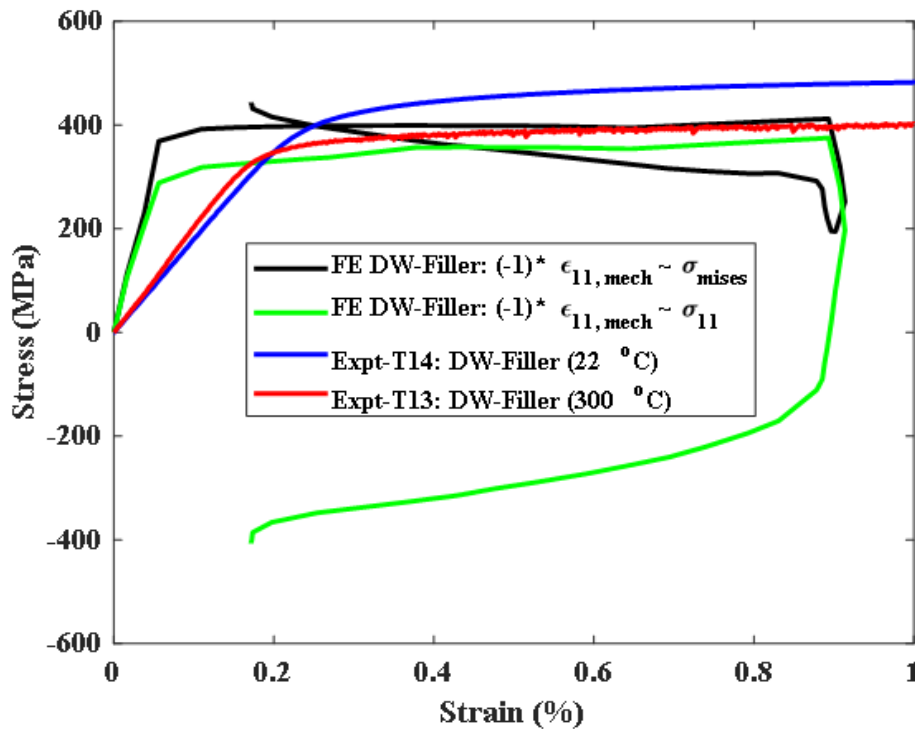


Figure 7. 15 Experiment versus FE model (case-1) simulated stress-strain curve

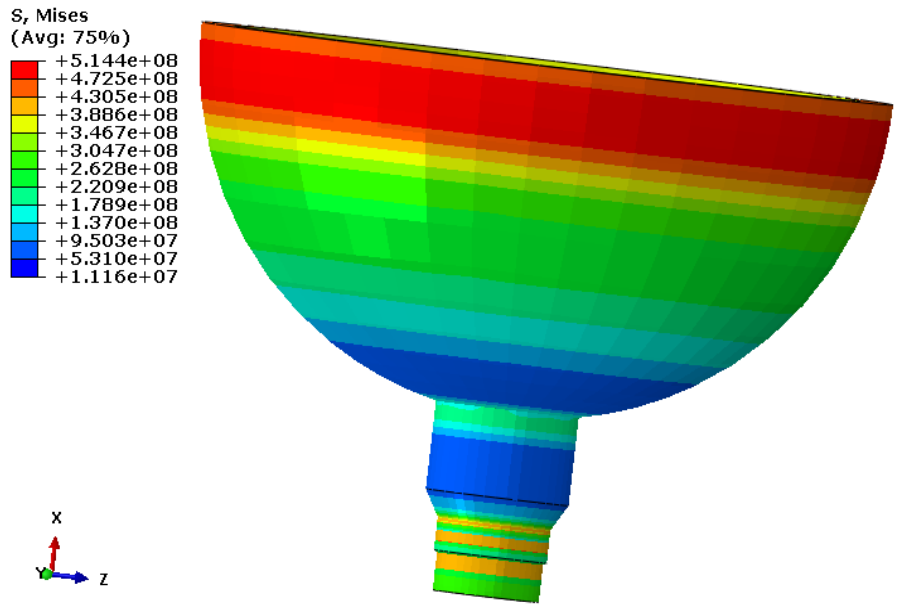


Figure 7. 16 Simulated OD-side Von Mises stress contour after 0.13212 days (3.1709 hours) from the start of the heat-up operation

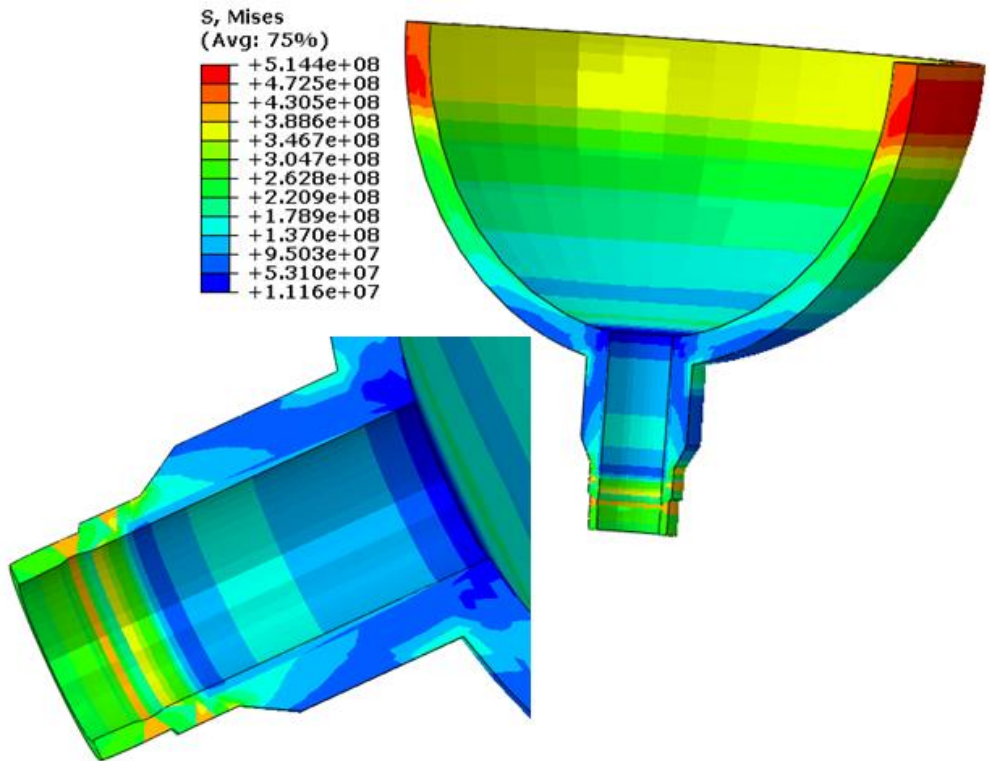


Figure 7. 17 Simulated ID-side Von Mises stress contour after 0.13212 days (3.1709 hours) from the start of the heat-up operation

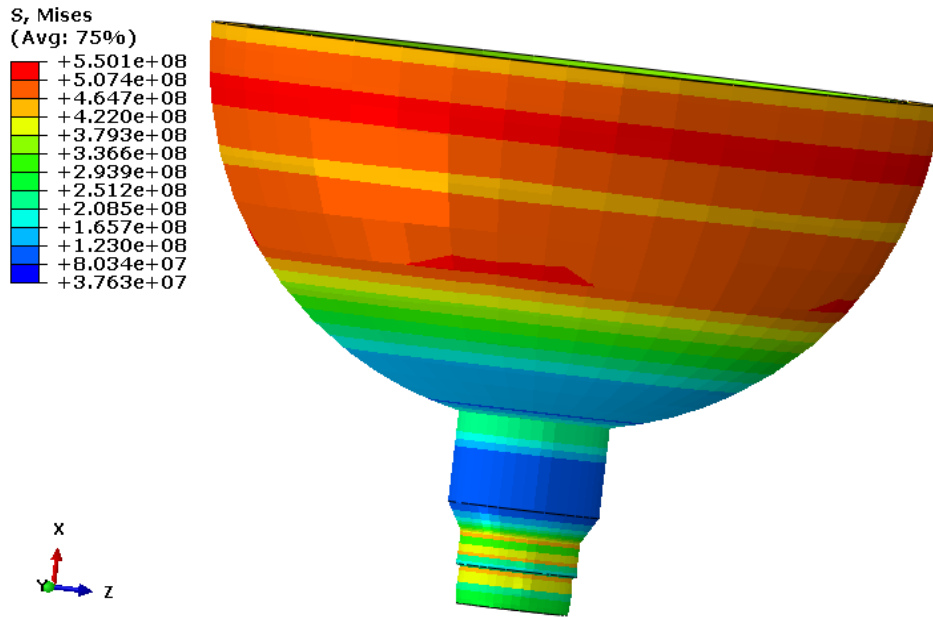


Figure 7. 18 Simulated OD-side Von Mises stress contour after 1.3717 days (32.921 hours) from the start of the heat-up operation

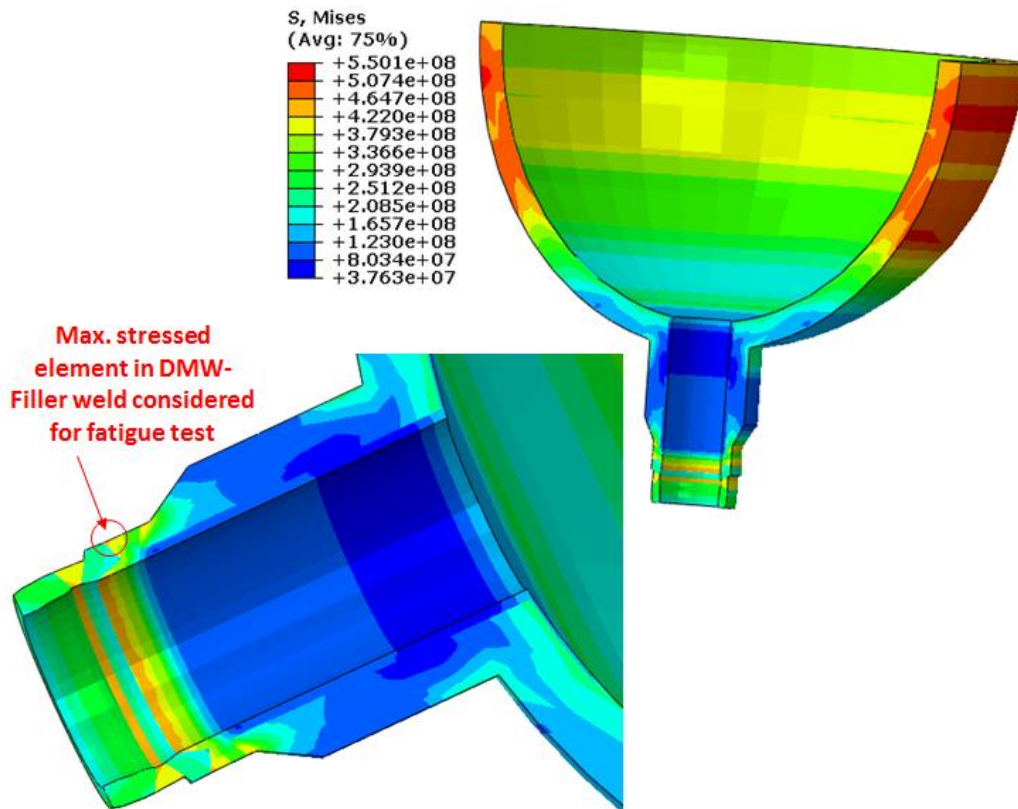


Figure 7. 19 Simulated ID-side Von Mises stress contour after 1.3717 days (32.921 hours) from the start of the heat-up operation

Table 7. 6 Summary of maximum stress and strain at the highest stressed element in the DMW-filler region of the nozzle assembly

Parameters	Values
Maximum temperature experienced (°C)	347.3
Maximum Von Mises stress (MPa)	443.126
Yield stress (MPa) of DMW-filler weld at 300°C	359.72
Maximum axial total strain (%)	1.25625
Maximum axial thermal strain (%)	0.342548
Maximum axial mechanical strain (%)	0.9137
Maximum principal total strain (%)	1.4067
Maximum principal thermal strain (%)	0.342548
Maximum principal mechanical strain (%)	1.0642

8 Fatigue Life Estimation of Pressurizer-Surge Line Nozzle under In-Air and PWR-Water Environment and under Design-Basis Loading Cycles

In this section, we describe the results of a hybrid model- and test-based method to estimate the fatigue life of a PRZ-SL nozzle under in-air and PWR-water environments and under design-basis loading cycles.

8.1 Various Methods for Component-level Fatigue Estimation

Figure 8.1 shows a chart of different possible methods for component fatigue life estimation, with their advantages and disadvantages. Under the LWR program, we are mostly developing Method 1 [15] and Method 2 [13, 14] for estimating reactor component fatigue life under long-term operations. In the work discussed below, we have chosen Method 1 as a preliminary step to estimate the fatigue life of a PRZ-SL nozzle. The fatigue lives are estimated under simulated design-basis loading cycles. Method 1 (see Figure 8.1) is a hybrid method that depends on both FE simulation and fatigue test results. The FE simulation results for a PRZ-SL nozzle were discussed in section 7. On the basis of the 3D-FE simulated (from the thermal-mechanical stress analysis) strain history, we conducted uniaxial fatigue tests of DMW-filler weld specimens to estimate the fatigue life of the PRZ-SL nozzle. This approach assumes that the DMW-filler weld is the weakest link in the PRZ-SL nozzle. However, for more accurate life prediction of the nozzle, the individual materials that compose the PRZ-SL nozzle must be fatigue-tested under the relevant strain history (based on the FE models described in Section 7). The shortest life among all the fatigue lives thus determined will be the life of the overall component.

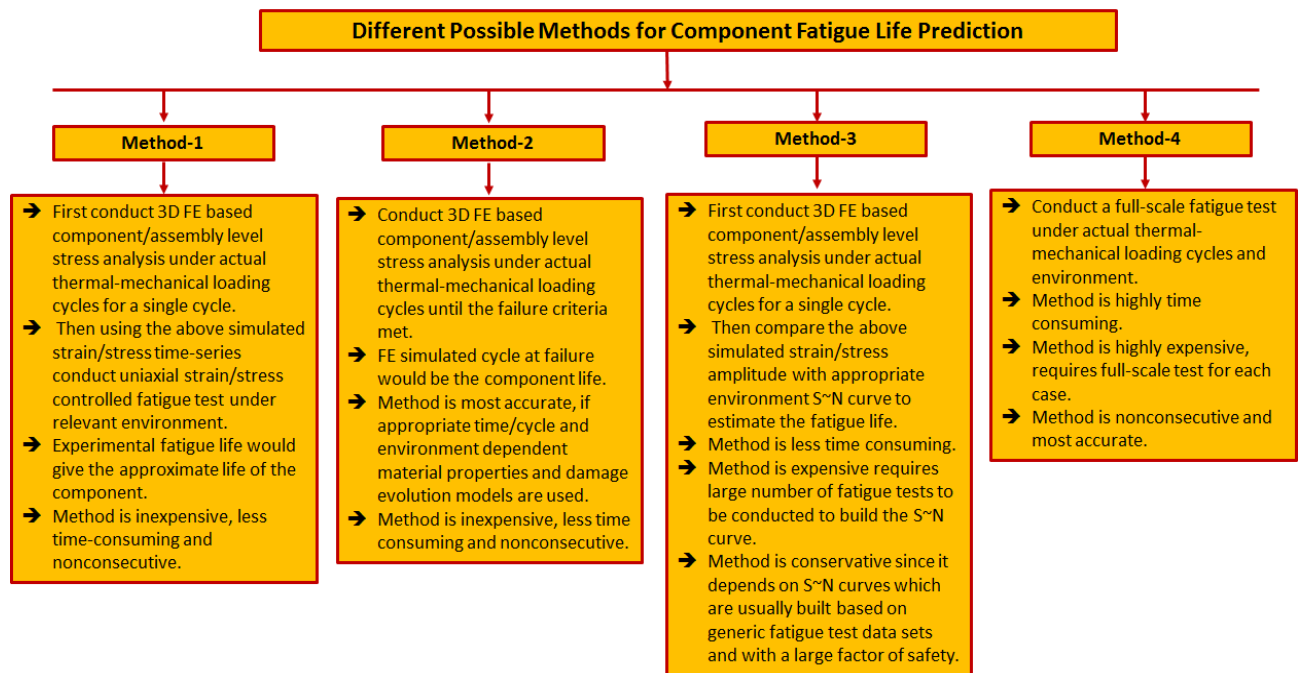


Figure 8. 1 Chart showing different possible methods for fatigue life prediction of full-scale component/assembly.

8.2 Uniaxial Fatigue Test Results of DMW-filler Weld Specimens

Three uniaxial fatigue tests of DMW-filler weld specimens were conducted to supplement the Method 1-based component fatigue life estimation. The fatigue test setup and fatigue test results are discussed below.

8.2.1 Fatigue test setup

Both in-air and PWR-water loop tests were conducted. The in-air test setup was shown in Figure 2.6 of Section 2. The tests under PWR primary-water-coolant conditions were conducted using the Argonne fatigue test loop shown in Figure 8.2. Figure 8.3 shows example thermocouple readings at different locations of the PWR-water test-loop during the heat-up and actual test of a DMW-filler weld specimen. Figures 8.4 and 8.5, respectively, show the pressure and flow velocity of the test loop during the heat-up and actual test of the DMW-filler weld specimen.

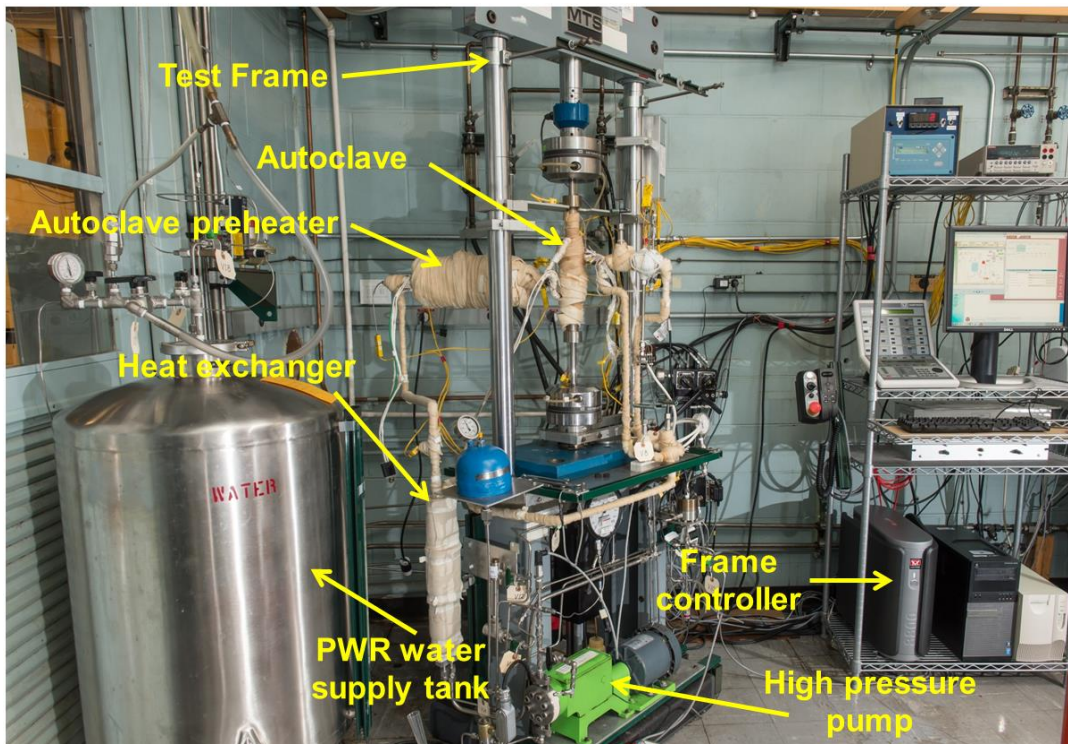


Figure 8. 2 Environmental test loop showing different subsystems.

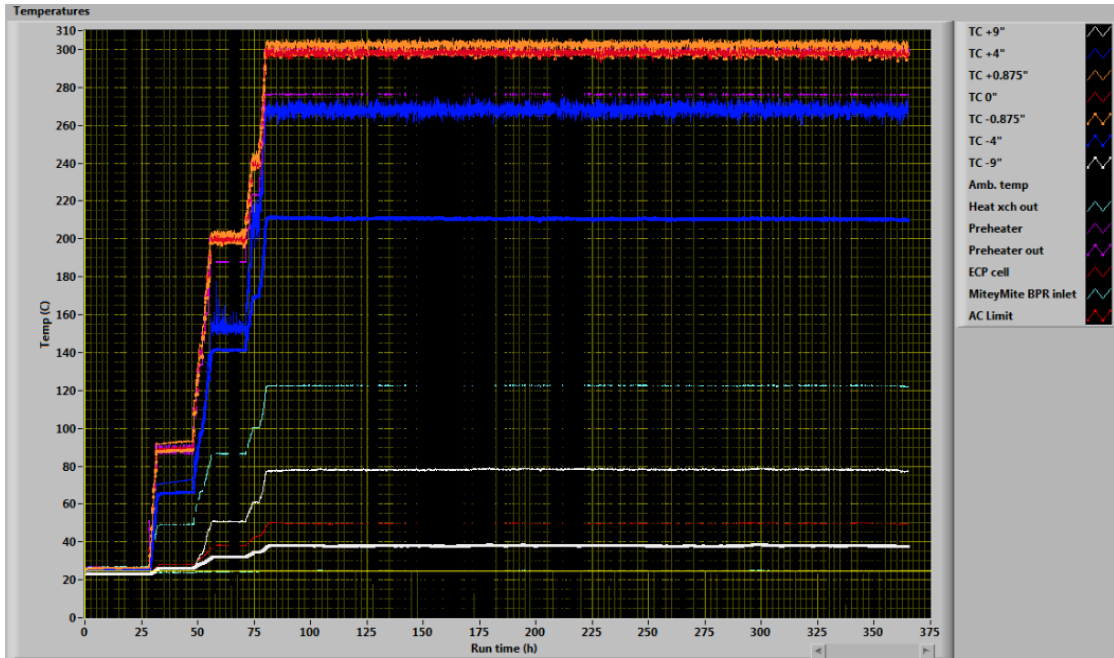


Figure 8. 3 Thermocouple readings at different locations of the PWR-water test-loop during the heat-up and actual test

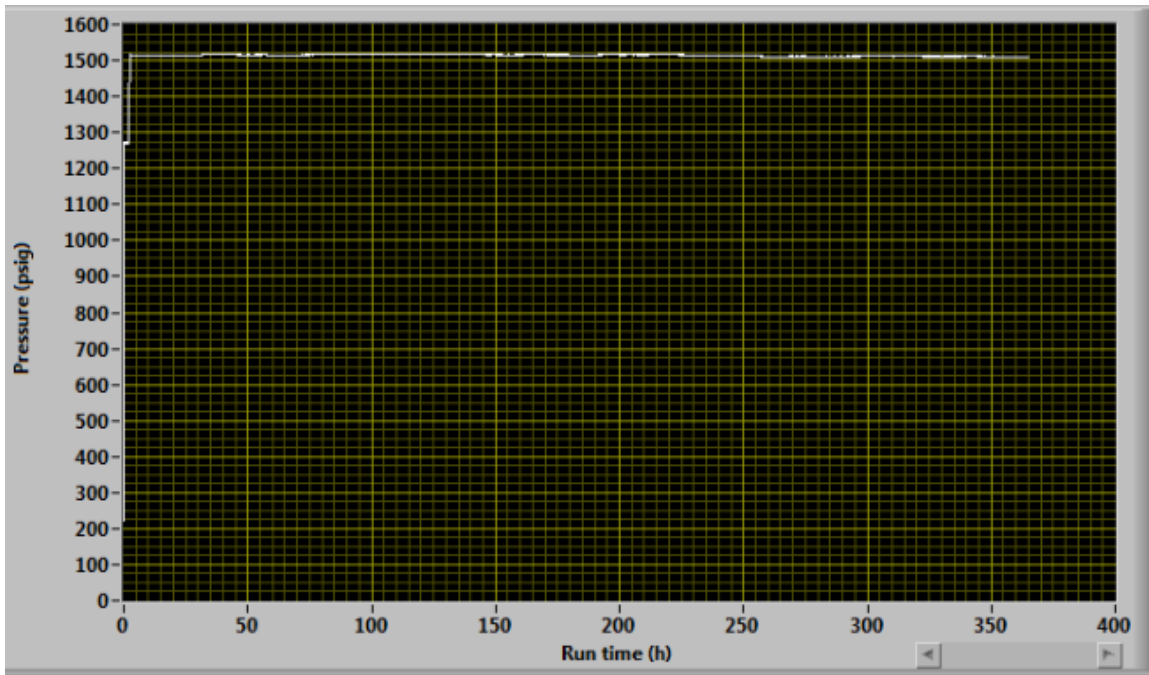


Figure 8. 4 Pressure histories at of the PWR-water test-loop during the heat-up and actual test

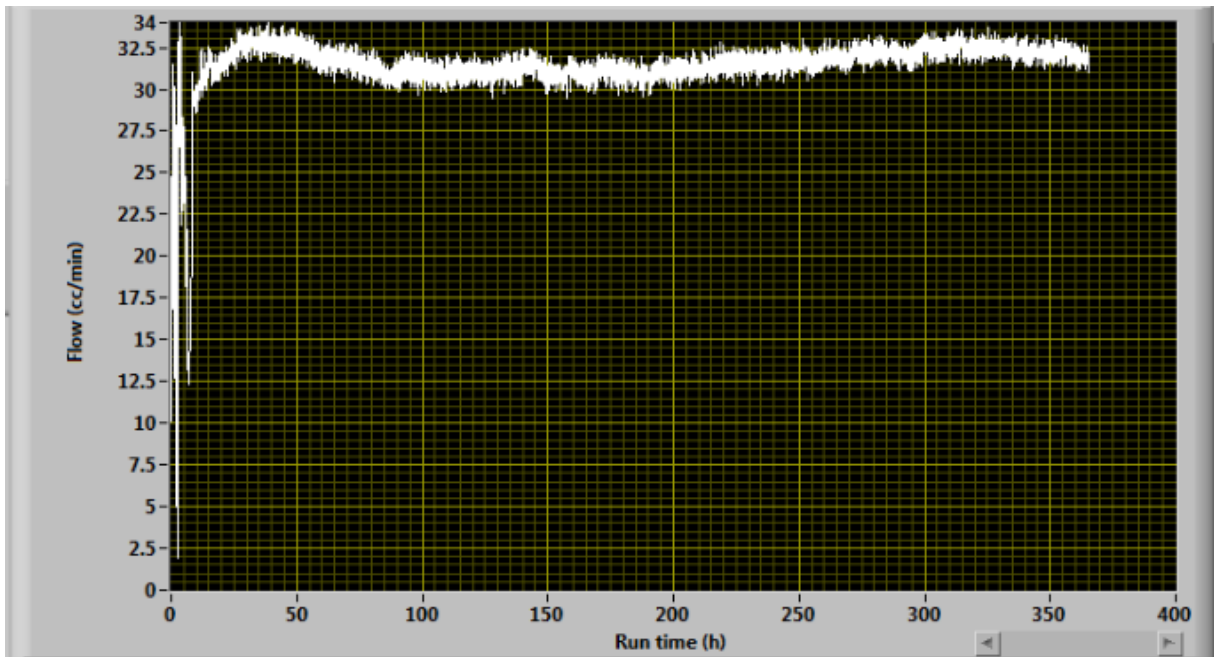


Figure 8. 5 Flow velocity of the PWR-water test-loop during the heat-up and actual test

8.2.2 Test inputs for fatigue tests

Three uniaxial fatigue tests of the DMW-filler weld specimens were conducted on the basis of the FE-simulated mechanical strain profile. The strain profile at the maximum stressed element of the DMW-filler weld of the PRZ-SL nozzle assembly (see Figure 7.19) was selected as the fatigue test input. The mechanical strain profile is shown in Figure 7.8. The strain profile was simulated for a single fuel cycle of duration 435.38 days. To conduct the fatigue tests (with thousands of cycles) within a reasonable time period, the strain profile shown in Figure 7.8 was rescaled in the time-axis. We had chosen the data points on the time-axis with the intention to achieve a strain rate of 0.1%/s and 0.01%/s. Figure 8.6 shows the rescaled (in the time-axis) mechanical strain history. Figure 8.7 shows strain rates of the rescaled strain history, showing that the desired strain rate of 0.1%/s was achieved (in both the positive and negative directions). It is worth noting that the strain rate changes sign when the actual strain (in the FE-simulated strain profile) changes sign or tends to become steady. Also note that in a design-basis type loading cycle, the strain rate only changes during the heat-up and cool-down operations and becomes steady during steady-state power operation. During steady-state power operation, to reduce the test time, we assumed a shorter duration (approximately the time between 10 and 15 seconds in Figure 8.6) and a steady-state strain amplitude. Ideally, it was possible to use the rescaled strain profile shown in Figure 8.6 to conduct the in-air fatigue tests. However, note that a strain-controlled test could not be conducted under PWR-water conditions because an extensometer (which is used for measuring the gauge area strain in an in-air test) could not be placed inside the autoclave of the PWR test loop. Hence all the reported tests were conducted under similar test control conditions, such as by controlling the displacement between the two crossheads or hydraulic grips of the test frames (stroke

displacement). To meet the requirement of conducting all the tests under stroke-control mode, the rescaled strain profile shown in Figure 8.6 was converted to an equivalent stroke profile. The conversion was based on a strain-stroke mapping function. The mapping function was created on the basis of a tensile-test (T13: DMW-filler weld test) data set. Figure 8.8 shows the derived stroke history that was finally applied to the test specimen; Figure 8.9 shows the equivalent applied stroke rate used while conducting the stroke-controlled tests. Note that Figures 8.6 to 8.9 show the strain/stroke profile corresponding to a desired strain rate of 0.1%/s. For 0.01%/s the time axis has to be changed accordingly. Also note that at the end of each cycle, the stroke was brought to zero to maintain simplicity in the test procedure (Figure 8.8). For all three tests, the amplitude was kept the same but the strain rates were different (ET-F54 and EN-F56 were conducted at an intended strain rate of 0.1%/s, whereas EN-F55 was conducted at an intended strain rate of 0.01%/s). Table 8.1 summarizes the test input and observed fatigue lives. Note that to allow time for conducting the next test (EN-F56), and because there was an anomaly at the start of the EN-F55 test (the test tripped after starting and was then restarted), it was decided to abandon the EN-F55 test before its final failure.

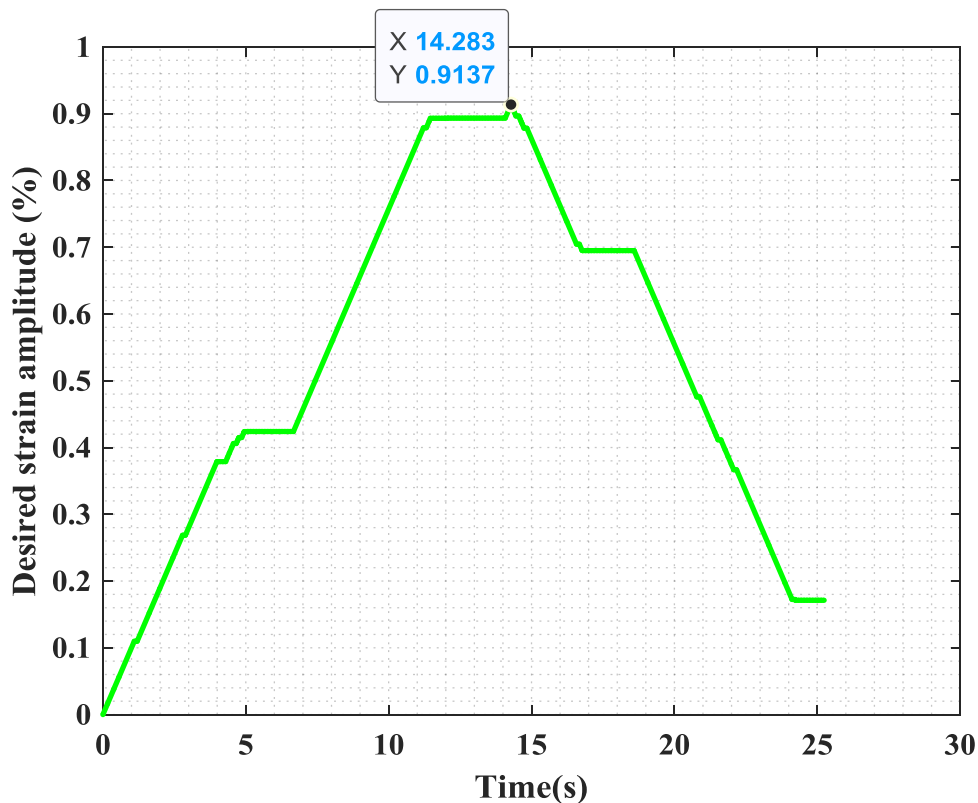


Figure 8. 6 FE simulated and rescaled (in time-axis) mechanical strain history at the maximum stressed element of DMW-filler weld region (of PRZ-SL nozzle).

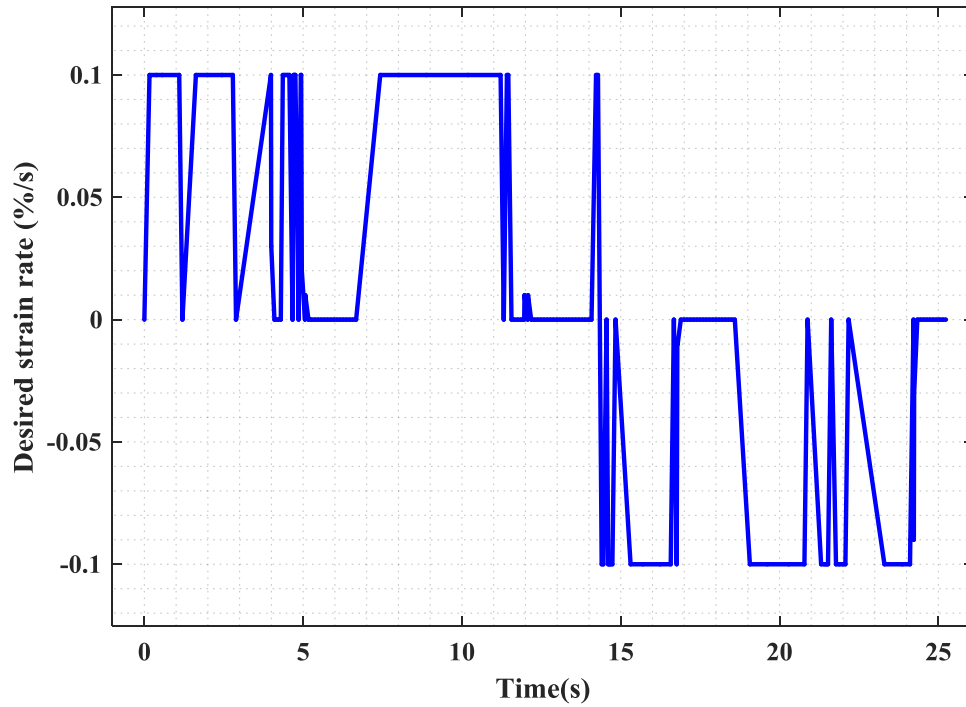


Figure 8. 7 Strain rates of the rescaled strain history shown in Figure 8.6

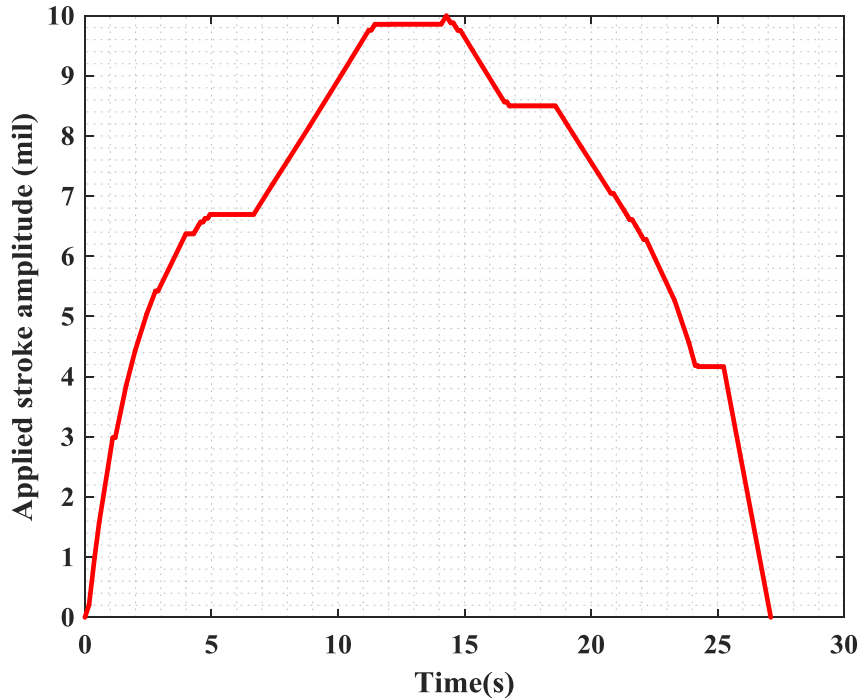


Figure 8. 8 Mapped stroke history applied to the test specimen.

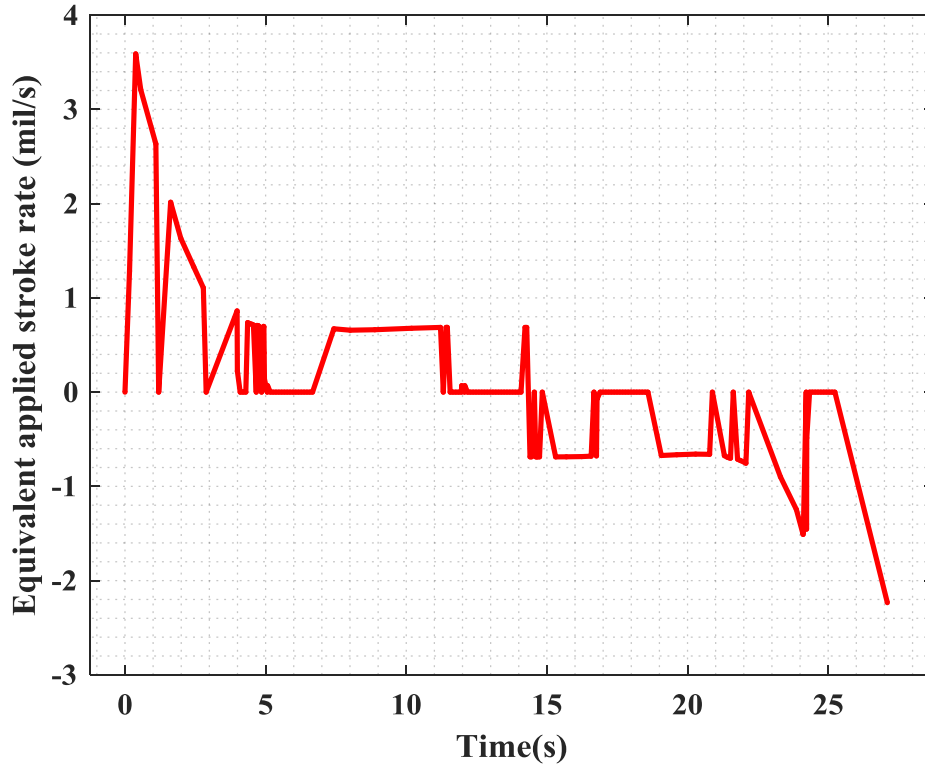


Figure 8. 9 Stroke rates of the stroke profile shown in Figure 8.8

Table 8. 1 Loading, environment and fatigue lives of DMW/filler weld specimens

Test No.	Loading and Environment	25% load drop life (fatigue cycles)
ET-F54	<ul style="list-style-type: none"> ⇒ Stroke controlled in-air test ⇒ Intended strain rate = 0.1%/s ⇒ Stroke amplitude as given in Figure 8.8 	13147
EN-F55	<ul style="list-style-type: none"> ⇒ Stroke controlled PWR-water test ⇒ Intended strain rate = 0.01%/s ⇒ Stroke amplitude as given in Figure 8.8 	6227 (test abandoned)
EN-F56	<ul style="list-style-type: none"> ⇒ Stroke controlled PWR-water test ⇒ Intended strain rate = 0.1%/s ⇒ Stroke amplitude as given in Figure 8.8 	9312

8.2.3 Study of the time-evolution of environmental effects

Table 8.1 provides the fatigue lives of the specimens tested under in-air and PWR-water environments. Clearly, the EN-F56 specimen shows a reduction in life relative to the ET-F54 specimen: i.e., the life of the PWR-water specimen (EN-F56) was reduced by a factor of 1.418 compared to the life of the corresponding in-air specimen (ET-F54). It is not clear that the reduction factor either falls within the usual band of fatigue-life scatter (due to variability in material microstructure) or is due to an environmental effect that can be accounted for through an environmental correction factor [33], as shown in Eq. 8.1:

$$F_{en} = \frac{N_{air}}{N_{water}} = \frac{13147}{9312} = 1.418 \quad (8.1)$$

To accurately identify whether there is any environmental effect, it is necessary to look more closely at the time-series (cycle-dependent) measurements obtained from both the in-air (ET-F54) and PWR-water (EN-F56) tests. For example Figure 8.10 shows the cycle versus applied stroke and observed frame actuator position for the in-air (ET-F54) fatigue test; Figures 8.11 and 8.12, respectively, show the cycle versus observed gauge-area stress and cycle versus observed gauge-area strain for the in-air (ET-F54) fatigue test case. Similarly, Figure 8.13 shows the cycle versus applied stroke and observed frame actuator position for the PWR-water (EN-F56) fatigue test, and Figure 8.14 shows the corresponding cycle versus observed gauge-area stress for the PWR-water (EN-F56) fatigue test case. Comparing the stress histories (Figure 8.11 versus Figure 8.14) of ET-F54 and EN-F56 does not readily show whether there is any environmental effect. By comparing the frame position histories in Figures 8.10 and 8.13, it can be seen that the EN-F56 specimen experiences slightly higher displacement after 2000 fatigue cycles. This could be a sign of an environmental effect, but is still not definitive.

Another option is to look at strain histories. Strain history is available for the in-air test (where it is measured through a gauge area extensometer) but unfortunately is not available for the water test (since it couldn't be measured inside an autoclave). Nevertheless, Figure 8.12 shows that there is an initial ratcheting of strain up to the first 100 cycles, and after that, the overall amplitude stabilizes. This type of strain ratcheting is possible in an actual reactor loading environment but not possible in a strain-controlled fatigue test. Note that most of the conventional approaches for fatigue life estimation (see Method 3 in Figure 8.1) are primarily based on strain-controlled test data based S-N curves. Although it is easier to use the S-N curve-based approach, the related life estimation method doesn't necessarily reflect the actual behavior (e.g., time evolution of strain, etc.) of the reactor material under thermal-mechanical loading environments.

Since little information could be obtained from the regular cycle-versus-amplitude histories shown in Figures 8.10–8.14, we estimated the time-series of mean observed parameters and their amplitudes. The purpose was to check whether there is any significant environmental effect visible through the mean strain/stress or through the strain/stress amplitudes. For example Figures 8.15 and 8.16, respectively, show the comparison of cycle versus observed stress amplitude and cycle versus observed mean stress for the in-air (ET-F54) and PWR-water (EN-F56) fatigue test cases. From Figure 8.15, it can be seen that the air-versus-water data show a nearly constant bias between their observed amplitudes. This bias is evident from the start of the test and could be due to the difference in

microstructure of the ET-F54 and EN-F56 specimens. This type of initial bias can lead to different fatigue lives (even if the tests were conducted under the same loading and environment say even under the in-air environment). The usual scatter in fatigue lives is sometimes due to this type of initial bias. Nevertheless, by checking the results of mean stress histories (in Figure 8.16), it can be seen that there is not much distinguishable environmental effect on mean stress either.

Figure 8.17 shows a Goodman-type curve of observed mean stress versus observed stress amplitude for the in-air (ET-F54) and PWR-water (EN-F56) fatigue test cases. This figure also shows there no visible environmental effect. In addition, Figure 8.17 shows the Goodman curve plotted using the corresponding tensile test data (T13: DMW-filler weld) and its comparison with the ET-F54 and EN-F56 data.

Figure 8.18 shows the cycle versus observed gauge-area strain amplitude for the in-air (ET-F54) test only; Figure 8.19 shows the corresponding cycle versus observed gauge-area mean strain for the in-air (ET-F54) test case. From Figure 8.19, it can be seen that there is a clear shift in mean strain, which is possible if the strain is not artificially controlled. Since there is no strain information available for the PWR-water test case, we can check the strain ratcheting behavior by indirect means, i.e., by comparing the amplitude of actuator-positions and the corresponding mean actuator-positions (which are somehow related to gage area strain amplitude and mean strain).

For example Figure 8.20 shows the comparison of cycle versus observed actuator-position amplitude for the in-air (ET-F54) and PWR-water (EN-F56) fatigue test cases, and Figure 8.21 shows the comparison of cycle versus observed mean actuator position for the in-air (ET-F54) and PWR-water (EN-F56) fatigue test cases. From Figure 8.20 it can be seen that, as seen for stress amplitude, there is an initial bias in position amplitudes and that bias persisted up to the final failure of both specimens. Also, this figure doesn't clearly show any environmental effects on the time evaluation of actuator-position amplitudes. This result implies that there would be no visible effect on strain amplitudes even if it could be measured for the EN-F56 test case. However, from the mean actuator position histories (shown in Figure 8.21), it can clearly be seen that there is a time-evolution of environmental effect. This figure indirectly says that had strain been measured for the EN-F56 test case, the mean strain could have shown significant differences along the time-axis compared to the corresponding in-air test (ET-F54). From Figure 8.21, it can also be seen that the environmental effect mostly kicked in at approximately 1000 fatigue cycles (that is, at roughly 11% of the life of the EN-F56 specimen). However, note that the environment effect can kick in much earlier if a slower strain rate or loading rate followed. We plan to study the strain rate effect in the future. Nevertheless, from the above-discussed results, we can make the following four important observations:

- a) Under realistic reactor loading, mean strain and strain amplitude may not stay steady, as they do in artificially strain-controlled test cases.
- b) Strain or similar parameters (such as, in this case- frame actuator position) should be considered as the main damage-affecting variables rather than considering stress as the damage-affecting variable.
- c) The evolution of environmental effect significantly affects the mean strain, leading to faster ratcheting of strain in a PWR-water environment.
- d) A mechanism-based understanding of the environmental effect (like the above discussion) is necessary for accurate fatigue life estimation of reactor components.

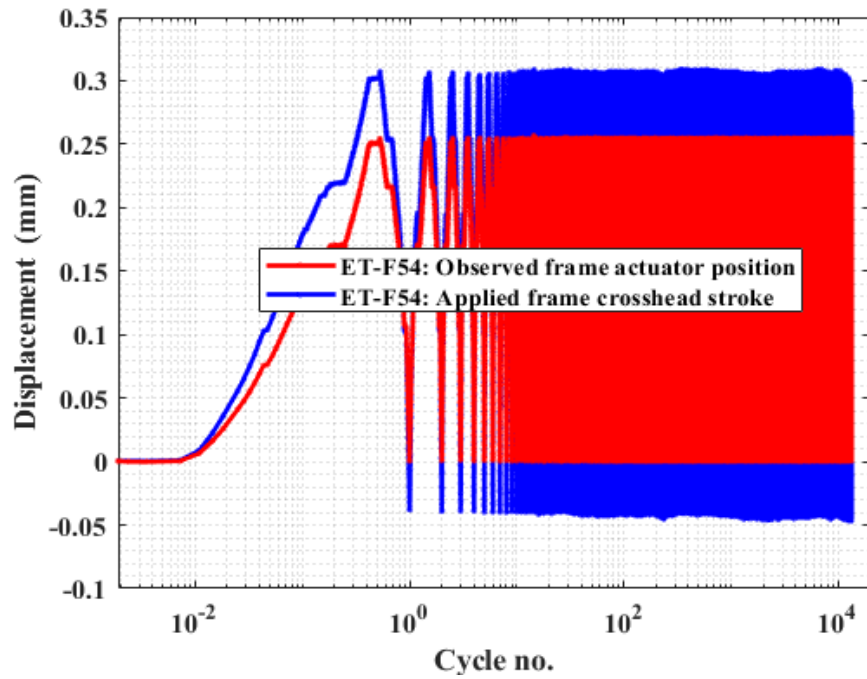


Figure 8.10 Cycle versus applied stroke and observed frame actuator position for in-air (ET-F54) fatigue test

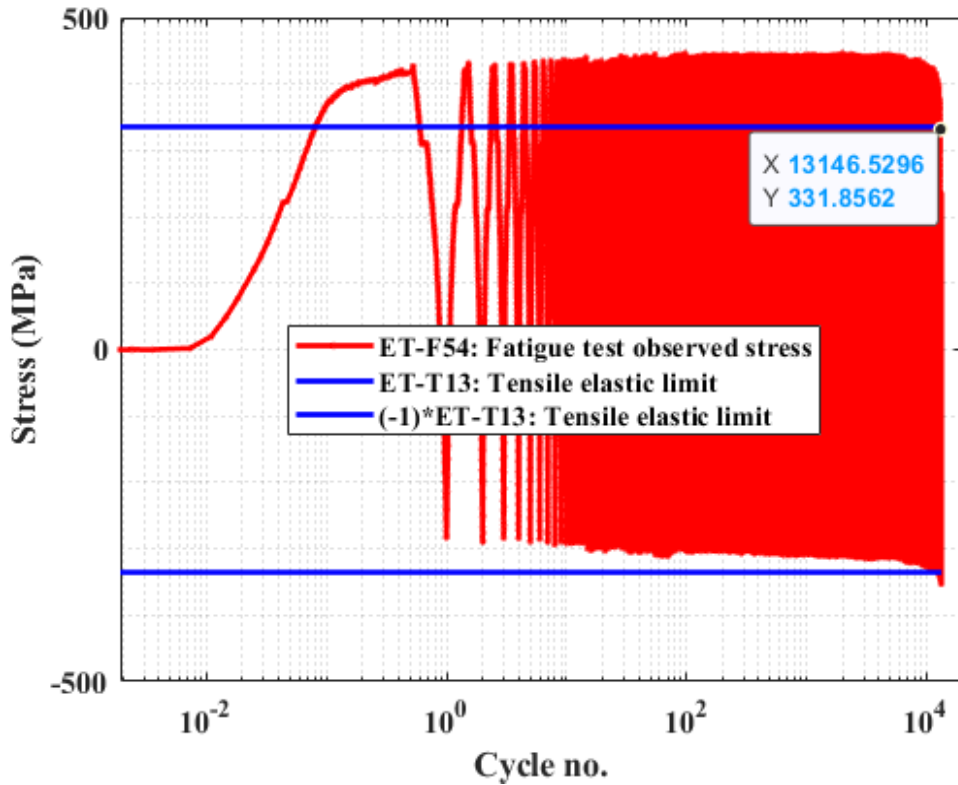


Figure 8.11 Cycle versus observed gauge-area stress for in-air (ET-F54) fatigue test

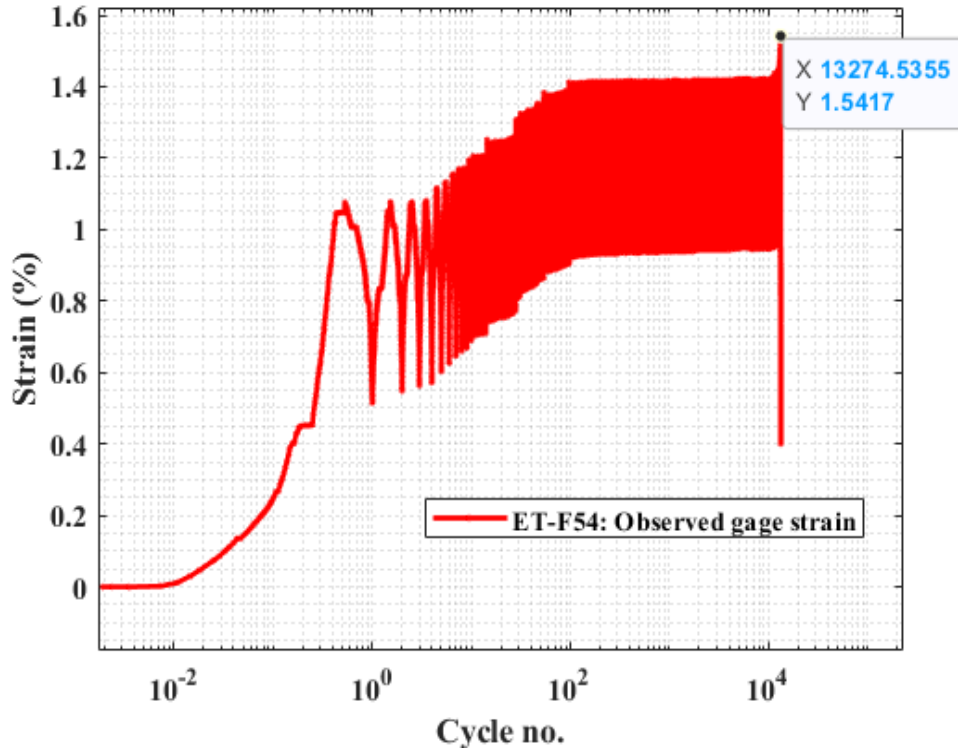


Figure 8. 12 Cycle versus observed gauge-area strain for in-air (ET-F54) fatigue test

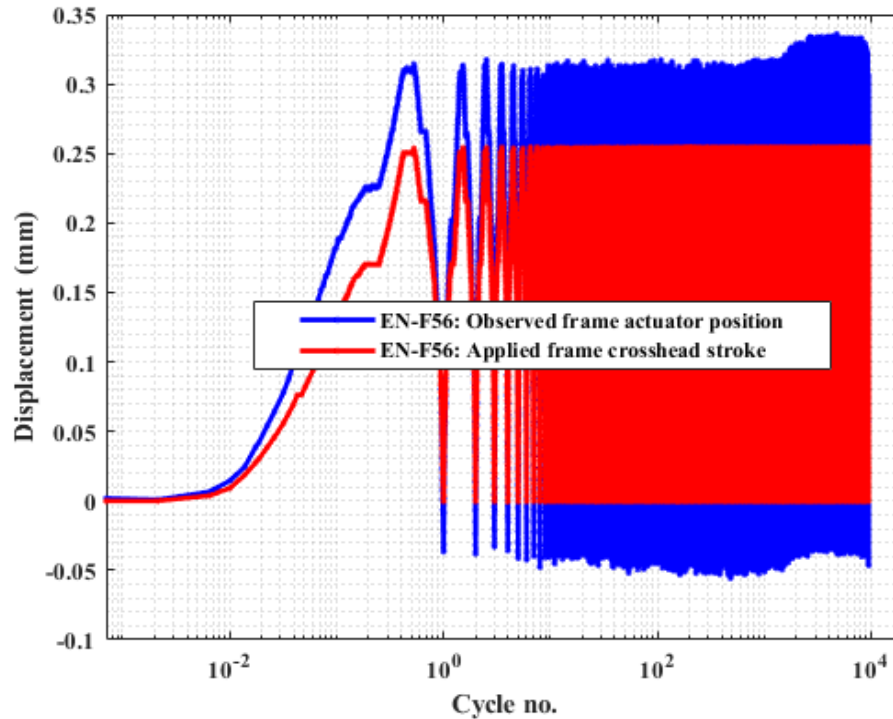


Figure 8. 13 Cycle versus applied stroke and observed frame actuator position for PWR-water (EN-F56) fatigue test.

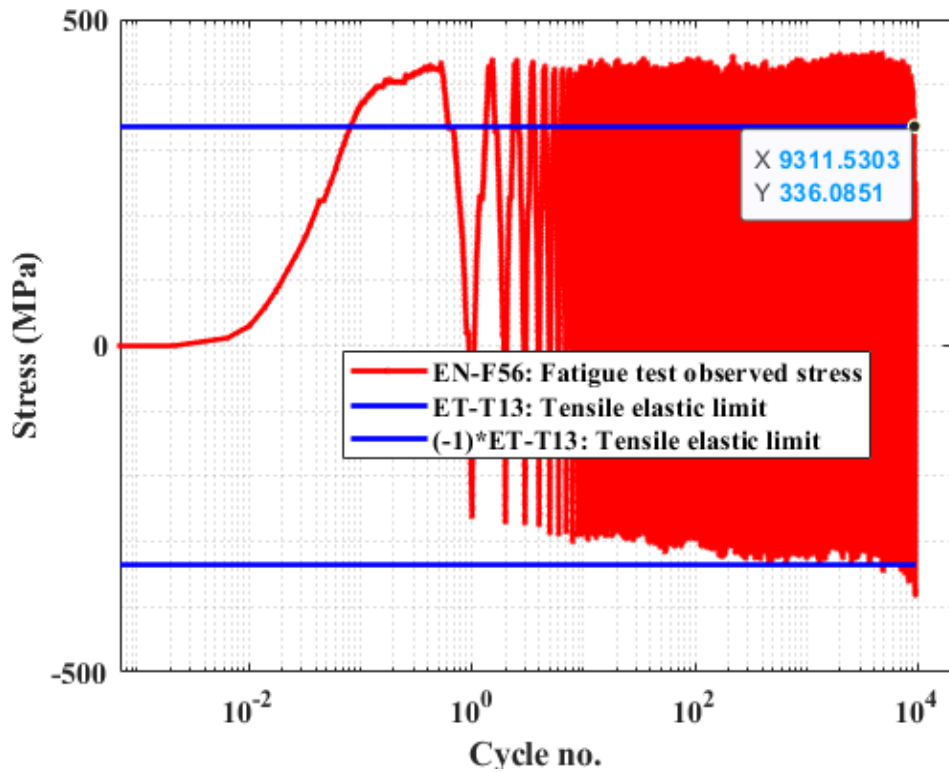


Figure 8. 14 Cycle versus observed gauge-area stress for PWR-water (EN-F56) fatigue test.

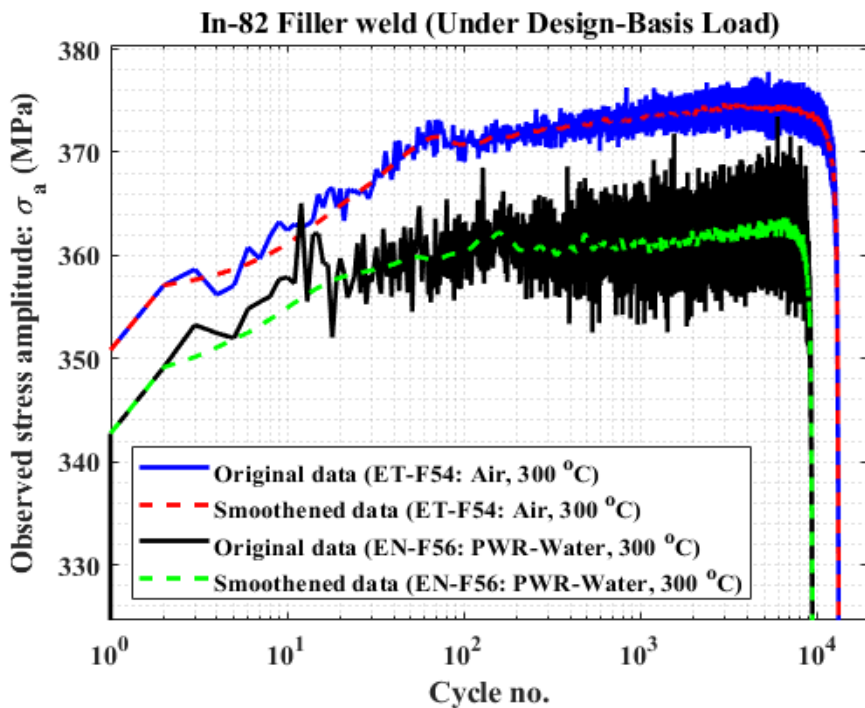


Figure 8. 15 Comparison of cycle versus observed stress amplitude for in-air (ET-F54) and PWR-water (EN-F56) fatigue tests.

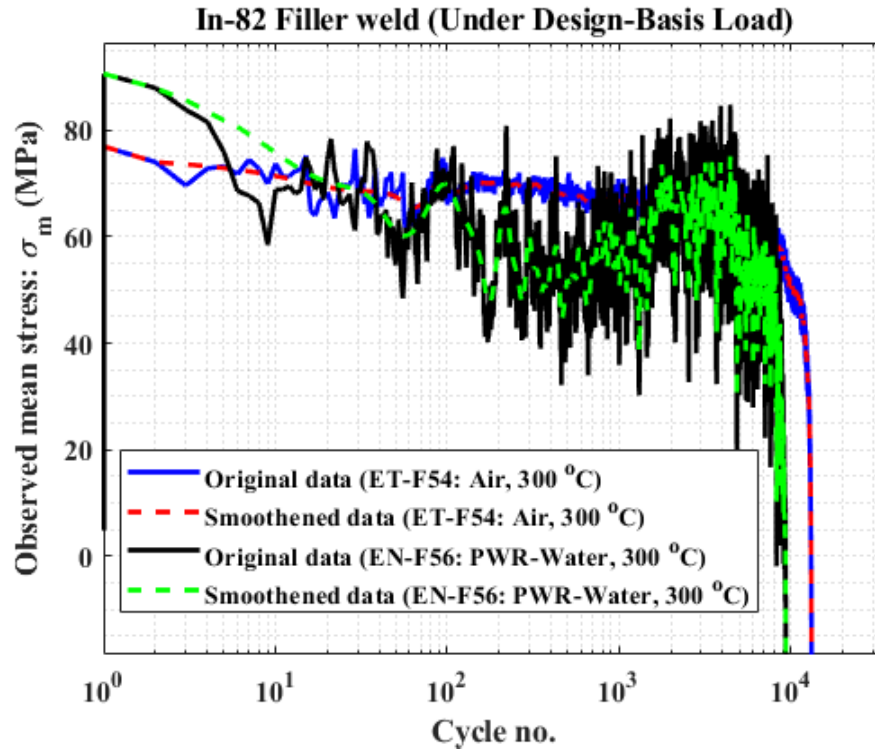


Figure 8. 16 Comparison of cycle versus observed mean stress for in-air (ET-F54) and PWR-water (EN-F56) fatigue tests.

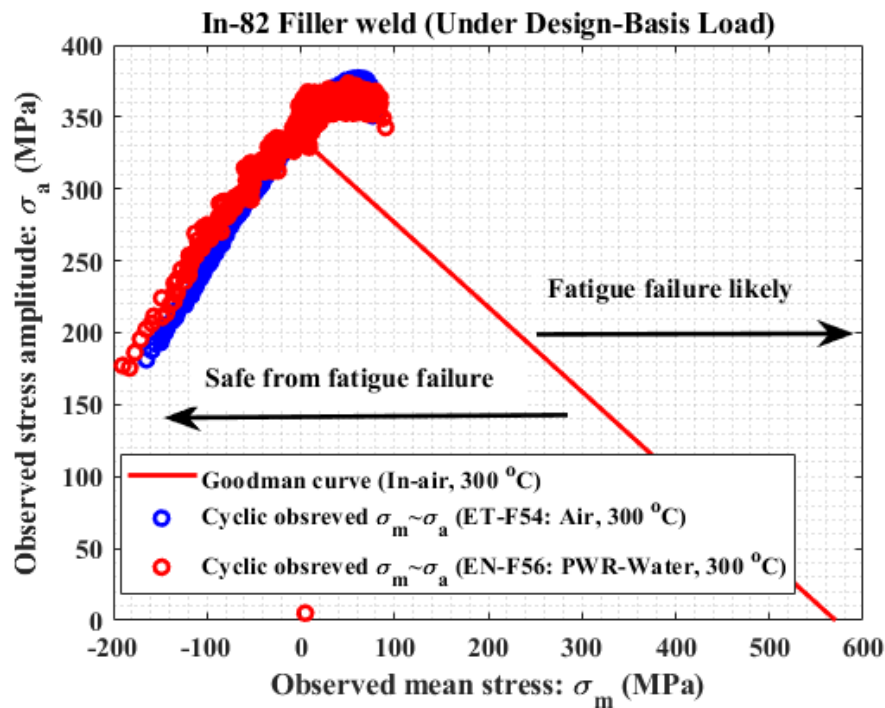


Figure 8. 17 Comparison of observed mean stress versus observed stress amplitude for in-air (ET-F54) and PWR-water (EN-F56) fatigue tests.

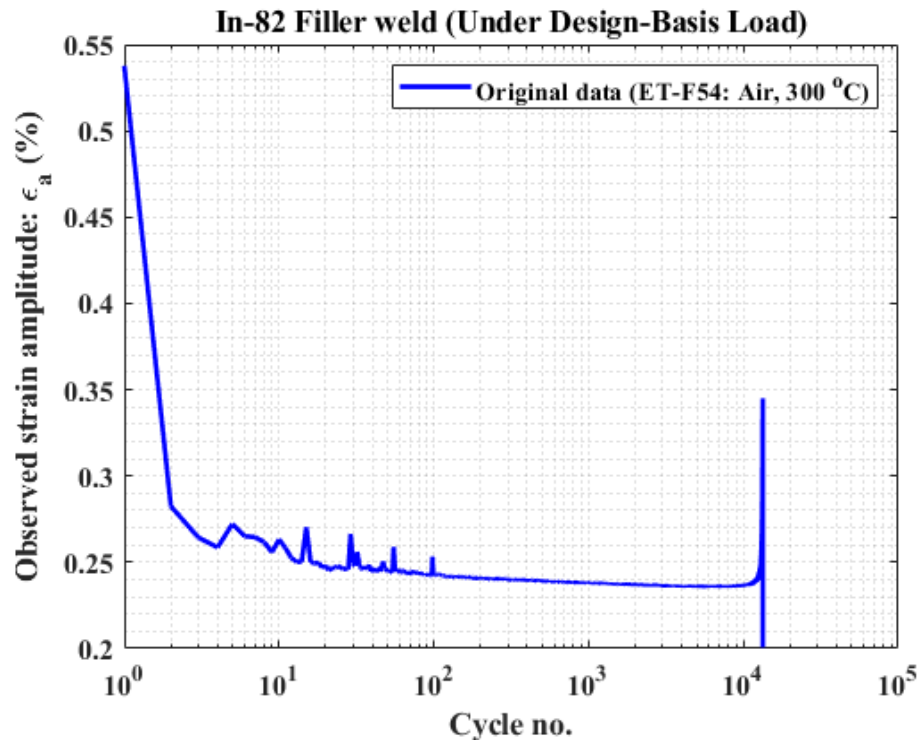


Figure 8. 18 Cycle versus observed gauge-area strain amplitude for in-air (ET-F54) test.

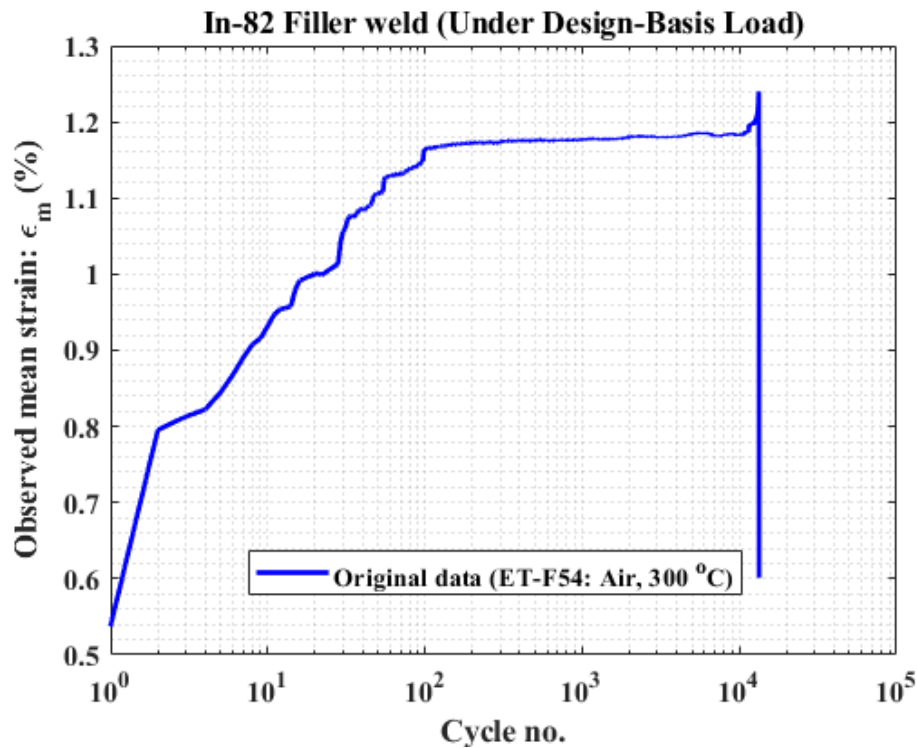


Figure 8. 19 Cycle versus observed gauge-area mean strain for in-air (ET-F54) test.

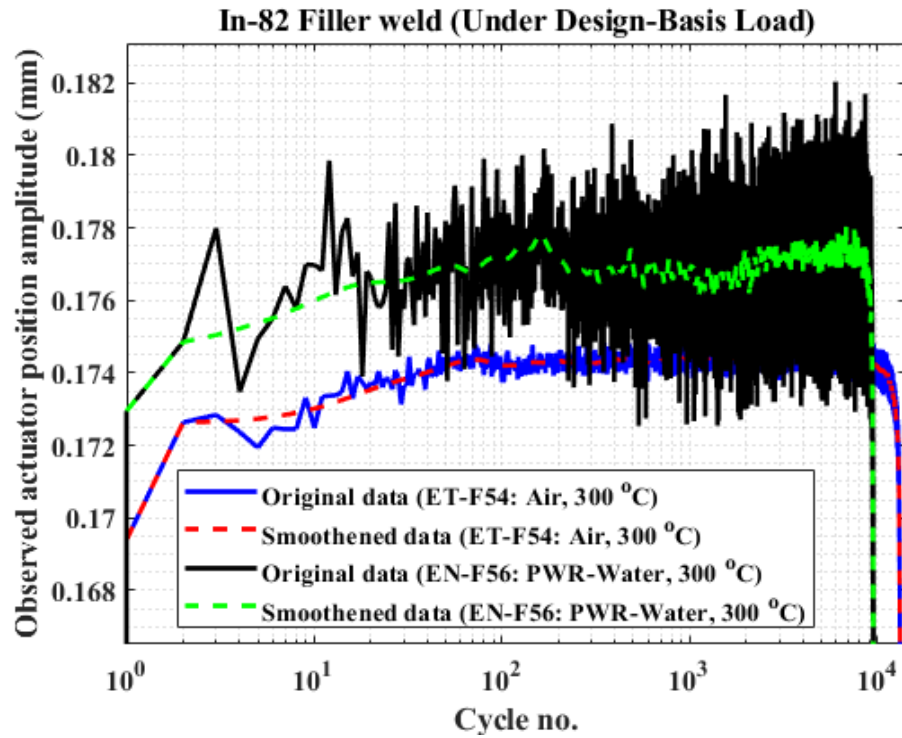


Figure 8. 20 Comparison of cycle versus observed actuator-position amplitude for in-air (ET-F54) and PWR-water (EN-F56) fatigue tests.

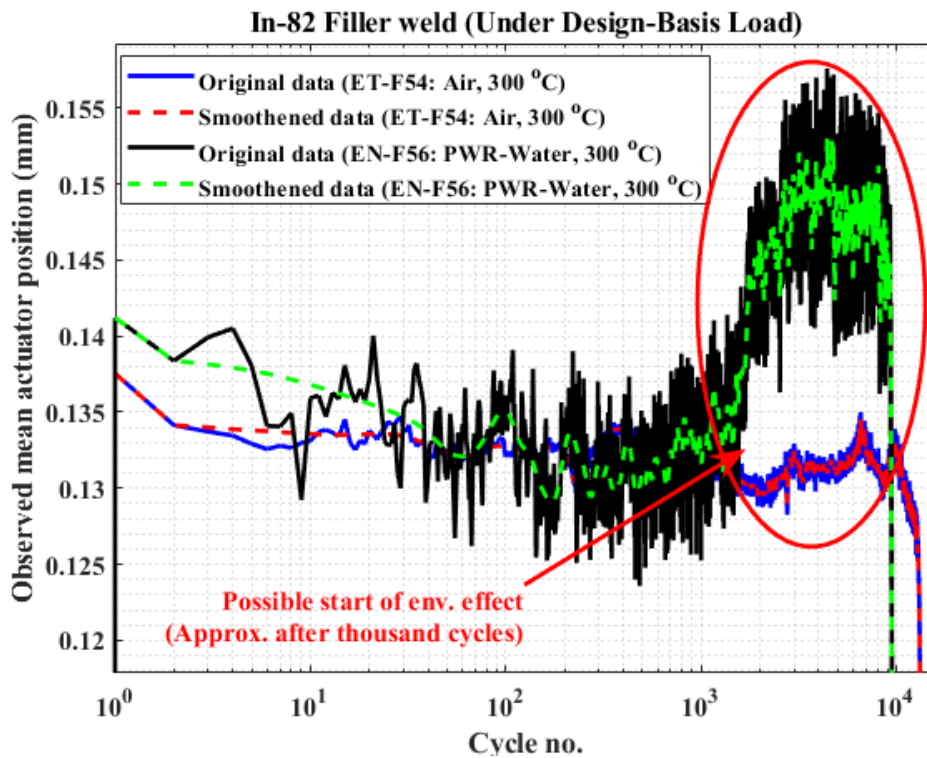


Figure 8. 21 Comparison of cycle versus observed mean actuator-position for in-air (ET-F54) and PWR-water (EN-F56) fatigue tests.

9 Summary and Future Studies

9.1 Summary

In this report, we have presented work in the following major areas:

- 1) A complete material-property database is presented. This database can be used for thermal-mechanical stress analysis of most of the reactor pressure boundary components comprising base metal and welds. The properties were estimated on the basis of 21 tensile tests conducted (either in FY 2019 or earlier) with the support of the LWRS program. The property database includes tensile properties, hardening properties, and expansion coefficients for 316SS base metal, 508LAS base metal, 316SS-316SS SMWs, and 316SS-508LAS DMWs (both In-82 filler welds and In-182 butter welds). The properties have been recorded in an easily searchable SQL database.
- 2) An ABAQUS-MATLAB-PYTHON-based software framework was developed to conduct weld layup-related manufacturing process modeling. This automated process drastically simplifies the effort required to model welds with a large number of weld passes (and with each pass consisting of multiple weld chunks). The procedure was demonstrated by modeling the SMWs and DMWs and the associated heat transfer in a pressurizer-surge-line nozzle.
- 3) Preliminary results are presented on a procedure to estimate the fatigue life of a pressurizer-surge-line nozzle assembly under design-basis loading cycles. The procedure depends on the combined use of FE-based thermal-mechanical stress analysis under the desired loading cycle and uni-axial fatigue experiments based on the FE-simulated strain profile.
- 4) For the design-basis loading cycle-based asymmetric fatigue testing of DMW-filler weld specimens, it is found that during the initial fatigue cycles the strain rapidly ratchets and then stabilizes. In contrast to the typical $R=-1$ type symmetrical strain-controlled test results, this type of strain ratcheting result is plausible and more realistic.
- 5) The sensitivity of cyclic strain and stress to a PWR-water environment was studied, and it is found that the effect of environment is more prominent in cyclic strain (or related displacement) measurements than cyclic stress measurements. Hence, it is suggested that one use strain as a measure of the cyclic aging/damage while developing mechanistically based approaches for environmental fatigue modeling.

9.2 Future Studies

Following are few possible areas in which the discussed work (in this report) can be further extended:

- 1) Develop a parallel-computing-based framework to perform the stress analysis of safety-critical reactor components/assemblies (such as pressurizer-surge-line-hot-leg connected assemblies) with thousands of nodal degrees of freedom and for thousands of fatigue cycles.
- 2) Develop FE-based stress analysis models with connected system displacement boundary conditions to include the effect of various load paths on the assembly.
- 3) Further, develop the FE-based weld manufacturing process modeling framework to capture the effect of weld residual stress in a component-level thermal-mechanical stress analysis.
- 4) Conduct more symmetrical and asymmetrical cycle fatigue testing (under both in-air and PWR-water conditions) of DMW filler and butter welds to further characterize these materials under cyclic loading and PWR-water environments.
- 5) Conduct more fatigue tests of DMW specimens using different strain rates and hold times to study their effects on environment fatigue life.
- 6) Develop time-evolution-based material models of DMWs and include those properties in FE-based cyclic stress analysis models.
- 7) Develop methodologies (such as using machine learning techniques) to estimate strain from other observed sensor measurements (such as under noisy PWR-water conditions for which strains are not easily measurable).
- 8) Develop probabilistic models such as fault tree and probabilistic time-series evolution models to predict risk based structural integrity.
- 9) Develop fully validated physical-digital-twin framework for real-time fatigue state monitoring and condition based damage state and remaining useful life prognostics.
- 10) Use the artificial intelligence and data analytics techniques to predict the time-series fatigue test data (both from laboratory specimen and actual component), but without conducting the time-consuming and costly actual tests (e.g. of very slow strain rate environmental fatigue tests, which take very long time to conduct).

References

1. https://energyworkshops.sandia.gov/wp-content/uploads/2018/10/Sandia_Blade_Workshop_NSE_Composites_toSandia.pdf
2. https://lessonslearned.faa.gov/DanAir/FS_vs_DTI.pdf
3. https://www.faa.gov/documentLibrary/media/Advisory_Circular/AC20-107B.pdf
4. Mohanty, S. (2010). *Structural health monitoring and condition based fatigue damage prognosis of complex metallic structures*. PhD, Thesis, Arizona State University, USA.
5. Mohanty, S., Jagielo, B., Iverson, W., Bahn, C., Soppet, W. K., Majumdar, S. and Natesan, K., "Online Stress Corrosion Crack and Fatigue Usages Factor Monitoring and Prognostics in Light Water Reactor Component: Probabilistic Modeling, System Identification and Data Fusion Based Big Data Analytics Approach September 2014, ANL/LWRS-14/2 (<http://www.osti.gov/scitech/biblio/1168230>).
6. Chattopadhyay, A. and Mohanty, S., Book chapter: "Gaussian Process Damage Prognosis under Random and Flight Profile Fatigue Loading", Machine Learning and Knowledge Discovery for Engineering Systems Health Management, Editors Ashok Srivastava and Jiawei Han, Chapman and Hall/CRC Press, Taylor and Francis Group (<http://www.amazon.com/gp/search?index=books&linkCode=qs&keywords=1439841780>)
7. Mohanty, S., Chattopadhyay, A., and Rajadas, John N. "Dynamic Strain Mapping and Real-Time Damage State Estimation under Biaxial Random Fatigue Loading", CIDU 2010 conference Mountain View, CA, October 5th - 7th, 2010, USA (one of the highest downloaded paper from NASA site, can be found from <https://c3.nasa.gov/dashlink/projects/35/>)
8. <https://www.nasa.gov/centers/ames/research/humaninspace/humansinspace-ivhm.html>
9. Rudolph, J., Bergholz, S., Heinz, B., & Jouan, B. (2012). AREVA Fatigue Concept—A Three Stage Approach to the Fatigue Assessment of Power Plant Components," in. *Nuclear Power Plants*.
10. Andrs, D., Berry, R., Gaston, D., Martineau, R., Peterson, J., Zhang, H., ... & Zou, L. (2012). *Relap-7 level 2 milestone report: Demonstration of a steady state single phase pwr simulation with relap-7* (No. INL/EXT-12-25924). Idaho National Laboratory (INL).
11. Mohanty, S., Soppet, W. K., Majumdar, S. and Natesan, K., "Thermal-mechanical stress analysis of PWR pressure vessel and nozzles under grid load-following mode: Interim report on the effect of cyclic hardening material properties and pre-existing cracks on stress analysis results. No. ANL/LWRS--16/01. March 2016, (<https://www.osti.gov/scitech/biblio/1249554>).
12. Mohanty, S., Soppet, W. K., Majumdar, S. and Natesan, K. "Tensile and Fatigue Testing and Material Hardening Model Development for 508 LAS Base Metal and 316 SS Similar Metal Weld under In-air and PWR Primary Loop Water Conditions", September 2015, ANL/LWRS-15/02 (<http://www.osti.gov/scitech/biblio/1224989>)
13. Mohanty, S., Barua, B., Listwan, J., Majumdar, S. and Natesan, K., Final Report on CFD and Thermal-Mechanical Stress Analysis of PWR Surge Line under Transient Condition Thermal Stratification and an Evolutionary Cyclic Plasticity Based Transformative Fatigue Evaluation Approach without Using S~N Curve, No. ANL/LWRS-17/03, Rev-1, September 2017 (<https://www.osti.gov/biblio/1480513>)

14. Mohanty, S., Barua, B., Listwan, J., Majumdar, S. and Natesan, K., “Implementation of ANL’s mechanics based evolutionary fatigue modeling through ABAQUS-WARP3D based high-performance computing framework,” Report No. ANL/LWRS-18/01. Argonne National Laboratory, April 2018 (<https://www.osti.gov/biblio/1480516>)
15. Mohanty, S., Park, J.P., Franken, D., Listwan, J., Majumdar, S. and Natesan, K., “A Deterministic and Probabilistic Framework for Forecasting of Time-Series Damage States and Associated End-of-Life of a Pressurizer Water Reactor Surge Line under Design-Basis and/or Grid-Load-Following Loading Conditions,” Report No. ANL/LWRS-18/02. Argonne National Laboratory, September 2018. (<https://www.osti.gov/biblio/1557591>)
16. Mohanty, S., Soppet, W. K., Majumdar, S. and Natesan, K. “Report on Assessment of Environmentally-Assisted Fatigue for LWR Extended Service Conditions”, September 2013, ANL/LWRS-13/3 (<https://www.osti.gov/biblio/1168222>).
17. https://www.aksteel.com/sites/default/files/2018-01/316316L201706_2.pdf
18. <http://www.pinnaclealloys.com/wp/wp-content/uploads/2015/11/Pinnacle-Alloys-E316-E316L-16-2.8.pdf>
19. <https://inldigitallibrary.inl.gov/sites/sti/sti/6269576.pdf>
20. <http://www.specialmetals.com/assets/smc/documents/smw/fm82.pdf>
21. <http://www.specialmetals.com/assets/smc/documents/smw/we182.pdf>
22. <http://www.specialmetals.com/assets/smc/documents/alloys/inconel/inconel-alloy-600.pdf>
23. Chaboche J. L., (1986) Time-independent constitutive theories for cyclic plasticity, *International Journal of Plasticity* 2: 149–188.
24. Mohanty, S., Soppet, W. K., Majumdar, S., & Natesan, K. (2015, July). Effect of pressurized water reactor environment on material parameters of 316 stainless steel: a cyclic plasticity based evolutionary material modeling approach., Paper no. PVP2015-45701, In ASME 2015 Pressure Vessels and Piping Conference (pp. V01AT01A039-V01AT01A039). American Society of Mechanical Engineers.
25. American Society of Mechanical Engineers’ (ASME’s) Pressure Vessel and Piping Code, 2017.
26. Mohanty, S., Soppet, W. K., Majumdar, S. and Natesan, K. “System-Level Heat Transfer Analysis, Thermal-Mechanical Cyclic Stress Analysis, and Environmental Fatigue Modeling of a Two-Loop Pressurized Water Reactor: A Preliminary Study”, April 2015, ANL/LWRS-15/1 (<http://www.osti.gov/scitech/biblio/1179020>).
27. W. Ramberg and W. R. Osgood, “Description of stress-strain curves by three parameters,” Technical Note No. 902, National Advisory Committee for Aeronautics, Washington DC., 1943.
28. Kim, Y. J., Huh, N. S., Kim, Y. J., Choi, Y. H., & Yang, J. S. (2004). On relevant Ramberg-Osgood fit to engineering nonlinear fracture mechanics analysis. *Journal of Pressure Vessel Technology, Transactions of the ASME*, 126(3), 277-283.
29. Ajit, K. P., Gautam, A., & Sarkar, P. K. (2016). Ductile behaviour characterization of low carbon steel: a CDM approach/Opis duktilnega vedenja maloogljičnega jekla po pristopu CDM. *Strojnikski Vestnik-Journal of Mechanical Engineering*, 62(5), 299-308.
30. Brickstad, B., & Josefson, B. L. (1998). A parametric study of residual stresses in multi-pass butt-welded stainless steel pipes. *International Journal of Pressure Vessels and Piping*, 75(1), 11-25.

31. Murugan, S., Kumar, P. V., & Raj, B. (1998). Temperature distribution during multipass welding of plates. *International journal of pressure vessels and piping*, 75(12), 891-905.
32. IAEA Report (2008), IAEA Nuclear Energy Series, "Heavy Component Replacement in Nuclear Power Plants: Experience and Guidelines", No. NP-T-3.2
33. Chopra, O. K., & Stevens, G. L. (2018). *Effect of LWR Water Environments on the Fatigue Life of Reactor Materials (NUREG/CR-6909, Revision 1) – Final Report*. United States Nuclear Regulatory Commission, Office of Nuclear Regulatory Research.

This page intentionally left blank



Nuclear Engineering Division

Argonne National Laboratory
9700 South Cass Avenue, Bldg. 208
Argonne, IL 60439

www.anl.gov



Argonne National Laboratory is a U.S. Department of Energy
laboratory managed by UChicago Argonne, LLC